First measurement of the inclusive ϕ meson production cross-section in pp collisions at $\sqrt{s}$ = 7 TeV and search for CP violation in the $B_s \to \phi\phi$ decay at LHCb

DISSERTATION

zur Erlangung des Doktorgrades der Naturwissenschaften
des Fachbereichs Physik der Technischen Universität Dortmund

vorgelegt von
DIPL. PHYS. SEBASTIAN SCHLEICH

im Oktober 2011

Gutachter: Prof. Dr. Bernhard Spaan
Priv.-Doz. Dr. Reiner Klingenberg

Abstract

Several studies towards the measurement of *CP* violation in the $B_s^0 \to \phi\phi$ decay channel with the LHCb experiment at the Large Hadron Collider at CERN are presented in this thesis. An important input to this analysis is precise knowledge of the detector performance and the ϕ meson production in proton-proton collisions. As a study targeting both goals, the first measurement of the inclusive ϕ meson production cross-section in pp collisions at a center-of-mass energy of $\sqrt{s} = 7\,\text{TeV}$ is carried out.

The *CP* violating phase in the $B_s^0 \to \phi\phi$ decay is predicted to vanish in the Standard Model of particle physics, but it could adopt finite values in some models beyond the Standard Model. Hereby this phase can distinguish different models and be a direct hint of "New Physics" in the case that a non-vanishing phase is measured.

The first step to an analysis of the $B_s^0 \to \phi\phi$ decay is the implementation of a signal pre-selection. The experimental techniques to extract the *CP* violating phase in this decay channel are developed and tested on samples simulated by event generators. Furthermore, the projective performance of the LHCb detector is determined from simulated samples and the signal and background yield expectation is extrapolated from data. Based on these analyses, the statistical uncertainty on the *CP* violating phase is predicted as 0.23 ± 0.04 for one nominal year ($2\,\text{fb}^{-1}$) of LHCb data taking.

As premise for *CP* violation studies, the detector performance needs to be understood. Further, since simulated samples are part of the analysis process, good agreement between the predictions and the real data is necessary. The ϕ meson production in pp collision is governed by the non-perturbative QCD regime, which event generators describe by phenomenological models that need to be tuned to data. The measurement of the inclusive ϕ meson production cross-section is an important probe of strangeness production in the context of this tuning effort.

The differential ϕ meson production cross-section is determined as a function of the ϕ transverse momentum p_T and rapidity y in the region $0.6 < p_T < 5.0\,\text{GeV}/c$ and $2.44 < y < 4.06$. The total ϕ meson production cross-section in this range is $\sigma(pp \to \phi X) = 1758 \pm 19(\text{stat})\,^{+43}_{-14}(\text{syst}) \pm 182(\text{syst})\,\mu\text{b}$, where the first systematic uncertainty depends on the p_T and y region and the second is related to the overall scale. Predictions based on the PYTHIA 6.4 generator underestimate the cross-section.

Zusammenfassung

Verschiedene Studien im Hinblick auf die Messung von *CP*-Verletzung im Zerfall $B_s^0 \to \phi\phi$ mit dem LHCb-Detektor am Large Hadron Collider LHC am CERN werden in dieser Arbeit vorgestellt. Wichtig für diese Analyse sind eine gute Kenntnis der Detektorperformanz und der ϕ-Meson-Produktion in Proton-Proton-Kollisionen. Als Analyse am Schnittpunkt dieser beiden Themengebiete wird die erste Messung des inklusiven ϕ-Meson-Produktionswirkungsquerschnitts in pp-Kollisionen bei einer Schwerpunktsenergie von $\sqrt{s} = 7\,\text{TeV}$ durchgeführt.

Die *CP*-verletzende Phase im Zerfall $B_s^0 \to \phi\phi$ wird vom Standardmodell der Elementarteilchenphysik zu Null vorhergesagt, aber sie kann in einigen Modellen über das Standardmodell hinaus endliche Werte annehmen. Damit kann diese Phase verschiedene Physikmodelle diskriminieren und unter Umständen ein direkter Hinweis auf „Neue Physik“ sein, falls eine von Null abweichende Phase gemessen wird.

Der erste Schritt zu einer Analyse des Zerfalls $B_s^0 \to \phi\phi$ ist die Implementierung einer Signal-Vorselektion. Ferner werden die experimentellen Techniken zur Extraktion der *CP*-verletzenden Phase in diesem Zerfallskanal entwickelt und auf von Ereignisgeneratoren simulierten Samples getestet. Schließlich wird die erwartete Performanz des LHCb-Detektors im $B_s^0 \to \phi\phi$-Kanal auf Basis von simulierten Daten und der aus echten Daten extrapolierten Signal- und Untergrunderwartung bestimmt. Basierend auf diesen Analysen wird die statistische Unsicherheit auf die *CP*-verletzende Phase zu 0.23 ± 0.04 mit einem nominellen Jahr Datennahme ($2\,\text{fb}^{-1}$) vorausgesagt.

Eine wesentliche Voraussetzung für Studien von *CP*-Verletzung ist eine gute Kenntnis der Detektorperformanz. Weil weiterhin simulierte Daten ein Teil des Analyseprozesses sind, ist gute Übereinstimmung zwischen Vorhersage und echten Daten notwendig, was hier in Bezug auf ϕ-Mesonen untersucht wird. Die ϕ-Meson-Produktion in pp-Kollisionen wird wesentlich durch das nichtperturbative Regime der QCD geprägt. Es wird von Ereignisgeneratoren durch phänomenologische Modelle beschreiben, welche an Daten angepasst werden müssen. Die Messung des inklusiven ϕ-Meson-Produktionswirkungsquerschnitts ist ein wichtiger Test der Strangeness-Produktion im Kontext dieses Anpassungsprozesses.

Der differenzielle ϕ-Meson-Produktionswirkungsquerschnitt wird als Funktion des Transversalimpulses p_T und der Rapidität y des ϕ-Mesons im Bereich $0.6 < p_T < 5.0\,\text{GeV}/c$ und $2.44 < y < 4.06$ gemessen. Der totale ϕ-Meson-Produktionswirkungsquerschnitt in diesem Bereich ist $\sigma(pp \to \phi X) = 1758 \pm 19(\text{stat})\,^{+43}_{-14}(\text{syst}) \pm 182(\text{syst})\,\mu\text{b}$, wobei die erste systematische Unsicherheit vom p_T- und y-Bereich abhängt und die zweite sich auf die globale Skalierung bezieht. Die Daten werden mit Vorhersagen des Ereignisgenerators PYTHIA 6.4 verglichen, die den Wirkungsquerschnitt unterschätzen.

Contents

– blank page –

Introduction

The Standard Model is the most comprehensive and experimentally tested theory in high energy physics. Although there are no measurements which are in direct contradiction to the Standard Model, it still leaves open questions. Naming some of them, the Higgs boson is needed in the theoretical framework, but its existence is not established experimentally. Furthermore, observations suggest a high dominance of matter over antimatter in the universe. Under the assumption that the universe was initially composed of equal portions of matter and antimatter, this requires the three Sakharov conditions [1] baryon number violation, *C* next to *CP* violation and thermal non-equilibrium to hold. The Standard Model *does* indeed predict *C* and *CP* violation, but at a small level, which is why so far unknown sources of *CP* violation are searched for – for example in neutral *B* meson mixing and decays.

The Large Hadron Collider (LHC) aims at putting the Standard Model on probe by finding signatures that argue for physics models beyond the Standard Model. The LHC is capable of colliding proton beams or ion beams and started normal operation at CERN in late 2009. There are four major experiments at the LHC, one of which is the Large Hadron Collider beauty (LHCb) experiment, which adopts an indirect searching strategy: physics beyond the Standard Model, for example "new" –so far unobserved– particles, might alter the coupling constants in rare processes and hereby the degree of *CP* violation.

The $B_s^0 \to \phi\phi$ decay is a theoretically clean handle on *CP* violation in neutral *B* meson mixing and decay: since the Standard Model predicts a vanishing *CP* violating phase in this channel, a nil test could reveal physics effects that the Standard Model does not incorporate. First evidence of the $B_s^0 \to \phi\phi$ decay was published by the CDF collaboration in 2005 [2]. The branching fraction of this decay is as low as $\mathcal{BR}(B_s^0 \to \phi\phi) = [2.40 \pm 0.21(\text{stat}) \pm 0.27(\text{syst}) \pm 0.82(\text{BR})] \cdot 10^{-5}$ [3][1] and measurements of triple product asymmetries have first been carried out by CDF [4, 5]. Triple products are odd under time reversal and hereby sensitive to *CP* violation assuming the *CPT* theorem [6]. Two of these asymmetries have been measured, one of which is consistent with the Standard Model prediction zero and the other exhibits a 1.8σ deviation [5]. LHCb was also able to carry out such a triple product measurement after roughly one year of data taking, which is already competitive with the one cited above [7]. There is no indication of *CP* violation in the LHCb measurement either, however, both measurements leave room for discoveries due to the relative large statistical uncertainties. The early measurement by LHCb is an indication that it will deliver plentiful high quality data in the future to directly extract the *CP* violating phase in the $B_s^0 \to \phi\phi$ decay by an angular analysis as described in this thesis.

Next to studies towards the analysis of *CP* violation in the $B_s^0 \to \phi\phi$ decay, which are described in this thesis, the author's working group contributed to the development of an inclusive ϕ trigger [8]. In view of these efforts it came in naturally to also contribute to pioneering ϕ reconstruction on real data as soon as LHCb started data taking. Not only is understanding the ϕ reconstruction and LHCb's particle identification system an essential step towards studies of $B_s^0 \to \phi\phi$, but also is the determination of the ϕ production cross-section an important measurement, as explained in the following.

[1] The studies presented here refer to [3]; this number was very recently updated to $\mathcal{BR}(B_s^0 \to \phi\phi) = [2.32 \pm 0.18(\text{stat}) \pm 0.82(\text{syst})] \cdot 10^{-5}$ [4].

A tool commonly used in high energy physics are Monte Carlo based event generators, which strive for a realistic description of particle interactions. Whereas so-called "hard" processes are accessible to perturbative QCD calculations, the so-called underlying minimum bias event falls into the non-perturbative regime. Event generators like PYTHIA [9] describe it based on phenomenological models, which need to be tuned on data. This tuning requires measurements of particle-antiparticle ratios, meson-baryon ratios and inclusive particle production cross-sections. LHCb contributed considerably to this field of research. For example, LHCb's first publication was a measurement of K^0_S production spectra [10]. Furthermore, analyses of the J/ψ production cross-section [11] and the $\overline{p}/p$, $\overline{\Lambda}/\Lambda$ and $\overline{\Lambda}/K^0_S$ ratios were carried out [12, 13]. Measurements of ϕ meson production have been reported by various experiments [14–19] for different center-of-mass energies and different kinematic coverage. LHCb is fully instrumented in the forward region and thus yields unique results complementary to previous experiments and to the other LHC experiments. A measurement of the inclusive ϕ cross-section is carried out within the scope of this thesis. Being the first ϕ cross-section measurement at $\sqrt{s} = 7\,\text{TeV}$, it is an important input to future Monte Carlo tunes.

This thesis can be subdivided into four major parts:

1. **Motivation**

   Chapter 1 outlays the theoretical framework. It introduces the Standard Model and its open questions. Sources of *CP* violation are presented and experimental handles introduced. Finally, the basis of event generation with PYTHIA is explained.

2. **Experimental setup**

   In Chapter 2, the LHC project is presented and the LHCb experiment is described. This description first gives an overview over the detector hardware before it moves on to the online- and offline- analysis software.

3. **Studies of *CP* violation in the $B^0_s \to \phi\phi$ channel**

   In Chapter 3, the method of extracting the $B^0_s \to \phi\phi$ decay from LHCb data is presented. A selection is analyzed on Monte Carlo generated samples and a so-called stripping line is developed. Finally, the B^0_s mass peak is reconstructed in the $B^0_s \to \phi\phi$ channel from early LHCb data and compared to event generator predictions and previous measurements.

   The extraction of the *CP* violating phase in the $B^0_s \to \phi\phi$ decay is complicated by the final state being an admixture of *CP* eigenstates. Chapter 4 explains how these are disentangled on a statistical basis with a maximum likelihood fit. This fit procedure is verified on Monte Carlo generated samples and studies of the expected statistical uncertainty on the *CP* violating phase are presented.

4. **Inclusive ϕ meson production cross-section**

   Chapter 5 introduces the inclusive ϕ analysis strategy and the data-taking conditions. Being one of the first analyses to strongly depend on LHCb's particle identification (PID) system, intensive studies of its performance are carried out. In Chapter 6, studies of the systematic effects are presented before the cross-section results are given in Chapter 7.

CHAPTER 1

Motivation

The Standard Model is a theoretical description of elementary particle interactions, which is in good agreement with the particle physics experiments carried out up to now. It can be considered the "baseline" theory of particle physics, even though physics beyond the Standard Model is assumed to exist. This chapter opens up reviewing the Standard Model and outlining the questions which it leaves unanswered (Section 1.1).

One of the open questions is the amount of *CP* violation, an asymmetry of physics processes between matter and antimatter. *CP* violation is necessary to explain the abundance of matter in the universe and the Standard Model *does* entail it by the Cabibbo-Kobayashi-Maskawa (CKM) mechanism (Section 1.2). However, the degree of CP violation predicted by the SM is considered as too low [20, 21] to explain the amount of matter in the universe, so that new sources of *CP* violation, beyond the Standard Model, are searched for. Oscillations of neutral B mesons, quark-antiquark bound states of a b plus an s or d, are an important probe of *CP* violation. These oscillations are described (Section 1.3) by the meson being prepared as superposition as two quantum-mechanical states, which can be either detected as meson or antimeson. The $B_s^0 \to \phi\phi$ and $B_s^0 \to J/\psi\,\phi$ decays are finally presented as testing grounds for *CP* violation.

Experimental analyses like the one discussed above rely to some part on Monte Carlo simulated samples based on event generators. While hard processes like the production of B mesons are accessible by perturbative quantum chromodynamics (QCD) calculations, the modeling of the underlying minimum bias event falls in the soft QCD regime. Here, predictions base on phenomenological models, which need to be tuned to data. A brief introduction to one of these models is given in Section 1.4 and the importance of inclusive production studies like the measurement of the ϕ meson (predominantly a bound state of a strange quark and a strange antiquark) production cross-section is stressed.

1.1. The Standard Model

The elementary particles, quarks and leptons, are grouped in three generations, each of which comprises two particle types. These are the following quarks:

u	up	c	charm	t	top
d	down	s	strange	b	bottom

and the following leptons:

ν_e	electron-neutrino	ν_μ	muon-neutrino	ν_τ	tau-neutrino
e	electron	μ	muon	τ	tau

Each of these particles can not only occur as *particle*, but also as *antiparticle*.

Interactions are mediated by gauge bosons, which are

- $W^\pm$ and Z^0 bosons for the charged and the neutral weak currents
- photons γ for the electromagnetic interaction
- gluons g for the strong interaction.

The Standard Model, a relativistic quantum field theory, provides a universal description of these interactions, which is reviewed e.g. in References [22–25].

The Standard Model Lagrangian $\mathcal{L}_{\mathrm{SM}}$ can be broken up into the following parts:

$$\mathcal{L}_{\mathrm{SM}} = \mathcal{L}_{\mathrm{SU(3)}} + \mathcal{L}_{\mathrm{SU(2)}_L \otimes \mathrm{U(1)}_Y} \ . \tag{1.1}$$

Here, the first term describes the quantum chromodynamics (QCD), which is an SU(3) group with eight types of gluons as gauge bosons. The second term is the Lagrangian of the Glashow-Salam-Weinberg (GSW) model [26, 27], which unifies the weak interaction and the electromagnetic interaction.

Interaction strengths depend on a *coupling constant* and the *charge* of a particle with respect to this interaction, which has opposite sign for particles and their antipartners. These charges are the *color* for the strong interaction and *weak isospin* next to *electrical charge* for the electroweak interaction. Leptons do not participate in the strong interaction, since only quarks carry color. The coupling of the strong interaction increases with lower energies and correspondingly larger distances, whereas asymptotic freedom occurs at small length scales [28, 29]. Quarks are subject to confinement meaning they are only observed in bound states called hadrons. The experimentally established ones are mesons, built of a quark-antiquark pair and baryons consisting of three quarks which can either be quark or antiquark. As an exception, the top quark does not hadronize because of its instant decay.

The weak interaction acts on all particle types, but it is sensitive to their handedness: The SU(2) group acts on the left-handed doublets (L) shown below, whereas right-handed particles (R) are singlets under these transformations.

$$\begin{pmatrix} u \\ d \end{pmatrix}_L \quad \begin{pmatrix} c \\ s \end{pmatrix}_L \quad \begin{pmatrix} t \\ b \end{pmatrix}_L \qquad u_R \quad d_R \quad c_R \quad s_R \quad t_R \quad b_R$$

$$\begin{pmatrix} \nu_e \\ e \end{pmatrix}_L \quad \begin{pmatrix} \nu_\mu \\ \mu \end{pmatrix}_L \quad \begin{pmatrix} \nu_\tau \\ \tau \end{pmatrix}_L \qquad e_R \quad \mu_R \quad \tau_R$$

Assuming neutrinos to occur only left-handed, no mass is attributed to them by the Higgs mechanism described below. Yet, it is possible to extend the Standard Model with right-handed neutrinos as discussed in Section 1.1.2.

The $W^{\pm}$ and Z^0 bosons gain mass due to spontaneous symmetry breaking through the Englert-Brout-Higgs-Guralnik-Hagen-Kibble mechanism [30–32]. In order to attribute a mass also to the fermions, an additional term, the Yukawa interaction, has to be introduced. It describes couplings between the Higgs- and the fermion field through 3×3 mass matrices, which are different for the up- and down-type field in each doublet. These matrices are not necessarily diagonal and hereby they mix between different generations, but they can be diagonalized using an appropriate transformation. In contrast, the gauge interaction does not mix the different families, so that the aforementioned transformation has to be done in calculations of the weak interaction of (physical observable) mass eigenstates. For charged currents ($W^{\pm}$ mediated), they introduce the 3×3 Cabibbo-Kobayashi-Maskawa matrix V_{CKM} (see Section 1.2), which accounts for intergenerational processes. Neutral currents, however, are left unchanged by this transformation, so that flavor changing neutral currents can only occur at higher orders of perturbation theory (loop level).

1.1.1. Symmetries and symmetry breaking

The Standard Model is strongly based on discrete and continuous symmetries [33]. Symmetries, which are transformations that leave the Lagrangian invariant, play an important role in many fields of physics: They are linked to conservation laws through Noether's theorem: As an example, which is valid not only in quantum-mechanical but also classical context, *continuous* symmetries like rotational- or translational invariance are equivalent to angular momentum or momentum conservation. Another group of symmetries are *discrete symmetries*, for example permutations, which govern Bose-Einstein or Fermi-Dirac statistics in quantum mechanics.

As already addressed in the previous section, the Standard Model describes particle interactions through *continuous* local gauge symmetries. Here, the SU(3) group governs the strong interaction, whereas the $\mathrm{SU}(2) \otimes \mathrm{U}(1)$ is the symmetry of the GSW model, which is spontaneously broken by the Higgs mechanism.

Next, the behavior of the Standard Model under the following discrete symmetries shall be reviewed [34], since the question whether or not they are conserved plays a crucial role. For example, they relate the interactions of particles to the ones of antiparticles and thus, have a deep impact on cosmology (Section 1.1.2).

- **Parity *P***
  Inverts the sign of all space-like coordinates. Therefore, it swaps the handedness of a coordinate system and the sign of momentum and helicity.
- **Time reversal *T***
  Inverts the sign of the time coordinate, i.e. also of the velocity, the momentum, angular momentum and spin.
- **Charge conjugation *C***
  Inverts the sign of all charge-like quantum numbers. Thus, it transforms a field describing a particle into the corresponding antiparticle's one.

As described in the previous section, the weak interaction differentiates between handedness. Due to the chirality dependence introduced by that, it should violate parity conservation. This parity

violation has been observed experimentally first in β^- decays of ^{60}Co [35]. Cobalt was embedded in a crystal which allowed to polarize the cobalt nuclei after cooling the system down to 0.01 K. The emission direction of the β^- was measured in dependence of the magnet polarity and the temperature. At low temperature, when the ^{60}Co nuclei were polarized, the β^- had a preferred direction, which establishes *P* violation.

Whereas the weak interaction is found to violate parity, historically speaking, the assumption was sensible that it would conserve *CP* [36]: It couples to left-handed particles and right-handed antiparticles and an antiparticle state can be generated by applying the *CP* operation on a particle state. However, *CP* violation was experimentally established in the neutral K meson system [37].

A relativistic local quantum field theory like the Standard Model is invariant under simultaneous application of *C*, *P* and *T* according to the *CPT* theorem [6]. As a consequence, *CP* violation is equivalent to *T* violation.

1.1.2. Open questions of the Standard Model

The Standard Model is in excellent agreement with experimental findings. It has passed precision measurements and historically, it proved of a high predictive power, for example it correctly predicted the existence and the mass of the top quark. The particles involved in the Standard Model are all observed except for the Higgs boson. Still, there are many open questions, which are addressed in this section based on the review in Reference [38].

If created in the big bang, matter and antimatter should be produced in equal portions. The current state of the universe is that we live in an abundance of matter and the possibility of having a "patch work" where antimatter is concentrated at other places of the universe would contradict experimental findings. – One would observe annihilation radiation at the boundary and the subsequent annihilation would alter the cosmic microwave background spectrum [39].

Three conditions, baryon number violation and *C* next to *CP* violation during rapid expansion in non-thermal equilibrium [1, 21] could explain the excess of matter. Actually, *CP* violation is part of the Standard Model, but its degree is considered as low [20, 21], which is why further sources of *CP* violation are searched for. Another problem linked to *CP* violation is that the strong interaction is found to be *CP* conserving. While this is not per se in contradiction with the Standard Model, it does not give a compelling reason except for fine-tuned parameters. The Peccei-Quinn theory offers a solution by introducing a spontaneously broken symmetry. It would naturally explain why the *CP* violating term in the QCD Lagrangian vanishes, but it requires an additional particle, the Axion, which is experimentally not established.

Apart from not explaining the provenance of matter, the Standard Model has another problem: The gravitational forces in galaxies are linked to the amount of matter and can be estimated from their gamma radiation emitted, but these observations do not fit to the speed of motion of stars and gases in galaxies [39]. A conclusion could be that there is more, "dark" matter, which also interacts gravitationally, but is invisible. The nature of this dark matter is not experimentally established.

The Higgs mechanism offers an explanation for the masses of the massive gauge bosons and also for quarks and leptons through the Yukawa mechanism. However, the particle masses are proportional to their Yukawa coupling constants which are not predicted by the Standard Model. Furthermore, the existence of the Higgs boson is not experimentally established, though strong bounds on its mass exist from precision measurements.

Calculating the quantum corrections to the mass of the Higgs boson provokes the *fine tuning* problem: the relatively low mass of the Higgs boson could be explained only by careful choice of parameters, which appears "unnatural".

The Standard Model as presented in the previous section does not contain right handed neutrinos because no mass is assigned. One possible explanation for neutrino oscillations (though not the only one according to Reference [34]) are massive neutrinos, which could be embedded in several possible ways in the Standard Model. For example, neutrinos could be their own antiparticles (Majorana particles).

Finally, the Standard Model incorporates all known forces except for gravity, so the question arises whether first, it is possible to formulate a theory of quantum gravitation and whether second, it is possible to unify this force with the strong and the electroweak force.

While it is clear that the Standard Model yields precise results in many fields of particle physics, extensions of the Standard Model or new theories are designed which should be compatible with the Standard Model in these fields. As one example, by assigning a supersymmetric partner for each type of elementary particle, supersymmetry [40] solves the hierarchy problem naturally. Further, light supersymmetric particles are good candidates for dark matter. However, there is no experimental evidence for supersymmetry up to now.

Due to the large variety of theories, an all-embracing presentation of New Physics models would go far beyond the scope of this thesis. However, as motivation for the studies presented in this thesis it is sufficient to understand a basic idea: in the next sections, it will be shown that *CP* violation in the Standard Model is closely linked to interference effects in loop calculations, in particular the couplings and the virtual particles in the loop diagrams. Consequently, models with new particles could alter the degree of *CP* violation, which positions studies of *CP* violation as important "indirect" probe of New Physics.

1.2. *CP* violation in the Standard Model and the CKM matrix

By construction of the Standard Model, *CP* violation can arise in processes where two complex transition amplitudes interfere, which have a relative phase to each other. Such a phase is introduced in charged currents of the weak interaction by the Cabibbo-Kobayashi-Maskawa (CKM) matrix [41, 42], which properties are described in this section.

As indicated in Section 1.1, the GSW model distinguishes weak eigenstates and mass eigenstates, which introduces the CKM matrix in the charged currents of the weak interaction. A common convention is to choose the basis such that the weak- and mass-eigenstates coincide for up-type quarks. Then, the weak eigenstates (d', s', b') are linked to the mass eigenstates (d, s, b) through the relation reviewed e.g. in Reference [43]:

$$\begin{pmatrix} d' \\ s' \\ b' \end{pmatrix} = V_{\mathrm{CKM}} \begin{pmatrix} d \\ s \\ b \end{pmatrix} \qquad \text{with: } V_{\mathrm{CKM}} = \begin{pmatrix} V_{ud} & V_{us} & V_{ub} \\ V_{cd} & V_{cs} & V_{cb} \\ V_{td} & V_{ts} & V_{tb} \end{pmatrix} . \tag{1.2}$$

The CKM matrix is a unitary, complex matrix and as such, it might depend on three real angles and six phases [44]. However, since the phases of the quark mass eigenstates are not physically relevant, five of these phases can be eliminated, which leaves *three angles* and *one phase*. This phase is the only source of *CP* violation in the Standard Model, except for strong *CP* violation, which is theoretically possible, but not realized by nature.

In the absence of right-handed neutrinos, no mass is established for neutrinos by the Yukawa mechanism. Also, the charged-lepton mass eigenstates coincide with the flavor eigenstates, i.e. no "CKM like" matrix is necessary. Following this model, there is no *CP* violation in the lepton sector [34]. However, since massive neutrinos would be a plausible explanation for neutrino oscillations, the model might have to be extended to incorporate neutrino masses. These extensions can lead to *CP* violation in leptonic interactions, too [34].

1.2.1. Parametrization of the CKM matrix

The most common parametrization [44, 45] for the CKM matrix is

$$V_{\mathrm{CKM}} = \begin{pmatrix} c_{12}c_{13} & s_{12}c_{13} & s_{13}e^{-i\delta} \\ -s_{12}c_{23} - c_{12}s_{23}s_{13}e^{i\delta} & c_{12}c_{23} - s_{12}s_{23}s_{13}e^{i\delta} & s_{23}c_{13} \\ s_{12}s_{23} - c_{12}c_{23}s_{13}e^{i\delta} & -s_{23}c_{12} - s_{12}c_{23}s_{13}e^{i\delta} & c_{23}c_{13} \end{pmatrix} \tag{1.3}$$

with $s_{ij} = \sin\theta_{ij}$ and $c_{ij} = \cos\theta_{ij}$ and the complex phase δ.

The hierarchy of the CKM matrix is best expressed in the Wolfenstein parametrization [44, 46] in the four parameters λ, A, ρ and η. With λ being approximately the Cabbibo angle $\lambda \approx 0.23$, the matrix is expanded as a series in orders of λ:

$$V_{\mathrm{CKM}} = \begin{pmatrix} 1-\frac{1}{2}\lambda^2 & \lambda & A\lambda^3(\rho - i\eta) \\ -\lambda & 1-\frac{1}{2}\lambda^2 & A\lambda^2 \\ A\lambda^3(1-\rho-i\eta) & -A\lambda^2 & 1 \end{pmatrix} \tag{1.4}$$

$$+ \lambda^4 \begin{pmatrix} -\frac{1}{8} & 0 & 0 \\ \frac{1}{2}A^2\lambda[1-2(\rho+i\eta)] & -\frac{1}{8}(1+4A^2) & 0 \\ \frac{1}{2}A\lambda(\rho+i\eta) & \frac{1}{2}A[1-2(\rho+i\eta)] & -\frac{1}{2}A^2 \end{pmatrix} \tag{1.5}$$

$$+ O(\lambda^6) + \dots \,. \tag{1.6}$$

1.2.2. Unitarity triangles

Per definition in an unitary matrix, the scalar product of any two distinct rows or columns vanishes. This yields the following *unitarity relations*:

$$\sum_i V_{ij}V_{ik}^* = \delta_{jk} \qquad \sum_j V_{ij}V_{kj}^* = \delta_{ik} \,. \tag{1.7}$$

The six vanishing relations are illustrated as triangles in the complex plane. All these unitarity triangles have the same area $J/2$, where the Jarlskog invariant J

$$\Im\left[V_{ij}V_{kl}V_{il}^*V_{kj}^*\right] = J\sum_{m,n}\varepsilon_{ikm}\varepsilon_{jln} \tag{1.8}$$

is a phase-convention independent measure of *CP* violation [44, 47].

The unitarity relation

$$V_{ud}V_{ub}^* + V_{cd}V_{cb}^* + V_{td}V_{tb}^* = 0 \tag{1.9}$$

where all terms are $O(\lambda^3)$ (see Equation 1.4), has been subject to intensive studies since the angle [44]

$$\beta = \arg\left(-\frac{V_{cd}V_{cb}^*}{V_{td}V_{tb}^*}\right) \tag{1.10}$$

plays a crucial role in B^0-$\bar{B}^0$ mixing (Section 1.3.1). The measurement is ambiguous in the sense that both β and $(90^\circ - \beta)$ are valid solutions. The world average $\beta = (21.4 \pm 0.8)^\circ$ or $\beta = (68.6 \pm 0.8)^\circ$ [48] is dominated by results from the *B* experiments BaBar [49] and Belle [50]. Further experimental data will be added by the LHCb experiment (presented in Chapter 2).

Another important unitarity relation

$$V_{us}V_{ub}^* + V_{cs}V_{cb}^* + V_{ts}V_{tb}^* = 0 \tag{1.11}$$

can be constrained by measurements of B_s^0 mixing. These have been carried out by CDF, D0 and LHCb [48] and are a major research topic of LHCb. The summands are $O(\lambda^2)$ except $V_{us}V_{ub}^*$ being $O(\lambda^4)$, thus the angle [44]

$$\beta_s = \arg\left(-\frac{V_{ts}V_{tb}^*}{V_{cs}V_{cb}^*}\right) \tag{1.12}$$

is small. Its world average $(0.47^{+0.13}_{-0.21})$ or $(1.09^{+0.21}_{-0.13})$ [44] includes measurements by CDF [51] and D0 [52]. Assuming unitarity the angle can be predicted at high precision in the Standard Model from other CKM angle measurements. Hereby, a comparison of precise measurements of β_s with the Standard Model expectation can reveal potential inconsistencies in the theory. Mark that the quotient in β_s is inverse with respect to simply replacing *d* by *s* in Equation 1.10 to assure a positive sign of the angle.

1.3. *CP* violation in neutral meson mixing and decay

Mixing of neutral mesons is an important field where *CP* violation can arise. The description here is focused on B_s^0 mesons, which are bound states of a $\bar{b}$ and an *s* quark, while very similar methods are applicable to B^0 mesons (bound states of $\bar{b}$ and *d*). First, the theoretical description of B_s^0-$\bar{B}_s^0$ mixing is presented. Then, a classification of *CP* violation is made and in the end, measures of *CP* violation in the $B_s^0 \to \phi\phi$ and $B_s^0 \to J/\psi\phi$ decay channel are presented.

In the following, the case without the negligible *CP* violation on the decay amplitude (see Section 1.3.2) under the assumption that *CPT* is conserved is dealt with. Refer to Reference [34] for a detailed treatment including direct *CP* violation or without assuming *CPT*.

1.3.1. B_s^0-$\bar{B}_s^0$ mixing

The following review of neutral meson mixing, based on References [34, 53, 54], centers at B_s^0 mesons; for B^0, D^0 and K^0 different approximations are made, but the principal formalism is the same. To ease the formulation, c and $\hbar$ are set to 1 in the description of the mixing formalism, i.e. decay widths and mass differences have the unit of inverse time.

In the Wigner-Weisskopf approximation [34, 55], the oscillation and decay of the mesons are modeled by a wave function which is a superposition of two flavor eigenstates:

$$|\Psi(t)\rangle = \begin{pmatrix} |B_s^0(t)\rangle \\ |\bar{B}_s^0(t)\rangle \end{pmatrix} . \tag{1.13}$$

In this equation,

- $|B_s^0(t)\rangle$ is defined as a state that was produced as B_s^0 at $t = 0$ and
- $|\bar{B}_s^0(t)\rangle$ as a state that was produced as $\bar{B}_s^0$ at $t = 0$.

The time evolution is given by the following Schrödinger equation:

$$i\frac{\partial}{\partial t}|\Psi(t)\rangle = \hat{H}\,|\Psi(t)\rangle . \tag{1.14}$$

In order to incorporate both, mixing and decay, the 2×2 matrix operator $\hat{H}$ must be a sum of two hermitian matrices, where the second one, describing the decay, has an imaginary coefficient:

$$\hat{H} = \hat{M} - \frac{i}{2}\hat{\Gamma} . \tag{1.15}$$

$\hat{H}$ is not hermitian and, since $\hat{M}$ and $\hat{\Gamma}$ do not generally commute, it is not normal and hereby not diagonalized by a unitary matrix. However, it can still be diagonalized by a similarity transformation with the Ansatz [54]:

$$i\frac{\partial}{\partial t}\,X^{-1}\,|\Psi(t)\rangle = (X^{-1}\hat{H}X)\,X^{-1}\,|\Psi(t)\rangle \tag{1.16}$$

with

$$X = \begin{pmatrix} p & p \\ p & -q \end{pmatrix} \qquad X^{-1} = \frac{1}{2pq}\begin{pmatrix} q & p \\ q & -p \end{pmatrix} . \tag{1.17}$$

The mass eigenstates are given by

$$\begin{pmatrix} |B_L(t)\rangle \\ |B_H(t)\rangle \end{pmatrix} = X^{-1}\begin{pmatrix} |B_s^0(t)\rangle \\ |\bar{B}_s^0(t)\rangle \end{pmatrix} \tag{1.18}$$

and the transformed operator matrix has the form

$$(X^{-1}\hat{H}X) = \mathrm{diag}(\mu_L, \mu_H) \tag{1.19}$$

with the eigenvalues

$$\mu_L = m_L - \frac{i}{2}\Gamma_L \qquad \mu_H = m_H - \frac{i}{2}\Gamma_H . \tag{1.20}$$

Equation 1.16 is solved by the time evolution

$$\begin{pmatrix} |B_L(t)\rangle \\ |B_H(t)\rangle \end{pmatrix} = \begin{pmatrix} e^{-i\mu_L t} & 0 \\ 0 & e^{-i\mu_H t} \end{pmatrix}\begin{pmatrix} |B_L\rangle \\ |B_H\rangle \end{pmatrix} . \tag{1.21}$$

The time evolution of the flavor eigenstates can be calculated by transforming this solution back:

$$\begin{pmatrix} |B_s^0(t)\rangle \\ |\bar{B}_s^0(t)\rangle \end{pmatrix} = X \begin{pmatrix} e^{-i\mu_L t} & 0 \\ 0 & e^{-i\mu_H t} \end{pmatrix} X^{-1} \begin{pmatrix} |B_s^0\rangle \\ |\bar{B}_s^0\rangle \end{pmatrix} \tag{1.22}$$

$$= \begin{pmatrix} g_+(t) & \frac{q}{p} g_-(t) \\ \frac{p}{q} g_-(t) & g_+(t) \end{pmatrix} \begin{pmatrix} |B_s^0\rangle \\ |\bar{B}_s^0\rangle \end{pmatrix} \tag{1.23}$$

with

$$g_+(t) = e^{-imt} e^{-\Gamma t/2} \left[\cosh\frac{\Delta\Gamma t}{4} \cos\frac{\Delta m t}{2} - i \sinh\frac{\Delta\Gamma t}{4} \sin\frac{\Delta m t}{2} \right] \tag{1.24}$$

$$g_-(t) = e^{-imt} e^{-\Gamma t/2} \left[-\sinh\frac{\Delta\Gamma t}{4} \cos\frac{\Delta m t}{2} + i \cosh\frac{\Delta\Gamma t}{4} \sin\frac{\Delta m t}{2} \right] \tag{1.25}$$

and[1]

$$\Delta m = m_H - m_L \tag{1.26}$$

$$\Delta\Gamma = \Gamma_L - \Gamma_H \, . \tag{1.27}$$

From these time evolutions, the decay probabilities of B_s^0 and $\bar{B}_s^0$ to the final state $|f\rangle$ can be calculated as $\left|\langle f|H|B_s^0\rangle\right|^2$ and $\left|\langle f|H|\bar{B}_s^0\rangle\right|^2$:

$$\Gamma\left(B_s^0(t) \to f\right) \propto |A_f|^2 e^{-\Gamma t} \left[\cosh\frac{\Delta\Gamma t}{2} - \Re(\lambda_f) \sinh\frac{\Delta\Gamma t}{2} - \Im(\lambda_f) \sin(\Delta m t) \right] \tag{1.28}$$

$$\Gamma\left(\bar{B}_s^0(t) \to f\right) \propto |A_f|^2 e^{-\Gamma t} \left[\cosh\frac{\Delta\Gamma t}{2} - \Re(\lambda_f) \sinh\frac{\Delta\Gamma t}{2} + \Im(\lambda_f) \sin(\Delta m t) \right] \, , \tag{1.29}$$

with

$$\lambda_f = \frac{q}{p}\frac{\bar{A}_f}{A_f} \, . \tag{1.30}$$

The amplitude ratio in λ_f is composed of the decay amplitudes of a $\bar{B}_s^0$ and a B_s^0 into the final state $|f\rangle$. In detail, four such amplitudes can be defined taking into account all combinations of B_s^0/ $\bar{B}_s^0$ and $|f\rangle/|\bar{f}\rangle$:

$$A_f = \langle f|H|B_s^0\rangle \qquad A_{\bar{f}} = \langle \bar{f}|H|B_s^0\rangle \tag{1.31}$$

$$\bar{A}_f = \langle f|H|\bar{B}_s^0\rangle \qquad \bar{A}_{\bar{f}} = \langle \bar{f}|H|\bar{B}_s^0\rangle \, . \tag{1.32}$$

The time dependent *CP* asymmetry follows directly from Equation 1.28 and 1.29:

$$A_{CP}(t) = \frac{\Gamma\left(\bar{B}_s^0(t) \to f\right) - \Gamma\left(B_s^0(t) \to f\right)}{\Gamma\left(\bar{B}_s^0(t) \to f\right) + \Gamma\left(B_s^0(t) \to f\right)} = \frac{\Im(\lambda_f)\, \sin(\Delta m t)}{\cosh(\frac{1}{2}\Delta\Gamma t) \, - \, \Re(\lambda_f)\, \sinh(\frac{1}{2}\Delta\Gamma t)} \, . \tag{1.33}$$

The numerator in Equation 1.33 being composed of a time-dependent oscillatory part and the constant $\Im(\lambda_f)$, the latter is the crucial measure of the degree of *CP* violation. The quotient q/p

[1] The sign convention for $\Delta\Gamma$ is adopted from Reference [53].

in Equation 1.30 is related to the mixing, as obvious from Equation 1.23 and the second quotient is related to the decay.

The crucial difference between the B_s^0 and B^0 system is $|\Delta\Gamma/\Gamma|$, which is in the order of 1% for B^0 and 10% for B_s^0 [44]. Thus, Equation 1.33 is simplified for B^0 by setting the denominator to 1. A further difference is the oscillation's angular frequency given by $\Delta m(B^0) = 0.507 \pm 0.004\,\mathrm{ps}^{-1}$ [56] (average value dominated by [57, 58]) and $\Delta m(B_s^0) = 17.77 \pm 0.12\,\mathrm{ps}^{-1}$ [59].

1.3.2. Types of *CP* violation

CP violation is categorized into three types [44] using the quantities defined above:

1. *CP* violation in decay ($\left|\bar{A}_{\bar{f}}/A_f\right| \neq 1$)
2. *CP* violation in mixing ($|q/p| \neq 1$)
3. *CP* violation in interference between mixing and decay ($\Im(\lambda_f) \neq 0$)

The $B_s^0 \to \phi\phi$ and $B_s^0 \to J/\psi\,\phi$ decays are examples of type 3, which will be elaborated in the next section.

1.3.3. Parametrization of *CP* violation in $B_s^0 \to \phi\phi$ and $B_s^0 \to J/\psi\,\phi$

The terms in Equation 1.30 can be rewritten in polar form introducing a mixing phase Φ_M and a decay phase Φ_A:

$$\frac{q}{p} = e^{2i\Phi_M} \tag{1.34}$$

$$A_f = Ae^{i\Phi_A}e^{i\delta_A} \tag{1.35}$$

$$\bar{A}_f = \eta_f Ae^{-i\Phi_A}e^{i\delta_A}\,. \tag{1.36}$$

Φ_M and Φ_A are *CP*-odd *weak phases* and δ_A is a *CP*-even *strong phase*. The naming convention should not be mistaken as an allusion to the weak and the strong interaction [34]. Examples for strong phases are those that arise from final state interactions which are the same for two *CP* conjugate final states [34]. The strong phases cancel out when analyzing decays into a *CP* eigenstate, which eliminates theoretical uncertainty:

$$\lambda_f = \eta_f\, e^{2i(\Phi_M - \Phi_A)}\,. \tag{1.37}$$

In other words, *CP* violation in the interference of mixing and decay arises if there is a *phase difference* between the mixing process and the decay process.

The quantity η_f in Equation 1.37 is the *CP* eigenvalue of the final state. For the $\phi\phi$ state it is defined as

$$\eta_f = (-1)^L \tag{1.38}$$

with the angular momentum L between the two ϕ mesons.

The phase Φ_M is half the argument of the transition amplitude from a B_s^0 to a $\bar{B}_s^0$, which is proportional to $V_{ts}V_{tb}^*$ (see Figure 1.1). The dominant decay amplitude of the $B_s^0 \to J/\psi\,\phi$ decay is

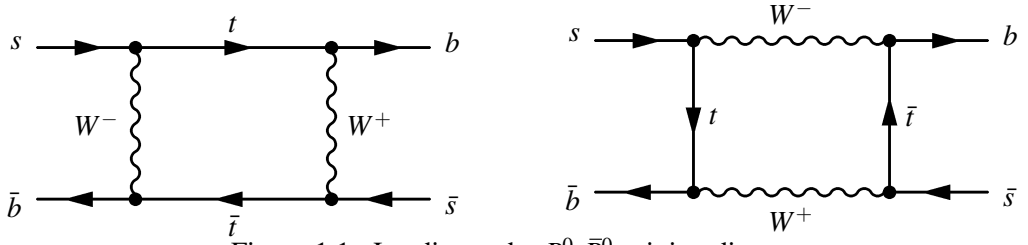

Figure 1.1.: Leading order B_s^0-$\bar{B}_s^0$-mixing diagram.

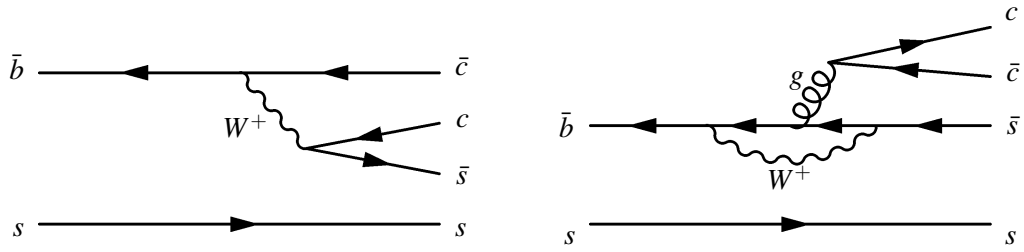

Figure 1.2.: Tree diagram at leading order (left) and penguin diagram (right) for the $B_s^0 \to J/\psi\phi$ decay.

proportional to $V_{cs}V_{cb}^*$, as visible in the tree diagram in Figure 1.2. Finally, the $B_s^0 \to \phi\phi$ decay amplitude is determined to be proportional to $V_{ts}V_{tb}^*$ from Figure 1.3:

$$\Phi_M = \arg(V_{ts}V_{tb}^*) \tag{1.39}$$
$$\Phi_A(B_s^0 \to J/\psi\phi) = \arg(V_{cs}V_{cb}^*) \tag{1.40}$$
$$\Phi_A(B_s^0 \to \phi\phi) = \arg(V_{ts}V_{tb}^*)\,. \tag{1.41}$$

The measurable *CP* violating phase ϕ_s is (compare to Equation 1.37 and 1.12):

$$\phi_s := -\arg(\lambda_f/\eta_f) = \begin{cases} -2\arg\left(-\frac{V_{ts}V_{tb}^*}{V_{cs}V_{cb}^*}\right) = -2\beta_s & \text{for } B_s^0 \to J/\psi\phi \\ 0 & \text{for } B_s^0 \to \phi\phi\,. \end{cases} \tag{1.42}$$

LHCb's search for New Physics (see Section 1.1.2) includes the measurement of ϕ_s in both channels[2]. If New Physics would contribute to the tree-level decay process, it would already have been found. Thus, it could contribute to the B_s^0-$\bar{B}_s^0$ mixing box diagram, which would lead to a correction in $\phi_s(B_s^0 \to J/\psi\phi)$. If the potential New Physics shares the flavor structure with the Standard Model, it would affect the penguin and the box diagram in the $B_s^0 \to \phi\phi$ channel alike, i.e. $\phi_s(B_s^0 \to \phi\phi)$ would remain unchanged. If, however, a non-vanishing phase is measured in the $B_s^0 \to \phi\phi$ decay channel, the combination with the results from $B_s^0 \to J/\psi\phi$ determines whether this is due to the box or the penguin diagram.

The measurement of $\phi_s(B_s^0 \to \phi\phi)$ is experimentally particularly attractive: due to the practically vanishing Standard Model value, it is theoretically very clean. In contrast, there is a "penguin pollution" in the $B_s^0 \to J/\psi\phi$ decay from higher order loop diagrams like the one in Figure 1.2.

Assuming that a new phase enters uniquely in the penguin decay diagram of $B_s^0 \to \phi\phi$, a comparison with the $B^0 \to \phi K_S^0$ decay can help estimating the expectations, since it proceeds via the

[2]This work being focused on the $B_s^0 \to \phi\phi$ decay channel, the symbol ϕ_s will refer to the $B_s^0 \to \phi\phi$ channel unless otherwise stated.

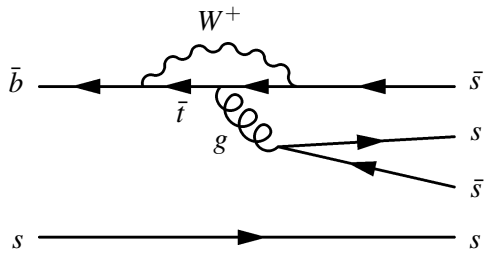

Figure 1.3.: Leading order $B_s^0 \to \phi\phi$ decay diagram.

same diagram. The golden channel for the determination of $\sin(2\beta) = 0.68 \pm 0.02$ [48] is the $B^0 \to J/\psi K_S^0$ decay, which is a tree level process at leading order. In the Standard Model, the $B^0 \to \phi K_S^0$ channel should yield almost the same result $\sin(2\beta_{\text{eff}}) = 0.56^{+0.16}_{-0.18}$ [48, 60, 61] up to negligible corrections. If the phase difference δ_d is assigned to New Physics, the expectation for the *CP* violating phase in $B_s^0 \to \phi\phi$ is:

$$\delta_d = 2\beta_{\text{eff}} - 2\beta = -0.12^{+0.16}_{-0.18} \,. \tag{1.43}$$

This chapter was aimed at motivating the study of *CP* violation in *B* meson decays and introducing the basic concepts. The actual analysis in the case of $B_s^0 \to \phi\phi$ and $B_s^0 \to J/\psi\phi$ is complicated by the fact that different angular momenta are possible in the final state and hereby –see Equation 1.38– the final state is an admixture of *CP* eigenstates with opposite-sign η_f. Section 4.1 explains how this problem is solved experimentally.

1.4. Event generation with Pythia

A strict theoretical treatment of pp interactions is at present impossible for several reasons [9]: First of all, due to triple gluon vertices and the large coupling constant, QCD produces high multiplicity final states. Treating these as a "single process" in perturbative calculations would be a challenge. Furthermore, higher order corrections like bremsstrahlung corrections would have to go in, too, complicating the analytical approach even more. Finally, the incoming and outgoing partons are subject to confinement, which is inaccessible to perturbative calculations.

Monte Carlo based event generators tackle the aforementioned challenges by a factorization approach: the pp interaction is factorized into several subprocesses, which can be handled more conveniently. The PYTHIA event generator is described in the following because it is dominantly used at the LHC and the standard LHCb MC production relies on it.

The major steps when generating an event are [9]:

1. Two partons of the incoming protons interact in a hard QCD process. The interaction of partons of a certain type can be treated in leading order perturbative QCD, while the probability to find a parton of type i, which carries a fraction x of the total momentum, is given by the parton-distribution functions $f_i(x)$. These distribution functions are determined from deep inelastic scattering experiments.

2. There are radiative corrections to the leading-order results, which would need a complicated higher order perturbative approach. PYTHIA, however, models the initial- and final state radiation by the parton shower approach, which factorizes the process into a series of $1 \to n$ branchings. Final states with a larger number of particles can easily be modeled by iterating this basic branching process.

3. The last step is hadronization, subdivided into fragmentation and the subsequent decay of non-stable particles. Fragmentation is the transition from a state of high mass partons into a state of colorless low mass hadrons, in which the partons are confined. Since there is no explicit theory on that, PYTHIA instead relies on the Lund string fragmentation model [62]. Its key feature is to model the confinement potential between partons by a color dipole field the energy of which increases linearly with separation ($\kappa \approx 1$ GeV/fm). As an illustrative example, take a color singlet pair of quarks $q\bar{q}$ created in an e^+/e^- collision. As these quarks move apart, the color string is stretched between them and it eventually breaks up to create a new pair of quarks $q'\bar{q}'$, which are now also part of the string. If the invariant mass of the strings is high enough, more of these breaks might occur up to the point where where only on-mass-shell hadrons remain, each of which is represented by its constituent quarks and the connecting strings.

The description above neglected the role of the remaining two partons from each incoming proton. These may take part in additional hard interactions, simulated by PYTHIA's multiple interaction model, which determines the underlying event structure. Either the initial partons or –in the case that they interacted– their bachelor particles participate in the fragmentation process. As a rule of thumb, the hard interaction determines the general energy flow in the event, whereas the details of the event structure are governed by hadronization effects.

The aforementioned description was focused on inelastic, non-diffractive events. Further event types are elastic collisions, where the two protons are scattered with minimal momentum transfer, and diffractive collisions. In diffractive collisions, either one (single diffractive) or both (double diffractive) protons transit into an excited state, which decays soon after. Elastic and diffractive

events are characterized by very low multiplicities and hereby, they play no role in the B meson production and a minor role in ϕ production. PYTHIA has dedicated models for these event types.

In hadron collisions, b quarks are generated by the processes gluon fusion ($gg \to b\bar{b}$), gluon splitting ($g \to b\bar{b}$) and flavor excitation (a heavy quark from one beam particle is put on shell in a scattering process), which contribute in equal order to the total cross-section [63]. In contrast, light quarks up to the s can arise not only from perturbative subprocesses, but also from non-perturbative hadronization. Potential sources of ϕ mesons are production from strange sea quarks [17], from gluon fusion or from the fragmentation process. Hereby, they are an important probe of the hadronization in contrast to the third generation, the production of which is determined by perturbative calculations [63].

In view of the phenomenological nature of the event generator model, it is rather descriptive than predictive. PYTHIA 6.4 has been tuned simultaneously to LEP, Tevatron and SPS data resulting in the Perugia tunes with the central parameter set Perugia 0 [64].

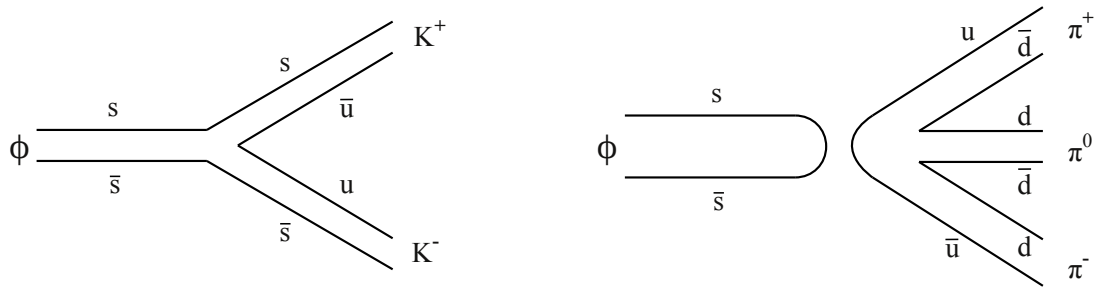

Figure 1.4.: Diagram of $\phi \to K^+K^-$ decay (left) and $\phi \to \pi^+\pi^0\pi^-$ decay (right).

For reasons of completeness –after reviewing the ϕ production– their decay is briefly addressed. The ϕ predominantly decays to the final states K^+K^- (49.2%), $K^0_L K^0_S$ (34.0%) and $\pi^+\pi^-\pi^0$ (15.3%). The decay into two kaons is close to the phase space boundary ($2m^+_K = 987.4\,\mathrm{MeV}/c^2$) and from this point of view the decay into three pions should be preferred. However, the latter is OZI suppressed (Figure 1.4) [65, 66]. The ϕ detection in LHCb is constrained to the $\phi \to K^+K^-$ decay channel since it allows the cleanest reconstruction.

CHAPTER 2

LHCb experiment at the LHC

2.1. Large Hadron Collider complex

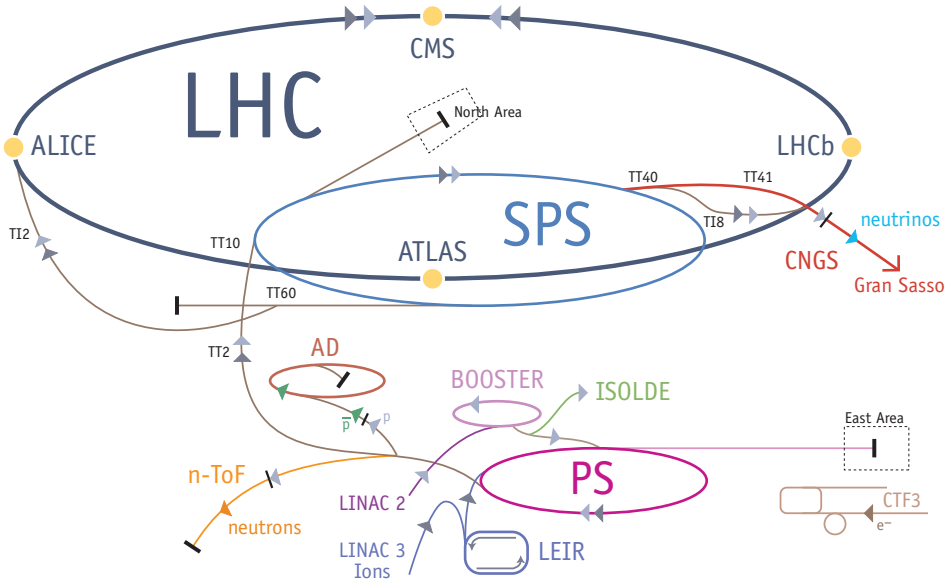

Figure 2.1.: CERN accelerator complex [67]. Pre-accelerators of the Large Hadron Collider (LHC) are the Super Proton Synchrotron (SPS), the Proton Synchrotron (PS), the BOOSTER, the Low Energy Ion Ring (LEIR) and the Linear Accelerators LINAC2/3. Further facilities are the Antiproton Decelerator (AD), the CERN Neutrinos to Gran Sasso beam (CNGS), the n-ToF experiment (Neutrino Time Of Flight) and the Isolde experiment (Isotrope Separator Online Device). Transfer lines (names starting with "T") connect the accelerators. The Clic Test Facility (CTF-3) is designed to test components for future accelerators.

The Large Hadron Collider (LHC) [68], operated by the European Organization for Nuclear Research (CERN), is built to answer some of the questions risen in Section 1.1.2. Approved by the CERN council in December 1994, the LHC is designed as 25.66 km long twin-aperture ring accelerator capable of colliding protons and lead ions. Along the ring, the particles are kept on track by 1232 superconducting bending magnets with a magnetic flux density of 0.535 T to 8.33 T operating at temperatures near absolute zero.

The particles are brought to collision in the four major experiments ATLAS, CMS, ALICE and LHCb. ATLAS [69] and CMS [70] are general purpose detectors aiming for example at direct discovery of so far unobserved particles like the Higgs or SUSY candidates. LHCb [71] is designed for an indirect search for physics beyond the Standard Model by studying rare decays and *CP* violation, e.g. in B meson oscillations. Finally, ALICE [72] is built to study the quark gluon plasma. There are two smaller experiments: TOTEM [73], positioned near the CMS experiment

measures the total pp cross-section and LHCf [74] is temporarily installed near ATLAS to carry out particle flux and energy measurements in the forward region. Figure 2.1 gives an overview over the LHC, the experiments and the LHC pre-accelerator chain.

While currently running at $\sqrt{s} = 7\,\text{TeV}$, the design center-of-mass energy of the LHC is 14 TeV. The particles are filled into the ring in bunches. When accelerating protons, the filling is $1.15 \cdot 10^{11}$ protons per bunch and the typical bunch length is 7 to 11 cm. At 40 MHz, the harmonic number is 3564, however, only a maximum number of 2808 buckets can be filled to account for injection and extraction technicalities. In other words, the LHC is filled with several trains of bunches spaced at 25 ns (corresponding to roughly 7.5 m).

The nominal instantaneous luminosity is $L = 10^{34}\ \text{cm}^{-2}\text{s}^{-1}$ in the ATLAS and the CMS experiment, $10^{32}\ \text{cm}^{-2}\text{s}^{-1}$ in LHCb and $10^{27}\ \text{cm}^{-2}\text{s}^{-1}$ in ALICE during lead ion runs. The data taking conditions in LHCb and the integrated luminosity delivered to this experiment are detailed in Section 2.8. A common challenge to all LHC experiments are event rates in the order of $10^8/s$, which puts high demands on the readout electronics, the trigger and the offline data processing. On top, the physically interesting processes are highly suppressed: compared to the total pp cross section of 100 mb, the b- and t-meson production cross-sections are 200 times and 10^7 times lower, while Higgs production is even suppressed by more than nine orders of magnitude [75].

The first full circulation of beam all around the LHC ring took place on September 10$^{\text{th}}$ 2008 [76] and the commissioning progressed quickly in the following days. However, just before commissioning of all eight sectors of the LHC for $\sqrt{s} = 10\,\text{TeV}$, a severe incident happened on September 19$^{\text{th}}$ 2008 [77, 78]: an improper 13kA interconnection of the superconductors between two dipole magnets became resistive and broke as consequence of thermal runaway. An electric arc punctured and partly *evaporated* the helium enclosure. Consequently, large amounts of helium were heated up and traveled up to vacuum barriers, which were structurally damaged. In the following year, roughly 750 meters of the LHC had to be exchanged and 3.8 kilometers of beam line had to be cleaned before the LHC could restart on November 20$^{\text{th}}$ 2009. The first proton-proton collisions were delivered three days after [79].

The maximum center-of-mass energy is restricted to $\sqrt{s} = 7\,\text{TeV}$ until further consolidation work is carried out during a longer shutdown. Furthermore, the whole LHC physics program was set back by more than a year. As an example, in the $B_s^0 \to \phi\phi$ analysis treated in this thesis, a full angular analysis on real data could already have been carried out if the incident would not have happened or if it had been less severe.

2.2. LHCb detector

In pp collisions, $b\bar{b}$ pairs are produced in scattering of proton constituents [63, 82] which are most likely to have asymmetric momenta [83]. Consequently, the b and $\bar{b}$ tend to emerge at small opening angles to each other and to the beam axis (Figure 2.2). This is why the LHCb experiment targeting studies of B meson decays is built as forward spectrometer with an angular coverage from 10 to 300 mrad horizontally and 10 to 250 mrad vertically.

The general detector layout of LHCb [71] is shown in Figure 2.3. The reference frame, which origin is in the interaction point, is right-handed with $+y$ pointing upwards and $+z$ pointing from the interaction point into the spectrometer. The direction pointing $+z$ is also referred as "downstream" as opposed to "upstream", which points to $-z$.

The silicon Vertex Locator (VELO) is built around the interaction point (IP). Further detector elements are (ordered by their z position), a Ring Imaging Čerenkov Detector (RICH1), the Tracker

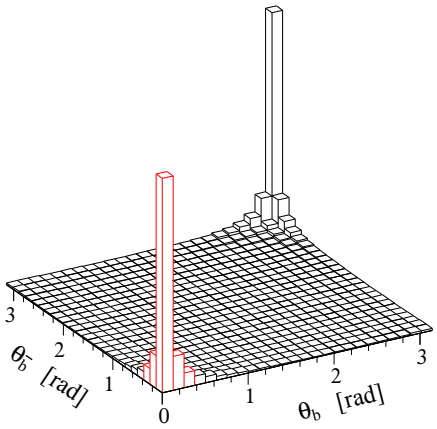

Figure 2.2.: Polar angle distribution of the b and $\bar{b}$ in $b\bar{b}$ pair production calculated by the PYTHIA event generator [80].

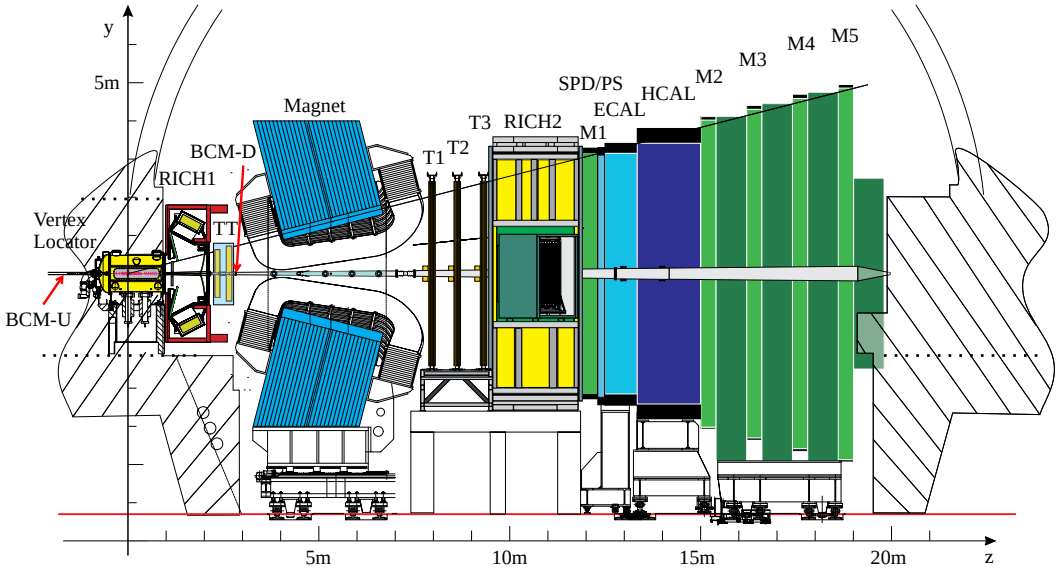

Figure 2.3.: LHCb detector drawing (side view) [71, 81]. The Vertex Locator (VELO) is built around the interaction point (IP) at $x = y = z = 0$. Further detector components are the two Ring Imaging Čerenkov Detectors (RICH1 and RICH2), the Tracker Turicensis (TT), the magnet, the three tracking Stations (T1-T3) and five muon stations (M1-M5). The calorimetry system consists of Silicon Pad Detector (SPD), Preshower (PS), the Electromagnetic Calorimeter (ECAL) and the Hadronic Calorimeter (HCAL). Finally, there are two Beam Conditions Monitor stations (BCM-U and BCM-D).

Turicensis (TT) and the spectrometer magnet. Upstream of the VELO and downstream of the TT, there are the two Beam Conditions Monitor stations BCM-U and BCM-D. Behind the magnet, there are the three main tracking stations (T1-T3) and another Čerenkov Detector (RICH2). Next is the calorimetry system, which comprises the Scintillating Pad Detector (SPD), a preshower (PS), the Electromagnetic Calorimeter (ECAL) and the Hadronic Calorimeter (HCAL). In front of the SPD, there is a first muon station M1 and behind the calorimeters, there are four muon stations M2-M5. The following sections will discuss the different detectors based on References [71, 84].

2.2.1. Tracking detectors

Track reconstruction is provided by the tracking devices VELO, TT and the tracking stations T1-T3. Knowing the curvature of the trajectories in the spectrometer magnet and its field strength, the particle momentum can be calculated. The integrated magnetic field of the magnet, dominantly directed parallel to the y axis, is about 4 Tm and data is taken at both polarities, "up" and "down".

Vertex Locator

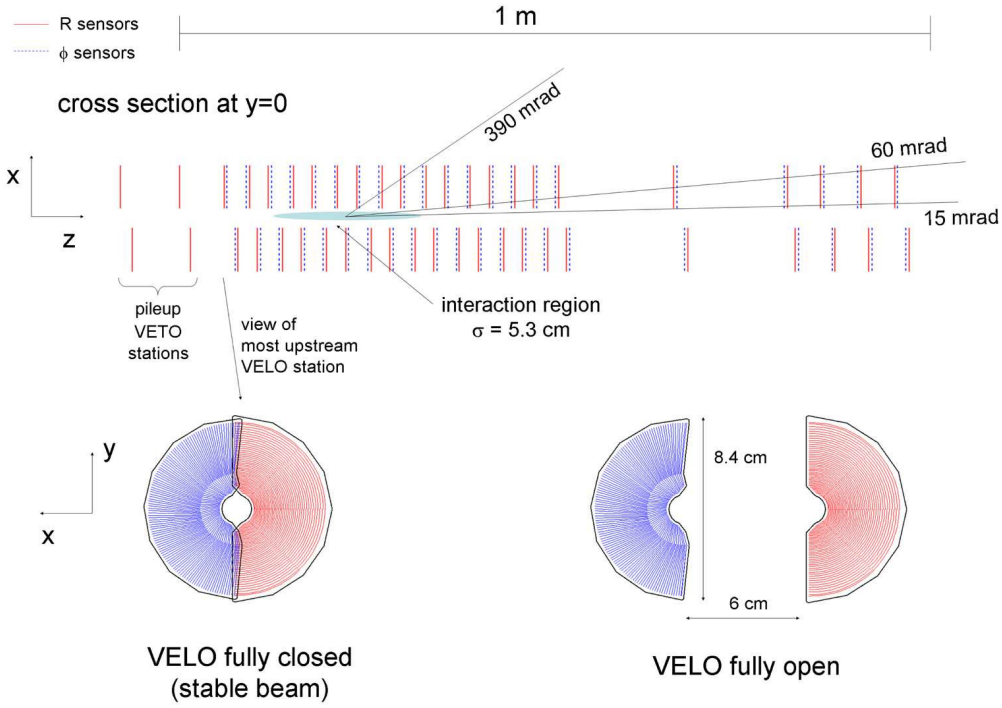

Figure 2.4.: Schematic drawing of VELO sensor arrangement (top) and overlap of sensors in closed and open position (bottom) [71].

As will be shown in Equation 2.13, measurements of B meson oscillations require precise knowledge of the B proper time at decay, calculated from the particle's momentum and flight distance. Since the momentum resolution is generally high (0.3–0.5% uncertainty), the challenge is to achieve best vertex resolution. The vertex resolution, in turn is improved with the quality of the tracking detectors and with minimizing the distance between tracking device and vertex.

The VELO is composed of two roughly 1 m long half-shells, each of which is equipped with 23 sensor stations (Figure 2.4). Each sensor station is built of two parallel silicon strip detectors, one of which is segmented in r direction and one in φ direction (except for the two most upstream ones, "pileup stations", which have r sensors only). The sensor surface extends over a radial distance to the beam between 8.2 mm and 42.0 mm The pitch of the sensors varies between $40-100\,\mu$m and a hit resolution of roughly $10-25\,\mu$m can achieved. This is necessary to obtain the desired B lifetime resolution in the order of $40-50$ fs.

Since the VELO would lie within the LHC beam envelope at injection, it is designed as movable device, which is driven into its working position only under stable beam conditions.

Tracker Turicensis

The Tracker Turicensis[1] TT comprises four silicon strip detector planes, each of which covers an area of 1.5 m (in x) times 1.3 m (in y). The detectors with 183 µm pitch are aligned vertically in the first and the fourth layer (x layer), while the two inner layers have a stereo-angle of $\pm 5^\circ$ (u, v layer). Two pairs, the x,u and the v,x layers are separated by a distance of roughly 27 cm in z direction.

Since long lived particles like K_S^0 decay outside of the VELO, the detection of their bachelor particles in the TT is essential to still determine their tracks' curvatures in the magnet. Similarly, the TT, lying in the fringe field of the magnet, helps to determine the momentum of low momentum particles which leave the acceptance before reaching the T stations.

Inner Tracker and Outer Tracker

The three main tracking stations behind the magnet cover an area of 6.0 m times 4.9 m each. Each station is built of four module layers, where the same angular alignment with x,u,v,x layers is chosen as explained above for the TT.

The major surface of the tracking stations is covered by the Outer Tracker (OT) built in straw tube technology: each OT module is composed of two monolayers of straw tubes with 4.9 mm diameter. By measuring the drift time of deposited charges in the Argon-CO_2-Oxygen gas volume a spatial resolution of 200 µm can be achieved.

Since the inner region close to the beam pipe is characterized by a higher occupancy, the straw tube technology is not optimal there. This is why the Inner Tracker (IT), installed at each tracking station in the region near the beam pipe is built in silicon strip technology with 198 µm pitch. These modules offer a spatial resolution of 50 µm. Each station of the IT is built of four layers with the same stereo angles as for TT and OT.

2.2.2. Ring imaging Čerenkov detectors

Particles passing through matter can emit Čerenkov light cones with opening angle

$$\cos\theta = \frac{1}{n\beta} \tag{2.1}$$

with the refractive index n of the traversed medium and $\beta = \frac{v}{c}$, where v is the particle's velocity and c the speed of light in vacuum. Čerenkov light emission occurs at momenta above the critical momentum defined by the condition $\beta > \beta_t = \frac{1}{n}$. Since the occurrence of Čerenkov radiation and the opening angle are a function of the particle momentum and the used radiator's reflective index, particle hypotheses can be inferred if the momentum is known.

This works only in a certain momentum range: above the threshold and an upper bound is given by the fact that the Čerenkov angle approaches a critical angle $\cos\theta_C = 1/n$ common to all particle types. LHCb covers a wide momentum range by using three radiators (Figure 2.5). The RICH1 detector covers momenta from 1 to 60 GeV/c with Aerogel and C_4F_{10} and RICH2 covers the range from 15 to 100 GeV/c using CF_4.

[1] The TT was designed as Trigger Tracker. Since this nomenclature is questionable under the final LHCb trigger strategy, it was renamed after the former Roman settlement Turicum, which inhabitants contributed considerably to the design and construction of the TT.

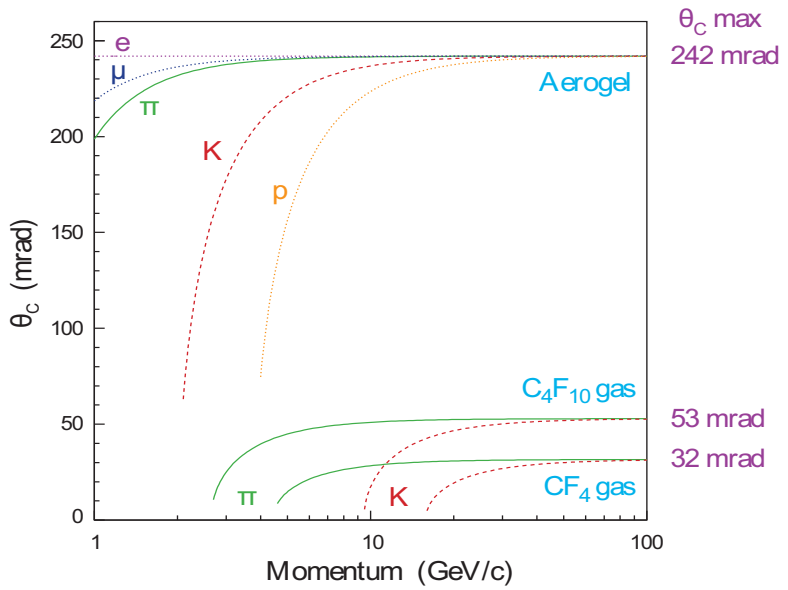

Figure 2.5.: Čerenkov angle versus particle momentum for the RICH radiators [71].

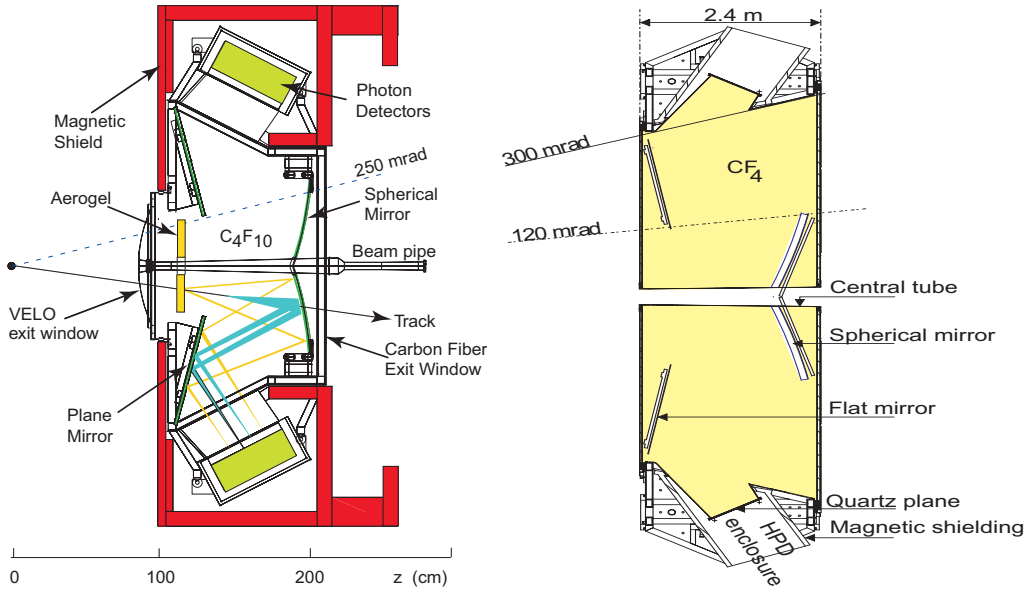

Figure 2.6.: Side view schematic drawing of RICH1 (left) and top view of RICH2 (right) [71].

The working principle of the RICH detector is illustrated in Figure 2.6. Depending on the radiator, around 6 to 30 [84] Čerenkov photons are emitted by the traversing particle and this light cone is deflected by two mirrors onto hybrid photo detectors (HPD) [85] outside of the LHCb acceptance, where an image like the one in Figure 2.7 is projected. The single photoelectron resolution for the RICH system is 2.6 mrad (Aerogel), 1.5 mrad (C_4F_{10}) and 0.7 mrad (CF_4).

Particle identification in the RICH is based on an event-global approach [84]: the photon hit distribution expected from the reconstructed tracks is calculated under all possible combinations of particle hypotheses and for each of these, the likelihood of describing the image seen in the detec-

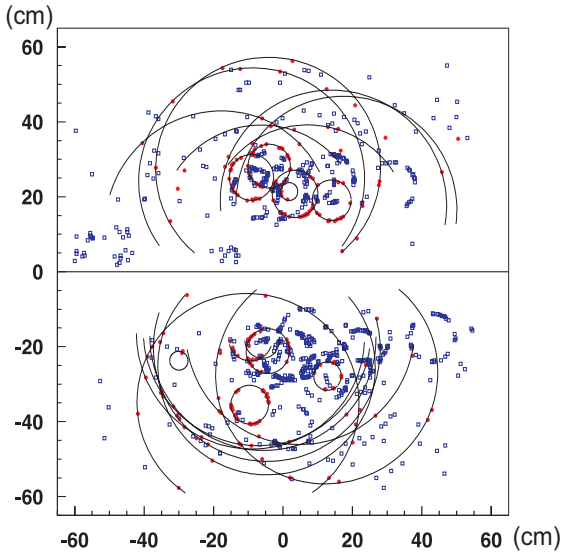

Figure 2.7.: Simulation of typical LHCb event in RICH1 [71].

tor is calculated. Based on the maximum of these likelihoods, where a certain particle may go in as particle type x, a single particle's hypothesis can be exchanged by particle type y and the global likelihood under this hypothesis can be compared to the maximum one. In the case of kaons, the delta-log-likelihood DLL$(K-\pi)$ is the discriminating variable. To shorten the description, it is abbreviated as PIDK throughout this thesis.

It is evident from Equation 2.1 and Figure 2.6 that the particle identification (PID) efficiency is a function of track momentum and from geometrical constraints. On top, it depends on the requirement put on the delta-log-likelihood: the kaon-pion separation is best in the range 20-60 GeV/c with kaon identification efficiencies well above 90% and pion misidentification rates below 5% (Figure 2.8). At higher momenta, a compromise between background rejection and signal retention has to be made.

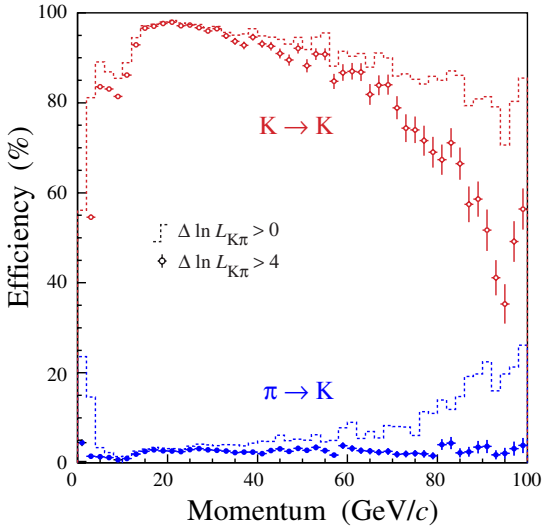

Figure 2.8.: Simulated kaon identification efficiency and pion misidentification rate as function of momentum for two different values of PIDK [84].

2.2.3. Calorimeters

The working principle of the calorimeters is based on electromagnetic shower production in the ECAL and hadronic shower production in the HCAL. The shower particles traverse scintillators and the intensity of the detected scintillation light is a measure of the deposited energy. Since the calorimeters are segmented in the (x, y) plane, positional information can also be inferred. The segmentation is adapted to the occupancy, so there are smaller cells in the center than at the fringes of the acceptance.

The first calorimeter system in z-direction is the SPD/PS, built of two layers of 15 mm thick scintillating pads and a 15 mm thick (corresponding to 2.5 radiation lengths X_0) lead absorber in between. The SPD allows distinguishing charged particles, which leave a signal in it, from neutral particles, which traverse it without signal. Since electrons start an electromagnetic shower in the lead absorber, the PS helps in distinguishing electrons from charged hadrons.

The electromagnetic calorimeter is formed by 66 layers of 2 mm lead absorber and 4 mm scintillator. Corresponding to 25 radiation lengths, the ECAL absorbs photons and electrons effectively.

The HCAL is built as tile calorimeter where scintillator and steel absorber plates are aligned parallel to the beam direction. It is built of 6 mm steel plates in alternation with detection layers. The latter are composed of 4 mm steel spacers and 3 mm thick scintillator plates. In z direction, 6 of these 20 cm long plates (scintillator or steel spacer) are assembled in alternation to build up the 120 cm depth of the HCAL, corresponding to 5.6 hadronic interaction lengths λ_I. The readout fibers run in parallel to the tiles (and to the beam) to the back of the detector where they are read out by photomultipliers.

2.2.4. Muon system

Electromagnetic shower production from muons is highly suppressed at LHCb energies and they do not participate in the strong interaction either, which is why they penetrate the whole detector up to the muon stations. The first muon station is placed in front of the calorimeters to improve p_T measurements in the trigger. The other four muon stations are placed behind the calorimeters, lined up in alternation with 80 cm thick iron absorbers, which filter out non-muonic background. An additional iron shield is installed at the very end of the detector to filter out background particles from the LHC ring.

The detector technology applied in the muon system is mostly based on multiwire proportional chambers (MWPC). However, triple-GEM (gas electron multiplier) foil detectors are used in the innermost region of M1 because of their higher radiation tolerance.

2.2.5. Beam Conditions Monitor

Sensitive detector components, in particular the VELO, need special protection against radiation exposure in the case of beam instabilities or accidents. This is provided by the Beam Conditions Monitor (BCM) system [81], which is LHCb's only system to protect the detector in these cases.

Two BCM stations, each built of 8 CVD diamonds (chemical vapor deposition), are installed at the beam pipe in close vicinity to the VELO. Increased radiation levels can for example be caused by scraping of the beam at the beam pipe or by interactions of the beam with clouds of residual gas atoms. They result in secondary particles that traverse the BCM sensors inducing electrical

currents. These are analyzed by the BCM real-time data processing system which requests an emergency beam dump in the LHC if necessary. The reaction time of the BCM is 40 µs, i.e. slightly less than half the time of a beam revolution. On the LHC side, the beam abort becomes effective in less than 200 µs.

Directly interfacing the LHC interlock hardware, highest reliability is required for the BCM, which is accomplished by the design described in Reference [81]. As a safety device, the BCM system has been running continuously since June 2008 and has proved excellent performance. It successfully triggered more than 50 emergency dumps, each time acting as specified. Three of these beam aborts were triggered upon circulating beams, mostly due to interactions of the beam with residual gas clouds. Post-mortem data provided by the BCM significantly helped in understanding the cause of these beam aborts and hereby contributed to the LHC commissioning.

2.3. Trigger

LHCb has a two staged trigger system: level-0 (L0) trigger and High Level Trigger (Hlt). The L0 trigger, based on custom hardware, runs at the beam crossing rate of 40 MHz and has an output rate around 1 MHz. It exploits the relatively high B meson mass, which results the bachelor particles on average having a higher transverse momentum or transverse energy than the background. For this reason, the L0 trigger is sensitive to the highest E_t hadron, electron and photon clusters in the calorimeters and the highest p_T muons in the muon chambers. On top, the VELO pileup system estimates the number of primary interactions to filter out events where a too high pileup (multiple pp interactions in one event) prevents an effective analysis.

The High Level Trigger running on a computing farm is subdivided into Hlt1 with an output rate of 30 kHz and Hlt2 with 2 kHz output rate written to disc. The Hlt1, divided into several so-called alleys, performs a first rough reconstruction of particle trajectories in the VELO and the tracking stations to confirm or reject the L0 decision and furthermore tests the absence of charged particles in a L0 decision based on a γ or π^0.

Given the already reduced input rate compared to previous trigger stages, Hlt2 can reconstruct the event on a track basis using simplified but similar algorithms as in the offline processing. Hlt2 is organized in so-called trigger lines, each of which performs a specific selection. There are some exclusive selections targeted at one decay channel, however, most lines adopt an inclusive approach, like the Inclusive ϕ line (*Hlt2IncPhi*) [8, 86]. The latter triggers on ϕ particles with properties typical for B decay products, like high transverse momentum and separation from the primary vertex. In a similar way, topological lines search for particular geometrical event properties like decay vertices detached from primary vertices, which are a signature of B decays. Some trigger lines, in particular those collecting data in control channels or high-yield physics processes, are limited by so-called prescales defined as random rejection of events.

The trigger is adapted to the running conditions by a trigger configuration key (TCK), which determines the active lines and the requirements and cut values used in them. For example, only a very limited number of trigger lines were active at the time of the LHC startup, which will be further elaborated in Section 5.2. The TCK may be changed between different *runs*, where a run (identified by a consecutive run number) is defined as a period of continuous and stable data taking.

2.4. Luminosity measurement in LHCb

The instantaneous luminosity is determined as [87]

$$L = \frac{N_1 N_2 f N_b}{2\pi\sqrt{(\sigma_{1x}^2 + \sigma_{2x}^2)(\sigma_{1y}^2 + \sigma_{2y}^2)}} \tag{2.2}$$

for the simple case of Gaussian beam profiles with width σ_x and σ_y in x and y direction. N_1 and N_2 are the bunch intensities, f the beam revolution frequency and N_b the number of colliding bunches. Absolute measurements of the instantaneous luminosity [88] need dedicated beam steering and hereby, they cannot be performed under nominal running conditions. This is why the absolute scale is determined intermittently – and during regular data taking, relative measurements are normalized to the absolute ones.

The absolute luminosity scale is given by the beam currents and a determination of the beam profile enabled by the following methods:

- The Van der Meer scan method [89] sweeps the beams across each other in horizontal and vertical direction. For separation Δu of the beams in direction u (denoting x or y), the luminosity scales as follows with respect to the one given in Equation 2.2:

$$L(\Delta u) = L\, e^{-\frac{\Delta u^2}{2(\sigma_{1u}^2 + \sigma_{2u}^2)}}, \tag{2.3}$$

  which allows the determination of the transverse beam profiles.

- The Beam-Gas Imaging method [90] determines the beam profiles from beam-gas interactions, which can be detected using the high-performance tracking capabilities of the VELO.

- The Beam-Imaging during Van der Meer scan [91] allows to determine the beam profiles from the distribution of pp vertices.

The permanent relative luminosity measurements are based on so-called luminosity counters, which are certain quantities that scale linearly with the luminosity. These are the number of vertices and tracks in the VELO, the number of hits in the SPD and the transverse energy deposition in the calorimeters [92].

2.5. Offline data processing

Data accepted by the trigger during data taking is stored at CERN's grid computing center and replicated on grid centers distributed over Europe. There, the offline processing runs in a centrally managed effort. The two major tasks are reconstruction and stripping.

2.5.1. Reconstruction

The first step in the offline processing is to reconstruct the particle trajectories (tracks) from the hits seen by the detector.

The tracking starts with the search for track seeds in the VELO and the T stations because the magnetic field is low there. These are matched to track segments in the rest of the tracking system. There are five different track types: VELO tracks are exclusively detected in the VELO

and T tracks only in the main tracking stations. Upstream tracks are detected in the VELO and the TT while downstream tracks are seen in TT and the main tracker. Finally, long tracks are detected in all tracking devices.

Since the number of particle trajectories in a typical event is in the order of 100, the reconstruction is a demanding combinatorial effort. Not only are there inefficiencies, i.e. real tracks that can not be reconstructed, but also so-called *ghost* and *clone* tracks. Ghost tracks emerge from the combination of hits from more than one particle trajectory to form a fake track. Due to their random nature, candidates from ghost tracks are a non-peaking background and hereby negligible. Clone tracks are multiple reconstructions of the same real track. These can happen for example in the VELO where for clusters of hits there can be ambiguity whether these are due to a single particle or due to two particles flying in close vicinity. Consequently, there is a chance that a larger cluster is mistaken as unification of clusters from *two* tracks and thus, two tracks are reconstructed from this instead of one. The reconstruction of clones is partly mitigated by so-called clone-killer algorithms, whose clone rejection, however, needs to be balanced with track retention efficiency.

The tracks are the basis of particle candidate reconstruction (see next section) and the primary vertex reconstruction. A primary vertex is the point of a pp interaction and characterized by a large number of emerging tracks, which common crossing point is estimated. With several pp collisions per event (see Section 2.1), there can also be several primary vertices.

2.5.2. Stripping

The tracks found in the reconstruction are combined to build particle candidates, where constraints are put on the tracks as well as the candidates. For example, in the $B_s^0 \to \phi\phi$ decay, charged kaon candidates are combined to ϕ candidates and a pair of ϕ candidates are combined to B_s^0 candidates where at each step, constraints on the mass, the transverse momentum and the probability for the bachelor particles emerging from the same place, are made. A reconstructed B meson candidate is assumed to emerge from that primary vertex to which it has the lowest impact parameter. The flight distance of the B from the PV to its decay vertex and its momentum determine its decay proper time.

Given the high number of tracks and the variety of physics channels analyzed by LHCb, the candidate reconstruction runs in a central effort, the stripping. The stripping framework runs several stripping lines, each specialized at a certain physics process. The candidates found in the stripping are saved and accessible in the later processing without redoing the combinatorial effort described above. In order to easier manage the amount of data later, candidates are sorted into different streams oriented at the context of the analysis. The stripping lines developed in this thesis run in the `BetaS`-stream ($B_s^0 \to \phi\phi$ line) and the `Calibration`-stream (Inclusive ϕ line).

Each stripping line has to be optimized to retain as much signal as necessary and as little as possible to meet constraints set by the allocated computing power. However, some lines like the Inclusive ϕ line target a high-yield physics process and hereby need to be limited by prescales similar to the ones in the trigger (see Section 2.3).

2.6. Production of Monte Carlo simulated samples

Monte Carlo produced samples based on Event Generator predictions play an important role for studying detector effects, developing and training algorithms and determining selection efficiencies. In LHCb, the generation of these samples is handled by the GAUSS framework [93], which

provides interfaces to the event generator packages commonly used in high energy physics. Unless otherwise stated, the term "MC sample" will refer to the LHCb MC10 generation: it models pp interactions with $\nu = 2.5$ at $\sqrt{s} = 7\,\text{TeV}$ with PYTHIA 6.4 [9], while the decay of non-stable particles is handled by EVTGEN [94]. Previous MC productions are DC06 ($\sqrt{s} = 14\,\text{TeV}$, $\nu = 1$) and MC09 ($\sqrt{s} = 10\,\text{TeV}$, $\nu = 1$). Each of these samples was simulated according to the running conditions projected at the time of sample creation, which explains the different settings. Elastic, diffractive and non-diffractive events are contained in the LHCb MC samples.

Samples with different event types are generated: Minimum bias MC attempts to model typical pp interactions without any specific constraints. However, in view of the relatively low $b\bar{b}$ cross-section and the small branching ratio of many of the processes of interest, analyzing these on minimum bias MC is not feasible from a computing point of view. This is why also preselected samples are generated that are constrained to certain processes. For example, a $b\bar{b}$ sample contains only events where a $b\bar{b}$ pair was generated and signal MC contains events of a certain signal process type, like the $B_s^0 \to \phi\phi$ decay.

The MC samples discussed above model the detector data as close as possible: after generating the physics processes in the pp interaction and the decay of all non-stable particles their trajectories and their interaction in the LHCb detector are modeled using Geant4 [95]. Finally, the detector response is simulated, which results in a data sample very similar to raw data. The offline processing can treat real data and MC almost the same way.

Truthmatching can be applied to tracks on MC, which checks if a reconstructed track is compatible with a particle's trajectory at generator level. A track is defined as truthmatched if 70% of its hits coincide with the MC particle's path.

Since the MC production process is very computing intensive, so-called toy-MC is used if possible. It plays a role in the validation of maximum likelihood fits: data is generated according to the probability density function used in the fit and the fit procedure is run on that sample. By repeating this process very often, the residual distribution of the fit results can be analyzed. The fit pull, defined as the distribution of the difference between the fitted parameter and the generation parameter, normalized to the uncertainty estimated by the fit, should be a Gaussian with mean zero and width 1 for an unbiased fit.

2.7. Flavor tagging

The analysis of time dependent asymmetries

$$A(t) = \frac{\overline{N}(t) - N(t)}{\overline{N}(t) + N(t)} \tag{2.4}$$

in neutral B meson oscillations is an important handle on CP violation (Section 1.3). Here, $N(t)$ ($\overline{N}(t)$) is the number of particles decaying at time t, which were created as *mesons* (*anti-mesons*) at $t = 0$. The knowledge of the initial flavor (*meson* or *anti-meson*) is provided by the flavor tagging framework, which outputs the tagging decision

$$\xi = \begin{cases} +1 & \text{for a } B_s^0 \text{ or } B^0 \text{ at } t = 0 \\ 0 & \text{if the production flavor is unknown (untagged)} \\ -1 & \text{for a } \bar{B}_s^0 \text{ or } \bar{B}^0 \text{ at } t = 0 \end{cases} \tag{2.5}$$

and a mistag probability η, which estimates the chance for the tagging decision to be wrong.

2.7.1. Definition of tagging quality parameters

In a perfect world, each B meson's initial flavor would be exactly determined, but in reality, one is left with N_R correctly tagged, N_W wrong tagged and N_U untagged events out of a total of $(N_R + N_W + N_U)$ events.

This defines:

$$\text{tagging efficiency:} \qquad \varepsilon_{\text{tag}} = \frac{N_R + N_W}{N_R + N_W + N_U} \tag{2.6}$$

$$\text{mistag probability:} \qquad \omega_{\text{mis}} = \frac{N_W}{N_R + N_W} \tag{2.7}$$

$$\text{dilution:} \qquad D = \frac{N_R - N_W}{N_R + N_W} = 1 - 2\,\omega_{\text{mis}} \tag{2.8}$$

$$\text{tagging power:} \qquad \varepsilon_{\text{eff}} = \varepsilon_{\text{tag}}\, D^2 \ . \tag{2.9}$$

The dilution has a very clear interpretation in the analysis of the amplitude of time dependent particle-antiparticle decay asymmetries. Due to the finite mistag probability, the measured quantities $N_m(t)$ depend on the real ones $N(t)$ as follows:

$$N_m(t) = (1 - \omega_{\text{mis}})\, N(t) + \omega_{\text{mis}}\, \overline{N}(t) \tag{2.10}$$

$$\overline{N}_m(t) = (1 - \omega_{\text{mis}})\, \overline{N}(t) + \omega_{\text{mis}}\, N(t) \tag{2.11}$$

$$A_m(t) = \frac{\overline{N}_m(t) - N_m(t)}{\overline{N}_m(t) + N_m(t)} = D\, A(t) \ . \tag{2.12}$$

Thus, the measured amplitude is lower than the real one by a factor D. A similar damping effect on the amplitude is caused by a finite lifetime resolution, which "smears" the oscillation out. Consequently, good knowledge of these parameters is necessary since the amplitude result would be biased otherwise.

As a side effect of the extenuated amplitude, also the statistical uncertainty is increased. In total, the significance s of a B meson oscillation amplitude measurement on S signal and B background candidates scales as follows [96, 97]:

$$s \sim \sqrt{\frac{\varepsilon_{\text{eff}}}{2}}\, \frac{S}{\sqrt{S+B}}\, e^{-\frac{1}{2}(\Delta m \sigma_t)^2} \ . \tag{2.13}$$

Thus, the tagging power ε_{eff} needs to be maximized and the proper time resolution σ_t minimized. From the oscillation's angular frequency Δm (see Section 1.3.1), the periodic time of the B_s^0 oscillation is seven times LHCb's lifetime resolution of roughly 0.05 ps and the periodic time of B^0 oscillations is 250 times the resolution. Thus, good proper time resolution is particularly important for studies of B_s^0 meson oscillations.

The global tagging power can be optimized by introducing tagging categories [98]. Sorting candidates into k categories yields the total efficiency and tagging power:

$$\varepsilon_{\text{tag}}^{\text{comb}} = \sum_{k=1}^{N} \varepsilon_{\text{tag,k}} \qquad \varepsilon_{\text{eff}}^{\text{comb}} = \sum_{k=1}^{N} \varepsilon_{\text{tag,k}}\, (1 - 2\omega_k)^2 \ . \tag{2.14}$$

It is higher than the tagging power calculated for the combined sample, without tagging categories, which is due to the non-linearity in Equation 2.9. As limit case of taking more and more tagging categories, it is also possible to use per-event mistags, which is the approach followed in this thesis.

2.7.2. Tagging in LHCb

In the following, the general LHCb tagging strategies are shortly reviewed. The implementation details are explained in Reference [99].

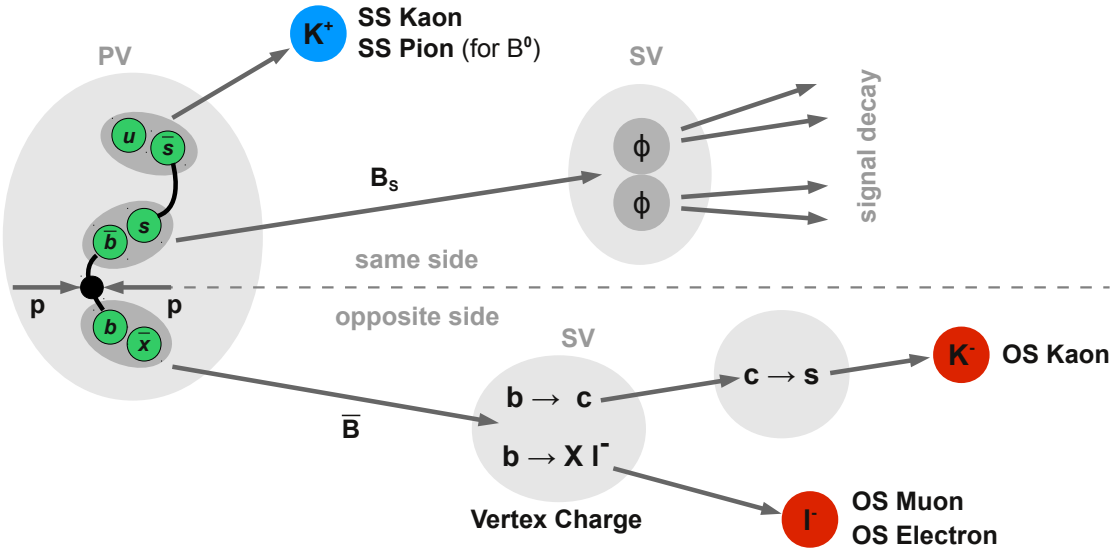

Figure 2.9.: Working principle of different taggers.

Since $b\bar{b}$ pairs are predominantly produced in the same direction, there is a good chance to find a pair of them in the LHCb acceptance. The B meson under study is called "signal" meson, whereas the other is called "non-signal" B. This definition is of course dependent from the process under study, but very helpful in the context of tagging since there are two main categories of taggers: same side (SS) taggers exploit particles produced in the hadronization process of the signal B, whereas opposite site (OS) taggers base their decision on the associated non-signal B.

- Same Side Taggers

  As illustrated in Figure 2.9, a strange quark from an $s\bar{s}$ pair is necessary for the $\bar{b}$ quark to hadronize into a B_s^0 meson. In 50% of all cases [99], the other strange quark hadronizes into a charged kaon, the charge of which correlates to the initial flavor of the B_s^0 meson. Similar considerations can be made for B^0 meson production, where a $d\bar{d}$ pair can lead to correlated charged pion production. The challenge is to correctly assign the kaon or pion to the B quark given large primary vertex backgrounds, which are even higher for the SS Pion than the SS Kaon tagger.

- Opposite Side Taggers

  Opposite Side Taggers analyze the charge of decay products of the non-signal B. There are three major strategies:

  1. The OS Electron and OS Muon taggers exploit $b \to Xl^-$ decays in the secondary vertex, where the charge of the lepton correlates to the initial b quark's charge.

  2. The OS Kaon tagger is based on the $b \to c \to s$ decay chain. If the final s quark hadronizes into a charged kaon, its charge is correlated to the initial b quark's charge.

3. The OS Vertex Charge tagger performs an inclusive reconstruction of the opposite secondary vertex assuming this is a B decay vertex. This reconstruction combines all tracks which are compatible with coming from the vertex. The tagging decision is based on a p_T-weighted sum of the charges of the contributing tracks.

The probability for the tagging decision to be correct is analyzed for each single tagger by a neural network (multilayer perceptron [100]) based on event properties. Then, the decisions of the single taggers are an average of the tagging decisions, weighted by their mistag probabilities. Output of this procedure is a combined tagging decision ξ and mistag estimate η for each tagged B candidate. MC samples are used for the neural network training, while the calibration of the per-event mistag probability distributions using an affine linear function is done by analyzing control channels on data.

2.8. LHCb run conditions and startup performance

As shortly addressed in Section 2.1, LHCb's design value for the instantaneous luminosity is $L = 10^{32}\,\mathrm{cm}^{-2}\mathrm{s}^{-1}$. This is achieved by focusing the beams less in LHCb compared to ATLAS and CMS, where the transverse beam size is 70.9 µm (RMS) instead of 16.7 µm [71]. Doing so, the average number of pp interactions is reasonably low, which improves the reconstruction performance and retards the radiation-induced aging process. The design foresees to run at an average of one pp interaction per event ($\nu = 1$).

LHCb's demand for a luminosity below the LHC's maximum offers another advantage: the instantaneous luminosity within each fill decreases with time because of proton losses and emittance growth of the beam. In LHCb, these losses over a fill can be compensated [101] by re-adjusting the beam steering during a fill to tune the delivered instantaneous luminosity to the desired value, a technique referred to as luminosity leveling.

The LHCb detector started data taking end of 2009 at a center-of-mass energy of $\sqrt{s} = 900\,\mathrm{GeV}$ before moving up to 7 TeV in the beginning of 2010. At this center-of-mass energy, an integrated luminosity of $1\,\mathrm{fb}^{-1}$ has been collected by LHCb so far (Figure 2.10), where the data collection efficiency of LHCb was above 90%. In order to achieve this high integrated luminosity, ν was risen to compensate for the below-nominal LHC filling patterns. Figure 2.10 shows the number μ of *visible* interactions per event, which account for a fraction of roughly 70% [102] of *all* interactions. Consequently, LHCb has been running at $\nu = 2.0$ to 2.5 in 2011. In contrast, the first data at $\sqrt{s} = 7\,\mathrm{TeV}$ was taken at very low ν in the order of 0.1, which makes it ideal for minimum bias studies like the inclusive ϕ cross-section measurement.

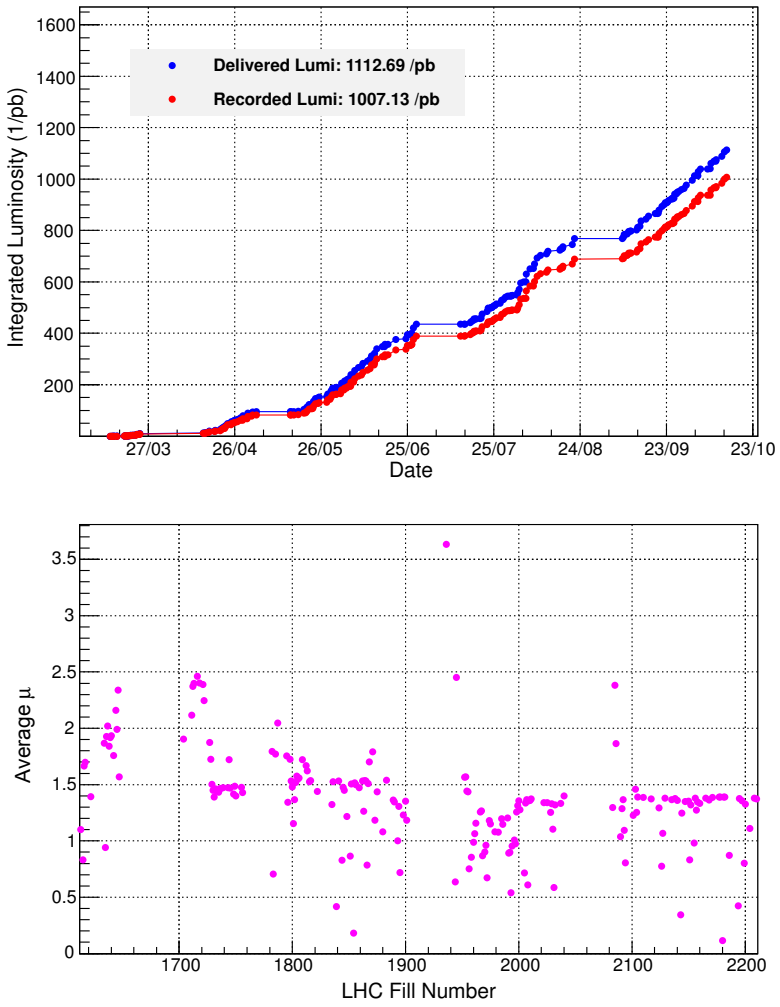

Figure 2.10.: Integrated luminosity delivered to and recorded by LHCb at $\sqrt{s} = 7\,\text{TeV}$ (top) [103]. Average number μ of *visible pp* interactions per bunch crossing (bottom) [103]. The range of fill numbers in the bottom plot covers the same time span as the upper plot.

CHAPTER 3

Signal extraction in the $B_s^0 \to \phi\phi$ channel

This chapter focuses on the extraction of the $B_s^0 \to \phi\phi$ signal from data and Monte Carlo generated samples. First, the basic concepts of this selection are presented and the discriminant variables are introduced (Section 3.1).

Then, efforts to extract the $B_s^0 \to \phi\phi$ signal on previous generated samples (DC06) are shortly reviewed next to a selection on a later sample (MC09). This was the basis for the $B_s^0 \to \phi\phi$-stripping line (Section 3.2), which is the premise for any offline analysis of the $B_s^0 \to \phi\phi$ channel because it handles the candidate selection in LHCb's global stripping effort.

Since the size of MC generated background samples is too small to allow a reliable prediction of the background levels, the selections optimized on MC suffered from uncertainties whether their background rejection is good enough. Thus, the description moves on confronting the selections optimized on MC generated samples with "real data" samples taken by the LHCb detector (Section 3.3).

Had the LHC started data taking in Summer 2008 as originally planned, a sample of several thousands of $B_s^0 \to \phi\phi$ candidates would have been selected up to now enabling the full angular analysis for *CP* violation studies presented in Chapter 4. However, due to the severe incident with an initially unknown delay, which finally added up to a shutdown of one year (see Section 2.1), the data set used in the studies presented here only reveals a couple of signal candidates. Still, first studies of the $B_s^0 \to \phi\phi$ selection on data can be carried out on this data sample. It will be shown that the selection needs to be tightened to extract the signal peak, which is –due to the small MC sample sizes discussed above– done on data. This results in an optimized selection used for further studies, hereby also in Chapter 4.

This selection in turn is put on probe on MC generated samples in Section 3.4. It will be shown that the number of candidates seen on data is in rather good agreement with event generator predictions using recent measurements of the inclusive b pair production cross-section [104] and the $B_s^0 \to \phi\phi$ branching ratio [3].

A similar cross-check between data and generated samples is done concerning Hlt2 (Section 2.3) trigger decisions in Section 3.5. Since there is a dedicated trigger line for ϕ selection [8], the acceptance rates of this line is analyzed on data and on generated samples and the gain in signal yield achieved by the Inclusive ϕ trigger line is investigated.

Finally, the background lifetime distribution is analyzed (Section 3.6), since it is –next to the signal and background expectation– an important input to study the physics performance in the $B_s^0 \to \phi\phi$ channel (presented later, in Section 4.3.5).

3.1. Selection criteria

As explained in Section 2.5.2, the $B_s^0 \to \phi\phi$ reconstruction works "bottom-up": first, charged kaon candidates that are consistent with originating from a common vertex are combined to ϕ candidates, which in turn are combined to form B_s^0 candidates. At all steps quality requirements are applied to discriminate between signal and background candidates.

The inclusive ϕ production cross-section is analyzed in Chapter 5 to 7 of this thesis. Results of this studies are that the inclusive ϕ production is very high and that the ϕ reconstruction has to fight with large backgrounds. These two facts both lead to high primary backgrounds in the $B_s^0 \to \phi\phi$ analysis. Thus, by a vertex isolation requirement, the $B_s^0 \to \phi\phi$ selection exploits the specific decay topology (Figure 3.1) with the B_s^0 decaying in a secondary vertex (SV), which is detached from its primary vertex (PV). As an unwanted side-effect, the selection efficiency is lower for small B_s^0 decay times, so a lifetime bias is created by the selection which needs to be corrected for (Section 4.2.1 and 4.3.3).

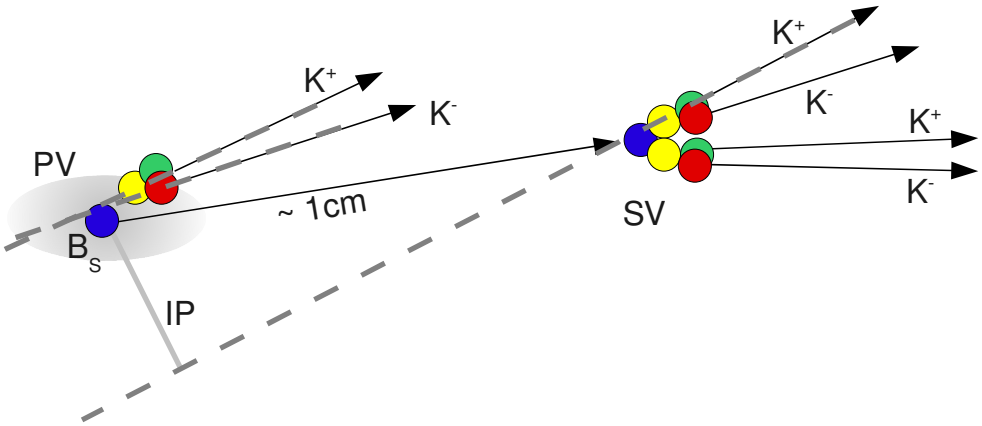

Figure 3.1.: Sketch of the $B_s^0 \to \phi\phi$ decay topology. In the SV, the B_s^0 meson (blue) decays to two ϕ mesons (yellow), which in turn decay to K^+K^- (green, red). In addition, a ϕ originating from the PV is illustrated.

The specific properties of the decay in view of its reconstruction are discussed in Reference [105]. In the following, the applied selection requirements are defined. Except for the ϕ transverse momentum product [106] and the B_s^0 impact parameter, introduced by the author, they are found in Reference [105].

- **$p_t(K)$ – kaon transverse momentum** (Figure 3.2)
  Due to the relative high B_s^0 mass, its decay products are produced with ample transverse momenta. This is not the case for minimum bias events, where e.g. ϕ mesons are produced predominantly at low p_T (compare Figure 7.2 in Section 7.2). Rejecting low transverse momentum candidates thus significantly reduces prompt background.
- **MINIP $\chi^2(K)$ – minimum kaon impact parameter significance** (Figure 3.2)
  The minimum impact parameter is the smallest distance from any primary vertex of the straight line prolongating the kaon flight direction. As illustrated in Figure 3.1, it can generally be larger for non-prompt kaons than it is for prompt kaons. However, putting a constraint on the impact parameter itself is not optimal since –for a poorly reconstructed track– its size is largely influenced by the track's uncertainty. Consequently, it is more powerful to cut on the significance of the impact parameter than on the actual value.

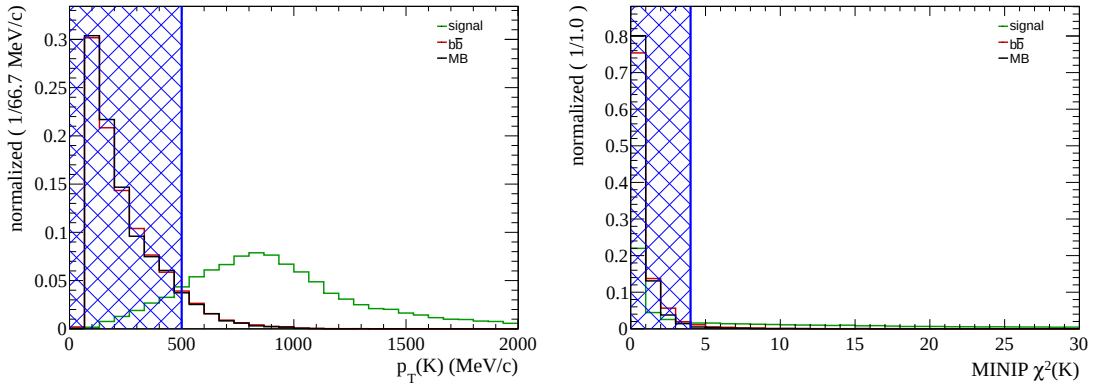

Figure 3.2.: Distribution of minimum kaon transverse momentum (left) and minimum kaon impact parameter significance (right) on MC10 for signal-, $b\bar{b}$- and minimum-bias-sample. The region excluded by the requirements in Table 3.2 is hatched. In both plots, the denominator is the number of all candidates that can be combined on that sample and where all bachelor kaons fulfil PIDK > -5.

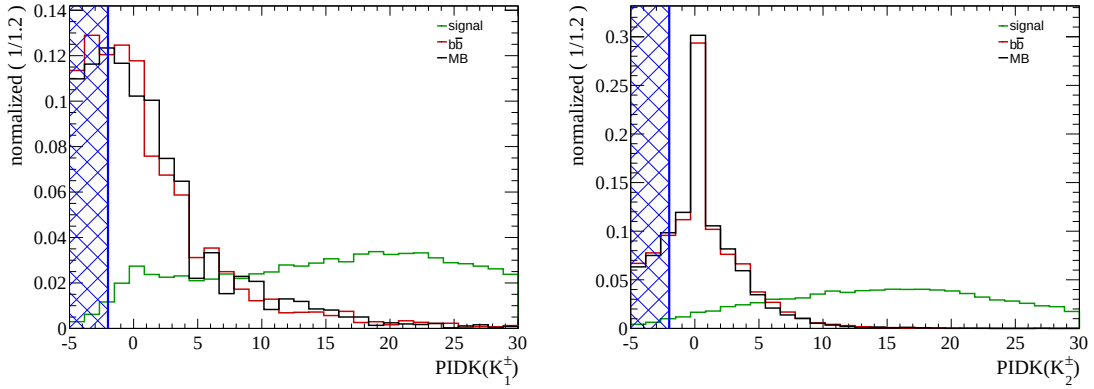

Figure 3.3.: Distribution of PIDK for kaons originating from the ϕ with the lower (left) and the higher (right) transverse momentum (see caption of Figure 3.2 for details).

- **PIDK(K) – RICH delta-log likelihood between kaon and pion hypothesis** (Figure 3.3) Since pions are produced at higher rates than kaons, a large combinatorial background to ϕ production is build by misreconstructing pions as kaons (see Figure 5.1). This type of background is very efficiently reduced by the PIDK from the RICH system, the delta-log likelihood between the kaon and the pion hypothesis. At PIDK $= 0$, both hypotheses are equally probable, at higher PIDK values, the particle is more probable to be a kaon than a pion. Since in general, the two bachelor ϕ of a B_s^0 differ in terms of transverse momentum, the PIDK distribution is different for kaons originating from the ϕ with the lower p_T and from the one with the higher p_T. Hence, a high-precision analysis on data needs to re-weight the efficiencies with the kinematic distributions of the ϕ.

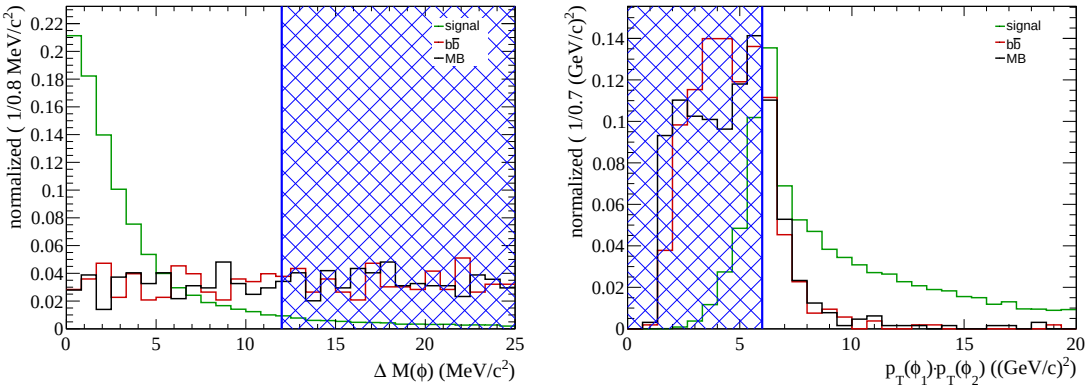

Figure 3.4.: Distribution of the difference of the ϕ candidate mass from the nominal ϕ mass (left). Distribution of the product of ϕ transverse momenta (right). Signal-, $b\bar{b}$- and a minimum-bias-sample are compared on MC10. The region excluded by the requirements in Table 3.2 is hatched. In both plots, the selection criteria on kaon properties, shown in Figure 3.2 to 3.3 are already applied.

- **$\Delta M(\phi)$ – ϕ mass window** (Figure 3.4)
  To reduce combinatorial background when reconstructing the B_s^0 meson only those ϕ mesons are retained which lie in a mass window of $m(\phi) \pm \Delta M(\phi)$, where $m(\phi)$ is the nominal ϕ mass [44].

- **$p_t(\phi_0) \cdot p_t(\phi_1)$ – ϕ transverse momentum product** (Figure 3.4)
  A cut on the product of the transverse momenta of the ϕ is more efficient than cutting only on the minimum of the ϕ transverse momentum [106]. This results in a hyperbolic cut shape in the $p_T(\phi_1) - p_T(\phi_2)$ plane, i.e. B_s^0 candidates with two low-p_T ϕ are more likely rejected than those where at least one has a very high transverse momentum. A cut on the ϕ transverse momentum is not made: since $\frac{m(\phi)-2\,\mathrm{m(K^{\pm})}}{m(\phi)}$ is only 3%, the two ϕ daughters have roughly the same transverse momentum so that a cut on $p_T(K)$ has a similar effect as a cut on $p_T(\phi)$.

- **Vertex $\frac{\chi^2}{\mathrm{Ndof}}(\phi)$ and vertex $\frac{\chi^2}{\mathrm{Ndof}}(B_s^0)$ – Vertex quality** (Figure 3.5)
  The vertex fitter seeks the optimal vertex position from two or more tracks by minimizing the vertex χ^2, which is the sum of the squared distances of the extrapolated tracks to the vertex position, weighted by the uncertainties. Since each track carries two degrees of freedom (Ndof) [107] and the vertex is parametrized by three coordinates, the ϕ vertex has $\mathrm{Ndof} = 1$ and the B_s^0 vertex has $\mathrm{Ndof} = 5$. The expectation value for $\frac{\chi^2}{\mathrm{Ndof}}$ is one, so that setting a maximum on the χ^2 suppresses candidates with poor vertex quality, which are likely to be combinatorial background.

- **IP $\chi^2(B_s^0)$ – B_s^0 impact parameter significance** (Figure 3.6)
  Since the B_s^0 meson emerges from a PV, it should have a low impact parameter with respect to the associated PV, which is exploited by cutting on the significance of this quantity. In case more than one PV is reconstructed in an event, the associated PV of a candidate is the one to which it has the lowest impact parameter.

- **DIRA(B_s^0) – B_s^0 direction angle** (Figure 3.6)
  The B_s^0 momentum, reconstructed from the sum of the daughter particles' momenta, should point to the candidate's associated PV for true B_s^0 candidates. Thus, the angle between

the reconstructed momentum and the B_s^0 flight path, i.e. the line through the associated PV and SV, should be small. The cosine of the angle between the two directions is defined as direction angle (DIRA).

- **$\Delta M(B_s^0) - B_s^0$ mass range** (Figure 3.8)
  B_s^0 meson candidates are retained in a mass range of $\pm\Delta M(B_s) = 300\,\mathrm{MeV}/c^2$ around the nominal B_s^0 mass to provide sufficient sideband data.

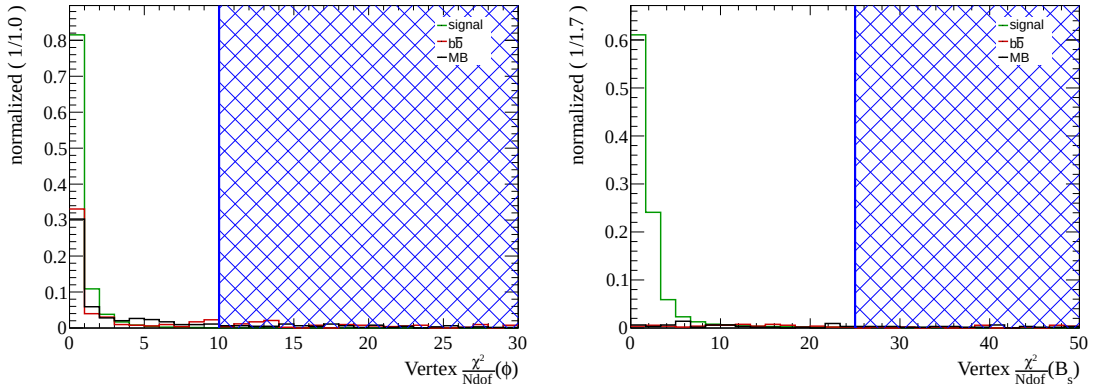

Figure 3.5.: Distribution of vertex quality criterion χ^2/Ndof of ϕ (left) and B_s^0 (right) candidates (see caption of Figure 3.4 for details).

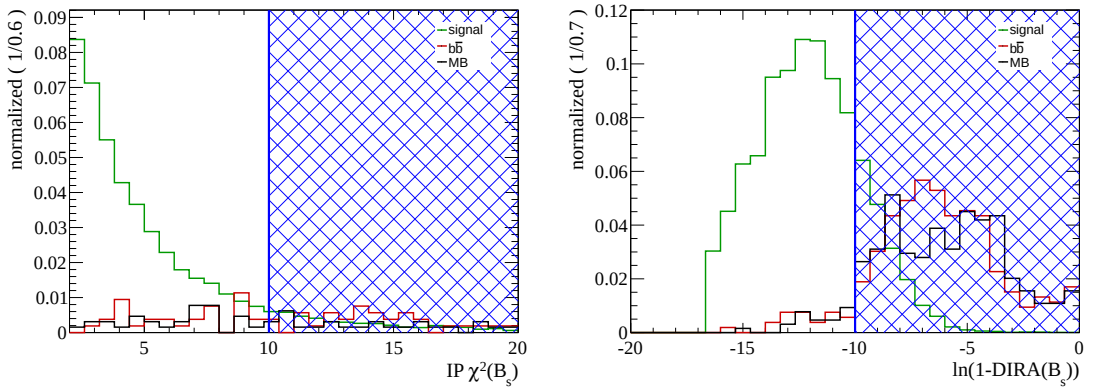

Figure 3.6.: Distribution of B_s^0 impact parameter significance (left). Distribution of natural logarithm of the difference between 1 and the B_s^0 direction angle (right) (see caption of Figure 3.4 for details).

3.2. $B_s^0 \to \phi\phi$ selection optimization on simulated samples

An optimization of the $B_s^0 \to \phi\phi$ selection on DC06 Monte Carlo at $\sqrt{s} = 14\,\mathrm{TeV}$ is described in Reference [106], pointing out that the knowledge of the backgrounds is highly limited by MC sample size and thus poor. Only an upper limit for the background yield is calculated ibidem. It is done on a $b\bar{b}$ inclusive sample, thus implicitly assumes that there are no backgrounds from non-$b\bar{b}$ events. This is to be understood as an approximation done because no sufficiently large minimum bias sample was available.

The MC09 sample was simulated at a center-of-mass energy of $\sqrt{s} = 10\,\text{TeV}$, which was the assumed LHC running condition upon sample creation. An analysis of this sample shows that the distribution of the crucial discriminant variables is very similar to the DC06 sample. Since additionally, the constraints given by the sample size are the same, one arrives at an MC09 selection, which is very similar to the DC06 one presented in Reference [106]. A selected signal sample was provided [108], which the LHCb collaboration used for MC09 trigger efficiency studies. A full MC09 analysis was carried out [108], but it is not described here in favor of a presentation of the MC10 analysis, which superseded the MC09 one.

Based on the MC09 selection, a new stripping line was developed. As documented in References [108–112], it was continuously adapted to the current data taking conditions and followed the quickly evolving stripping framework. Only the currently up-to-date version [113] is presented here. It is based on a loose PIDK requirement, vertex quality and kinematic criteria. The selection requirements, summarized in Table 3.1 are mostly chosen looser than in the offline analysis in order to allow further studies with looser cuts offline. In addition to the main $B_s^0 \to \phi\phi$ stripping line with a mass window of $25\,\text{MeV}/c^2$, a sideband line is implemented, which selects any candidate with a ϕ mass from the kinematic border up to a mass of $1090\,\text{MeV}/c^2$. It is prescaled by a factor of 0.05.

Running over all triggered LHCb events, the stripping is a computing intensive task, which puts some constraints on the selections run there. The maximum time for each stripping line and event is 1 ms and the maximum event acceptance rate is 0.05% [114], which is checked centrally in LHCb. The $B_s^0 \to \phi\phi$ stripping line meets these requirements [115].

In particular the timing is a challenge for the $B_s^0 \to \phi\phi$ channel due to high combinatorial backgrounds when building the ϕ candidate. This is addressed by putting requirements on the kaon properties, i.e. early in the reconstruction chain. The LHCb software framework provides so called "Standard Particles", e.g. `StdLoosePhi` in order to prevent each selection from redoing the combinatorics. Selections building on these can then filter them by applying further selection criteria. However, timing studies showed that the use of these is not advantageous for the $B_s^0 \to \phi\phi$ stripping line, i.e. it is faster to redo the combinatorics after applying cuts on the kaons than it is to filter through all `StdLoosePhi`.

Table 3.1.: Selection criteria in $B_s^0 \to \phi\phi$ stripping line (version: [113]).

PIDK(K)	$>$	-5	
MINIP$\chi^2(K)$	$>$	3.5	
$p_t(K)$	$>$	450 MeV/c	
$\Delta M(\phi)$	$<$	25 MeV/c^2	(see text)
$M(\phi)$	$<$	1090 MeV/c^2	(see text)
Vertex $\frac{\chi^2}{\text{Ndof}}(\phi)$	$<$	10	
$p_t(\phi_0) \cdot p_t(\phi_1)$	$>$	2 (GeV/c)^2	
Vertex $\frac{\chi^2}{\text{Ndof}}(B_s^0)$	$<$	25	
$\Delta M(B_s^0)$	$<$	300 MeV/c^2	

3.3. Extraction of the $B_s^0 \to \phi\phi$ signal from data

The selection optimized on Monte Carlo is applied to real data[1] collected between July and October 2010 at $\sqrt{s} = 7\,\text{TeV}$. It equals an integrated luminosity of $(36.5 \pm 3.6)\,\text{pb}^{-1}$.

In Figure 3.7, no mass peak is visible on top of the combinatorial background, which proves the selection criteria to be too loose. This is in no contradiction to the findings of the optimization done on Monte Carlo: the MC sets (DC06/MC09) differ from the real data in terms of expected interactions ν per event. While ν equals 1 in the aforementioned MC samples, it is in the order of 2.5 in real data. Furthermore, the background description by MC is questionable: The analysis of the inclusive φ production cross-section presented in Chapter 5 to 7 of this thesis shows that the φ production is underestimated by a factor of 2 in the region of interest and hereby the combinatorial background will certainly also be higher on data than on MC.

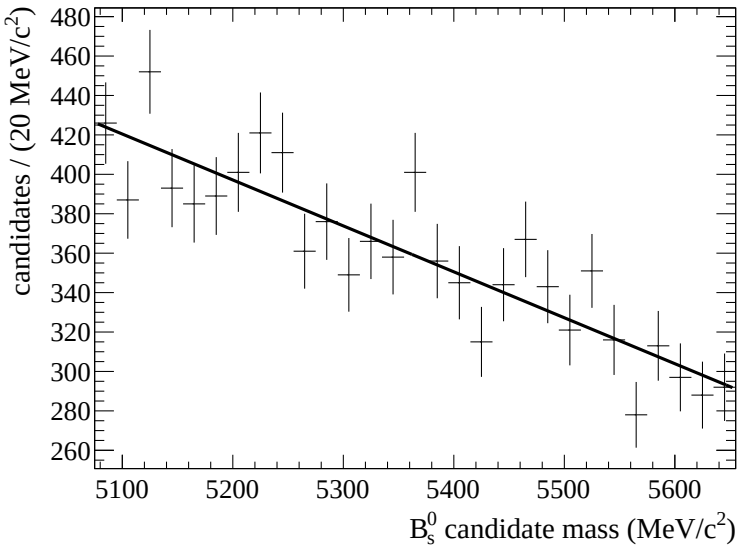

Figure 3.7.: B_s^0 mass spectrum on data using the selection optimized on MC. The crosses represent histogrammed data with its uncertainties and a straight line fit is added.

The selection has been optimized on data, which could potentially enhance fluctuations and hereby create a bias. However, the objective is not to extract an explicit cross-section result, but rather to gain a first understanding of the $B_s^0 \to \phi\phi$ selection on data. Also, a comparison of the extracted signal yield with simulation expectations will show reasonable agreement, which suggests the mass peak to be not only a fluctuation.

In the optimization process, the MC10 distributions of the selection variables, shown in Figure 3.2-3.6, are used to determine sensible working points. The maximization criterion is the signal over background ratio in the mass spectrum, avoiding lifetime-biasing requirements as much as possible. The number of signal- and background- candidates (n_S and n_B) are determined by an unbinned extended maximum likelihood fit, where the signal probability density function (PDF) is a Gaussian with mean $m_{B_s^0}$ and width $\sigma_{m_{B_s^0}}$ and the background PDF is a linear function with slope s_B.

[1] run 74621-81685, reconstructed in version Reco08-Stripping12b

The most pronounced signal peak is gained with the selection requirements summarized in Table 3.2 and the corresponding B_s^0 mass spectrum is shown in Figure 3.8. As presented in Table 3.3, $n_S = 38.4 \pm 7.6$ signal candidates are found. The fitted B_s^0 mass is in agreement with the world average [44] and the width agrees reasonably with the MC expectation in Table 4.6.

The expected $B_s^0 \to \phi\phi$ yield for one year of nominal data taking is extrapolated by scaling the luminosity of the data sample up to $2\,\text{fb}^{-1}$, which yields 2129 ± 471 signal and 6922 ± 295 background candidates per year (in a mass range of $\pm 300\,\text{MeV}/c^2$ around the nominal B_s^0 mass). The likelihood fit is repeated on only those candidates that were accepted by the *Hlt2IncPhi* trigger, resulting in an annual expectation of 1704 ± 377 signal and 2190 ± 338 background candidates.

Table 3.2.: Selection cuts optimized on data.

PIDK(K)	$>$	-2
MINIP$\chi^2(K)$	$>$	4
$p_t(K)$	$>$	500 MeV/c
$\Delta M(\phi)$	$<$	12 MeV/c^2
Vertex $\frac{\chi^2}{\text{Ndof}}(\phi)$	$<$	10
$p_t(\phi_0) \cdot p_t(\phi_1)$	$>$	6 (GeV/c)^2
IP$\chi^2(B_s^0)$	$<$	10
Vertex $\frac{\chi^2}{\text{Ndof}}(B_s^0)$	$<$	25
DIRA(B_s^0)	$>$	0.99995
$\Delta M(B_s^0)$	$<$	300 MeV/c^2

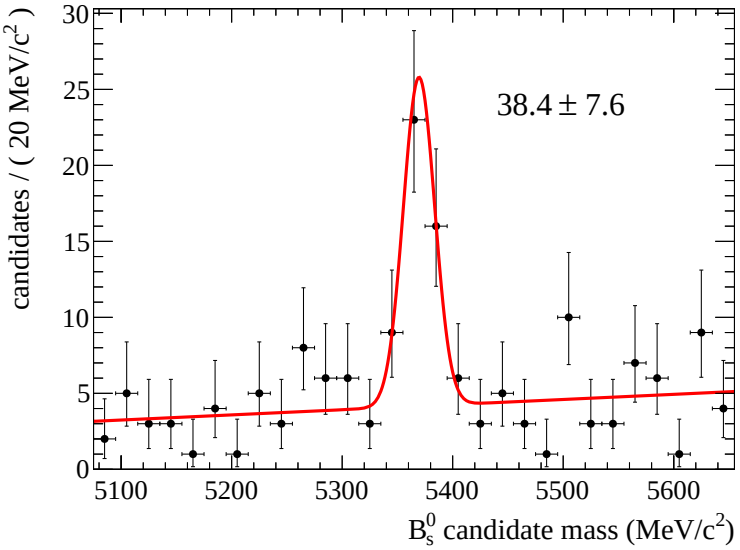

Figure 3.8.: B_s^0 mass spectrum on data after optimization. Histogrammed data is shown with its uncertainties. A Gaussian signal with linear background function is fitted to the data.

Table 3.3.: Numerical results of fit shown in Figure 3.8.

$m_{B_s^0}$	5369.5 ± 3.2	MeV/c^2
$\sigma_{m_{Bs}}$	14.2 ± 2.7	MeV/c^2
n_S	38.4 ± 7.6	
n_B	123 ± 12	
s_B	0.24 ± 0.16	$(\text{MeV}/c^2)^{-1}$

3.4. Yield estimation from simulated samples

In the following, the yield determined on data is compared to predictions based on Monte Carlo. For comparison with previous signal yield expectations at the nominal LHC center-of-mass energy $\sqrt{s} = 14\,\text{TeV}$ see References [106, 116].

The number $n_{B_s^0}$ of reconstructed $B_s^0 \to \phi\phi$ candidates expected in a data sample of a certain luminosity $\mathcal{L}$ is given by the following formula:

$$n_{B_s^0} = \mathcal{L} \cdot \sigma_{b\bar{b}} \cdot n_{b\bar{b}} \cdot f_{B_s^0} \cdot \mathcal{BR}(B_s^0 \to \phi\phi) \cdot (\mathcal{BR}(\phi \to K^+K^-))^2 \cdot \varepsilon_{\text{gen}} \cdot \varepsilon_{\text{sel}} \cdot \varepsilon_{\text{trig}} \,. \tag{3.1}$$

The $b\bar{b}$ cross-section $\sigma_{b\bar{b}}$ (values of the parameters introduced here are given in Table 3.4) at $\sqrt{s} = 7\,\text{TeV}$ is taken from Reference [104]. This needs to be multiplied by $n_{b\bar{b}} = 2$ because b quarks are produced pair-wise and both of them hadronize into a B meson. A fraction $f_{B_s^0}$ [44] of these are B_s^0 mesons, which in turn decay into the $\phi\phi$ final state with the branching fraction given in Reference [3]. Since the ϕ reconstruction is done in the K^+K^- mode, the square of the $\phi \to K^+K^-$ branching fraction [44] needs to be taken into account.

The selection efficiency on signal MC has to take two steps into account: to save computing time in the production of Monte Carlo simulated signal events, a coarse geometrical cut is applied already in the event generation, which requires the signal candidate to lie in a region slightly larger than the LHCb acceptance. The efficiency ε_{gen} of this cut is determined by GAUSS [117, 118].

Due to the low visible $B_s^0 \to \phi\phi$ branching fraction it is safe to assume that there are not two $B_s^0 \to \phi\phi$ decays in an event, thus the selection efficiency ε_{sel} is determined as the quotient of the number of truthmatched candidates that pass the selection divided by the total number of events in the MC sample. Clones, which are build at a fraction of roughly 3%, are not double-counted, i.e. at most one candidate is counted in each event. Similar to ε_{sel}, the trigger efficiency $\varepsilon_{\text{trig}}$ is defined as the number of selected candidates that would be accepted by the trigger divided by the number of candidates that pass the selection.

Two different MC samples are used for this study. Initially, it was carried out using MC09, as soon as an MC10 sample became available, it was repeated on this one.

MC09: The sample[2] contains $1 \cdot 10^6$ events at magnet polarity "down" at $\sqrt{s} = 10\,\text{TeV}$. For this study to be self-consistent, versions of the LHCb software are employed which were actively developed with MC09 Monte Carlo[3]. In particular, a similar version has been used for collaboration-wide efforts of trigger optimization and evaluation [119], so that reasonable results can be expected in terms of simulated trigger response.

[2] generated in the "Sim04Reco03" setting

[3] version v24r2 of the LHCb software framework DAVINCI and setting "Effective_Nominal" for the trigger.

MC10: The sample is generated[4] at $\sqrt{s} = 7\,\text{TeV}$ and $\nu = 2.5$. It contains $1 \cdot 10^6$ events, half of which at each magnet polarity. Reconstruction, trigger and stripping have been applied to the sample in a global effort[5].

Table 3.4.: Determination of the expected signal candidate yield from MC09 and MC10 in a nominal year of data taking ($2\,\text{fb}^{-1}$). The symbols are defined in the text.

Quantity	value	comment
$\mathcal{L}$	$2\,\text{fb}^{-1}$	per year
$\sigma_{b\bar{b}}$	$(284 \pm 53) \cdot 10^{-6}\,\mu\text{b}$	from [104]
$n_{b\bar{b}}$	2	
$f_{B_s^0}$	0.122 ± 0.014	from [44]
$\mathcal{BR}(B_s^0 \to \phi\phi)$	$(2.40 \pm 0.89) \cdot 10^{-5}$	from [3]
$\mathcal{BR}(\phi \to KK)$	0.489 ± 0.005	from [44]
ε_{gen}	0.17 ± 0.01	
ε_{sel}	0.0857 ± 0.0003	MC09
$\varepsilon_{\text{sel}} \cdot \varepsilon_{\text{trig}(\textit{Hlt2Global})}$	0.0165 ± 0.0001	
expected candidates	2274 ± 989	
ε_{sel}	0.0740 ± 0.0003	MC10
$\varepsilon_{\text{sel}} \cdot \varepsilon_{\text{trig}(\textit{Hlt2IncPhi})}$	0.0170 ± 0.0001	
expected candidates	2337 ± 1017	

Based on Equation 3.1, an annual signal yield is calculated for MC09 and MC10. Since the analysis on MC09 is based on *Hlt2Global*[6], the expected annual yield from Table 3.4 of 2274 ± 989 is compared to the total number of 2129 ± 471 candidates extrapolated on data. The expectation on MC10 relying exclusively on the *Hlt2IncPhi* trigger line the annual expectation of 2337 ± 1017 should be compared to the extrapolation on data only based on that trigger line, which are 1704 ± 378 candidates. An alternative point-of view would be to determine the number of *Hlt2IncPhi*-triggered candidates from data to determine $\mathcal{BR}(B_s^0 \to \phi\phi)$ from data using the constants for MC10 from Table 3.4. The result $\mathcal{BR}(B_s^0 \to \phi\phi) = (1.8 \pm 0.6) \cdot 10^{-5}$ would be in agreement with the CDF measurement [3] $(2.40 \pm 0.89) \cdot 10^{-5}$. However, as noted in Section 3.3, systematic effects are not taken into account here, so this number is rather meant as indication that the $B_s^0 \to \phi\phi$ signal extraction is understood at first order.

3.5. Analysis of trigger decisions

As outlined in Section 2.3, specific code targeted at ϕ reconstruction, the Inclusive ϕ trigger (*Hlt2IncPhi*), is implemented at Hlt2 level. This is the motivation to compare the signal acceptance rate of the *Hlt2IncPhi* trigger to the one of other Hlt2 lines. Since each trigger line can in principle introduce different biases on the B_s^0 decay proper time or the bachelors' angular distribution, each of these would require a separate dedicated study, so the analysis should focus on the most efficient lines only. This is because the acceptance ratio of the various lines can be different on MC and data, which would result in a different overall bias. Similar considerations hold for

[4] generated in the "Oct2010 Sim01" setting

[5] reconstruction version "Reco8", TCK `0x002E002A` and Stripping12

[6] A unification of all trigger lines, each tuned to meet certain well-balanced retention rates. It is based on studies carried out before the LHC startup to optimize the overall physics performance of LHCb.

the L0 and Hlt1 level, where again, each trigger line could introduce its own biases and thus need a separate treatment. However, for the MC studies presented here, the effective proper-time- and angular- efficiencies are determined on MC and applied to MC, thus this issue does not emerge here. This is why at this point, no distinction is made at L0 and Hlt1 level.

In previous studies on MC09 [119], the *Hlt2IncPhi* trigger [8, 86] has shown to be the most efficient for the $B_s^0 \to \phi\phi$ decay channel, followed by topological trigger lines. Here, this fact is studied in more detail on MC09, MC10 and data. Uncertainties quoted in this section are binomial errors based on the sample size.

MC09: The total efficiency for offline selected candidates to be triggered is $(20.1 \pm 0.1)\%$. This number (*Hlt2Global*), however, is an OR of *all*, i.e. several dozens, Hlt2 lines. $(96.9 \pm 0.6)\%$ of all Hlt2 triggered candidates are triggered by the *Hlt2IncPhi* trigger. The lines which have next highest efficiencies are parts of the topological trigger. Combining all five lines having an efficiency of larger than 5%, one covers $(98.9 \pm 0.6)\%$ of all triggered candidates, omitting the *Hlt2IncPhi* line, this fraction drops to $(67.7 \pm 0.6)\%$.

MC10: Like on MC09, the *Hlt2IncPhi* line has the highest efficiency, $(22.9 \pm 0.2)\%$, on MC10. Only so-called "Physics Triggers" are counted. Efficiencies for auxiliary lines[7] are not quoted here: they have a bandwidth limitation on data depending on the current data taking conditions which is not modeled in MC, so that the efficiencies would not be meaningful [120].

The next best triggers are topological lines, like on MC09. The four trigger lines that have an acceptance rate larger than 10% per line accept $(24.0 \pm 0.1)\%$ of the offline selected candidates, dropping the *Hlt2IncPhi* line, only $(20.7 \pm 0.2)\%$ would be accepted. Comparing the efficiency of the *Hlt2IncPhi* line of $(22.9 \pm 0.2)\%$ with the united efficiency for the four quoted most efficient lines, the *Hlt2IncPhi* line is $(95 \pm 1)\%$ efficient compared to the combination of these lines.

Data: The relative efficiency of different trigger decisions has been checked on data. The basis are all (triggered) and offline selected candidates in the aforementioned LHCb data sample. Since a non-negligible amount of background candidates is present in this sample, a tight cut on the B_s^0 candidate mass ($5316.3\,\mathrm{MeV}/c^2 < m(B_s^0) < 5416.3\,\mathrm{MeV}/c^2$) is applied. The largest acceptance rate is found for the *Hlt2IncPhi* line followed by topological trigger lines[8] [9]. Since there is still a non-negligible amount of background, in particular at low lifetimes, (compare Figure 3.10 and 4.7), this analysis is repeated for candidates with lifetimes larger than 0.5 ps and 1 ps.

Depending on the lifetime cut, the combination[10] of the *Hlt2IncPhi*-, the topological- and the muon- trigger accept $(84 \pm 5)\%$ (no lifetime cut), $(92 \pm 5)\%$ ($t > 0.5\,\mathrm{ps}$) or 100% ($t > 1.0\,\mathrm{ps}$) of all Hlt2 triggered *candidates* (including background). Without the *Hlt2IncPhi* line, these numbers drop by 25-30%. On the other hand, the *Hlt2IncPhi* line accepts $(66 \pm 6)\%$ (no lifetime cut) $(81 \pm 6)\%$ ($t > 0.5\,\mathrm{ps}$) or $(86 \pm 6)\%$ ($t > 1.0\,\mathrm{ps}$) of all triggered candidates.

In conclusion, simulations establish the *Hlt2IncPhi* trigger line as valuable for the analysis of the $B_s^0 \to \phi\phi$ decay channel since it is the most efficient trigger line and accepts a sizable fraction of all triggered candidates. Studies on data confirm the potential of this trigger line under real data taking conditions.

[7] *Hlt2IncPhiSidebands*-, *Hlt2IncPhiTrackFit*-, *Hlt2IncPhiRobust*-, *Hlt2Transparent*- and *Hlt2Express* decision

[8] *Hlt2TopoOSTF2BodyDecision*, *Hlt2TopoOSTF3BodyDecision*, *Hlt2TopoOSTF4BodyDecision*

[9] *Hlt2TopoTF3BodyReq3YesDecision*, which was temporarily used at detector startup only, but abandoned later on, is discarded.

[10] *Hlt2IncPhi*, *Hlt2TopoOSTF2BodyDecision*, *Hlt2TopoOSTF3BodyDecision*, *Hlt2TopoOSTF4BodyDecision*, *Hlt2IncPhiSidebandsDecision*, *Hlt2MuTrackDecision*

3.6. Lifetime distribution for background

In order to determine the background decay proper time distribution, the LHCb data sample is split up into categories of B_s^0 candidate decay time and a fit to the mass distribution is performed in each category. The fitted mass spectra are shown in Figure 3.9.

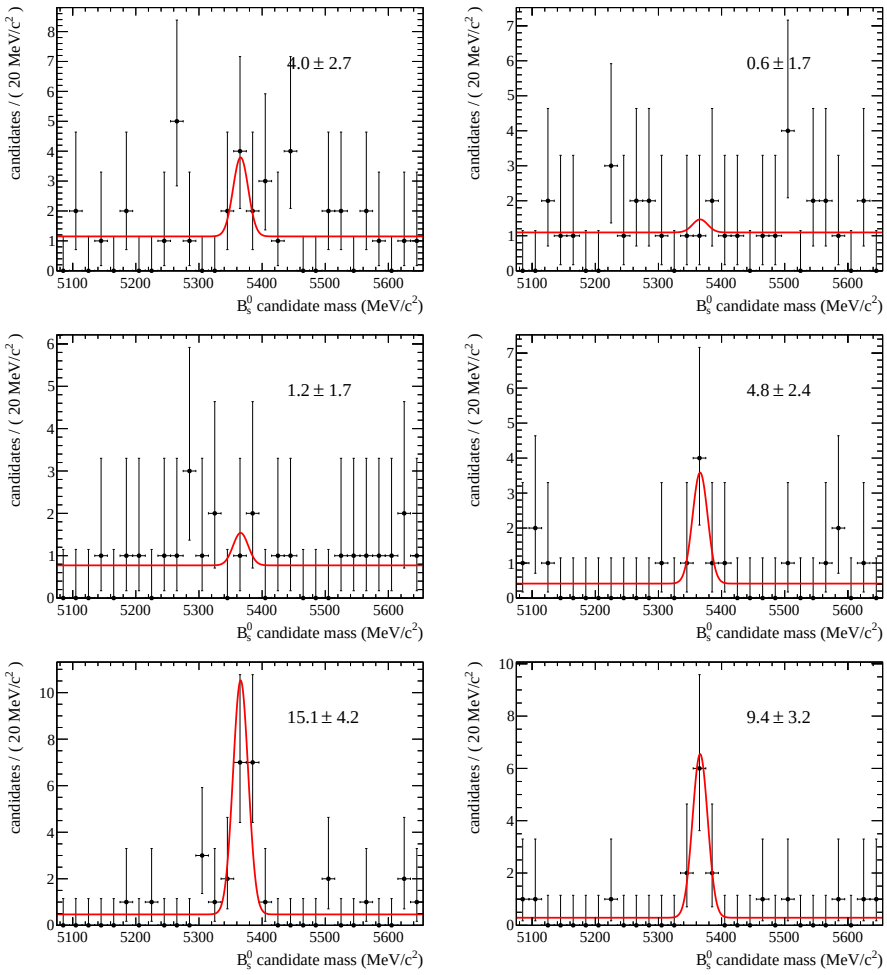

Figure 3.9.: B_s^0 mass spectrum for different ranges of B_s^0 decay time (ps): $(0-0.2)$ and $(0.2-0.4)$ (top), $(0.4-0.6)$ and $(0.6-1.0)$ (middle), $(1.0-2.0)$ and (>2.0) (bottom).

The number of candidates per category of decay background proper time (normalized to the bin size) is plotted in Figure 3.10. A Gaussian multiplied with the Heaviside step function and an exponential component are used to fit the data:

$$f_g \cdot H(t) \frac{2}{\sqrt{2\pi\sigma^2}} e^{-\frac{1}{2}\left(\frac{t}{\sigma}\right)^2} + (1-f_g) \cdot \frac{\alpha}{e^{(6\,\mathrm{ps})\alpha}-1} e^{\alpha t}\,, \tag{3.2}$$

which results in the parameters in Table 3.5. The fit's χ^2 is 2.1 at two degrees of freedom. The prompt peak is roughly 10 times wider than the lifetime resolution of LHCb (Table 4.3), which is in contrast to the $B_s^0 \to J/\psi\,\phi$ decay channel, for example, where the two values agree. A reason for this could be that in the $B_s^0 \to J/\psi\,\phi$ case, prompt J/ψ are cleanly reconstructed whereas the ϕ suffers from high combinatorial backgrounds.

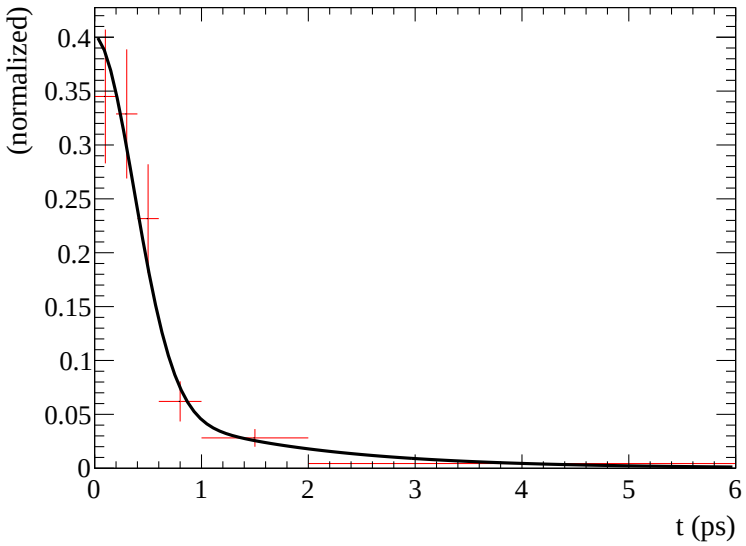

Figure 3.10.: Background decay proper time distribution from sideband data.

Table 3.5.: Optimized parameters describing the background lifetime distribution on data and their statistical uncertainty (see Equation 3.2).

σ	0.373 ± 0.048	ps
α	-0.70 ± 0.18	ps^{-1}
f_g	0.60 ± 0.12	

– blank page –

CHAPTER 4

Extraction of *CP* violation parameters from the $B_s^0 \to \phi\phi$ decay

As shortly addressed in Section 1.3.3, the final state in the $B_s^0 \to \phi\phi$ decay is a superposition of *CP*-odd and *CP*-even contributions. Since the measured *CP* asymmetry amplitude is sensitive to the sign of the final state's *CP* eigenvalue, these two contributions need to be disentangled. The following Section 4.1 explains in detail how this is possible on a statistical basis since the decays into the *CP*-odd and *CP*-even final states have a different angular distribution.

Physics parameters like the *CP* violating phase are extracted with an unbinned maximum likelihood fit. Section 4.2 presents the signal- and the background probability density function used in this fit. The signal part implements the angular- and time- dependent $B_s^0 \to \phi\phi$ decay model presented in Section 4.1.

As a proof-of-principle, the fit method is applied to a Monte Carlo simulated sample. In a first step, the resolution parameters and efficiencies are determined on this sample. Then, a fit to a simulated sample proves that the parameter set put in at production time can be reconstructed (Section 4.3).

Based on the properties of the simulated sample and the expected signal yield (Section 3.3), a prediction of the statistical uncertainty on the *CP* violating phase is made at the end of this chapter in Section 4.3.5.

4.1. Theoretical description

The $B_s^0 \to \phi\phi$ decay is a $P \to VV$ (pseudoscalar- to vector- vector- meson) decay, which puts constraints on the final state configuration because of angular momentum conservation. The formalism is similar to the $B_s^0 \to J/\psi\,\phi$ decay described e.g. in References [53, 121]. In the following, the bra-ket notation $|J,M\rangle$ with total angular momentum J and momentum M along the quantization axis, which is chosen along the ϕ flight direction in the B center-of-mass system, is applied to examine these configurations.

Following Clebsch-Gordan decomposition, three states with $M = 0$ can be established by a product state of two (vector) particles $|j,m_1\rangle\ |j,m_2\rangle$ with spin $j = 1$:

$$|0,0\rangle = \sqrt{1/3}|1,1\rangle|1,-1\rangle - \sqrt{1/3}|1,0\rangle|1,0\rangle + \sqrt{1/3}|1,-1\rangle|1,1\rangle \quad (4.1)$$

$$|1,0\rangle = \sqrt{1/2}|1,1\rangle|1,-1\rangle - \sqrt{1/2}|1,-1\rangle|1,1\rangle \quad (4.2)$$

$$|2,0\rangle = \sqrt{1/6}|1,1\rangle|1,-1\rangle + \sqrt{2/3}|1,0\rangle|1,0\rangle + \sqrt{1/6}|1,-1\rangle|1,1\rangle\ . \quad (4.3)$$

Since the initial state B_s^0 is given by a single pseudoscalar $|0,0\rangle$, the final state must have angular momentum $L \in 0,1,2$ in order to compensate for the spin and to conserve the total angular momentum between initial and final state. As pointed out in Equation 1.37 and 1.38, the angular momentum L of the final state plays a role in the calculation of the *CP* violation by determining the final state's *CP* eigenvalue: the states with $L = 0$ and $L = 2$ are *CP*-even, whereas the state with $L = 1$ is *CP*-odd. As pointed out in Reference [122], the *CP* asymmetry from the three different partial waves might dilute or cancel. However, they can be separated on a statistical basis using an angular analysis.

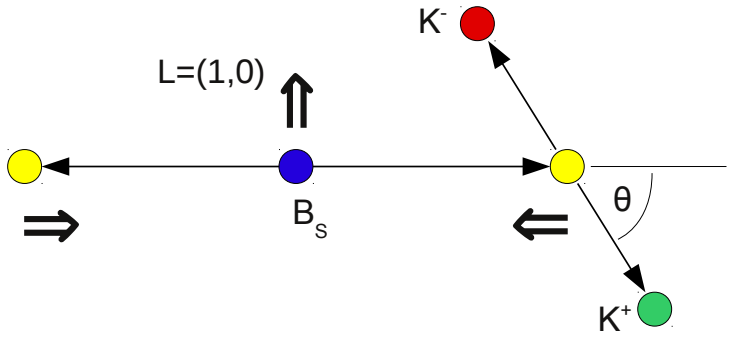

Figure 4.1.: Illustration of angular momenta for *CP* odd final state.

Figure 4.1 is a simplified illustration of the conditions in the *CP* odd state given in Equation 4.2. The spins of the ϕ mesons are oriented along the quantization axis and the total angular momentum orthogonally to this axis. This simple picture already hints the angular distribution: the decay of the vector meson into two pseudoscalar kaons preferably proceeds with the pseudoscalars being emitted orthogonally to the initial spin, so that angles of $\theta \to 90^\circ$ are more probable (compare to Equation 4.16 further down). In total, the angular distribution of the final states can be calculated using the helicity formalism [123]:

$$\frac{\mathrm{d}^3\Gamma}{\mathrm{d}\cos\theta_1\,\mathrm{d}\cos\theta_2\,\mathrm{d}(\varphi_1+\varphi_2)} \propto \left| \sum_{h=-1}^{1} H_h(t)\, D^{1*}_{h,0}(\varphi_1,\theta_1,0)\, D^{1*}_{h,0}(\varphi_2,\theta_2,0) \right|^2 . \quad (4.4)$$

Here, it has been taken into account that the two B_s^0 daughters must have equal helicity and that they decay into spin-0 particles. $H_h(t)$ (with $h \in \{-1,0,1\}$) are time dependent helicity amplitudes and $D^{1*}_{h,0}$ are Wigner D-functions. These are the matrix elements of the rotation operator [123]

$$R(\alpha,\beta,\gamma) = e^{-i\alpha J_z} e^{-i\beta J_y} e^{-i\gamma J_z}$$

$$\langle j,m'|R(\alpha,\beta,\gamma)|j,m\rangle = D^j_{m',m}(\alpha,\beta,\gamma) = e^{-i\alpha m'}\, d^j_{m',m}(\beta)\, e^{-i\gamma m}$$

with the reduced rotation matrices [44]

$$d^j_{m',m}(\beta) = \langle j,m'|e^{-i\beta J_y}|j,m\rangle \tag{4.5}$$

$$d^1_{0,0} = \cos\beta \tag{4.6}$$

$$d^1_{\pm 1,0} = \mp\sqrt{1/2}\,\sin\beta\,. \tag{4.7}$$

The latter are related to spherical harmonics Y_l^m by $d^l_{m,0}(\theta) = \sqrt{\frac{4\pi}{2l+1}}\, Y_l^m(\theta,\phi)\, e^{-im\phi}$.

The angles in Equation 4.4 are illustrated in Figure 4.2: θ_1 and θ_2 are the helicity angles of the K^+ in the corresponding ϕ rest frame and φ is the skew between the kaon decay planes. Since φ_1 and φ_2 are defined with respect to a reference frame with arbitrary rotation angle, only their *sum* φ is physically meaningful.

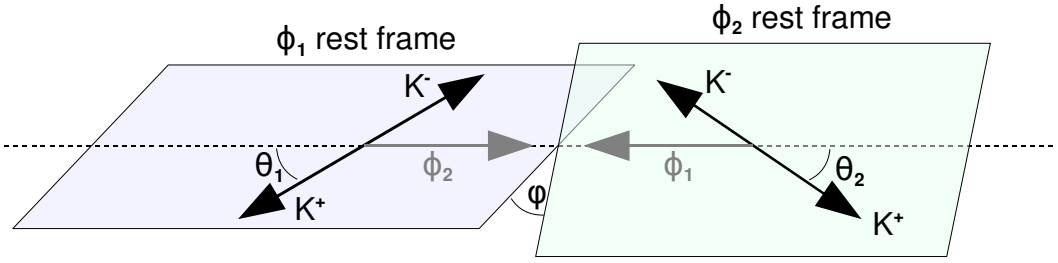

Figure 4.2.: Illustration of transversity angles in the $B_s^0 \to \phi\phi$ decay.

As shown in Reference [122], definite *CP* contributions can be projected out by a transition to transversity amplitudes, defined as follows:

$$A_0 = H_0 \tag{4.8}$$

$$A_\parallel = \sqrt{1/2}\,(H_{+1} + H_{-1}) \tag{4.9}$$

$$A_\perp = \sqrt{1/2}\,(H_{+1} - H_{-1})\,. \tag{4.10}$$

The amplitudes A_0 and $A_\parallel$ cover the *CP*-even contribution, whereas $A_\perp$ is the amplitude of the *CP*-odd state. These amplitudes have relative phases to each other, which are usually parametrized as

$$\delta_\perp = \arg(A_\perp/A_0) \tag{4.11}$$

$$\delta_\parallel = \arg\left(A_\parallel/A_0\right)\,. \tag{4.12}$$

From Equation 4.4 and 4.8-4.10, the helicity angle distribution in the $B_s^0 \to \phi\phi$ decay follows as [124]:

$$\mathcal{P}_{B_s^0}(t, \cos\theta_1, \cos\theta_2, \varphi) = \tag{4.13}$$

$$\frac{1}{\Gamma(B_s^0 \to \phi\phi)} \cdot \frac{\mathrm{d}^4\Gamma(B_s^0 \to \phi\phi)}{\mathrm{d}t\, \mathrm{d}\cos\theta_1\, \mathrm{d}\cos\theta_2\, \mathrm{d}\varphi} =$$

$$\frac{9}{32\pi}\Big[|A_0(t)|^2 \cdot 4\cos^2\theta_1 \cos^2\theta_2 \tag{4.14}$$

$$+ \left|A_\parallel(t)\right|^2 \cdot 2\sin^2\theta_1 \sin^2\theta_2 \cos^2\varphi \tag{4.15}$$

$$+ |A_\perp(t)|^2 \cdot 2\sin^2\theta_1 \sin^2\theta_2 \sin^2\varphi \tag{4.16}$$

$$+ \Im(A_\parallel^*(t)A_\perp(t)) \cdot -2\sin^2\theta_1 \sin^2\theta_2 \sin 2\varphi \tag{4.17}$$

$$+ \Re(A_0^*(t)A_\parallel(t)) \cdot \sqrt{2}\sin 2\theta_1 \sin 2\theta_2 \cos\varphi \tag{4.18}$$

$$+ \Im(A_0^*(t)A_\perp(t)) \cdot -\sqrt{2}\sin 2\theta_1 \sin 2\theta_2 \sin\varphi\Big]\,. \tag{4.19}$$

The proper time evolution differs for B_s^0 and $\bar{B}_s^0$ states, where the angular part in Equation 4.14-4.19 is the same. The time-dependent amplitudes, which are summarized e.g. in References [53, 121, 125] can be calculated from Equation 1.23 with the Ansatz of three complex transversity amplitudes and phases $\delta_\parallel$ and $\delta_\perp$. For example, the non-interfering terms, Equation 4.20 to 4.22 (4.26 to 4.28) follow directly from Equation 1.28 (Equation 1.29), where the substitutions $\Im(\lambda_f) = -\eta_f \sin\phi_s$ and $\Re(\lambda_f) = \eta_f \cos\phi_s$ are made in line with Equation 1.42.

The time evolution of an initially ($t = 0$) pure B_s^0 meson is:

$$|A_0(t)|^2 = |A_0(0)|^2 e^{-\Gamma t}\left[\cosh\frac{\Delta\Gamma t}{2} - \cos\phi_s \sinh\frac{\Delta\Gamma t}{2} + \sin\phi_s \sin(\Delta m t)\right] \tag{4.20}$$

$$|A_\parallel(t)|^2 = |A_\parallel(0)|^2 e^{-\Gamma t}\left[\cosh\frac{\Delta\Gamma t}{2} - \cos\phi_s \sinh\frac{\Delta\Gamma t}{2} + \sin\phi_s \sin(\Delta m t)\right] \tag{4.21}$$

$$|A_\perp(t)|^2 = |A_\perp(0)|^2 e^{-\Gamma t}\left[\cosh\frac{\Delta\Gamma t}{2} + \cos\phi_s \sinh\frac{\Delta\Gamma t}{2} - \sin\phi_s \sin(\Delta m t)\right] \tag{4.22}$$

$$\Re(A_0^*(t)A_\parallel(t)) = |A_0(0)||A_\parallel(0)| e^{-\Gamma t}\cos\delta_\parallel \cdot\left[\cosh\frac{\Delta\Gamma t}{2} - \cos\phi_s \sinh\frac{\Delta\Gamma t}{2} + \sin\phi_s \sin(\Delta m t)\right] \tag{4.23}$$

$$\Im(A_\parallel^*(t)A_\perp(t)) = |A_\parallel(0)||A_\perp(0)| e^{-\Gamma t}\cdot\Big[-\cos(\delta_\perp - \delta_\parallel)\sin\phi_s \sinh\frac{\Delta\Gamma t}{2} + \sin(\delta_\perp - \delta_\parallel)\cos(\Delta m t) - \cos(\delta_\perp - \delta_\parallel)\cos\phi_s \sin(\Delta m t)\Big] \tag{4.24}$$

$$\Im(A_0^*(t)A_\perp(t)) = |A_0(0)||A_\perp(0)| e^{-\Gamma t}\cdot\Big[-\cos\delta_\perp \sin\phi_s \sinh\frac{\Delta\Gamma t}{2} + \sin\delta_\perp \cos(\Delta m t) - \cos\delta_\perp \cos\phi_s \sin(\Delta m t)\Big]\,. \tag{4.25}$$

Similarly, the time evolution for an initially pure $\bar{B}_s^0$ meson is given by the following formulae, i.e. all $\sin(\Delta mt)$ and all $\cos(\Delta mt)$ dependent terms switch sign.

$$|\overline{A}_0(t)|^2 = |A_0(0)|^2 e^{-\Gamma t}\left[\cosh\frac{\Delta\Gamma t}{2} - \cos\phi_s \sinh\frac{\Delta\Gamma t}{2} - \sin\phi_s \sin(\Delta mt)\right] \tag{4.26}$$

$$|\overline{A}_\parallel(t)|^2 = |A_\parallel(0)|^2 e^{-\Gamma t}\left[\cosh\frac{\Delta\Gamma t}{2} - \cos\phi_s \sinh\frac{\Delta\Gamma t}{2} - \sin\phi_s \sin(\Delta mt)\right] \tag{4.27}$$

$$|\overline{A}_\perp(t)|^2 = |A_\perp(0)|^2 e^{-\Gamma t}\left[\cosh\frac{\Delta\Gamma t}{2} + \cos\phi_s \sinh\frac{\Delta\Gamma t}{2} + \sin\phi_s \sin(\Delta mt)\right] \tag{4.28}$$

$$\begin{aligned}\Re(\overline{A}_0^*(t)\overline{A}_\parallel(t)) = {} & |A_0(0)||A_\parallel(0)|e^{-\Gamma t}\cos\delta_\parallel \\ & \cdot\left[\cosh\frac{\Delta\Gamma t}{2} - \cos\phi_s \sinh\frac{\Delta\Gamma t}{2} - \sin\phi_s \sin(\Delta mt)\right]\end{aligned} \tag{4.29}$$

$$\begin{aligned}\Im(\overline{A}_\parallel^*(t)\overline{A}_\perp(t)) = {} & |A_\parallel(0)||A_\perp(0)|e^{-\Gamma t}\cdot\left[-\cos(\delta_\perp-\delta_\parallel)\sin\phi_s\sinh\frac{\Delta\Gamma t}{2}\right. \\ & \left. -\sin(\delta_\perp-\delta_\parallel)\cos(\Delta mt) + \cos(\delta_\perp-\delta_\parallel)\cos\phi_s\sin(\Delta mt)\right]\end{aligned} \tag{4.30}$$

$$\begin{aligned}\Im(\overline{A}_0^*(t)\overline{A}_\perp(t)) = {} & |A_0(0)||A_\perp(0)|e^{-\Gamma t}\cdot\left[-\cos\delta_\perp\sin\phi_s\sinh\frac{\Delta\Gamma t}{2}\right. \\ & \left. -\sin\delta_\perp\cos(\Delta mt) + \cos\delta_\perp\cos\phi_s\sin(\Delta mt)\right]\end{aligned} \tag{4.31}$$

The physics parameters can be extracted from Equation 4.13 to 4.31 on a statistical basis, however an ambiguity under the following *simultaneous* transformations remains [53]:

$$\phi_s \leftrightarrow \pi - \phi_s \tag{4.32}$$

$$\Delta\Gamma \leftrightarrow -\Delta\Gamma \tag{4.33}$$

$$\delta_\parallel \leftrightarrow -\delta_\parallel \tag{4.34}$$

$$\delta_\perp \leftrightarrow \pi - \delta_\perp\,. \tag{4.35}$$

This can be resolved by extending the PDF by the small so-called S-wave component, which has an angular distribution different from the other amplitudes [53]. It stems from decays over the pseudoscalar $f_0(980)$ resonance and from non-resonant decays.

4.1.1. Simulation parameters

Following studies in Reference [106], the so-called decay file in GAUSS was reworked for MC09 and later Monte Carlo productions. The $B_s^0 \to \phi\phi$ decay is now implemented by the EvtGen [94] decay model PVV_CPLH [53] instead of SVV_HELAMP [126] and the $\phi \to K^+K^-$ decay proceeds via the VSS decay model. With this implementation, the decay file describes the angular and time dependent decay rates which are introduced in the previous section.

At the same time, the strong phases of the decay amplitudes have been updated: as there were no measurements for the $B_s^0 \to \phi\phi$ decay, the current values from the $B^0 \to \phi K^*$ channel [127–129] were used, following the argumentation of kinematic similarity in Reference [106]. The actual values are: $\phi_s = 0$, $A_0(0) = 0.701$, $A_\parallel(0) = 0.506$, $\delta_\parallel = 2.40$, $A_\perp(0) = 0.502$, $\delta_\perp = 2.39$. A direct measurement of the amplitudes under the assumption $\phi_s = 0$ [4, 130], which appeared later, predicts a slightly smaller value for A_0 and a larger value for $A_\perp$ (three standard deviations difference).

4.2. Signal and background model

The purpose of the $B_s^0 \to \phi\phi$ analysis is to extract the "physics parameters"

$$\lambda_{\text{phys}} = (\Gamma,\ \Delta\Gamma,\ |A_0|^2,\ |A_\perp|^2,\ \delta_\perp,\ \delta_\parallel,\ \Delta m,\ \phi_s) \tag{4.36}$$

introduced in Equation 4.20 to 4.25 from data based on per-event measurements of the observables

$$x_i = (m,\ t,\ \cos\theta_1,\ \cos\theta_2,\ \varphi,\ \xi,\ D)\ . \tag{4.37}$$

These are the B_s^0 candidate mass m, the lifetime t, the three transversity angles (θ_1, θ_2, φ) from Figure 4.2, as well as the tagging decision ξ and the estimated tagging dilution D (calculated from the per-candidate mistag prediction η, see Section 2.7.2). As simplification, the vector $(t, \cos\theta_1, \cos\theta_2, \varphi)$ is abbreviated as $(t, \vec{\omega})$ in the following.

The probability density function (PDF) $\mathcal{P}$ is dependent from the observables x_i measured for each B_s^0 candidate (see Equation 4.37) and the parameters λ, which are a superset of λ_{phys} and introduced in the following. The total PDF is composed of a signal contribution $\mathcal{S}$ and a background contribution $\mathcal{B}$, which are defined in the following two sections.

$$\mathcal{P}(x_i;\lambda) = f_{\text{sig}} \cdot \mathcal{S}(x_i;\lambda) + (1 - f_{\text{sig}}) \cdot \mathcal{B}(x_i;\lambda) \tag{4.38}$$

The observables and parameters are summarized in Table B.1 and B.2 of Appendix B. In Section 4.2.1 and 4.2.2, the parameter argument λ is assumed implicitly to shorten the description.

The maximum likelihood method used for parameter estimation is based on minimizing the negative log-likelihood function

$$-\log(\mathcal{L})\ , \tag{4.39}$$

where the likelihood function is defined as:

$$\mathcal{L} = \prod_{i=1}^{N} \mathcal{P}(x_i;\lambda)\ . \tag{4.40}$$

Common tasks of a maximum likelihood fit like common PDF components, normalization of the PDF, handling of parameters and interfacing with Minuit [131] as minimization tool are usually handled by frameworks, e.g. RooFit [132] or a custom-made one described in Reference [133]. The latter is used for this study, so that the PDF and its presentation closely follow the similar $B_s^0 \to J/\psi\phi$ analysis described in References [53, 133].

4.2.1. Signal parametrization

The signal PDF is composed of the mass distribution $\mathcal{S}_M$, the combined time-and-angular PDF $\mathcal{S}_{TA}$ and the per-event dilution distribution $\mathcal{S}_D$

$$\mathcal{S}(m,t,\vec{\omega},\xi,D)\ =\ \mathcal{S}_M(m)\ \cdot\ \mathcal{S}_{TA}(t,\vec{\omega},\xi|D)\ \cdot\ \mathcal{S}_D(D)\ , \tag{4.41}$$

where the latter so-called Punzi term [134] is implemented as a histogrammed PDF, shown in Figure 4.4 (Section 4.3.1). The Punzi term is a consequence of Bayes' theorem: the PDF $\mathcal{S}_{TA}(t,\vec{\omega},\xi|D)$ being conditional with respect to D, the full PDF requires the distribution of D. Otherwise, the likelihood fit result would yield an incorrect result if the distribution of D differs between signal and background.

A double Gaussian with common mean $m_{B_s^0}$ describes the B_s^0 mass distribution in LHCb [53]:

$$\mathcal{S}_M(m) = f_{\sigma_{m,1}} \cdot \frac{1}{\sigma_{m,1}\sqrt{2\pi}} \cdot e^{-\frac{1}{2}\left(\frac{m-m_{B_s^0}}{\sigma_{m,1}}\right)^2} + (1-f_{\sigma_{m,1}}) \frac{1}{\sigma_{m,2}\sqrt{2\pi}} \cdot e^{-\frac{1}{2}\left(\frac{m-m_{B_s^0}}{\sigma_{m,2}}\right)^2} . \tag{4.42}$$

The angular- and time- related parts of the PDF are not separable and thus build a four dimensional PDF. The decay probability density function $\mathcal{P}_{B_s^0}(t,\vec{\omega})$ for a meson created as *particle* is given by Equation 4.13. For a meson created as *antiparticle*, the corresponding PDF $\mathcal{P}_{\bar{B}_s^0}(t,\vec{\omega})$ is derived from the same equation by replacing the amplitudes from Equation 4.20 to 4.25 by the ones from Equation 4.26 to 4.31.

As explained in Section 2.7, the tagger gives an estimate ξ of the initial flavor of the $B_s^0/\bar{B}_s^0$ meson according to Equation 2.5 and of the mistag probability η. In the following the assumption is made that the tagging algorithms behave symmetrically for B_s^0 and $\bar{B}_s^0$ and do not create artificial asymmetries[1].

Thus, the conditional PDFs $\mathcal{S}''_{TA}(t,\vec{\omega}|\xi,\eta)$ for tagging decision $\bar{B}_s^0$, untagged or B_s^0, respectively, are

$$\mathcal{S}''_{TA}(t,\vec{\omega}|-1,\eta) = (1-\eta)\cdot\mathcal{P}_{\bar{B}_s^0}(t,\vec{\omega}) + \eta\cdot\mathcal{P}_{B_s^0}(t,\vec{\omega}) \tag{4.43}$$

$$\mathcal{S}''_{TA}(t,\vec{\omega}|\quad 0,\eta) = \frac{1}{2}\left(\mathcal{P}_{B_s^0}(t,\vec{\omega}) + \mathcal{P}_{\bar{B}_s^0}(t,\vec{\omega})\right) \tag{4.44}$$

$$\mathcal{S}''_{TA}(t,\vec{\omega}|+1,\eta) = (1-\eta)\cdot\mathcal{P}_{B_s^0}(t,\vec{\omega}) + \eta\cdot\mathcal{P}_{\bar{B}_s^0}(t,\vec{\omega}) . \tag{4.45}$$

The distribution of tag decisions depends from the tagging efficiency ε_{tag}, so that the PDF which is unconditional with respect to ξ is, substituting the mistag probability by the dilution $D = 1-2\eta$:

$$\mathcal{S}''_{TA}(t,\vec{\omega},\xi|D) = \frac{\varepsilon_{\text{tag}}}{2}\,|\xi|\left(\frac{1+\xi D}{2}\mathcal{P}_{B_s^0}(t,\vec{\omega}) + \frac{1-\xi D}{2}\mathcal{P}_{\bar{B}_s^0}(t,\vec{\omega})\right) \tag{4.46}$$

$$= +\frac{1-\varepsilon_{\text{tag}}}{2}(1-|\xi|)\left(\mathcal{P}_{B_s^0}(t,\vec{\omega}) + \mathcal{P}_{\bar{B}_s^0}(t,\vec{\omega})\right) . \tag{4.47}$$

The lifetime resolution of the detector is accounted for by folding $\mathcal{S}''_{TA}$ with a double Gaussian resolution function. In contrast, angular resolution effects are negligible given the angular resolution found on simulated samples [53].

$$\mathcal{S}'_{TA}(t,\vec{\omega},\xi|D) = f_{\sigma_{\text{sig},1}}\int_{t'}\mathcal{S}''_{TA}(t',\vec{\omega},\xi|D)e^{-\frac{1}{2}\left(\frac{t-t'}{2\sigma_{\text{sig},1}}\right)^2}\mathrm{d}t' \tag{4.48}$$

$$= (1-f_{\sigma_{\text{sig},1}})\int_{t'}\mathcal{S}''_{TA}(t',\vec{\omega},\xi|D)e^{-\frac{1}{2}\left(\frac{t-t'}{2\sigma_{\text{sig},2}}\right)^2}\mathrm{d}t' \tag{4.49}$$

The reconstruction- and selection- efficiency $\varepsilon(t,\vec{\omega})$ can be an intricate, non- factorizable function of t and $\vec{\omega}$. It can be accounted for by a four dimensional histogram determined on MC, as shown in Reference [133], which yields the final PDF:

$$\mathcal{S}_{TA}(t,\vec{\omega},\xi|D) = \varepsilon(t,\vec{\omega})\cdot\mathcal{S}'_{TA}(t,\vec{\omega},\xi|D) . \tag{4.50}$$

[1] This is reasonable in view of the data sample sizes dealt with in this thesis, whereas in principle the different material interaction cross-section of K^+ and K^- can have a slight impact on the tagging power [99].

To account for the lifetime bias in the $B_s^0 \to \phi\phi$ decay (Section 3.1), the histogram approach is extended by a continuous function $\varepsilon(t)$:

$$\varepsilon(t,\vec{\omega}) = \varepsilon(t) \cdot \frac{\text{Accepted}(t,\vec{\omega})}{\text{Expected}(t,\vec{\omega})} \; . \tag{4.51}$$

The parametrization of $\varepsilon(t)$ is an extension of the function developed in References [80, 106]:

$$\varepsilon(t) = p_0 \cdot \frac{(t \cdot \text{ps}^{-1})^{p_3}}{p_1 + (t \cdot \text{ps}^{-1})^{p_3}} \cdot \left(1 - p_2 \cdot t \cdot \text{ps}^{-1}\right) \; . \tag{4.52}$$

The number of accepted candidates is taken from fully simulated and selected Monte Carlo and the number of expected candidates is calculated using the parameter setting from the Monte Carlo generation [133]. To determine $\varepsilon(t)$, this process is done twice: in a first step, this function is set to unity when determining the efficiency histogram. Then, the shape of $\varepsilon(t)$ is fitted on a projection of the efficiency on the t axis and the 4D histogram is filled again, taking $\varepsilon(t)$ into account. This approach ensures both: first, a smooth description of the efficiency at low decay proper times, second, correlations between the four variables in the efficiency function are also taken into account.

4.2.2. Background parametrization

As shown in Section 3.6, the background is composed of a prompt component $\mathcal{B}_{\text{Pr}}$ and a long-lived component $\mathcal{B}_{\text{LL}}$.

$$\mathcal{B}(m,t,\vec{\omega},\xi,D) \;=\; f_{\text{Pr}} \cdot \mathcal{B}_{\text{Pr}}(m,t,\vec{\omega},\xi,D) \;+\; (1-f_{\text{Pr}}) \cdot \mathcal{B}_{\text{LL}}(m,t,\vec{\omega},\xi,D) \tag{4.53}$$

An exponential slope is theoretically motivated for the background mass distribution. However, given the vanishing curvature, e.g. seen in the $B_s^0 \to J/\psi\phi$ decay [135], an affine linear function is preferred for reasons of stability.

The lifetime distribution of the long-lived contribution is modeled by an exponential slope with lifetime τ_{LL}, fold with a double Gaussian resolution function. As for the signal lifetime distribution, two resolution parameters $\sigma_{\text{LL},1}$, $\sigma_{\text{LL},2}$ are allowed where a fraction $f_{\sigma_{\text{LL},1}}$ of this background has the first resolution. Hereby the signal and background lifetime resolution are allowed to be different, however, not having an appropriate background sample the background lifetime resolution parameters are set to the same values as the signal ones for the studies presented here.

The selection requirement on the B_s^0 direction angle suppresses negative decay proper time values, as shown in Figure 3.10, so that the prompt background component is modeled by a Gaussian peak for positive lifetimes. Since on the one hand, this PDF falls steeply at zero, and on the other hand, the data sample shown in Figure 3.10 is rather limited, the shape should be determined by later studies on more data. Also, the angular distribution for background can be determined on sideband data. In absence of better knowledge[2], it is assumed flat for the studies described here.

[2]There are neither enough candidates on data nor on MC to estimate this. Reference [106] loosens some cuts to extract the background shape on the consequently larger sample, however, it is not a priori clear that this does not alter the shape.

The background PDF components are summarized in the following formulae. Here, m_0 is the nominal B_s^0 mass [44] and $H(m)$ is the Heaviside step function.

$$\mathcal{B}_{\mathrm{Pr}}(m,t,\vec{\omega},\xi,D) = \mathcal{B}_{\mathrm{Pr,\,M}}(M)\cdot\mathcal{B}_{\mathrm{Pr,\,T}}(t)\cdot\mathcal{B}_{\mathrm{Pr,\,A}}(\vec{\omega})\cdot\mathcal{B}_{\mathrm{Pr,\,Q}}(\xi)\cdot\mathcal{B}_{\mathrm{Pr,\,D}}(D)$$

$$\mathcal{B}_{\mathrm{Pr,\,M}}(m) \propto (1/(\mathrm{MeV}/c^2)+\alpha_{m,\mathrm{Pr}})\cdot(m-m_0) \tag{4.54}$$

$$\mathcal{B}_{\mathrm{Pr,\,T}}(t) \propto e^{-\frac{1}{2}\left(\frac{t}{\sigma_{\mathrm{Pr}}}\right)^2}\cdot H(t) \tag{4.55}$$

$$\mathcal{B}_{\mathrm{Pr,\,A}}(\vec{\omega}) = \frac{1}{8\pi} \tag{4.56}$$

$$\mathcal{B}_{\mathrm{Pr,\,Q}}(\xi) = \frac{1}{2}\varepsilon_{\mathrm{tag}}^{\mathrm{Pr}}|\xi|+(1-\varepsilon_{\mathrm{tag}}^{\mathrm{Pr}})(1-|\xi|) \tag{4.57}$$

$$\mathcal{B}_{\mathrm{LL}}(m,t,\vec{\omega},\xi,D) = \mathcal{B}_{\mathrm{LL,\,M}}(m)\cdot\mathcal{B}_{\mathrm{LL,\,T}}(t)\cdot\mathcal{B}_{\mathrm{LL,\,A}}(\vec{\omega})\cdot\mathcal{B}_{\mathrm{LL,\,Q}}(\xi)\cdot\mathcal{B}_{\mathrm{LL,\,D}}(D)$$

$$\mathcal{B}_{\mathrm{LL,\,M}}(m) \propto (1/(\mathrm{MeV}/c^2)+\alpha_{m,\mathrm{LL}})\cdot(m-m_0) \tag{4.58}$$

$$\mathcal{B}_{\mathrm{LL,\,T}}(t) \propto f_{\sigma_{\mathrm{LL},1}}\int_{t'}H(t')\,e^{-t'/\tau_{\mathrm{LL}}}\cdot\frac{1}{\sigma_{\mathrm{LL},1}\sqrt{2\pi}}\,e^{-\frac{1}{2}\left(\frac{t-t'}{2\sigma_{\mathrm{LL},1}}\right)^2}\mathrm{d}t' \tag{4.59}$$

$$\cdot(1-f_{\sigma_{\mathrm{LL},1}})\int_{t'}H(t')\,e^{-t'/\tau_{\mathrm{LL}}}\cdot\frac{1}{\sigma_{\mathrm{LL},2}\sqrt{2\pi}}\,e^{-\frac{1}{2}\left(\frac{t-t'}{2\sigma_{\mathrm{LL},2}}\right)^2}\mathrm{d}t'$$

$$\mathcal{B}_{\mathrm{LL,\,A}}(\vec{\omega}) = \frac{1}{8\pi} \tag{4.60}$$

$$\mathcal{B}_{\mathrm{LL,\,Q}}(\xi) = \frac{1}{2}\varepsilon_{\mathrm{tag}}^{\mathrm{LL}}|\xi|+(1-\varepsilon_{\mathrm{tag}}^{\mathrm{LL}})(1-|\xi|) \tag{4.61}$$

$$\tag{4.62}$$

As in the signal case, the per-event dilution distribution $\mathcal{B}_{\mathrm{LL,\,D}}(D)$, $\mathcal{B}_{\mathrm{Pr,\,D}}(D)$ are histogrammed PDFs. In absence of a sufficient background sample –as a first approach– the distribution on background is assumed to be the same as for the signal sample in the following studies.

4.3. Analysis of MC10 and estimation of the physics reach

This section aims at an analysis of selected MC candidates approximating a real data analysis as close as possible in order to predict the physics reach of the $B_s^0 \to \phi\phi$ channel in LHCb. This is done by first extracting the crucial parameters like resolutions, efficiencies and tagging power from selected and Hlt2 accepted MC10 candidates. By fitting to the selected MC candidates it will be shown that the parameters that have been put in at generation can be correctly extracted. In the last step, so-called toy Monte Carlo studies (Section 4.3.5) are carried out to estimate the statistical uncertainties on the physics parameters from Equation 4.36. The expected number of signal candidates, as well as the number and proper time distribution of background candidates is extrapolated from the measurements on data, which were presented in the previous chapter.

Similar studies on the $B_s^0 \to \phi\phi$ physics reach are presented in References [105, 106, 116]. However, first of all, these are carried out at nominal LHCb conditions, compared to which the actual data taking is at a lower center-of-mass energy of $\sqrt{s} = 7\,\mathrm{TeV}$ and a higher average number of interaction per event $\nu \approx 2.5$. For similar reasons, they are based on older versions of the LHCb

simulation, which – in particular in the trigger sector – is subject to constant evolvement. For example, the exclusive Hlt2 selection described in Reference [106] is now highly prescaled and selects only a little fraction of $B_s^0 \to \phi\phi$ events. Finally, in absence of any measurements at the LHC center-of-mass energy, these studies had to estimate the signal yield from simulations which suffers from high uncertainties on the $b\bar{b}$ production cross-section. Due to this uncertainty and lacking a sufficiently large background MC sample, the predicted selection efficiency on data does not match the actual one, as explained in Section 3.3.

4.3.1. Tagging on MC10

Studies of the flavor tagging[3] of $B_s^0 \to \phi\phi$ candidates are shortly summarized. The average tagging power on MC10, given in Table 4.1, is $\varepsilon D^2 = (6 \pm 1)\%$. This number is slightly lower than the one found on MC09[4], but a strict comparison is inappropriate, since the tagging framework has developed in the meantime and adapted to the new data sample. Furthermore, the tagging certainly suffers from the higher $\nu = 2.5$ on MC10 compared to MC09 with an average of one interaction per event.

Table 4.1.: Tagging power on MC10 using mean misstags.

ε	0.356 ± 0.004
ω_{miss}	0.288 ± 0.006
εD^2	0.064 ± 0.012

Per-event mistag probabilities or dilutions can only be used if the per-event properties predicted by the tagger are correct. In an actual analysis on data, the dependence between the prediction and the actual quantities is best verified using self-tagging control channels. However, for the purpose of this toy study, it is also possible on MC using truthmatching: depending on their predicted dilution $\langle D_{\text{pred}} \rangle$, candidates are subdivided in the tagging categories given in Reference [99]. The average dilution from truthmatch $\langle D_{\text{true}} \rangle$ for each category is plotted against the average predicted dilution $\langle D_{\text{pred}} \rangle$ in Figure 4.3. A straight line

$$\langle D_{\text{true}} \rangle = d_0 + d_1 \cdot \langle D_{\text{pred}} \rangle \tag{4.63}$$

is fitted to the data, which yields the results given in Table 4.2. The χ^2 of this fit with three degrees of freedom is 0.7. This low value reflects the fact that the tagger already gives reasonable predictions and thus, the correction is marginal.

Table 4.2.: Parameters of fitted function (Equation 4.63) in Figure 4.3.

d_0	0.048 ± 0.029
d_1	0.915 ± 0.057
$\rho(d_0, d_1)$	-0.91

The histogram of per-candidate-dilutions $\mathcal{S}_D(D)$, introduced in Section 4.2.1, is determined on the simulated signal sample (Figure 4.4). For the reasons given in Section 4.2.2, the same histogram is used for $\mathcal{B}_{\text{LL, D}}(D)$ and $\mathcal{B}_{\text{Pr, D}}(D)$ (introduced in Section 4.2.2).

[3] using version v28r2p2 of the LHCb software framework DAVINCI

[4] using version v24r0 of the LHCb software framework DAVINCI

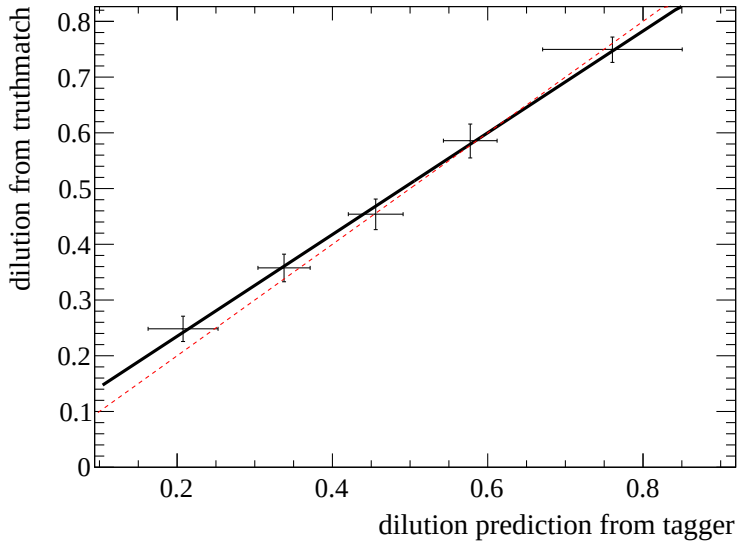

Figure 4.3.: Relationship between predicted ($\langle D_{\text{pred}} \rangle$) and true ($\langle D_{\text{true}} \rangle$) dilution. The data points are average values per tagging category. The solid black line is a fit, the dotted red line is $y = x$.

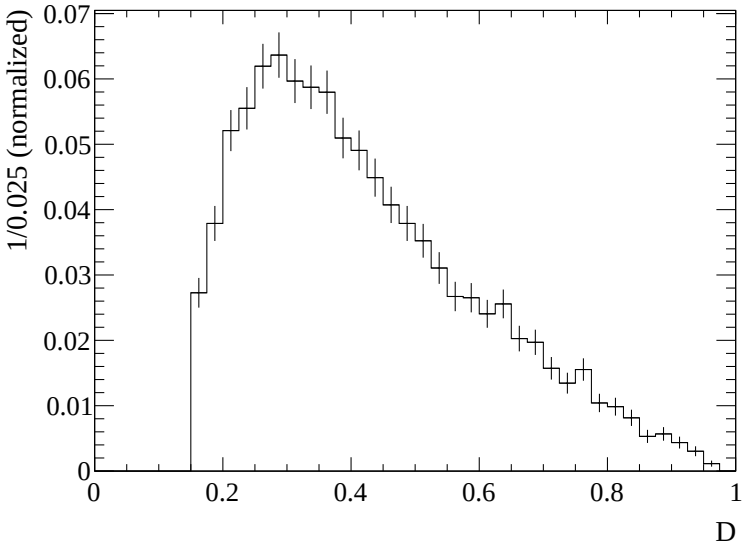

Figure 4.4.: Distribution of per-candidate dilutions on the simulated signal sample. The error bars indicate the statistical uncertainty due to the sample size.

4.3.2. Decay proper time resolution on MC10

The signal decay proper time resolution is determined by a fit to the residuals determined on the MC sample. Fitting a double Gaussian distribution yields the results in Table 4.3, where the correlations (Table 4.4) are sizable, as expected for a double Gaussian. The fit has a $\chi^2 = 54.7$ at 55 degrees of freedom.

If floated in the fit, the result for the Gaussian mean is $(0.8 \pm 3.0) \cdot 10^{-4}$, showing that the measurement of the decay proper time is unbiased for the B_s^0 candidates.

Table 4.3.: Signal decay proper time resolution parameters.

$f_{\sigma_t}^1$	0.65 ± 0.04
σ_1^{sig}	0.0283 ± 0.0009 ps
σ_2^{sig}	0.0543 ± 0.0019 ps

Table 4.4.: Signal decay proper time resolution fit – correlation matrix.

	$f_{\sigma_t}^1$	σ_1^{sig}	σ_2^{sig}
$f_{\sigma_t}^1$	1	-0.92	-0.94
σ_1^{sig}	-0.92	1	0.84
σ_2^{sig}	-0.94	0.84	1

4.3.3. Efficiency correction

The histogrammed four dimensional efficiency correction function is determined on approximately 15000 selected events as shown in Section 4.2.1. In the first step, the correction function $\varepsilon(t)$ according to Equation 4.52 is fitted yielding the parameters shown in Table 4.5. The fit has a χ^2 of 27.6 at 6 degrees of freedom. Since the efficiency correction is normalized to the total number of events, values *smaller* and *greater* than one are both expected. Figure 4.5 shows the efficiencies for the three helicity angles and the proper time as well as the result of the fit to the latter. Since the MC sample is relatively small with roughly one million of *generated* candidates, the plots in Figure 4.5 suffer from quite large fluctuations. The main effects, a slight efficiency drop at high $|\cos\theta|$ values and large decay times and a strong drop at low decay times, are nevertheless visible. While the drop at low decay proper times is clear from the lifetime biasing selection, the slope to higher lifetimes is not expected. It was observed in the $B_s^0 \to J/\psi\phi$ channel, too [136] and was identified as feature of older versions of the DaVinci analysis software, which has been fixed in newer versions [137].

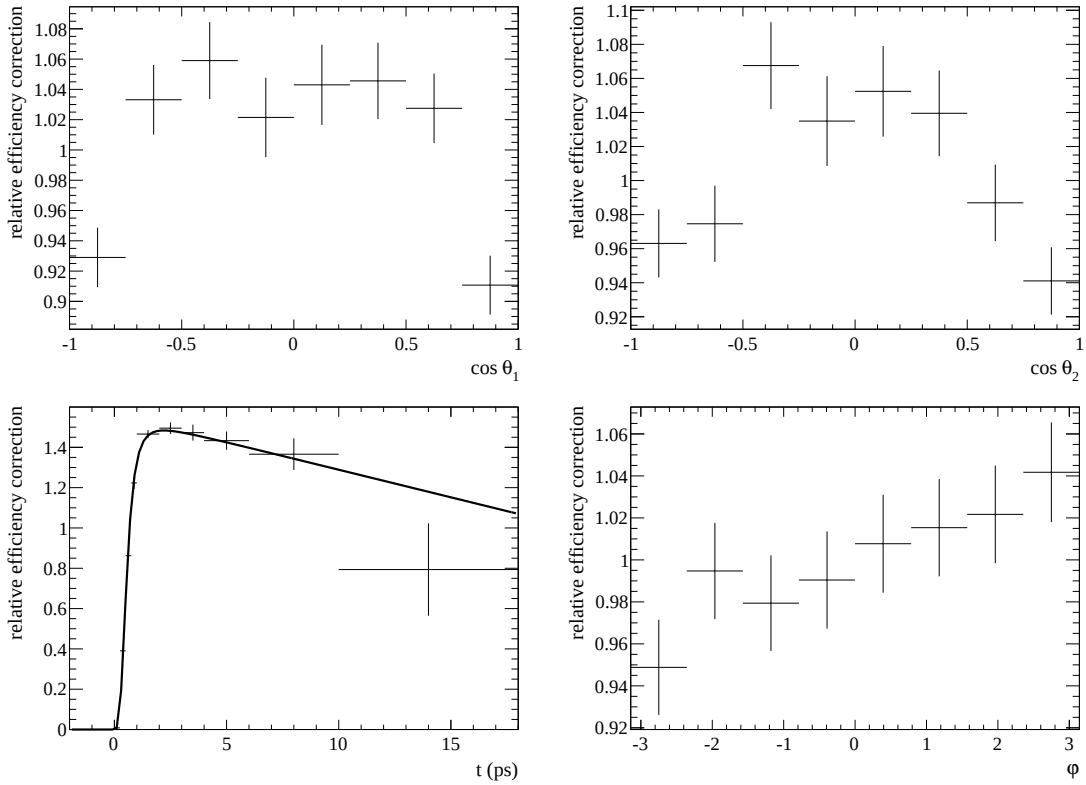

Figure 4.5.: Efficiency correction – MC10.

Table 4.5.: Parameters of signal lifetime efficiency $\varepsilon(t)$. See Equation 4.52 for definition.

p_0	1.563 ± 0.032
p_1	0.155 ± 0.016
p_2	0.0175 ± 0.0056
p_3	3.175 ± 0.085

4.3.4. Fit on MC10 sample

A fit to the sample of selected and Hlt2 triggered MC10 candidates is carried out, the results of which are listed in Table 4.6. The fit results for the physics parameters are in good agreement with the values used when generating of the data sample. No comparison is done for the mass resolution parameters since there is no a priori knowledge of them at generation time. The fitted mass deviates considerably from the nominal value $5366.3\,\mathrm{MeV}/c^2$ taken for the MC production [138]. This is however not a specific problem of the presented fitting procedure: the fit is in agreement with the histogram mean of the reconstructed candidate masses, i.e. the mass is already overestimated by the LHCb reconstruction. Since LHCb has proved to correctly measure the B_s^0 mass in other channels [139], this effect needs further investigation, even though it does not affect the extraction of the *CP* violating phase.

Projections of the MC sample on the helicity angle and proper time distributions are shown in Figure 4.6 together with the fitted functional shape. The fit curve is piecewise continuous due to the binned efficiency correction histogram. This is expected to become smoother with a sufficiently large MC sample.

Table 4.6.: Results of fit on MC10 sample and Δ/σ, their deviation from the nominal results normalized to the uncertainty.

	fit result	Δ/σ
$m_{B_s^0}$	5368.15 ± 0.11	16.1824
$f^1_{\sigma_m}$	0.828 ± 0.017	0.48
$\sigma_{m,1}$	12.00 ± 0.25	–
$\sigma_{m,2}/\sigma_{m,1}$	1.96 ± 0.10	–
$\lvert A_0\rvert^2$	0.4899 ± 0.0066	-0.01
$\lvert A_\perp\rvert^2$	0.2506 ± 0.0081	-0.17
$\delta_\parallel$	2.416 ± 0.024	0.64
$\delta_\perp$	2.42 ± 0.14	0.22
ϕ_s	0.015 ± 0.061	0.25
Γ	0.6782 ± 0.0064	-0.17
$\Delta\Gamma$	0.067 ± 0.017	0.42
Δm	17.837 ± 0.051	0.72

4.3.5. Physics reach with 2 fb^{-1}

Based on the analysis done on MC10, the statistical uncertainty on ϕ_s can be calculated as outlined in Section 4.3. The integrated luminosity of $2\,\mathrm{fb}^{-1}$ corresponds to the quantity of data collected in a "nominal" year of LHCb data taking.

In the toy-MC study, data samples are simulated according to the total PDF at a fixed parameter set and fits are performed to these data sample, where the parameters Γ, $\Delta\Gamma$, $|A_0|^2$, $|A_\perp|^2$, $\delta_\perp$, $\delta_\parallel$, Δm, ϕ_s, $m_{B_s^0}$, $\sigma_{m,1}$, $\sigma_{m,2}$, f_{sig}, $\alpha_{m,\mathrm{Pr}}$ and $\alpha_{m,\mathrm{LL}}$ are floating. This procedure of generating and fitting data is iterated 1000 times to yield the residual distribution of the parameters determined in the fit from which the variation of the fit result for given input parameters can be determined by an unbinned likelihood fit.

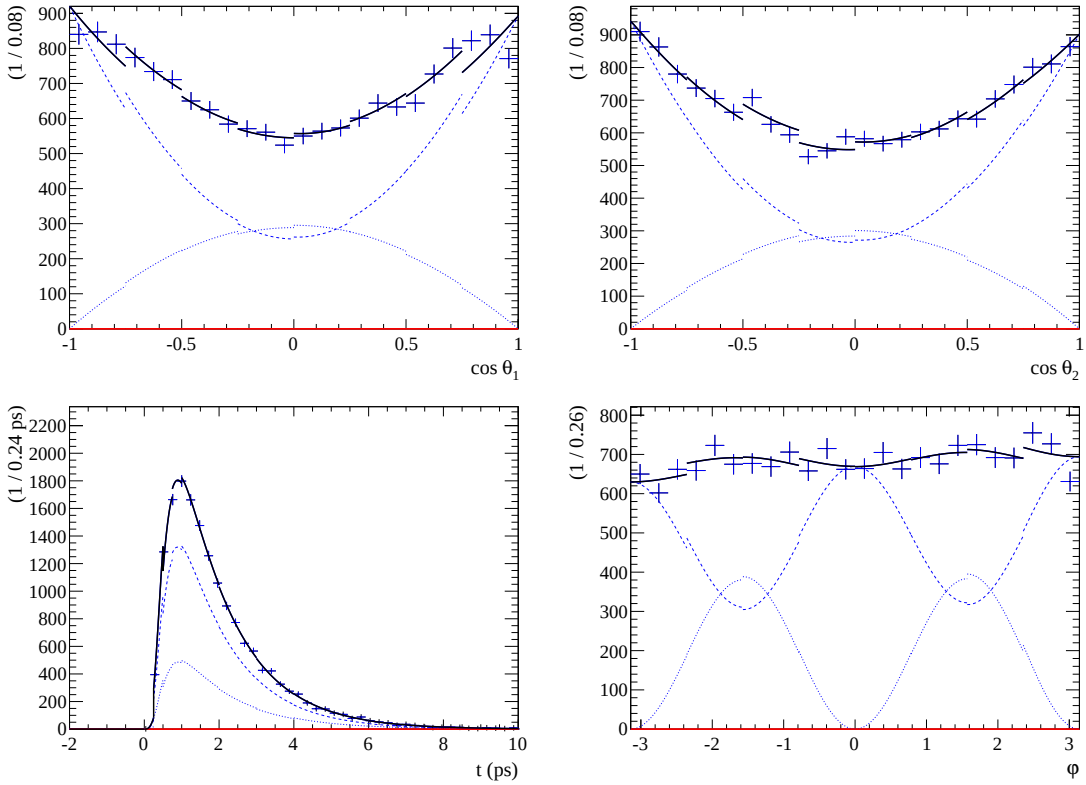

Figure 4.6.: Projection of the MC10 data set on the helicity angles and the B_s^0 proper time. The solid lines show the fit result, the dotted/dashed lines represent the *CP*-odd/*CP*-even contribution.

As an example, a projection of the toy MC distribution on the B_s^0 proper time is shown in Figure 4.7 illustrating the composition of the sample of signal and background candidates, the latter of which are simulated according to the parameters determined in Section 3.3 and 3.6. Two extreme cases are derived from the annual signal and background yield estimation in Section 3.3: first, the signal yield is assumed to be at the right border of the 1σ interval and the background yield at the left border, then the situation is swapped. The first case corresponds to $n_{B_s^0} = 2600$ and $f_{\text{sig}} = 0.282$, the second case is more pessimistic with $n_{B_s^0} = 1660$ and $f_{\text{sig}} = 0.187$.

Being the key parameter of the $B_s^0 \to \phi\phi$ analysis, the statistical uncertainty of ϕ_s with data samples of different size is given in Table 4.7. In order to estimate the effect of the actual value of ϕ_s on the sensitivity, the study is done for two values of ϕ_s, 0.0 and -0.3, where the results are comparable. In the two extreme cases mentioned above, the sensitivity on ϕ_s is $\sigma_{\phi_s} = 0.191 \pm 0.003$ and $\sigma_{\phi_s} = 0.265 \pm 0.004$. Smaller sample sizes with $n_{B_s^0} = 600$ and 1000 are also simulated for reasons of comparison. Here, the statistical uncertainty on ϕ_s is larger than the constraints estimated from the $B^0 \to \phi K^*$ channel in Equation 1.43. In other words, LHCb will be able to improve on the current knowledge by studies based on $2\,\text{fb}^{-1}$ of integrated luminosity and more.

Studies of systematic uncertainties [106] identified the modeling of the decay proper time efficiency function as well as the lifetime and angular background model as major sources of systematic effects on ϕ_s, which were determined to be in the order of 0.1.

Table 4.7.: Statistical uncertainties on ϕ_s for different signal and background candidate yields and two values of ϕ_s. The symbols are defined in the text.

$n_{B_s^0}$	f_{sig}	$\sigma_{\phi_s}\vert_{\phi_s=0}$	$\sigma_{\phi_s}\vert_{\phi_s=-0.3}$
600	0.187	0.61 ± 0.02	0.67 ± 0.02
1000	0.187	0.450 ± 0.009	0.424 ± 0.009
1660	0.187	0.265 ± 0.004	0.281 ± 0.005
1660	0.282	0.264 ± 0.004	0.280 ± 0.005
2600	0.282	0.191 ± 0.003	0.188 ± 0.003

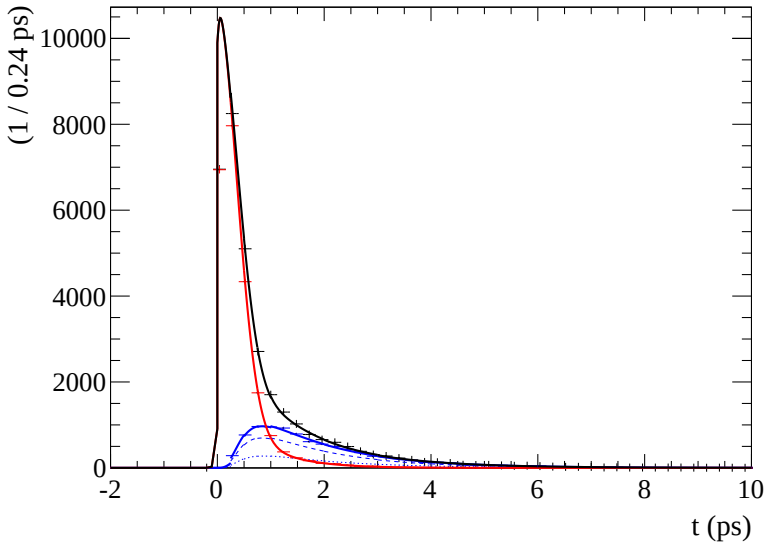

Figure 4.7.: Signal and background lifetime distribution used in Toy-MC ($n_{B_s^0} = 2600$, $f_{\text{sig}} = 0.282$).

CHAPTER 5

Inclusive ϕ production cross-section measurement at $\sqrt{s}$ = 7 TeV

As explained in Section 1.4, the description of minimum bias events by event generators is only as good as their phenomenological models are tuned to data. A measurement of the inclusive ϕ cross-section at LHC's unprecedented center-of-mass energy is an important ingredient to this tuning effort. Good knowledge of the backgrounds is as crucial as excellent understanding of the RICH based PID system to enable studies like the $B_s^0 \to \phi\phi$ analysis. The measurement of the inclusive ϕ production cross-section presented in this thesis targets both.

In the collaboration wide review process, the author's work was documented in internal analysis documents [140, 141][1]. Preliminary results of this analysis are published in a Conference Note [142] and the final results presented in this thesis are published in Physics Letters B [143].

This chapter opens up with an overview over the analysis and a presentation of the analysis strategy (Section 5.1). The study is done on very early data taken by LHCb at $\sqrt{s} = 7\,\text{TeV}$. The data sample and the corresponding Monte Carlo simulated sample used in this analysis are presented in Section 5.5 and the trigger conditions are analyzed (Section 5.2). A dedicated stripping line was introduced in the LHCb stripping framework by the author in order to enable the inclusive ϕ and further minimum bias analyses (Section 5.4).

The ϕ reconstruction efficiency is factorized into a non-PID related and a PID related component in order to determine the latter in a tag-and-probe approach on data. These efficiencies are dealt with in Section 5.6 and and 5.7. The signal extraction is closely linked to the efficiency determination using the tag-and-probe approach, which will be elaborated in Section 5.8.

The tag-and-probe approach assumes the PID efficiency to be independent between the two ϕ bachelor kaons. Correlations, which are intensively studied in Section 5.9, introduce a systematic uncertainty. The reasons for these correlations are investigated in Section 5.9.2. The experimentally accessible kinematic range is constrained by the particle identification system and will be analyzed in Section 5.9.3.

Systematic uncertainties of the analysis are investigated later, in Chapter 6, and the cross-section results are presented in Chapter 7.

[1] which additionally discuss supporting studies carried out by other working group members

5.1. Overview over the analysis strategy

The double-differential inclusive ϕ meson production cross-section is measured in bins of the transverse momentum p_T and the rapidity y:

$$p_T = \sqrt{p_z^2 + p_y^2} \tag{5.1}$$

$$y = \frac{1}{2}\ln\left(\frac{E+p_z}{E-p_z}\right) . \tag{5.2}$$

To account for the finite beam crossing angle ($200 - 300\,\mu$rad per beam), these quantities are boosted to the pp center-of-mass frame [144, 145].

For each bin, the double-differential cross-section is given by:

$$\frac{\Delta^2\sigma}{\Delta y\,\Delta p_T} = \frac{1}{\Delta y\,\Delta p_T}\cdot\frac{N_{\text{or}}}{\varepsilon_{\text{pid}}}\cdot\frac{1}{\mathcal{L}\cdot f_{\text{trig}}\cdot f_{\text{strip}}\cdot\varepsilon_{\text{rec}}\cdot\mathcal{BR}(\phi\to K^+K^-)} . \tag{5.3}$$

The integrated luminosity $\mathcal{L}$ is determined by the LHCb luminosity framework (Section 2.4). The trigger used when taking the data under study is 100% effective, but to cope with bandwidth requirements, prescales f_{trig} were applied. Further prescales f_{strip} were utilized in the stripping procedure.

N_{or} is the number of candidates surviving the reconstruction and PID based selection. The determination of the signal yield is based on a likelihood fit, which Section 5.8 will explain in detail.

There are two efficiencies in Equation 5.3, both determined as function of p_T and y:

- ε_{pid} is the efficiency related to PID (Section 5.7).
- ε_{rec} is the reconstruction efficiency excluding ε_{pid} (Section 5.6).

The reconstruction efficiency ε_{rec} is determined on Monte Carlo simulated samples. Previous analyses studied this efficiency and found generally good agreement between MC and data [11, 13, 104, 146]. In contrast, ε_{pid} is extracted from data because the ϕ analysis is one of the first to depend strongly on the PID system. Since the calibration of the RICH is done separately for the two polarities of the LHCb spectrometer magnet, the analysis is carried out separately for the subsamples defined hereby and the results are combined in the end[2]. The importance of the RICH for the ϕ reconstruction is demonstrated in Figure 5.1, which shows the mass distribution of all ϕ candidates reconstructed on an MC sample requiring the PIDK requirement on zero, one and two bachelor kaons. Without the RICH, the mass peak vanishes relatively to the high combinatorial background. Only after suppressing the background using the RICH system, a mass peak can be reconstructed. On the other hand, the signal efficiency (shown for truthmatched candidates in Figure 5.1) still remains reasonably high.

As opposed to a non-inclusive study, which would focus on a subset of the total ϕ meson production, for example only prompt[3] ϕ or only ϕ from inelastic, non-diffractive[4] (see Section 1.4) events, the inclusive cross-section measurement includes *all* ϕ mesons produced. The fraction of non-prompt ϕ mesons is expected to be smaller than 2% [143]. Diffractive events contribute to the ϕ cross-section at lower transverse momenta, with a fraction of up to 6% (see Section 6.2.6

[2] Plots show magnet polarity "up" unless otherwise stated.
[3] Prompt particles are those that emerge from the primary vertex.
[4] Elastic events are not further discussed since simulations predict them not to contribute to the ϕ production.

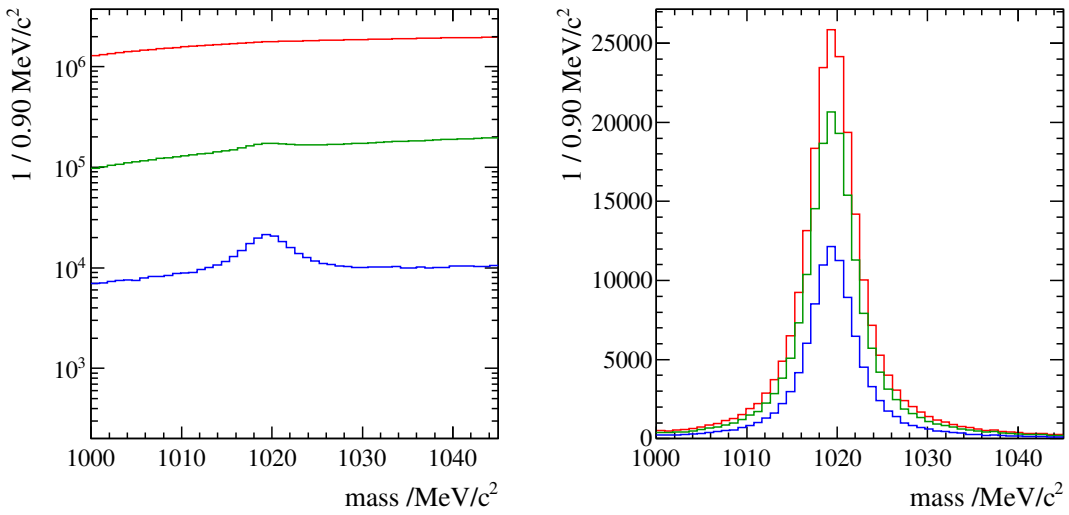

Figure 5.1.: MC signal and background (left) as well as truthmatched signal (right) with a PIDK > 15 requirement on zero (red), at least one (green) and two (blue) kaons.

on page 93). Separating different contributions to the ϕ cross-section in a non-inclusive approach would rely on simulations or assumptions (in particular concerning diffractive events), which would complicate the interpretation of the results in Monte Carlo tuning campaigns.

5.2. Trigger and Luminosity

The analysis is based on the so-called *MicroBias*[5] trigger at Hlt1 level. It imposes a track finding requirement in the VELO, which is 100% efficient on reconstructed ϕ events as measured on MC. The Hlt1 trigger line requires a random trigger[6] at L0 level and Hlt2 operated in pass-through mode in the given data taking period.

The measurement is based on data taken with two different trigger configuration keys: First[7], the *MicroBias* trigger ran without prescaling or rate limitation. Later[8], a fixed prescale $p_{\text{fixed}} = 0.001$ was imposed and in addition, a new trigger line, the rate-limited *MicroBias* trigger[9] was introduced: it features the same selection as the *MicroBias* trigger, but it is limited to a maximum rate of 500 Hz, which results in a floating prescale. The effective prescale for the unification of both trigger lines is determined offline by normalizing to the line with the fixed prescale. This is valid since the prescaler is random and thus, statistically independent from the selection.

$$p_{\text{effective}} = n_{\text{fixedfloated}} \cdot \frac{p_{\text{fixed}}}{n_{\text{fixed}}} \tag{5.4}$$

Here, $n_{\text{fixedfloated}}$ is the number of events accepted either by the fixed-prescale line or the floating-prescale line and n_{fixed} is the number of events accepted by the fixed prescale line. Since this normalization is done on the whole subsample, the statistical uncertainty on it is negligibly low.

[5] *MicroBiasRZVeloDecision*
[6] *ODIN.LumiTrigger*
[7] TCK `0x51710`
[8] TCK `0x81710`
[9] *MicroBiasRZVeloRateLimitedDecision*

Table 5.1.: Data subsamples and their properties.

Run number	Magnet polarity	TCK	f_{trig}	Luminosity / nb^{-1}
71474-71530	up	`0x51710`	1	1.25 ± 0.04
71857-71958	up	`0x81710`	0.1688 ± 0.0015	4.52 ± 0.16
71803-71806	down	`0x81710`	0.1159 ± 0.0007	8.31 ± 0.29
72020-72330	down	`0x81710`		
71807-71816	down	`0x51710`	1	0.63 ± 0.02
total:				14.71 ± 0.51

Offline processing starts with the global reconstruction and stripping[10]. Later, the integrated luminosity is determined by the central LHCb luminosity project[11] (Section 2.4).

The luminosity and the effective prescales f_{trig} are determined separately for the different run ranges given in Table 5.1. Figure of merit for the statistical power of a given data sample is the product of trigger prescale and luminosity, which is why the effective sizes of the magnet-up and magnet-down sample are very similar.

Cross-checks of the trigger prescale and luminosity determination have been carried out by analyzing data from the different TCKs separately, where good agreement is found. Two natural subsamples are defined by the two magnet polarities "up" and "down", which are analyzed separately as indicated in Section 5.1.

Table 5.2.: Bin boundaries for transverse momentum and rapidity. Subranges typed in **bold** are accessible experimentally. As an example, bin $(6, 12)$ covers the range $1.0 \leq p_T < 1.2\,\text{GeV}/c$ and $3.88 \leq y < 4.06$.

index	p_T (GeV/c)	y
1	[0.0; 0.2[	[1.90; 2.08[
2	[0.2; 0.4[	[2.08; 2.26[
3	[0.4; 0.6[	[2.26; 2.44[
4	**[0.6; 0.8[**	**[2.44; 2.62[**
5	**[0.8; 1.0[**	**[2.62; 2.80[**
6	**[1.0; 1.2[**	**[2.80; 2.98[**
7	**[1.2; 1.4[**	**[2.98; 3.16[**
8	**[1.4; 1.6[**	**[3.16; 3.34[**
9	**[1.6; 1.8[**	**[3.34; 3.52[**
10	**[1.8; 2.0[**	**[3.52; 3.70[**
11	**[2.0; 2.4[**	**[3.70; 3.88[**
12	**[2.4; 2.8[**	**[3.88; 4.06[**
13	**[2.8; 3.2[**	[4.06; 4.24[
14	**[3.2; 4.0[**	[4.24; 4.42[
15	**[4.0; 5.0[**	[4.42; 4.60[

[10] version Reco04Stripping05

[11] based on the calibration constants given by the conditions database tag *head-20110407*

5.3. Binning

Since the analysis was started basically at the same time as the data taking, there was no a priori knowledge about the size of the data sample used in the final analysis. Neither were all experimental challenges completely understood right from the beginning. This is why the analysis was designed with the generic 15×15 binning shown in Table 5.2. In the course of the analysis process the range $0.6 < p_T < 5.0\,\text{GeV}/c$ and $2.44 < y < 4.06$ turned out to be experimentally accessible, corresponding to 12 bins in p_T and 9 bins in y.

5.4. Selection – Inclusive ϕ stripping line

The ϕ meson candidates are reconstructed in the $\phi \to K^+K^-$ decay channel, which has a branching fraction of $(49.2 \pm 0.6)\%$ [147]. In events which contain at least one reconstructed primary vertex, oppositely charged long tracks[12] are combined and need to fulfill the following selection criteria:

- The ϕ candidate mass is required to lie between 995 and $1045\,\text{MeV}/c^2$.
- At least one kaon is supposed to pass a selection requirement on the RICH Delta-Log-Likelihood of PIDK > 15. There is no constraint on both kaons simultaneously at this point; this is done only later, in the process of determining the PID efficiency.

The selection has been implemented as stripping line in order to be run in LHCb's central stripping effort. To cope with LHCb's bandwidth requirements, a prescale f_{strip} has to be applied. This is chosen p_T-dependent, since the backgrounds rise steeply with falling transverse momentum:

$$f_{\text{strip}} = \begin{cases} 0.16 & \text{for candidates with } p_T < 1\,\text{GeV}/c \\ 0.50 & \text{for candidates with } p_T > 1\,\text{GeV}/c\,. \end{cases} \tag{5.5}$$

This defines a low p_T region and a high p_T region, which are later used in different stages of the analysis. Further stripping lines have been developed, which categorize candidates according to the kaons' transverse momentum instead of the ϕ mesons' p_T. These were designed for the RICH group's calibration efforts and used for example in measuring the $p/\overline{p}$ ratio [12].

5.5. Data and MC sample

The analysis is based on very early data[13] taken at $\sqrt{s} = 7\,\text{TeV}$ in May 2010. At this time, the trigger was not yet fully commissioned, i.e. a large part of the bandwidth was shared by the *MicroBias* trigger (Section 5.2). The Monte Carlo samples used in this analysis and in the supporting studies are mostly of type LHCb MC[14], totaling to 66 million magnet-down events and 59 million magnet-up events. Any quantity or efficiency determined on MC is analyzed independently for the two magnet polarities. The total minimum bias cross-section in the LHCb MC simulation is $\sigma_{\text{MC}}(pp \to X) = 91.05\,\text{mb}$, composed of the following PYTHIA process types: 48.80 mb inelastic-non-diffractive, $2 \times 6.84\,\text{mb}$ single diffractive, 9.19 mb double diffractive and 19.28 mb

[12] Long tracks are tracks reconstructed from hits in *all* tracking detectors, see Section 2.5.1.
[13] from run 71803 to 72330
[14] MC2010, produced in LHCb's central production using the Sim04Reco03 setting

elastic [143]. $\sigma_{\mathrm{MC}}(pp \to X)$ is the basis for the cross-section determination on MC for later comparison with data. Defining the number of generated pp collisions as N_{pp} and the number of $\phi \to K^+K^-$ decays as N_ϕ, the MC predicted cross-section is:

$$\sigma_{\mathrm{MC}}(pp \to \phi X) = \frac{N_\phi}{N_{pp} \cdot \mathcal{BR}(\phi \to K^+K^-)} \cdot \sigma_{\mathrm{MC}}(pp \to X) \; . \tag{5.6}$$

This determination solely depends on "counting" in the MC production process, in other words, no detector simulation goes in.

Analyzing MC events, exactly the same version of the analysis software[15] and the same selection[16] have been employed as in the stripping process. As the LHCb software framework is subject to constant development, the BRUNEL version used in LHCb's central reconstruction on data (v37r1) and MC (v37r3) is not exactly the same, though the changes introduced between these versions seem negligible [148]. Solely for the purpose of a cross-check, an MC sample totaling to 294118 events with one pp collision per event has been produced and reconstructed with different versions of BRUNEL (Figure 5.2) to assess potential differences. The number of candidates reconstructed without requiring PID information is 740 (BRUNEL v37r1), 738 (v37r3) and 742 (v37r6p1). The difference in ϕ signal candidates on these samples is less than 0.3%. This shows that using BRUNEL-v37r1 on MC does not entail any significant systematics.

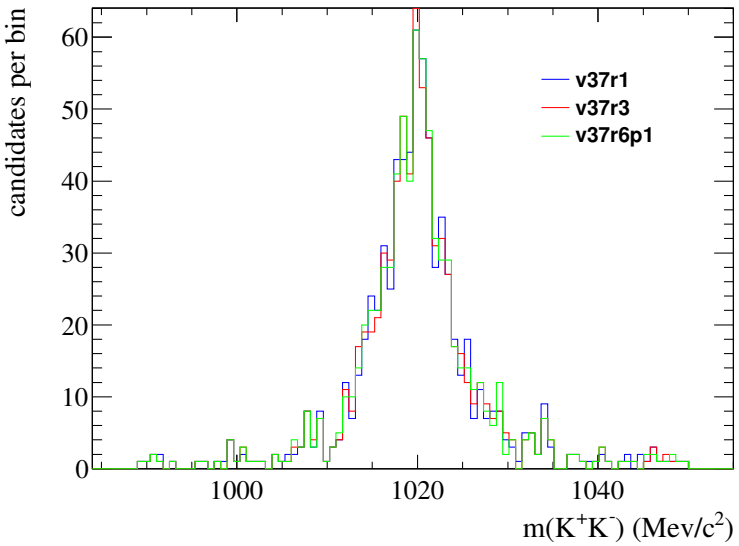

Figure 5.2.: Comparison of ϕ candidate reconstruction with different versions of BRUNEL (truth-matched candidates shown).

[15] DAVINCI v25r5p1

[16] Stripping05 selection, `/afs/cern.ch/lhcb/software/releases/DAVINCI/DAVINCI_v25r5p1/Phys/StrippingSelections/python/StrippingSelections/StrippingInclPhi.py`

Since the MC samples are produced with an average number of $\nu = 1$ collisions per event, whereas the number of multiple interactions is negligible under the data taking conditions in the above-mentioned run period, only events with exactly one collision per event are used from the MC samples. Studies carried out within the author's working group [141] show that after applying this requirement, the distribution of number of reconstructed primary vertices per event agrees rather well, except for a slight excess on data. This might be due to the fact that the track multiplicity distribution on data is also shifted to higher multiplicities compared to MC (Figure 5.3). The effect of the track multiplicity on the reconstruction and PID efficiency is elaborated in Section 6.2.2 and 6.3.

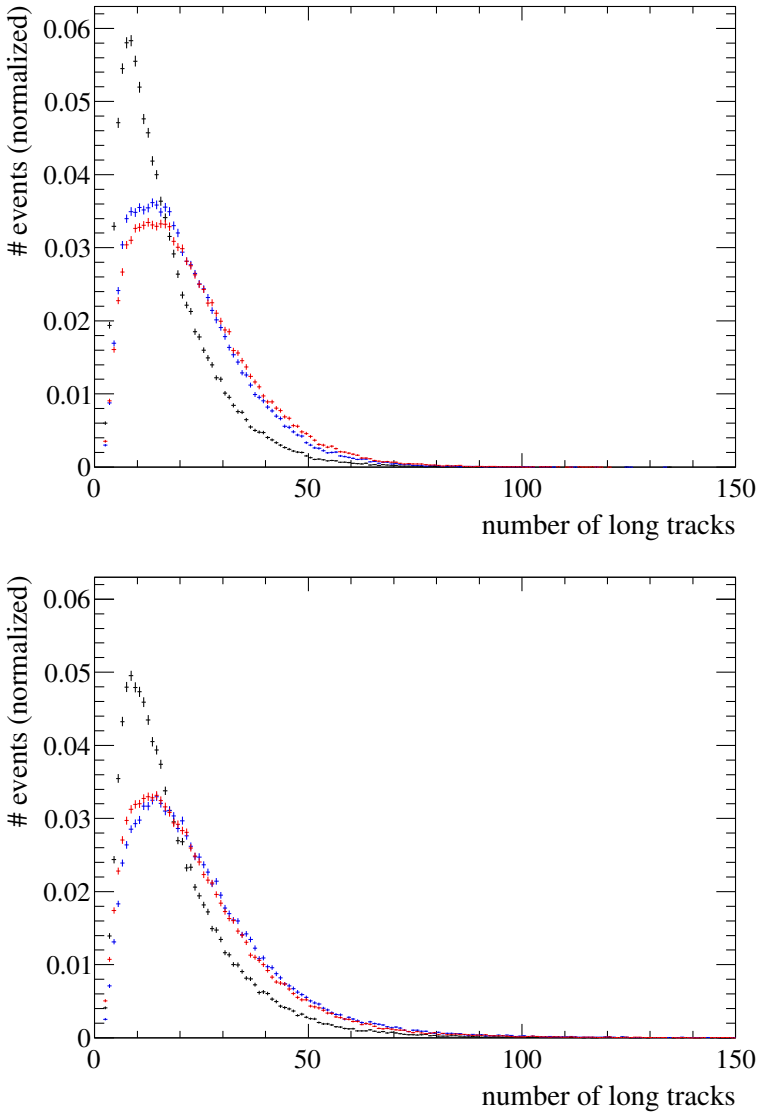

Figure 5.3.: Long track multiplicity distribution on MC (top) and data (bottom), with PID requirement applied on no (black), at least one (blue) and two (red) kaons.

5.6. Reconstruction efficiency (excluding particle ID)

The reconstruction efficiency ε_{rec} is the efficiency to reconstruct a ϕ candidate without imposing any PID requirement. Due to high combinatorial backgrounds, no mass peak is reconstructable before applying the PID criterion (Figure 5.1), but nevertheless ε_{rec} can be determined on MC using the truthmatching provided by the LHCb software framework: a track is considered matched if least 70% of the reconstructed track's hits are compatible with the MC particle's trajectory. Figure 5.4 indicates that the truthmatching offers a sharp discrimination between signal and background candidates, i.e. there are no background candidates left in the truthmatched sample. The efficiency for peaking signal candidates to be truthmatched is 100% with 2% uncertainty [149].

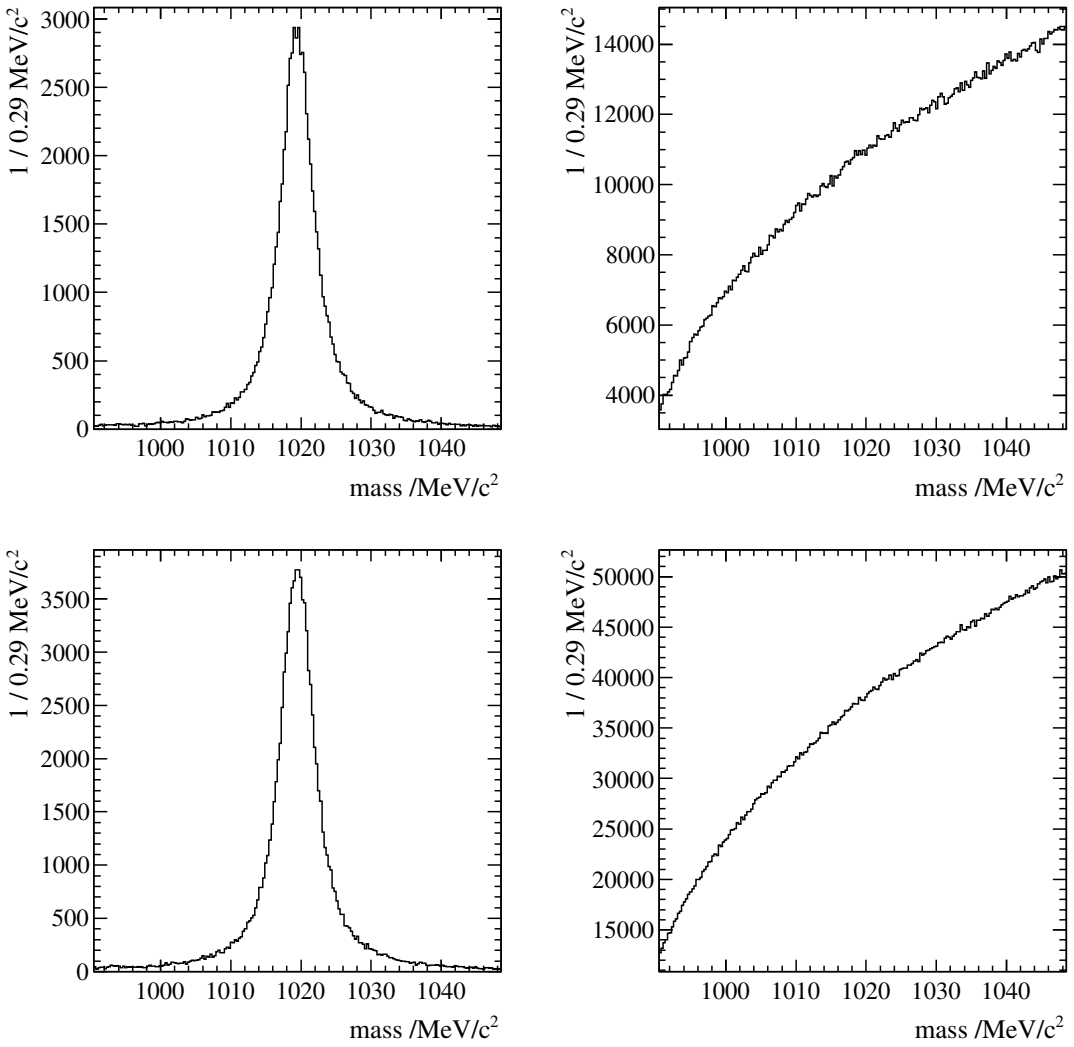

Figure 5.4.: Truthmatched (left) and explicitly *non*-truthmatched (right) ϕ candidates passing the stripping selection for high p_T (top) and low p_T (bottom) regions.

The reconstruction efficiency ε_{rec} covers kinematic and spatial effects like the dependence of the tracking efficiency from the track momentum and the geometrical detector acceptance. It is composed of two parts

$$\varepsilon_{\text{rec}} = \varepsilon_{\text{cand}} \cdot \varepsilon_{\text{PV}} \,, \tag{5.7}$$

where the first term is the efficiency to reconstruct a ϕ candidate in any event and the second term is the probability of this candidate being produced in an event where a primary vertex could be reconstructed (see Section 5.6.2).

5.6.1. ϕ candidate reconstruction efficiency

In bin i of p_T and y, the candidate reconstruction efficiency $\varepsilon_{\text{cand}}$ is given by the quotient of selected, truthmatched candidates $N_{sel.true}$ and the number of generated $\phi \to K^+K^-$ candidates N_{gen}:

$$\varepsilon_{\text{cand}} = \frac{N_{sel.true}}{N_{gen}} \,. \tag{5.8}$$

Limited MC sample size is taken into account by a binomial uncertainty:

$$\sigma_{\varepsilon_{\text{cand}}} = \sqrt{\frac{\varepsilon_{\text{cand}}(1-\varepsilon_{\text{cand}})}{N_{gen}}} \,. \tag{5.9}$$

As shown in Figure 5.5, the candidate reconstruction efficiency is around 70% in the central region and drops to 30-40% at the low-p_T edge of the considered kinematic range $0.6 < p_T < 5.0\,\text{GeV}/c$ and $2.44 < y < 4.06$. The uncertainties are around 1% in the high statistics regions and rise to 6% at high transverse momenta.

5.6.2. Primary vertex reconstruction efficiency

A primary vertex (PV) is by default required by the stripping framework and hereby events which do not contain at least one reconstructed primary vertex are sorted out. The ϕ stripping line has been altered later to explicitly overrule this undesired behavior, but the new version had to run with a stricter prescale resulting in a smaller effective sample size. Consequently, the first sample was preferred for the reasons given in the following.

The PV reconstruction efficiency is determined as conditional probability under the condition that a candidate has been reconstructed:

$$\varepsilon_{\text{PV}} = \frac{N_{sel.true.PV}}{N_{sel.true}} \,. \tag{5.10}$$

Here, $N_{sel.true.PV}$ is the number of selected, truthmatched candidates in events with reconstructed PV and $N_{sel.true}$ is defined in the previous section.

The efficiency ε_{PV} varies slightly with ϕ kinematics, but it is overall extremely high: larger than 99% in the region $p_T(\phi) < 1000\,\text{MeV}/c$ and nearly 100% for transverse momenta higher than that. A small sample without PV requirement[17] has been used to compare the PV reconstruction efficiency globally in the region of interest $0.6 < p_T < 5.0\,\text{GeV}/c$ and $2.44 < y < 4.06$ between data and MC. The efficiencies are higher than 0.999 on both, data and MC, and the difference between these two is not larger than 0.00022 ± 0.00002. This number, defining the systematic uncertainty of the primary vertex reconstruction efficiency, is negligibly small.

In conclusion, –due to the exceptionally high efficiency and the negligible systematic uncertainty– there is no effect of the primary vertex criterion on the analysis outcome.

[17] from the `MicroBias` stripping stream

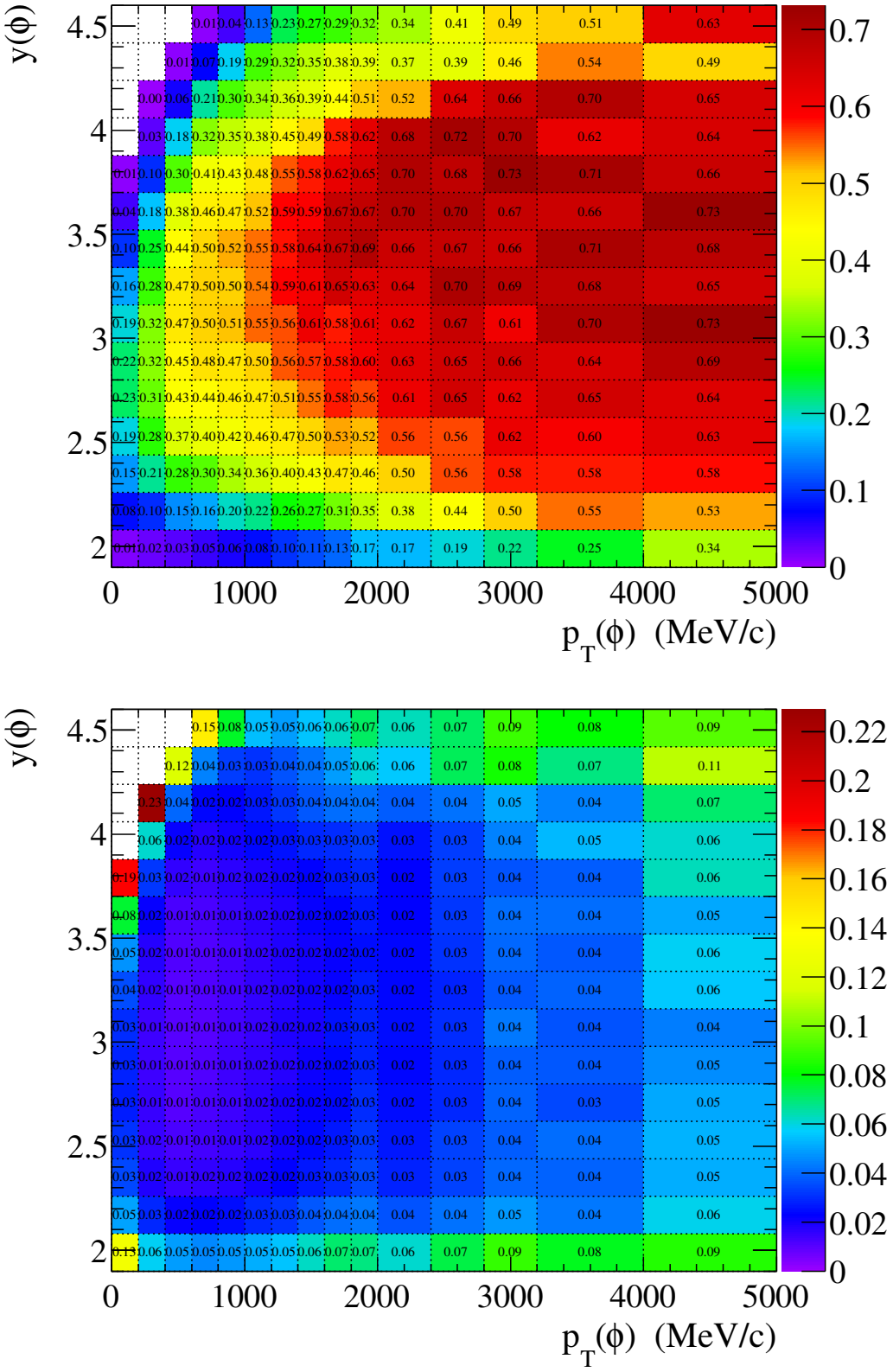

Figure 5.5.: Reconstruction efficiency (top) and relative binomial uncertainty (bottom).

5.7. Particle identification efficiency

The inclusive ϕ and the $p/\overline{p}$ ratio analysis [12] are among the earliest analyses to depend on the particle ID provided by the RICH, which offers a high background suppression. However, the RICH calibration is a complex procedure on data and a careful analysis of the selection efficiency on data is necessary. Both analyses employ a tag-and-probe approach using the data processed by the Inclusive ϕ stripping (Section 5.4).

Tag-and-probe is a two-step procedure: in a first step, the "tag" sample is formed by applying a requirement PIDK > 15 to at least one kaon ("OR" cut), in a second step, the requirement is imposed on both kaons ("AND" cut) to form the probe sample.

From the difference in signal yield between the tag- and the probe- sample, the efficiency of the OR cut can be inferred. This approach assumes the two kaons to be indistinguishable and the cut efficiencies to be independent. The first postulate is true because there is no significant dependence of the RICH efficiency from the meson charge, the second premise is intensively studied and a systematic uncertainty is deduced.

It is immediately evident from the working principle of the RICH that the efficiency must be a function of particle momentum. Further, the angle under which the particle enters the RICH plays a role due to acceptance effects. This is why the efficiency can be parametrized as function of any pair of variables describing these quantities. In the case of the inclusive ϕ analysis, the best option is to parametrize the efficiency in the same binning of ϕ properties as used for the analysis results.

5.7.1. Tag-and-probe

The following symbols are introduced for the mathematical treatment of the tag-and-probe approach:

- N_{rec} is the number of reconstructed candidates without applying any PID related requirement. This is the crucial quantity and equivalent to the quotient $\frac{N_{\text{or}}}{\varepsilon_{\text{pid}}}$ in Equation 5.3.
- N_{or} (compare Equation 5.3) is the number of candidates after requiring that at least one kaon passes the requirement PIDK > 15.
- N_{and} is the number of candidates after applying the criterion to both kaons.
- ε_K is the probability for any kaon to pass the PIDK > 15 selection criterion.

These numbers are related as follows:

$$N_{\text{or}} = N_{\text{rec}} \cdot \left(\varepsilon_K^2 + 2\varepsilon_K(1-\varepsilon_K)\right) \tag{5.11}$$

$$= N_{\text{rec}} \cdot \left(2\varepsilon_K - \varepsilon_K^2\right) \tag{5.12}$$

$$N_{\text{and}} = N_{\text{rec}} \cdot \varepsilon_K^2 \ . \tag{5.13}$$

From 5.12 and 5.13:

$$\frac{N_{\text{and}}}{N_{\text{or}}} = \frac{\varepsilon_K}{2-\varepsilon_K} \tag{5.14}$$

$$\Leftrightarrow \varepsilon_K = \frac{2N_{\text{and}}}{N_{\text{or}} + N_{\text{and}}} \ . \tag{5.15}$$

Finally, the number N_{rec} follows from Equation 5.13 and 5.15:

$$N_{\text{rec}} = \frac{(N_{\text{or}} + N_{\text{and}})^2}{4N_{\text{and}}} \,. \tag{5.16}$$

It is also possible to calculate the efficiency of the OR cut by combining Equation 5.12 and 5.15:

$$\varepsilon_{\text{pid}} = \frac{N_{\text{or}}}{N_{\text{rec}}} = \frac{4N_{\text{or}}N_{\text{and}}}{(N_{\text{or}} + N_{\text{and}})^2} \,. \tag{5.17}$$

5.8. Signal extraction

The number of candidates before any PID related requirement, i.e. the quotient $N_{\text{rec}} = \frac{N_{\text{or}}}{\varepsilon_{\text{pid}}}$ in Equation 5.3 is given by Equation 5.16. It is determined separately in each bin of ϕ kinematics (see Table 5.2 on page 66). The extraction of N_{rec} works by a simultaneous unbinned extended maximum likelihood fit to the tag- and the probe sample in that bin.

The attempt to extract the signal yields by fitting on the tag- and the probe sample separately is made in Reference [150] suffering from the necessity to propagate the uncertainties to N_{rec}. Also, Reference [150] does not mention inter-bin correlations artificially introduced by fixing width parameters from a global fit and no handle on them is presented. This is why a new signal extraction procedure was developed from scratch by the author and is presented here. It is implemented in the ROOFIT framework [132].

The signal part of the PDF is given by a Voigtian function, i.e. a Breit-Wigner, convolved with a Gaussian:

$$\mathcal{S}(m) = \int \frac{1}{(m' - m_0)^2 + \Gamma^2/4} \, e^{-\frac{1}{2}\frac{(m-m')^2}{s^2}} \, \mathrm{d}m' \,. \tag{5.18}$$

The reconstructed candidate mass m is the variable in the fit and the parameters are:

- m_0 the center of the mass peak,
- Γ the Breit-Wigner width and
- s the Gaussian variance.

The Breit-Wigner width Γ is fixed to the nominal value of $\Gamma = 4.26\,\text{MeV}$ [147], while m_0 and s are floating in the fit. A study of an alternative parametrization with a relativistic Breit-Wigner and a P-wave Breit-Wigner described by the author's working group in Reference [141] suggests the differences to be negligible. Thus, the non-relativistic Breit-Wigner is preferred for reasons of fit stability.

The background is described by an exponential function

$$\mathcal{B}(m) = 1 - e^{c_1 \cdot (m - c_2)} \,,$$

where both parameters are left floating in the fit.

The parameters m_0 and s are shared in the simultaneous fit, whereas c_1 and c_2 are independent for the tag- and the probe sample. Choosing a common mass for both samples is a natural choice. The Gaussian width should be mainly influenced by the kinematic properties of the ϕ, but it is not a priori clear whether the PID requirement does not also influence it. On truthmatched MC, the widths s on the tag- and the probe sample do not differ from each other by more than 10%. However, fixing the relative factor between the widths to 0.9, 1.1 respectively, has only very little impact (roughly 1%) on the cross-section result.

The reconstructed yields N_{rec}, as introduced in Equation 5.16, are shown in Figure 5.6 next to the statistical uncertainty. Plots of the data and the fit results for each bin can be found in Appendix C.

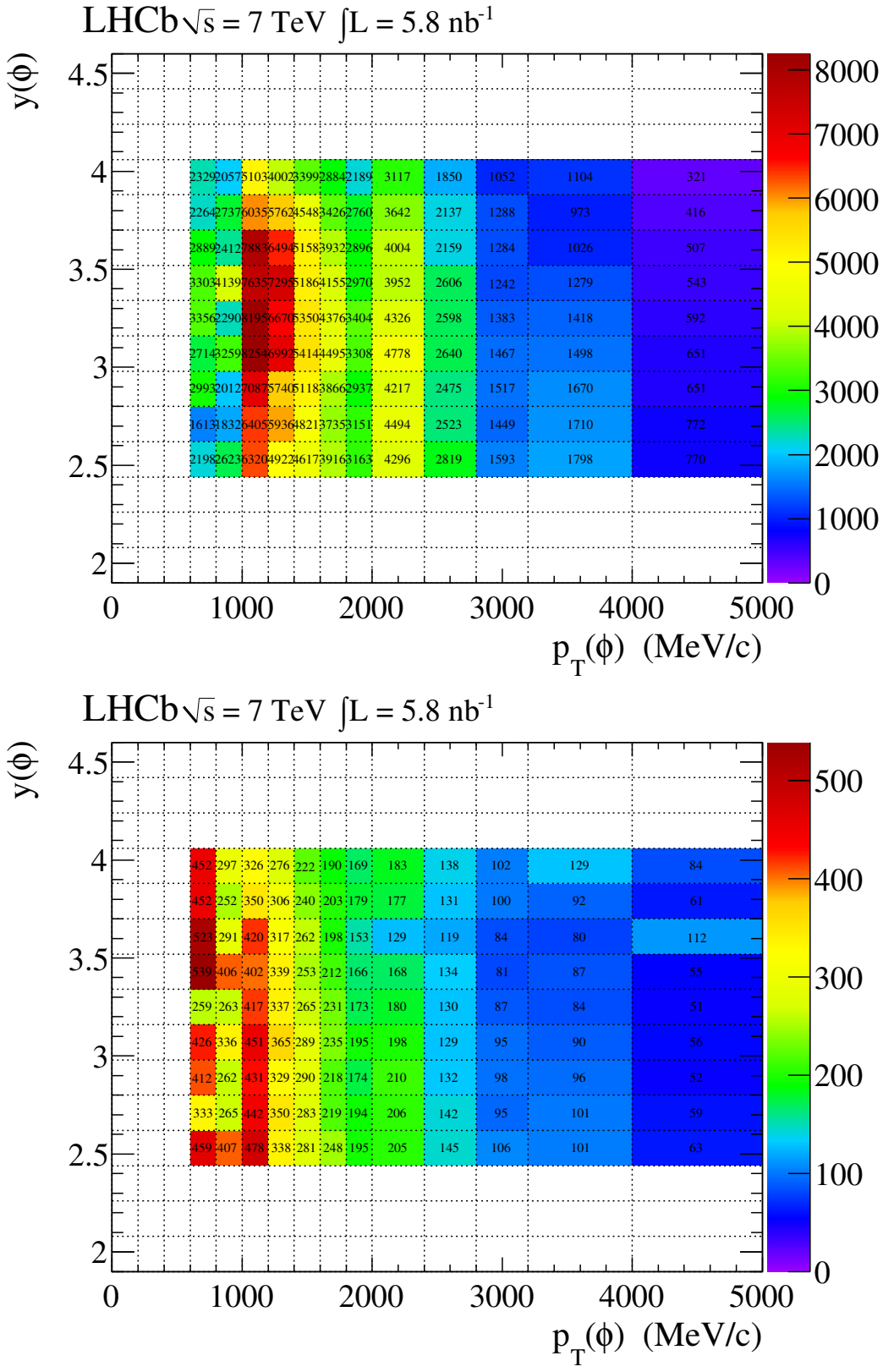

Figure 5.6.: The fitted yields N_{rec} (top) and their statistical uncertainties (bottom) determined on data using the tag-and-probe method.

5.9. Correlations in the PID system

As stressed in Section 5.7, the tag-and-probe approach is based on the assumption that the OR and the AND cut are statistically independent. This is exactly the case if the distribution of the PIDK variables, which the cut acts on, is uncorrelated for the two kaons. The validity of this hypothesis was investigated in studies within the author's working group [140] calculating the correlation coefficient ρ and its uncertainty σ_ρ [151] between the two kaons' PIDK distributions PIDK_1 and PIDK_2.

$$\rho = \frac{V_{12}}{\sqrt{V_{11}V_{22}}} \tag{5.19}$$

$$\sigma_\rho = \sqrt{\frac{1-\rho^2}{N-1}} \tag{5.20}$$

Here, N is the number of data points and V_{ij} is the covariance of PIDK_1 and PIDK_2:

$$V_{ij} = < x_1 \cdot x_2 > - < x_1 > \cdot < x_2 > \tag{5.21}$$

with $x_{1/2}$ as abbreviation for $\text{PIDK}_{1/2}$ and the expectation value $< x >$ of a distribution x.

In a bin-by-bin analysis of correlations on truthmatched MC (Figure 5.7), two particular regions with significant positive correlations between 10% and 40% are evident: one extends from $(p_T/(\text{MeV}/c)\,|\,y) = (600\,|\,3.1)$ to $(2200\,|\,2.3)$ and the other one from $(1500\,|\,3.6)$ to $(5000\,|\,3.1)$ On the other hand, there are specific regions with negative correlations around $(800\,|\,3.5)$ and $(4000\,|\,2.4)$. The reason for these correlations is examined in Section 5.9.2, but first, the influence on the analysis are discussed.

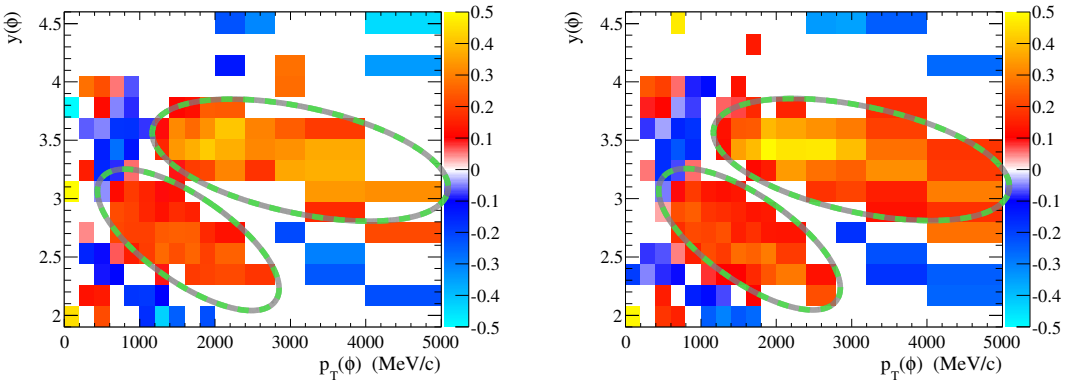

Figure 5.7.: Correlation coefficient ρ for PIDK_1 and PIDK_2 from truthmatched $\phi \to K^+K^-$ candidates on MC. The left plot is for magnet polarity "down", the right plot for polarity "up". Only correlations with significance greater than two are shown. Two regions with particularly large positive correlations are highlighted.

5.9.1. Systematic effects of correlations

The influence of the correlations between PIDK_1 and PIDK_2 on the tag-and-probe algorithm is studied with a simplified toy model, which is based on modeling the two PIDK values by a two-dimensional Gaussian with correlation ρ. As shown in Figure 5.8, a Gaussian is a reasonable approximation when it comes to modeling the basic effects. The basic idea of this model is presented and illustrated by the author's working group based on toy Monte Carlo studies in References [140, 152]. In the context of this thesis, it has been advanced with the analytical description presented below, which avoids the toy MC and hereby allows to formally extract uncertainties on the PID efficiencies from the model (see Section 6.3).

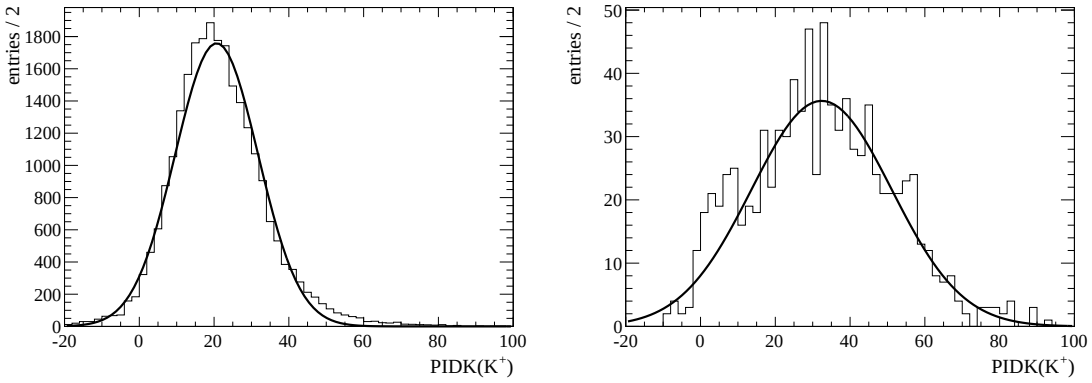

Figure 5.8.: PIDK distribution for kaons of candidates in different regions of ϕ p_T and y. $0.6 < p_T < 0.8\,\mathrm{GeV}/c$ and $2.44 < y < 2.62$ (left) and $1.6 < p_T < 1.8\,\mathrm{GeV}/c$ and $3.88 < y < 4.06$ (right)

A multivariate Gaussian with correlation ρ is parametrized as follows:

$$g(x,y,\rho) = \frac{1}{2\pi\sqrt{1-\rho^2}} \cdot \exp\left(\frac{1}{2\cdot(1-\rho^2)} \cdot (x^2 - 2\rho xy + y^2)\right) . \tag{5.22}$$

At a given cut value b, the fraction of events passing the AND and the OR cut, respectively, is calculated as follows:

$$G_{and}(b,\rho) = \int_{x=b}^{\infty}\int_{y=b}^{\infty} g(x,y,\rho)\,\mathrm{d}x\,\mathrm{d}y \tag{5.23}$$

$$G_{or}(b,\rho) = 1 - \int_{x=-\infty}^{b}\int_{y=-\infty}^{b} g(x,y,\rho)\,\mathrm{d}x\,\mathrm{d}y\,. \tag{5.24}$$

Based on Equation 5.23 and 5.24, the evolution of the efficiencies of the OR- and the AND- cut with ρ can be analyzed. In Figure 5.9, where this is done exemplarily for $\varepsilon_K = 0.8$, the following quantities are shown (similar to the toy Monte Carlo studies in References [140, 152]):

- **DLL cut single K:**
  The efficiency ε_K for a single kaon to survive the DLL cut is inserted to guide the eye.
- **OR cut:**
  The true efficiency of the OR cut from Equation 5.24
- **OR cut, uncorr.:**
  The efficiency of the OR cut under the assumption $\rho = 0$

- **AND cut:**
  The true efficiency of the AND cut from Equation 5.23

- **AND cut, uncorr.:**
  The efficiency of the AND cut, calculated under the assumption $\rho = 0$

- **reconstructed OR cut:**
  The efficiency of the OR cut, reconstructed with tag-and-probe

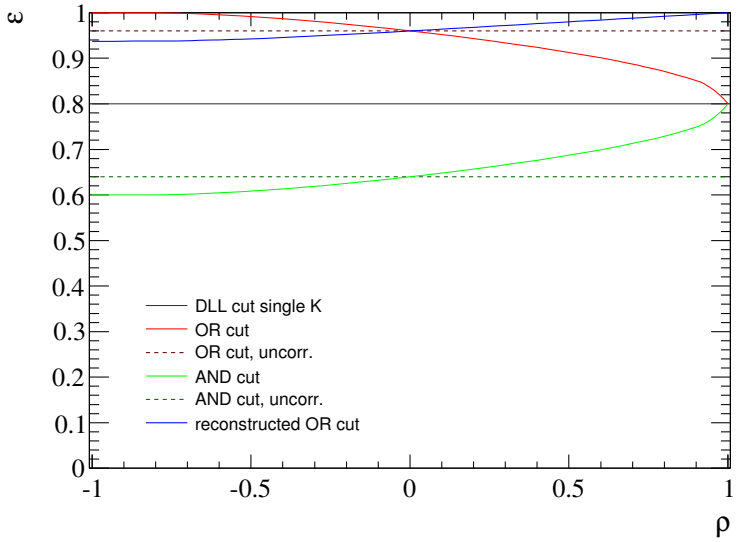

Figure 5.9.: Comparison of cut efficiencies with the ones derived from tag-and-probe. See text in Section 5.9.1 for definitions. The efficiency ε_K is 0.8 in this plot.

Other than the plot in Figure 5.9 suggests, the efficiency functional shapes accounting for the correlations are highly non-trivial, e.g. if analyzed at low values of ε_K. Nevertheless, three particular spots are easily understood:

- $\boldsymbol{\rho \equiv 1}$
  The two kaons always have the same value for PIDK, so that the efficiency that at least one of them passes the cut is the same as if both of them pass it. It is equal to ε_K.

- $\boldsymbol{\rho \equiv 0}$
  This is the assumption made in tag-and-probe, so the curves of the toy model cross the ones based on Equation 5.12 and 5.13.

- $\boldsymbol{\rho \equiv -1}$
  The two PIDK values are the additive inverse of each other: if of them is particularly high, the other one is particularly low. This explains a higher OR cut efficiency and a lower AND cut efficiency compared to the case without correlations.

An estimation of the systematic error of the tag-and-probe method is given by the comparison of the blue curve with the red one in Figure 5.9. Since, the efficiencies are mostly higher than in the example, the real effect is less pronounced as shown here. It will be treated as systematic uncertainty, as explained in Section 6.3

5.9.2. Analysis of correlations

In this section, correlations of the PIDK values of the two kaons in the tag-and-probe approach are investigated, for which several sources are conceivable:

- They might be an intrinsic effect of the tag-and-probe approach: by categorizing the candidates by the ϕ transverse momentum and rapidity, the kaons would be kinematically close which would account for the correlations.
- They might be caused by the interplay of different radiators. This would depend on the kinematic properties of the kaons, which are correlated for ϕ bachelor kaons.
- They might be caused by the Čerenkov rings of the two kaons overlapping in the RICH so that they enhance each other.
- Global quantities, for example the global track multiplicity, could introduce them because the PID efficiency depends on them.

These four hypotheses will be explained in detail and tested in this section.

Kaon PID efficiencies

The first hypothesis is that the PID correlations might be induced by the binning of ϕ in the ϕ kinematic plane. Thus, the kaons from a ϕ would be kinematically close which would account for the PID correlations. This might hint at the following alternative analysis strategy being superior: it would have been possible to take the efficiencies calculated for kaons depending on kaon kinematics, as presented in Reference [12], which would avoid the correlations under the aforementioned assumption.

To solidify the understanding of this statement, the efficiency for truthmatched K^+ originating from ϕ is analyzed in K^+ kinematics. A two-dimensional representation based on the logarithms of momentum and transverse momentum is chosen. The efficiency is shown in Figure 5.10 (left). The ϕ kinematics do *not* go in here. This efficiency calculation is repeated where only those K^+ are considered where the K^- have passed the PID cut, shown in Figure 5.10 (right). These are referred to as "biased" in the following.

The relative difference beween the biased and the unbiased efficiency is shown in Figure 5.11 next to its significance. This plot proves that even in the case that *kaons* are sorted in their respective kinematic bin, a bias is created by cutting on the PID of the other kaon. Thus, the observed correlations are *not* a problem of the analysis strategy, but an intrinsic feature of the LHCb detector.

This study is an idealized case of the alternative analysis strategy presented above. From the plots shown here, it is evident that both approaches suffer from the same detector effects.The alternative analysis strategy has been further benchmarked on LHCb MC. For both species, the efficiency of "biased" kaons, i.e. those where the other kaon has passed the PID cut, was analyzed in the binning given in Reference [12]. This categorizes in six equally sized bins in y from 2 to 5 and three bins in p_T, where the boundaries are at $800\,\mathrm{MeV}/c$ and $1200\,\mathrm{MeV}/c$. These efficiencies have been taken to infer the ϕ PID efficiency of the AND cut. This is an idealization of this version of the tag-and-probe approach, eliminating any fit induced biases. The relative difference between the tag-and-probe and the real efficiency is calculated. As seen in Figure 5.12, a vast bias is introduced.

In conclusion, calculating the PID efficiencies in bins of ϕ kinematics promises a more precise result in this analysis since this binning is naturally adapted to the physical properties of the

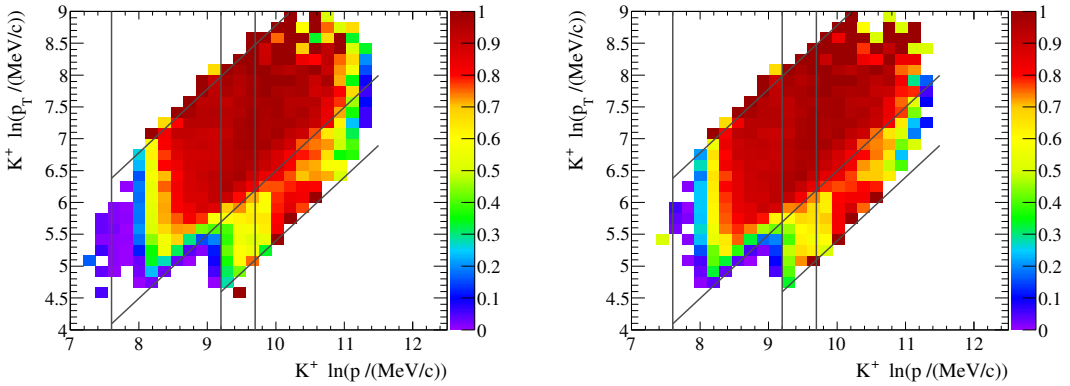

Figure 5.10.: Efficiency for kaons to fulfill the requirement PIDK > 15 for all K^+ (left) and for K^+ where the K^- also passes the PIDK constraint (right). Vertical lines are drawn at the three RICH thresholds for kaons and diagonal lines correspond to azimuthal angles of 10, 30 and 300 mrad.

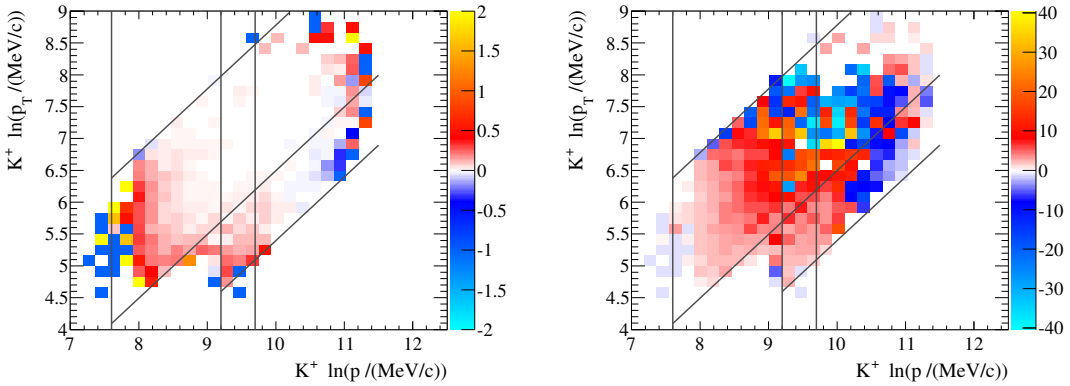

Figure 5.11.: Relative difference between non-biased and biased K^+ PID efficiency (left) and its significance (right). For details on the lines see Figure 5.10.

process under study. Adopting an extremely fine binning in kaon kinematics, results similar to the one binning in ϕ kinematics can be yielded on truthmatched Monte Carlo, but this offers no advantages. Neither is it feasible on data due to the limited sample size.

Contribution of different RICH radiators

Figure 5.10 provides an understanding of the efficiencies from the detector properties. Vertical lines at $\ln[p/(\mathrm{MeV}/c)] \approx 7.6$, ≈ 9.2 and ≈ 9.7 mark the RICH1 Aerogel, the RICH1 gas and the RICH2 threshold for kaons. Any straight line in that plane with slope 1 is a line of equal azimuthal angle. Thus, the efficiencies shown can easily be connoted with the detector's layout and response.

The potential effect of the different RICH radiators on the PID correlation is analyzed by classifying the kaons in their kinematic range. The transformation between ϕ and kaon kinematics is done on truthmatched LHCb Monte Carlo. For each ϕ-(y/p_T) bin, the kinematic distribution of the

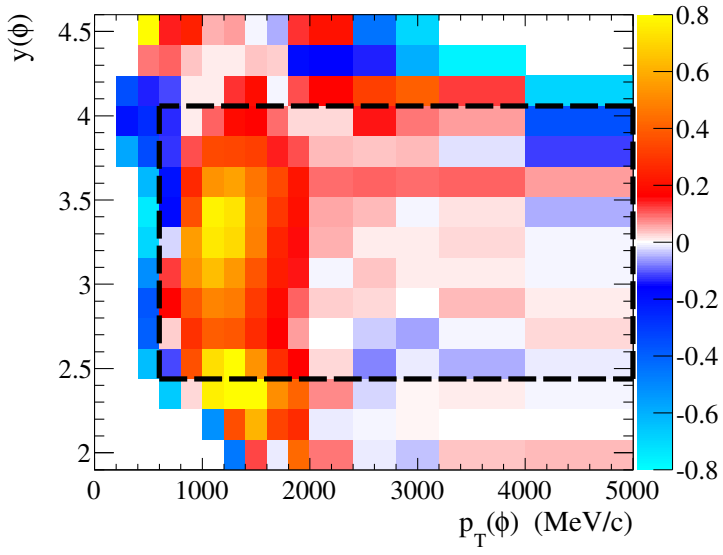

Figure 5.12.: MC study: Relative bias introduced when using efficiency definition in Reference [12] compared to the real efficiencies for the AND cut.

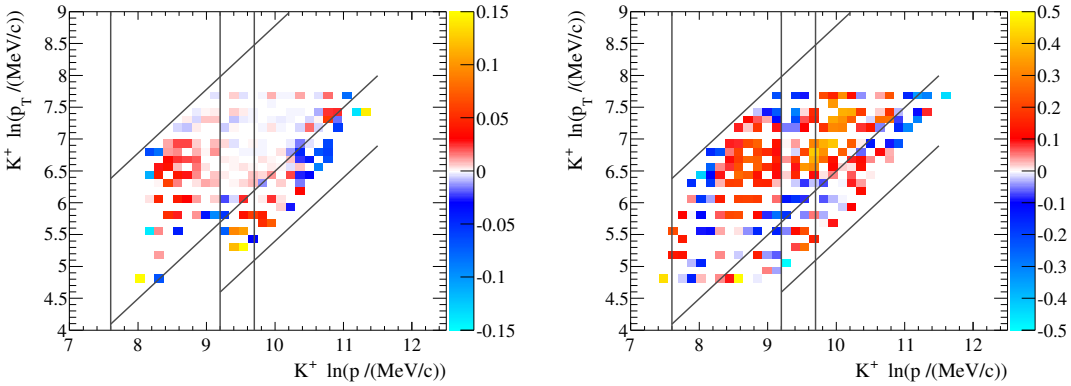

Figure 5.13.: Localization of regions with high relative systematic PID uncertainty (left) and correlations (right) in kaon kinematics. For details on the lines see Figure 5.10.

kaons is determined in the two-dimensional space of the kaons' logarithmic momentum and transverse momentum. At the center of this distribution, the PID systematic error and its correlation respectively, as calculated in the ϕ-(p_T/y) binning, is drawn as single data point (Figure 5.13).

As shown in Figure 5.14 there is a dominant region of high relative PID efficiency errors along the line connecting $(p_T/(\mathrm{MeV}/c)\,|\,y) = (600\,|\,3)$ and $(2200\,|\,2.3)$. From the study presented above and from kinematic considerations, it is evident that this region is populated by kaons that are below any RICH gas threshold and thus are detected in the RICH1 Aerogel only. Since this is the region with dominant uncertainties, the following studies concentrate on them. In conclusion, correlations can occur in any RICH radiator; they are even observed for kaons that have such a low momentum that they emit Čerenkov light in only a single radiator.

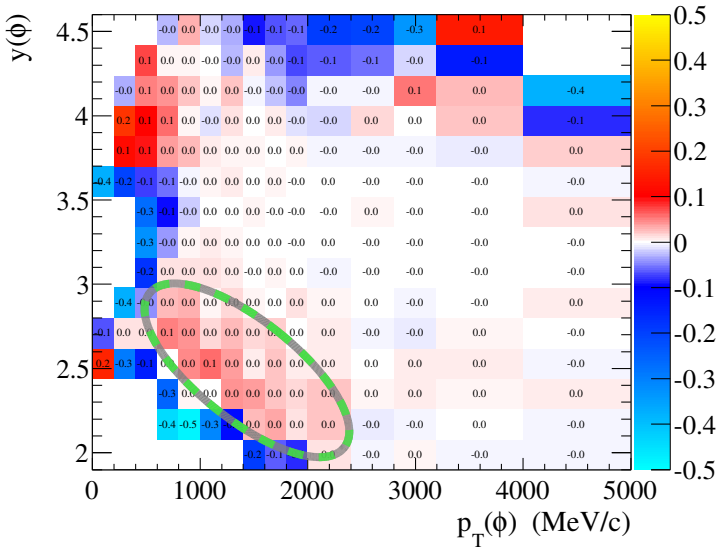

Figure 5.14.: Relative systematic error on OR cut efficiency due to tag-and-probe, analyzed on truthmatched Monte Carlo. A region with particular high relative errors within the analysis range is highlighted.

Ring overlap

As a further hypothesis, the correlations might be caused by the two rings in the RICH overlapping. A perfect testing ground for this is the RICH1 Aerogel: first, there are strong correlations in the corresponding kinematic region and second, any interplay between several RICH radiators is excluded for kaons that are above the Aerogel threshold but below any other radiator's threshold. Finally, the tracks are not yet separated by the spectrometer magnet, so that their trajectories are particularly close.

The distribution of angles between K^+ and K^- tracks when entering RICH1[18] is plotted versus the momentum in Figure 5.15 (left), which is interpolated as shown in Figure 5.15 (right). On top of the angular separation there is also a small spatial separation which is neglected. Rather, the kaons are assumed to originate from a common point in the Aerogel and to move apart at the angle introduced above. Hereby the kaons are further separated in reality than assumed in this study and consequently, its result may more readily be understood as an upper bound.

The fraction of hits from the first ring, modeled by a Gaussian distribution with momentum-dependent opening angle θ and $\sigma_\theta = 2.6\,\text{mrad}$, lying in a 3σ region of the second ring is plotted in Figure 5.16. Even with this simplified model, the ring overlap is less than 20-30% in the region where only RICH1 Aerogel is significant. Since the overlap rises with momentum, so should the correlations if they were caused by overlapping rings – no evidence for this behavior is seen in Figure 5.13.

Finally, as pointed out in Reference [84], the RICH PID algorithm described in Section 2.2.2 should naturally handle neighbored tracks: relying on reconstructed tracks, not only the light intensity is higher for two extremely close tracks but also the expectation derived from the neighbored tracks' trajectories.

[18] given by LHCb's track state vector at z = 990 mm

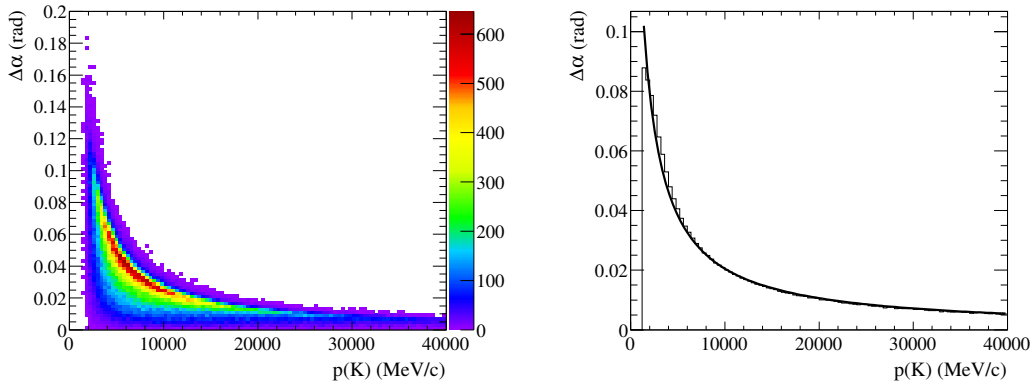

Figure 5.15.: Angle $\Delta\alpha$ between K^+ and K^- at the track state vector at the RICH1 entry versus track momentum.

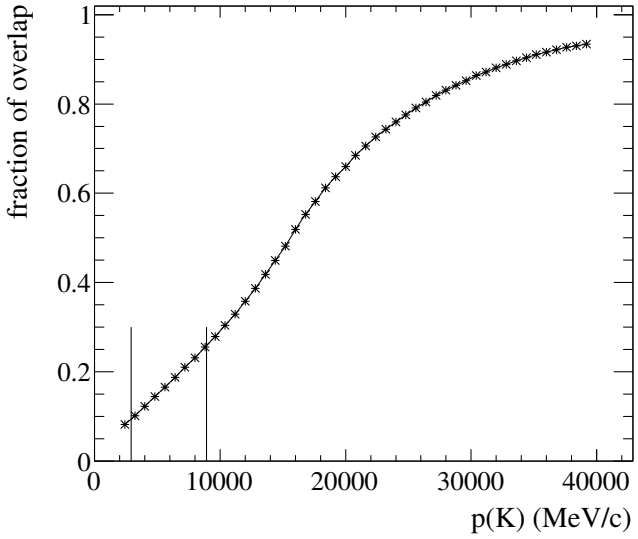

Figure 5.16.: Estimation of overlap between kaon rings in RICH1 Aerogel versus momentum. The working region of Aerogel is highlighted (compare Figure 2.5 on page 22).

Track multiplicities

The working principle of the RICH detector (see Section 2.2.2) is based on an event global approach of associating photon distributions on the HPD plane to the distribution of particle trajectories, the advantages of which have been highlighted above. With rising track multiplicities the hit multiplicity in the RICHes increases, too. As Figure 2.7 on page 23 suggests, this complicates the statistical separation of the different particles' contribution to the Čerenkov light pattern and hereby decreases the separation power of the particle identification system [84]. In the limit of infinite track multiplicities the whole RICH detector would be lit up and no information on single tracks could be inferred.

To analyze the effect of the global track multiplicity on the ϕ reconstruction, all ϕ candidates in a truthmatched MC sample are partitioned in n-quantiles of global track multiplicity in that event

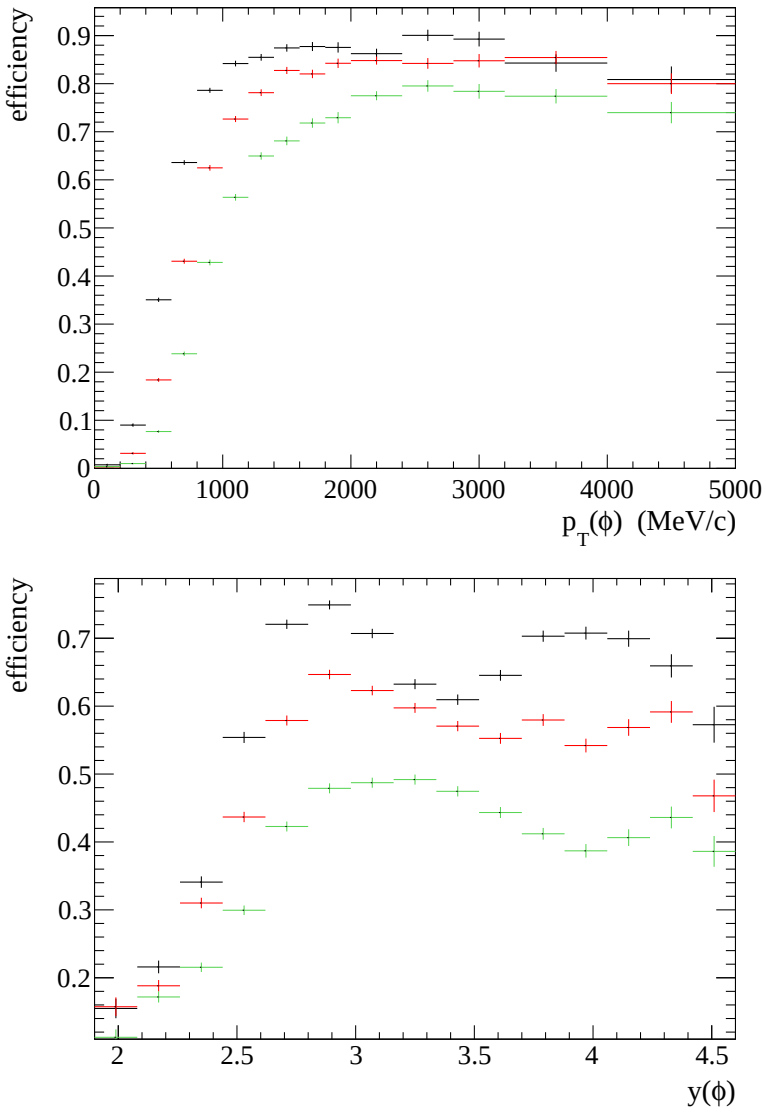

Figure 5.17.: Efficiency of PID AND cut for three ranges of global track multiplicity: 0-43 (black), 43-79 (red) and 79+ (green) projected on p_T with $2.44 < y < 4.06$ (top) and y with $0.6 < p_T < 5.0\,\mathrm{GeV}/c$ (bottom).

and the PID efficiency is plotted separately for these quantiles. As shown in Figure 5.17, the PID efficiency largely varies with track multiplicity, especially in the boundary regions such as the relevant kinematic range of RICH1 Aerogel. This implies correlations in a mathematically strict way: assume n classes of points in two-dimensional space, each of which is distributed following an uncorrelated two-dimensional Gaussian distribution with center $(x + n\varepsilon, y + n\varepsilon)$. Then, the unification of these points *does* show a correlation.

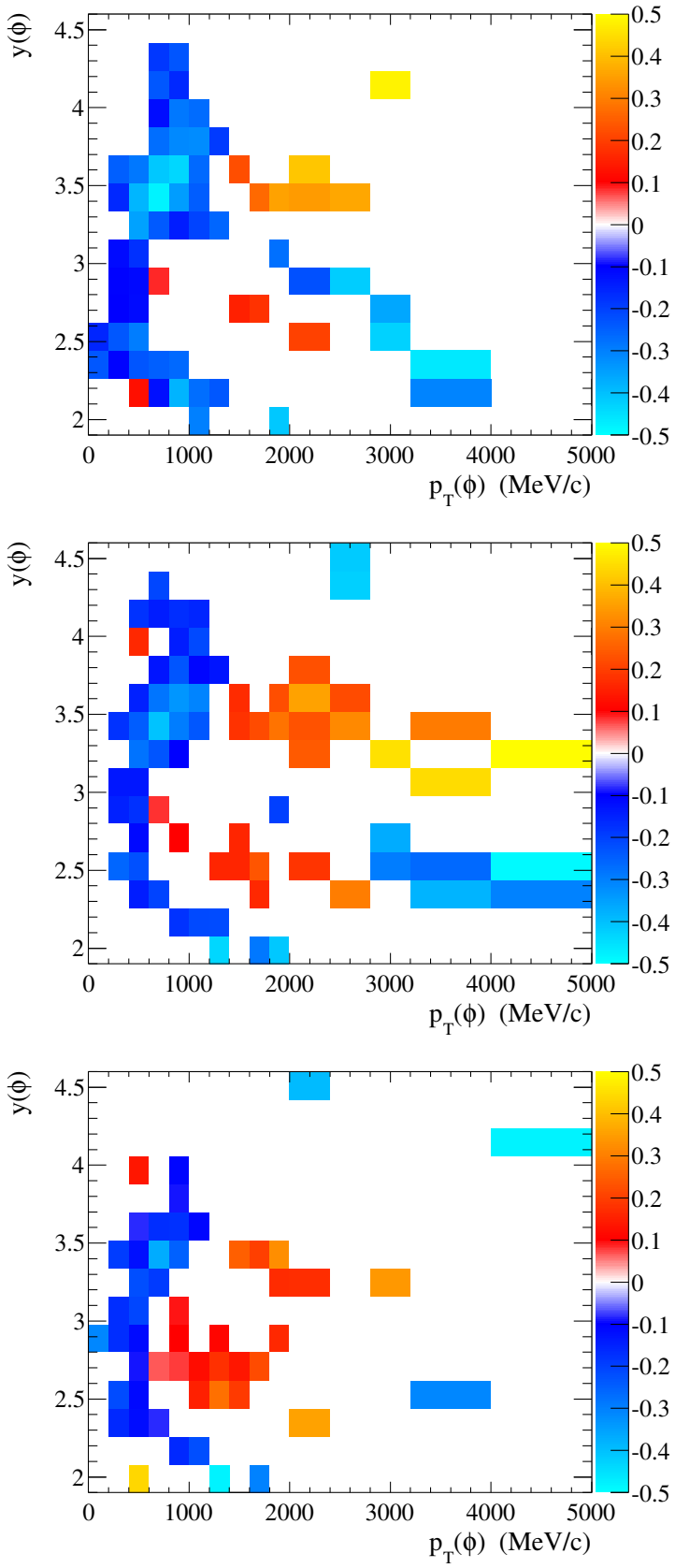

Figure 5.18.: Correlations between $PIDK_1$ and $PIDK_2$ for three different ranges of global track multiplicity: 0-43 (top), 43-79 and 79+ (bottom). Only correlations with significance greater than two are shown.

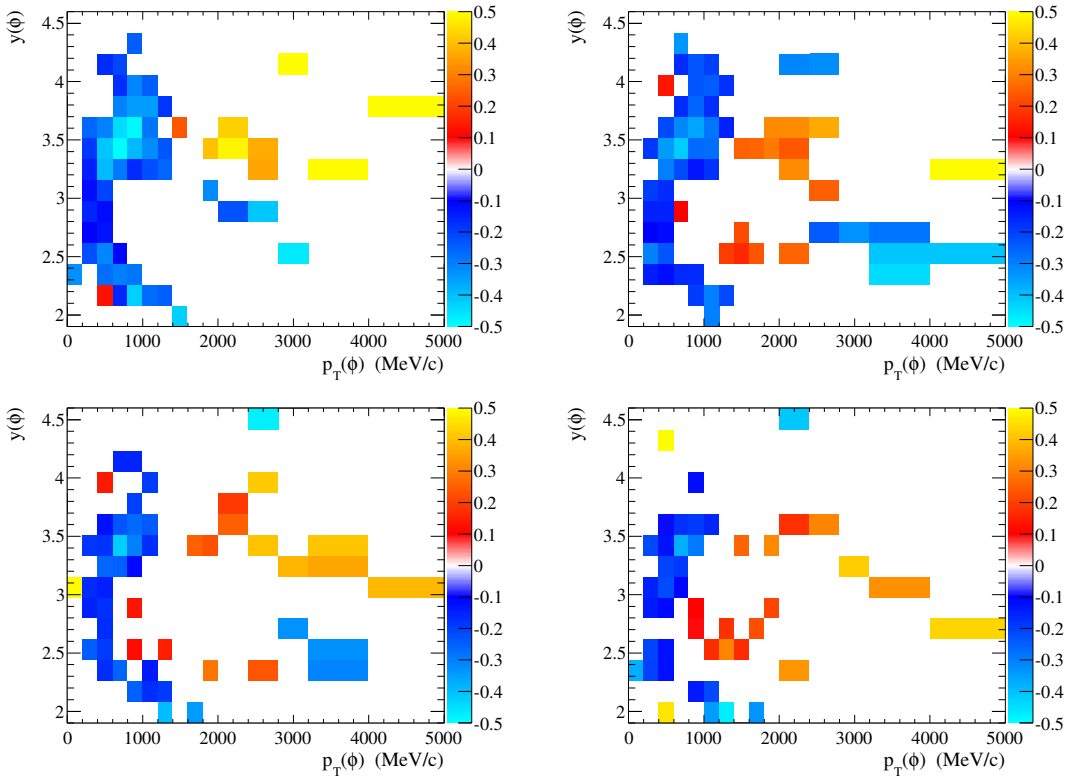

Figure 5.19.: Correlations between $PIDK_1$ and $PIDK_2$ for four different ranges of global track multiplicity: 0-35, 35-60 (top), 60-90, 90-354 (bottom). Only correlations with significance greater than two are shown.

Thus, the track-multiplicity dependence of the PID system produces correlations. The correlations between the K^+ and K^- PID are plotted as function of ϕ momentum and rapidity for different quantiles of track multiplicity. In Figure 5.18 the data set is split up in three parts of equal size. In Figure 5.19 it is split up in 4 parts of equal size and in Figure 5.20, one fourth of the data set is analyzed, but without imposing any requirement on the track multiplicity. Comparing Figure 5.18 and 5.19, the higher the number of classes of track multiplicity, the lower the correlations in the RICH Aerogel. In Figure 5.19, the positive correlations, which are present in the random sample (Figure 5.20), almost vanish.

Some regions of negative correlations are unmasked when categorizing the events according to their track multiplicity. These regions are the momentum- and geometrical-acceptance- boundaries of detector components of the RICH system, as shown in Figure 5.21. They are characterized by steep variations of the efficiency with the track's angle or momentum. Since K^+ and K^- of an individual ϕ have asymmetric flight directions, the PID efficiency cannot be expected to be symmetrical for them in those regions.

In conclusion, it has been shown that the PID correlations have a well founded physical reason – the detector response. The effect from correlations could be partly mitigated by categorizing the data sample by track multiplicity. However, since the signal extraction is based on maximum likelihood fits to these samples (Section 5.8), it is not possible to split up the samples for reasons of fit stability. This is why the effects from correlations are analyzed and an appropriate systematic uncertainty is assigned.

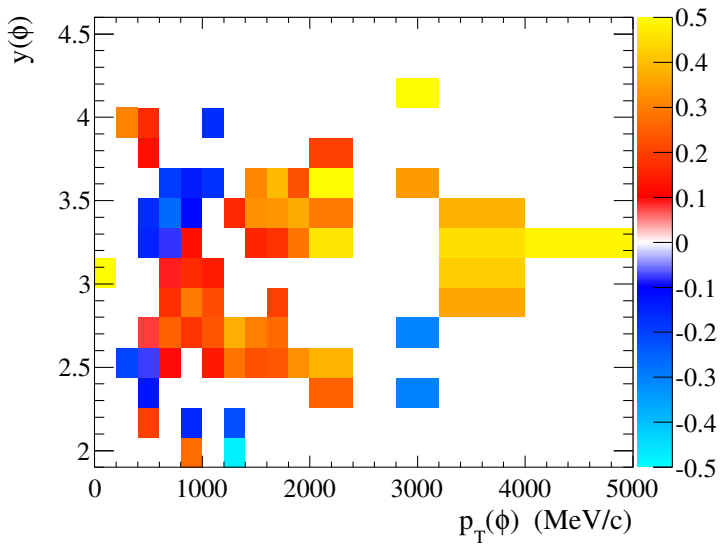

Figure 5.20.: Correlations between $PIDK_1$ and $PIDK_2$, 25% of the data set, randomly chosen. Only correlations with significance greater than two are shown.

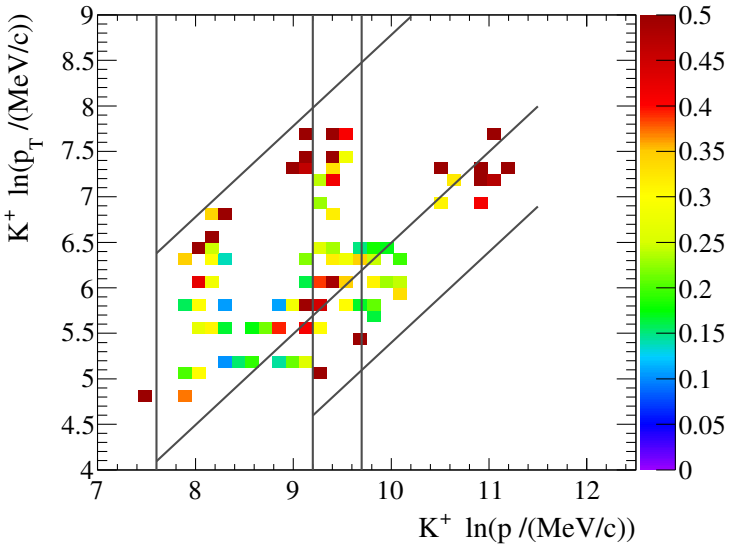

Figure 5.21.: Regions with negative correlations when categorizing in four categories of track multiplicity. Out of the four categories, the maximum of the absolute value of significant negative correlations is plotted for each bin.

5.9.3. Low p_T boundary for the analysis

As mentioned in Section 5.4, the analysis of the low-p_T region is challenging due to rising backgrounds and falling PID efficiencies. LHCb has measured the differential K^0_S production cross-section down to $p_T = 0$ [146], but the analysis of ϕ mesons differs in two key aspects: first of all, the mean of the meson production p_T spectrum rises with the meson mass and hereby the ϕ production spectrum approaches zero at a higher p_T than the K^0_S spectrum. Secondly, there are also some detector particularities to be taken into account, since the ϕ analysis requires the RICH system in contrast to the K^0_S analysis cited above. Thus, a careful analysis has been done how far the analysis can be extended towards lower p_T values.

In the region $400\,\text{MeV}/c < p_T < 600\,\text{MeV}/c$ and $3.0 < y < 3.7$, there are large relative uncertainties from the tag-and-probe approach (see Figure 5.14). First of all, as outlined in the previous section, this boundary region is characterized by strong negative correlations, which locally introduce a significant bias to the tag-and-probe approach. Furthermore, the PID AND cut efficiencies are as low as 30% in this range (Figure 5.22), which results in tiny fluctuations in the tagged-and-probed efficiency having a vast impact on the result. A reason for this low efficiency region is that many kaon tracks are not within the RICH acceptance. – These tracks have momenta below the RICH1 gas thresholds and angles lower than the RICH1 Aerogel acceptance. In conclusion, the geometrical detector acceptance sets the natural boundary for the inclusive ϕ measurements to the range $0.6 < p_T < 5.0\,\text{GeV}/c$.

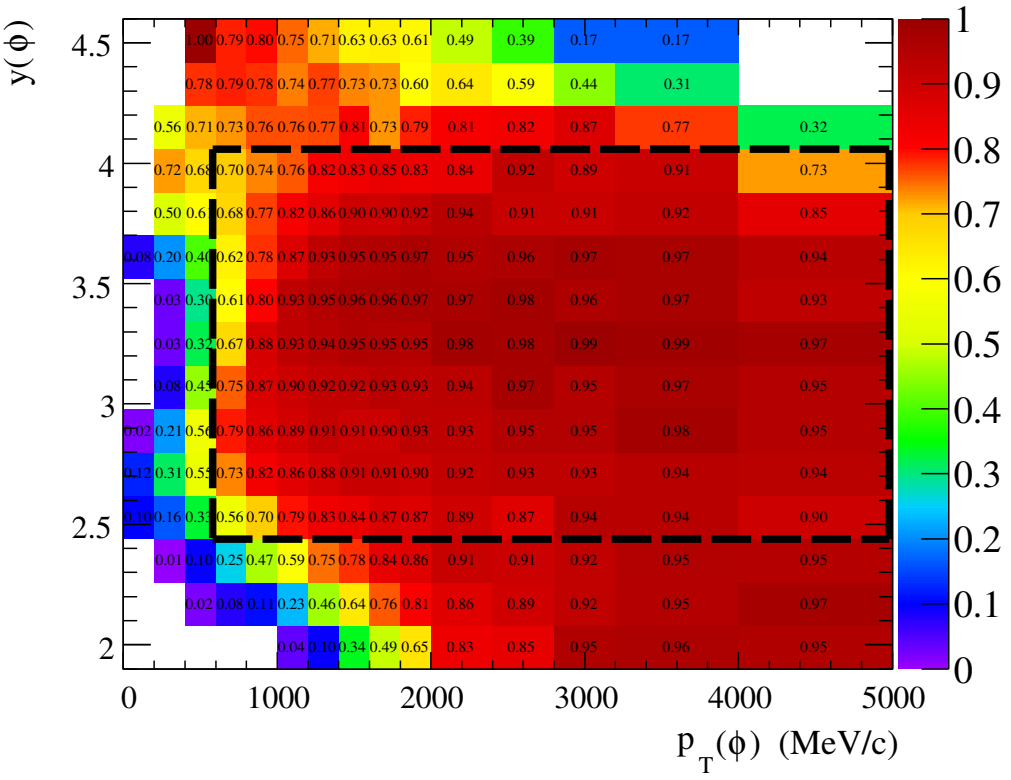

Figure 5.22.: PID AND cut efficiency on MC.

CHAPTER 6

Systematic uncertainties of the inclusive ϕ cross-section measurement

The first data taken by a high energy physics experiment traditionally plays a crucial role in solidifying the understanding of the detector. When methods that were previously developed and analyzed solely on simulated samples are applied on real data for the first time, careful cross-checks have to be carried out in order to assure their applicability on data. While analyses start on early data, these data samples are also used for studies of the alignment and the reconstruction efficiency, for example. Hereby the knowledge of the detector performance only improves with time, which is why relatively large systematic uncertainties have to be assigned in the beginning. Since on the other hand, physics processes with comparably high cross-sections are studied, the statistical uncertainties are moderate. The considerations above also hold for the ϕ cross-section measurement, which uncertainties are dominated by systematics for these reasons.

Some systematics are global scale uncertainties and affect all bins alike while some are independent between different bins. Finally, the systematic uncertainties due to the diffractive contribution are determined for sub-regions of the ϕ kinematic plane. The characteristic behavior of the systematics with respect to the binning are taken into account: when integrating over a set of bins, uncorrelated uncertainties are added in squares while correlated ones are summed.

The following list[1] summarizes the uncertainties that contribute to the analysis. Some further studies on uncertainties have been carried out and are described in the previous chapter, but are not listed here in the case that their effect was found to be negligible.

1. **Bin-wise systematics** are analyzed separately for each bin.
   - MC statistics in the determination of the reconstruction efficiency (Section 6.2.1)
   - PID systematics due to correlations (Section 6.3)
2. **Partly bin-wise systematics** are uniform for certain regions of bins.
   - Accounting of diffractives in reconstruction efficiency (Section 6.2.6)
3. **Global systematics** are the same for the whole kinematic region.
   - Tracking (Section 6.1)
   - Luminosity (Section 6.1)
   - Track multiplicity (Section 6.2.2)
   - Fit systematics (Section 6.4)
   - Truthmatching (Section 5.6)
   - Clone rate (Section 6.2.3)
   - Branching ratio of $\phi \to K^+K^-$ (Section 6.1)
   - Binning (Section 6.2.4)
   - Material interactions (Section 6.2.5)

The following section will group the systematic contributions by their origin, i.e. whether they arise from the determination of the reconstruction efficiency, the PID system or the signal extraction. The analysis of systematics is finally summarized in Section 6.5.

[1] The ordinal numbers in the list are arbitrary and used for reference purposes only.

6.1. External systematics

The two leading uncertainties arising from tracking and luminosity are determined centrally in LHCb. Since this analysis is carried out on the first couple of weeks of data taking at $\sqrt{s} = 7\,\text{TeV}$, the uncertainties on the tracking are still in the order of 4% per track [104]. The luminosity determination has an uncertainty on the scale of 3.5% [92]. Finally, the relative uncertainty on the $\phi \to K^+K^-$ branching ratio is 1.2% [147].

6.2. Systematic uncertainties of the reconstruction efficiency

6.2.1. MC sample size

The reconstruction efficiency determination from Equation 5.8 is afflicted by an uncertainty due to limited MC sample size. It is calculated according to Equation 5.9 and shown in Figure 5.5. In the high statistics region, it is in the order of 1% and rises up to 6% at the edge of the considered kinematic range, i.e. the uncertainty is higher where there is little data anyway.

6.2.2. Track multiplicity on data and MC

To account for the higher track multiplicity on data compared to MC (see Section 5.5), the candidate reconstruction efficiency is analyzed as function of long track multiplicity. The reconstruction efficiency, binned by the ϕ mesons' p_T and y has been calculated in several categories of long track multiplicity. Each of these two-dimensional efficiency histograms have been normalized to the global reconstruction efficiency and a weighted average of this quotient has been calculated (Figure 6.1).

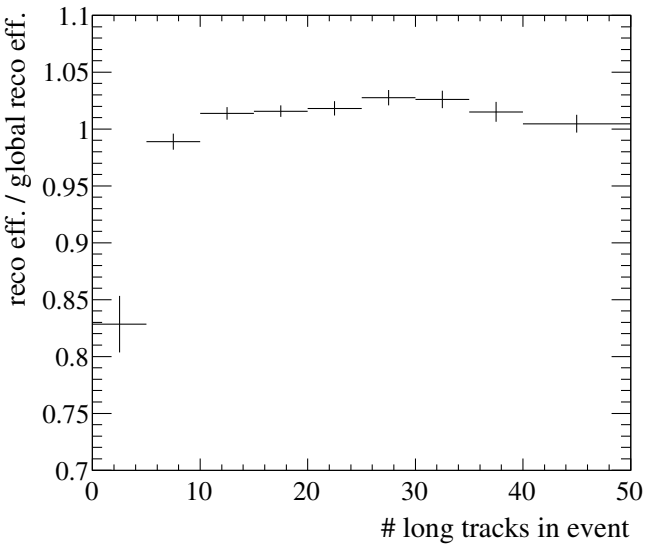

Figure 6.1.: Variation of the reconstruction efficiency with long track multiplicity, normalized to the global (multiplicity integrated) reconstruction efficiency.

The general agreement is mostly better than 3%, except for events with less than five long tracks. These constitute 5.8% / 4.5% of all events passing the reconstruction on MC / data, which means there are 1.3 percent points less events in that bin on data than in MC, so the effect of the lower efficiency for less than five long tracks is negligible. Consequently, a 3% uncertainty is assigned due to the track multiplicity dependence of the reconstruction efficiency.

6.2.3. Doubly identified tracks

As outlined in Section 2.5.1, there are doubly identified tracks ("clones") as result of the reconstruction procedure. The influence of clone tracks (Section 2.5.1) on the analysis has been analyzed in Reference [150]. Since clone tracks have flight directions at low angles to their "real" counterpart, this study [141, 150] is based on the angle between any combination of tracks in the event. As a result, there are clone tracks on both, data and MC, but the relative difference is less than 2%, which is assigned as systematic uncertainty.

6.2.4. Binning studies

Due to the finite detector resolution, there is a spillover between different bins. Studies of this spillover are described by the author's working group in [141] and shown to have an effect of less than 1% on the cross-section measurement.

Furthermore, the results in Section 7.2 will show that the measured p_T distribution (Figure 7.2 on page 102) differs in shape from the MC prediction. The data/MC ratio is flat at higher transverse momenta, but it falls quite steeply at low p_T, which implies that the weighting of efficiencies for different transverse momenta within each single p_T-bin differs between data and MC. A potential bias on the reconstruction efficiency determination is investigated by the following study.

First, the p_T-dependent distribution of the generated candidates $g_{\mathrm{MC}}(p_T)$, reconstructed candidates $r_{\mathrm{MC}}(p_T)$ and the reconstruction efficiency $\varepsilon_{\mathrm{MC}}(p_T)$ is determined on Monte Carlo. The reconstruction efficiency versus p_T is parametrized by the function

$$\varepsilon_{\mathrm{MC}}(p_T) = p_0 \cdot (1 - e^{p_1 \cdot (p_T - p_2)}) \tag{6.1}$$

and the spectrum of reconstructed candidates versus p_T by the function

$$r_{\mathrm{MC}}(p_T) = e^{(q_0 + q_1 \cdot p_T)} \; . \tag{6.2}$$

These parametrizations are fitted to the distributions on MC. The distribution of generated particles versus p_T is consequently described by

$$g_{\mathrm{MC}}(p_T) = \frac{r_{\mathrm{MC}}(p_T)}{\varepsilon_{MC}(p_T)} \; . \tag{6.3}$$

The reconstruction efficiency in bin i (range $[x_1, x_2]$) is formally defined as

$$\varepsilon_i = \frac{\int_{x_1}^{x_2} r_{\mathrm{MC}}(p_T)\, \mathrm{d}p_T}{\int_{x_1}^{x_2} g_{\mathrm{MC}}(p_T)\, \mathrm{d}p_T} \; . \tag{6.4}$$

Calculating the number of generated candidates per bin from the number of reconstructed candidates using ε_i yields the correct result on MC per definition.

Now it is assumed that both, the distribution of reconstructed and generated candidates on data equal distributions on MC multiplied by a 3rd order polynomial $f(p_T)$, which has been fitted to the data/LHCb-MC ratio in Figure 7.2. Taking this ratio into account, the correct number of generated particles on data would be

$$g_{\text{i, data}} = \int_{x_1}^{x_2} g_{MC}(p_T)\, f(p_T)\, \mathrm{d}p_T \ , \tag{6.5}$$

which is compared to the result using the binned efficiency from MC

$$g'_{\text{i,data}} = \frac{\int_{x_1}^{x_2} r_{MC}(p_T)\, f(p_T)\, \mathrm{d}p_T}{\varepsilon_i} \ . \tag{6.6}$$

The relative differences between $g_{\text{i, data}}$ and $g'_{\text{i,data}}$ are below 0.2% in the lowest p_T-bin and even lower in the rest of the bins. Consequently, the difference between the p_T distribution on data and MC is negligible.

6.2.5. Material interactions

The interaction of the daughter kaons within the LHCb detector is simulated with Geant4 [95]. The implementation in LHCb determines the interaction cross-sections from LHEP functions [153], which are parametrized fits to data [154]. For K/p and K/n interactions data [147] has uncertainties in the order of 1%. This would result in a roughly 1% effect on the number of interactions. Further, the conservative estimate is made [146] that the material budget is described better than with an error of 10% with a corresponding effect on the number of interactions per daughter particle. This uncertainty is clearly dominant compared to the former contribution. The hadronic interaction probability for kaons within 5 cm aluminum, mimicking the material of the LHCb detector up to the RICH2 [153] has been shown to be roughly $p = 10\%$ [153]. Under the above-mentioned assumptions, this would have an uncertainty of $\Delta p = 1\%$.

In [155] it has been shown for $K_s \to \pi^+\pi^-$ that the reconstruction efficiency ε_m for the mother particle, which bachelors did not interact with material, drops by 17.4% in the case that one of the daughters undergoes a material interaction. Since the location of the decay and the reconstruction is not the same for the ϕ mesons studied herein, this number is not exactly the same for ϕ mesons, which daughters traverse a longer path in the material than the K_s daughters. As a conservative estimate an $f_{\varepsilon_m} = 50\%$ change in the reconstruction efficiency for ϕ is assumed.

The total reconstruction efficiency ε_r includes ϕ mesons which bachelors have undergone material interactions and those that bachelors traversed the detector without interaction:

$$\varepsilon_r = \varepsilon_m \left[(1-p)^2 + f_{\varepsilon_m} \cdot (1-(1-p)^2)\right] \ . \tag{6.7}$$

The uncertainty on the material interaction is propagated to the reconstruction efficiency as follows:

$$\frac{\Delta\varepsilon_r}{\varepsilon_r} = \frac{2\,(1-p)\,(1-f_{\varepsilon_m})\,\Delta p}{(1-p^2)\,(1-f_{\varepsilon_m}) + f_{\varepsilon_m}} \ . \tag{6.8}$$

With the constants given above, the relative uncertainty due to material interactions is estimated to be

$$\frac{\Delta\varepsilon_r}{\varepsilon_r} \approx 1\% \ . \tag{6.9}$$

Since the PID efficiency is determined from data, any effect from potential non-visibility of kaons in the RICH is already taken into account by the tag-and-probe method and does not call for consideration here.

6.2.6. Diffractive and elastic events

The MC sample is composed of the different PYTHIA event types outlined in Section 5.5: this admixture might have an influence on the determination of the reconstruction efficiency if the efficiency is different for these event types and the sample composition on MC differs from the one on data. For elastic events the situation is well-arranged since no ϕ mesons are created in this event type. The fraction of ϕ from any diffractive collision compared to the total number of ϕ is below 6% in the region of interest (Figure 6.2).

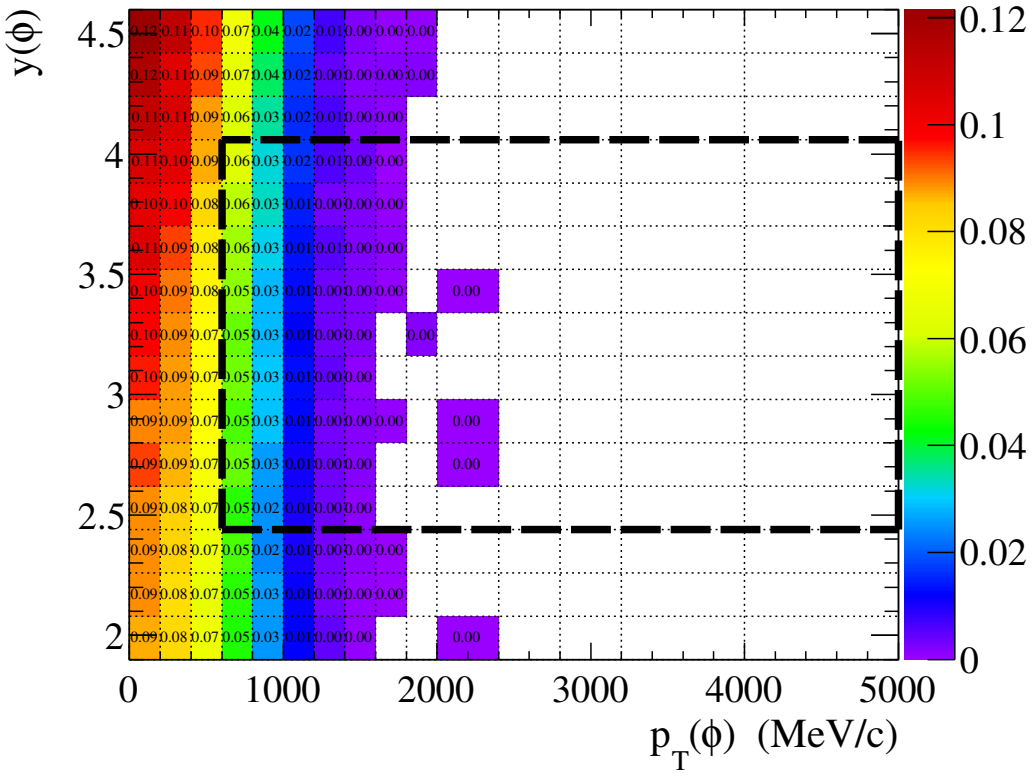

Figure 6.2.: Fraction of diffractive candidates in the total sample. The dashed box marks the analysis range $0.6 < p_T < 5.0\,\mathrm{GeV}/c$ and $2.44 < y < 4.06$.

The ratio of the reconstruction efficiency for candidates from diffractive events compared to the efficiency in non-diffractive events is analyzed on a simulated sample in three areas extending in the range $(2.44 < y < 4.06)$: $(0.6 < p_T < 1\,\mathrm{GeV}/c)$, $(1 < p_T < 1.4\,\mathrm{GeV}/c)$ and $(1.4 < p_T < 2\,\mathrm{GeV}/c)$. The ratio is $(94 \pm 2)\%$, $(93 \pm 5)\%$ and $(103 \pm 14)\%$ in these three bins. Due to the low number of diffractive candidates in the MC sample, the uncertainties cited above are relatively high, even though larger bin sizes are chosen here compared to the binning introduced in Section 5.3. Accounting for these uncertainties, the conservative estimate is made that the reconstruction efficiency for candidates in diffractive events is not lower than by a ratio of $r_e = 0.9$ compared to the one for non-diffractive candidates. Further, the assumption is made that the fraction of diffractive events is not more than a factor $f_m = 5$ higher on data than on MC. In another minimum bias study [13], the variation of the diffractive contribution is compared between different MC generators, which shows that the factor five chosen here is a conservative assumption.

In a similar approach as in the previous section, the total reconstruction efficiency ε_r is modeled

as

$$\varepsilon_r = \varepsilon_n[f_d\,(r_e - 1) + 1]\,,$$

where ε_n is the reconstruction efficiency for non-diffractive candidates and the fraction of diffractive candidates f_d is 6%, 3% and 1% in the three lowest p_T bins. The relative change of ε_r when replacing f_d by $f_d \cdot f_m$ is calculated as 2.4% / 1.2% / 0.4% in bins with p_T-index 4 / 5 / 6.

6.2.7. Angular effects

As opposed to the measurement of the J/ψ production cross-section, where the polarization has a deep impact on the results [11], no such effect is expected for ϕ: Since the $\phi \to K^+K^-$ decay takes place at the kinematic boundary, the two kaons have a very small angle to each other, irrespectively of the polarization. This assumption is proved by studies carried out within the author's working group [141], which show that first, the helicity angle distribution of the kaons is flat and second, the reconstruction efficiency in dependence of the helicity angle is flat, too.

6.3. Systematic uncertainties of the particle identification

The "nominal" cross-section result is the one determined with tag-and-probe, i.e. the effect of the correlations is not taken into account as a correction, but instead an uncertainty is assigned.

The full difference between this result and the one obtained when taking the correlations into account is given as systematic uncertainty related to the PID. It is determined based on the toy model presented in Section 5.9.1 using the correlation coefficients from truthmatched MC (Figure 5.7 on page 76). It has to be stressed that the actual PID efficiencies on MC are irrelevant for the final result because just the correlation coefficients are used to assess the systematic uncertainty. As these are a function of basic detector effects (see Section 5.9.2), the assumption that these are the same on data and MC is much safer than assuming that the actual PID efficiencies are correctly modeled.

Accounting for correlations, the fractions of candidates passing the AND (OR) cut is given by Equation 5.23 (5.24). Having measured N_{and} and N_{or} on data, the following integral equation can be solved for b_{wp} :

$$\frac{G_{and}(b_{wp},\rho)}{G_{or}(b_{wp},\rho)} = \frac{N_{\text{and}}}{N_{\text{or}}}\,. \tag{6.10}$$

The resulting OR cut efficiency, which takes into account the correlation ρ, follows as

$$G_{or}(b_{wp},\rho)\,. \tag{6.11}$$

The systematic error due to tag-and-probe disregarding the correlations is defined as

$$\sigma_{\text{PID, syst., rel.}} = \frac{\varepsilon_{\text{pid}} - G_{or}(b_{wp},\rho)}{\varepsilon_{\text{pid}}}\,, \tag{6.12}$$

where ε_{pid} is taken from Equation 5.17.

This quantity is intentionally signed: as obvious from Figure 5.9, the sign of the error made by tag-and-probe correlates with the sign of the correlation coefficient. In other words, the cross-section is overestimated in regions with positive correlations, and underestimated in regions with negative correlations.

Following this argumentation, the per-bin PID uncertainties are added with their sign when integrating over bins (for the total cross-section and projections).

The absolute value of the relative systematic uncertainty, as plotted in Figure 6.3, is influenced by both, correlation coefficients and signal yield. This is why the uncertainties are low – in the order of 1% – in the central region, where there is either a very high PID efficiency or low correlations. A critical region is the bottom left corner of the region of interest at low p_T and low y, since there are sizable correlations and a relative low efficiency. The largest systematic uncertainties are assigned in the region at large p_T and large y, however, this has a negligible impact on the total cross-section result because of a correspondingly low signal yield.

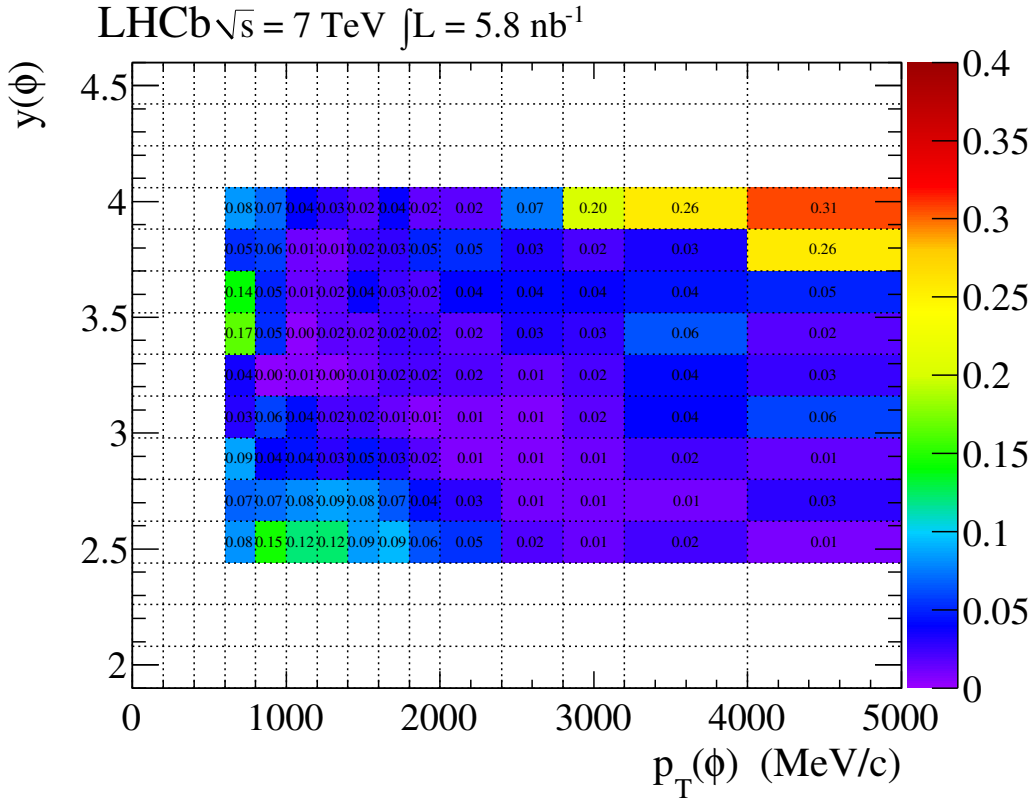

Figure 6.3.: Absolute value of the relative systematic uncertainty on the PID efficiency ε_{pid}.

6.4. Systematic uncertainties of the fit procedure

As a cross-check, the fit procedure is repeated with a different background shape, where the nominal exponential background shape is replaced by a first kind Chebyshev polynomial of the second degree:

$$\mathcal{B}_2(m) = 1 + c_1 \cdot m + c_2 \cdot \left(2m^2 - 1\right) \ . \tag{6.13}$$

Neither on data nor on MC does this change the integrated cross-section result by more than 1%.

Toy-MC pull studies have been carried out with both background parametrizations. The results for the nominal exponential background parametrization are plotted in Appendix D. The overall picture is compatible with Gaussian pull distributions with mean 0 and width 1.

The stability of the fit result against variations of the fit range size has been studied by redoing the fits on a varied range. Variations of the central value of the summed cross-section in the order of 5% (7%) are seen for MC using the exponential (polynomial) background shape and variations in the order of 1.6% (3.5%) are seen for data using the exponential (polynomial) background shape. The higher impact on the MC sample can be explained by the smaller sample size – speaking in terms of significances, data and MC behave alike. Since the exponential background shape is less affected by these variations, it is preferred and a 2% systematic uncertainty is assigned.

Finally, an uncertainty of 1% from describing the Gaussian width s on the tag- and the probe sample as a shared parameter has been derived in Section 5.8. In total, combining the uncertainties from the Gaussian width (1%), from the background shape (1%) and from the fit range (2%), a 3% uncertainty is assigned to the fit procedure.

6.5. Summary of systematics

The uncertainties analyzed on a bin-by-bin basis are shown in Figure 6.4. They are about 2% in the central region and rise to 6-7% at high p_T. There is a region with high uncertainties up to 30% in the top right corner of the region of interest (high p_T and high y), but due to the low number of candidates in that region it contributes little to the cross-section. At low p_T, in particular towards the left bottom corner of the analysis range, the uncertainties are generally in the order of 10%. There is a particular spot in the lowest p_T bins with $y \approx 3.5$ characterized by very high uncertainties. As discussed in Section 5.9.2, these are due to strong negative PID correlations in that region given by the geometric boundary of the RICH.

The uncertainty on the fraction of diffractive candidates is analyzed as function of p_T. It plays only a small role in the three lowest p_T slices, where the uncertainties are 2.4% / 1.2% / 0.4%.

The uncertainties on the global normalization scale are summarized in Table 6.1. They are clearly dominated by the uncertainty on the tracking efficiency.

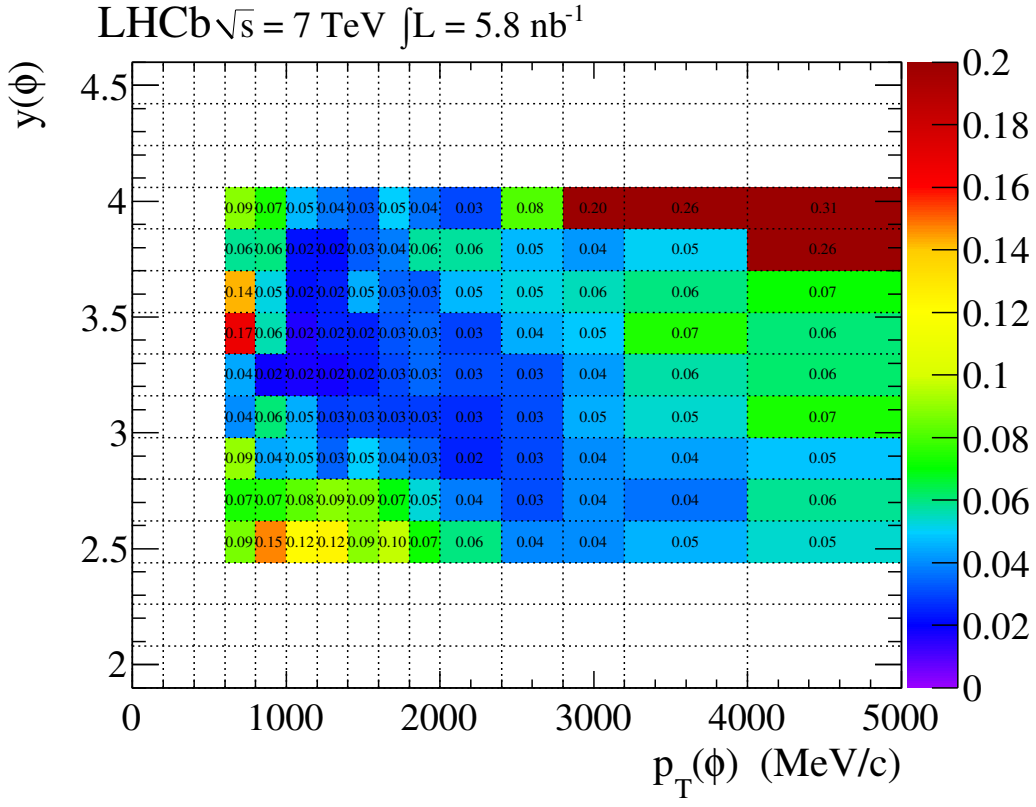

Figure 6.4.: Relative systematic uncertainties analyzed bin-by-bin – combined uncertainty on reconstruction efficiency and PID efficiency, introduced at the beginning of this Chapter on page 89.

Table 6.1.: Summary of relative uncertainties on the global normalization scale.

	(%)
Tracking	8
Luminosity (normalization)	3.5
Track Multiplicity	3
Fit systematics	3
Truth Matching	2
Clone Rate	2
Branching Ratio	1.2
Bin Migration	1
Material Interaction	1
total	10.3

– blank page –

CHAPTER 7

Results of the inclusive ϕ cross-section measurement

Next to the physical motivation of measuring the ϕ cross-section, the presented analysis is designed to put the RICH system under a real-life test. This is why this chapter first compares the PID efficiency on data and MC (Section 7.1) and then moves on to the cross-section results. While tables with the double-differential cross-sections are found in Appendix E, single-differential projections on the y and p_T axis are presented in Section 7.2. Then, cross-checks are presented which are designed as test-bench for the analysis procedure (Section 7.3). These include a comparison between the results from the two magnet polarities as well as a complete analysis on MC. This chapter closes up with a discussion of the results in the context of other minimum bias studies at the LHC (Section 7.4).

7.1. Particle identification efficiencies on data and in the simulation

The efficiency of the PID OR cut is generally lower on data than it is on MC (Figure 7.1). In the central region, with efficiencies around 100%, they are in rather good agreement, but in regions with generally lower efficiency – at lower transverse momenta and in the top right corner of the analysis range (high p_T and high y) – deviations are clearly visible. Here, the efficiency is up to 20 percent points lower on MC than on data, which is well above the systematic uncertainty (Figure 6.3) of the efficiency determination by the tag-and-probe approach.

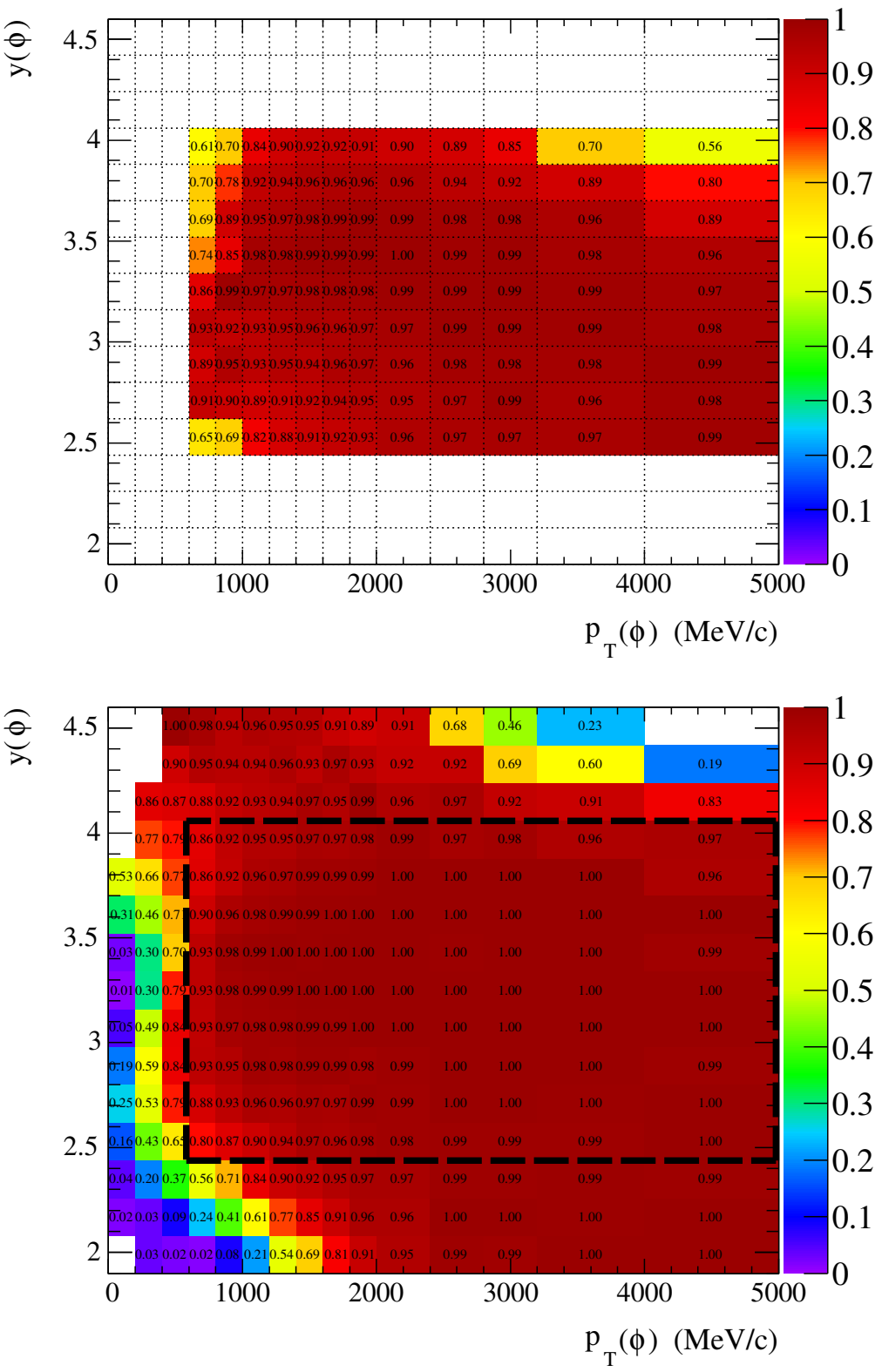

Figure 7.1.: PID efficiency ε_{pid} obtained using the tag-and-probe method on data (top) and from truthmatch on MC (bottom). On data, the presentation is constrained to the kinematic region of the analysis.

7.2. ϕ cross-section results

In the following, the cross-sections measured on data of the two magnet polarities is combined, where two methods are conceivable: a weighted average would minimize the statistical uncertainty whereas a non-weighted average is best to cancel potential systematical differences between the two data samples. However, since the sample size is as similar as stated in Section 5.5, these thoughts are more of a theoretical nature and the non-weighted average is calculated.

The global scale uncertainties and the uncertainty from diffractives (category 3 and 2 in the list at the opening of Chapter 6, page 89) are correlated between the two magnet polarities. Thus, the relative uncertainty of them is the same on the individual subsamples and on the average of these. Two contributions are, however, distinguished concerning the uncertainties in category 1 (page 89): the uncertainties due to MC sample size are uncorrelated between the two subsamples and added in square, where the PID related uncertainties are driven by the correlations between the PIDK values of the two kaons. As shown in Figure 5.7, these exhibit the same qualitative and quantitative behavior for magnet polarity "up" and "down", so that the systematic uncertainties on the two subsamples are correlated. The average is given as systematic on the combined cross-section numbers.

An integration of the cross-section over the whole region of interest $0.6 < p_T < 5.0\,\mathrm{GeV}/c$ and $2.44 < y < 4.06$, averaged over the two magnet polarities, yields the result

$$\sigma(pp \to \phi X) = 1758 \pm 19(\mathrm{stat})\,^{+43}_{-14}(\mathrm{syst}) \pm 182(\mathrm{syst})\,\mu\mathrm{b}\,, \tag{7.1}$$

where the first systematic uncertainty arises from the bin-dependent contribution, while the second one is the common systematic uncertainty. The combined differential cross-section values are given in Table E.1 to E.3 in Appendix E.

Projections on the y and p_T axes in the kinematic range $0.6 < p_T < 5.0\,\mathrm{GeV}/c$ and $2.44 < y < 4.06$ are shown in Figure 7.2. Event generator predictions of the cross-section, determined by Equation 5.6, are plotted along with the data. The simulations underestimate the measured ϕ production in the considered kinematic region by a factor 1.43 ± 0.15 (LHCb MC) and 2.06 ± 0.22 (Perugia 0). Additionally, the shape of the p_T spectrum and the slope in the y spectrum differ between the data and the simulation (see Fig. 7.2). Fitting a straight line $\frac{\mathrm{d}\sigma}{\mathrm{d}y} = a \cdot y + b$ to the y spectrum, the slope is $a = -44 \pm 27\,\mu\mathrm{b}$ on data, but $a = -181 \pm 2\,\mu\mathrm{b}$ for the default LHCb MC tuning and $a = -149 \pm 3\,\mu\mathrm{b}$ for the Perugia 0 tuning. Uncertainties given on a are statistical only. The mean p_T in the range $0.6 < p_T < 5.0\,\mathrm{GeV}/c$ is $1.24 \pm 0.01\,\mathrm{GeV}/c$ (data, stat. error only), $1.077\,\mathrm{GeV}/c$ (LHCb MC) and $1.238\,\mathrm{GeV}/c$ (Perugia 0 MC).

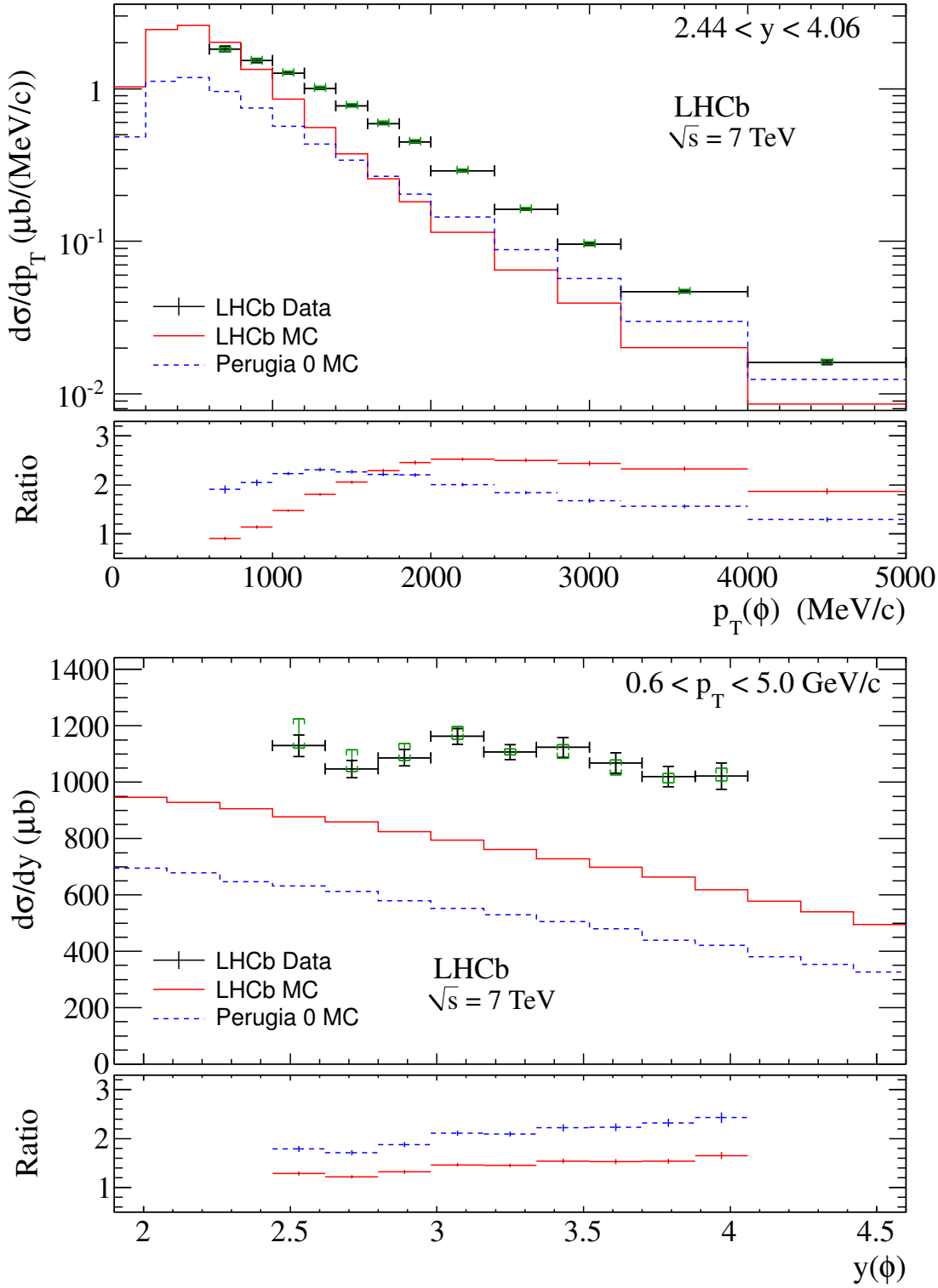

Figure 7.2.: Inclusive cross-section $\sigma(pp \to \phi X)$ as a function of p_T (top) and y (bottom) measured in data (black), combining both magnet polarities. It is compared to the LHCb MC prediction (red) and Perugia 0 PYTHIA tuning (blue) based on counting the number of candidates. The data points are plotted with their statistical uncertainty. The bin-dependent systematic uncertainty is given by the green braces, while the overall scale uncertainty from Table 6.1 is not plotted.

7.3. Cross-checks of the ϕ cross-section measurement

7.3.1. Validation on Monte Carlo

As validation, the complete analysis chain, i.e. including the PID efficiency determination from "data" is run on a sample of simulated candidates. This sample is similar to the "real data" in that it went through the full detector simulation. The integrated luminosity for that sample is calculated by multiplying the total number of pp collisions with the inverse of the total pp cross-section used in the MC production.

In Figure 7.3, the analysis output is compared to the a priori knowledge of the simulated cross-section from Equation 5.6. The agreement between the analysis result with the expectation is well within the statistical and systematic uncertainties. The systematics are mainly given by the PID related systematics, since these are present on MC, too. Systematics which only occur on data, like luminosity normalization or tracking uncertainty do not go in here, since they do not affect the MC analysis.

7.3.2. Comparison of analysis on both magnet polarities

As outlined in Section 5.1, the analysis is run separately for the two magnet polarities before the results are combined. The individual integrated cross-sections determined as in Section 7.2 are

$$\sigma'(pp \to \phi X) = \begin{cases} 1753 \pm 25(\text{stat})^{+45}_{-13}(\text{syst}) \pm 181(\text{syst})\,\mu\text{b} & \text{magnet polarity "up"} \\ 1763 \pm 28(\text{stat})^{+42}_{-14}(\text{syst}) \pm 182(\text{syst})\,\mu\text{b} & \text{magnet polarity "down"} \end{cases} \tag{7.2}$$

for the magnet "up" and the magnet "down" sample. This very good agreement is also seen in a comparison of the projections in Figure 7.4. Only statistical uncertainties are shown there since the dominant systematics affect both samples alike and thus cancel in the comparison.

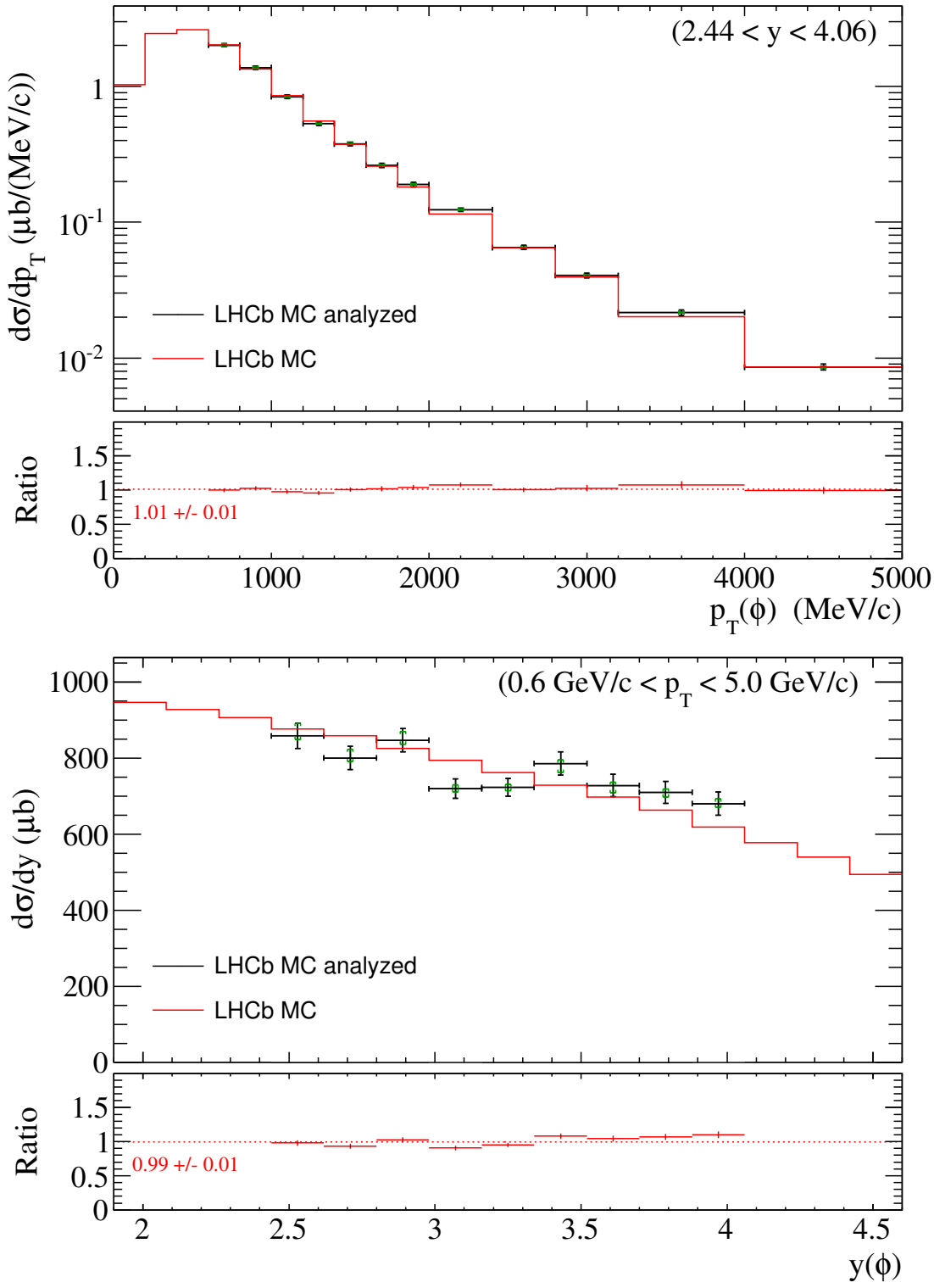

Figure 7.3.: Cross-section measured on the LHCb MC sample using the full analysis chain (black) and calculated on LHCb MC without detector simulation (red).

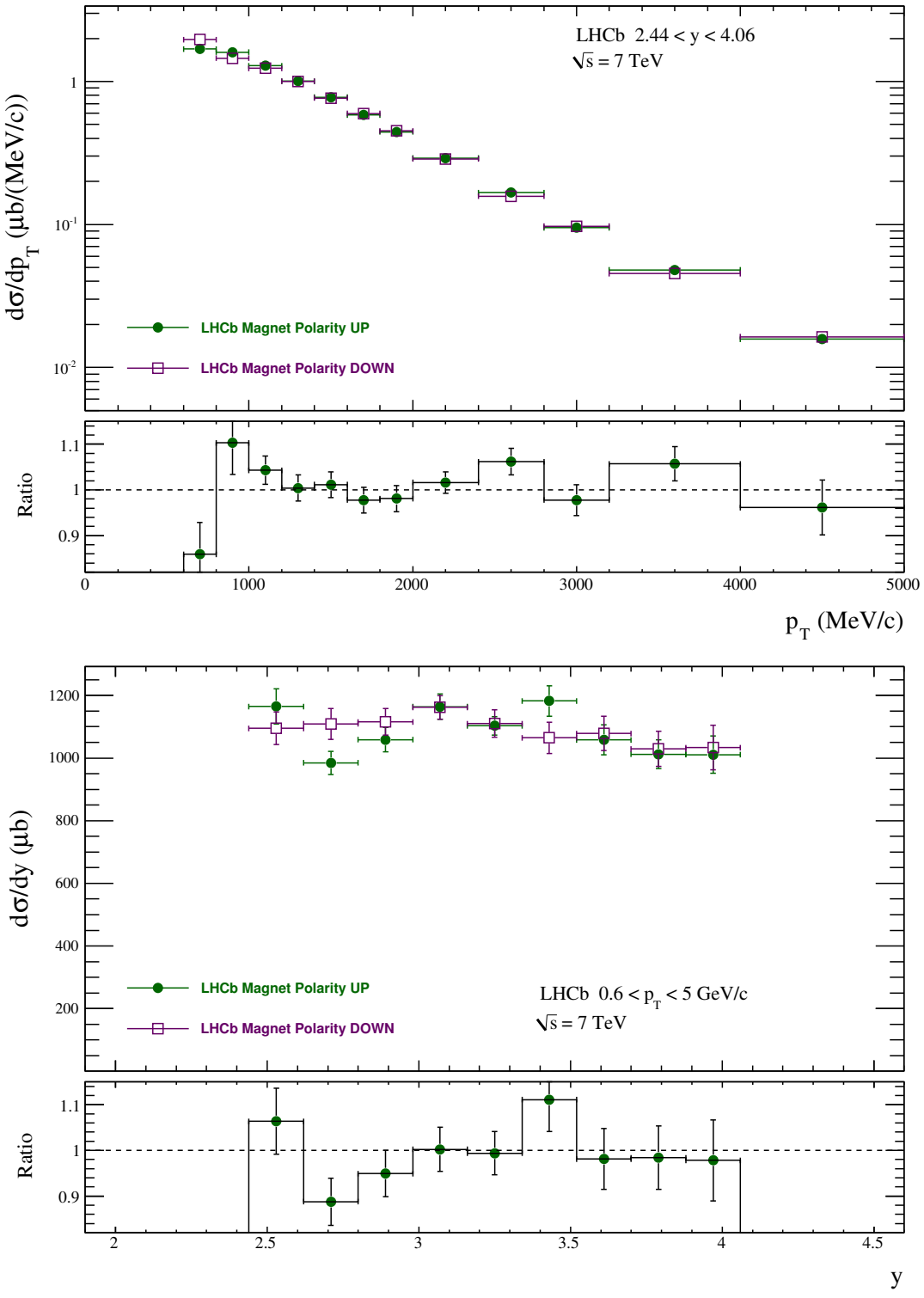

Figure 7.4.: Cross-section projections measured in the magnet "up" (green) and the magnet "down" (magenta) sample. The error bars include only the statistical uncertainties.

7.4. Discussion of ϕ cross-section result

The result presented in Section 7.2 reveals an underestimation of the ϕ production cross-section, in particular at higher transverse momenta. In view of the descriptive particle production model described in Section 1.4, there is no way of giving a simple theoretically founded answer on why the results presented in this chapter differ from the predictions. There are several parameters in PYTHIA some of which have a main effect on the production ratio of s to u quarks, baryons to mesons and vector to scalar particles. Furthermore, there are parameters for the spin-$3/2$-baryon to spin-$1/2$-baryon ratio and the strange baryon suppression [156]. While ϕ production might be enhanced by tuning the first parameter (s/u ratio), there is no such simple handle on the transverse momentum spectrum [157].

Operating on a large quantity of correlated parameters, tuning Monte Carlo generators adopts a global approach, based on a as many measurements as possible, for which the Perugia tunes mentioned in Section 1.4 are an example. Automated tools are developed to support this effort [158]. In other words, the measurement of the inclusive ϕ production cross-section is one important building block in a set of several measurements targeted at understanding the event structure in pp collisions under LHC conditions. Strangeness production is a crucial field of study where discrepancies between data and PYTHIA simulations were found by several LHC experiments.

CMS compared measurements of K^0_S, Λ and Ξ^- production [159] with PYTHIA predictions in the central rapidity range $y < 2$ and the transverse momentum range $0 < p_T < 10\,\text{GeV}/c$. At $\sqrt{s} = 900\,\text{GeV}$, best agreement is found for K^0_S, where the production is 20% above the (PYTHIA Perugia 0) expectation, whereas Λ and Ξ^- production are underestimated by a factor of 2. Measurements of K^0_S, Λ and Ξ^- production by ALICE [18] in the central range $y < 0.75$ observe a similar underestimation of the K^0_S and Ξ^- production rate as CMS, whereas the Λ production is found to be underestimated by a factor of 5. Furthermore, ALICE determined the ϕ production at $\sqrt{s} = 900\,\text{GeV}$, which was found to exceed the prediction by PYTHIA in Perugia 0 tune by a factor of 2. For most of the ALICE measurements discussed above, the agreement is better at lower transverse momenta. LHCb measured [10] the production cross-section of K^0_S in the forward region $2.5 < y < 4.0$, where the normalization was in agreement with predictions, but the p_T spectrum was found to be slightly harder on data than on MC. At $\sqrt{s} = 7\,\text{TeV}$, the K^0_S production, measured by CMS [159] is 40% above the expectation and Λ and Ξ^- production are underestimated by a factor $2-3$.

In conclusion, the measurement of the ϕ production cross-section presented in this thesis is in line with other analyses of strangeness production at the LHC in the sense that an underestimation of strange particle production, in particular at higher transverse momenta, is a general characteristic of PYTHIA predictions in Perugia 0 tune compared to LHC data.

The strange baryon-meson ratio $\overline{\Lambda}/K^0_S$ was measured by CMS [159] and LHCb [13] at $\sqrt{s} = 900\,\text{GeV}$ and $7\,\text{TeV}$, in the rapidity range $y < 2$ (CMS) and $2 < y < 4$ (LHCb). Both experiments determine this ratio to be 50% higher on data compared to PYTHIA in Perugia 0 tune. An enhanced strangeness production in pp collisions could be a hint for collective effects [159], however the fact that the $\overline{\Lambda}/K^0_S$ ratio does not rise with center-of-mass energy suggests that a more likely origin for the underestimation of ϕ production in PYTHIA is a too small strange quark creation probability in the Lund model's color strings [159], which can be tested in future simulator tunes.

Conclusions

The Large Hadron Collider started data taking at an unprecedented center-of-mass energy of $\sqrt{s} = 7\,\text{TeV}$ last year. Pioneering the analysis of this data is a challenge that emerges from the necessity to gain understanding of both, the detector and the data that is being recorded. On the one hand, the performance of the various detector elements has to be analyzed and carefully compared to simulation results; On the other hand, the description of the pp interactions by event generators needs to be validated.

A measurement of the inclusive ϕ production cross-section was presented as an important probe of strangeness production. A pre-selection for ϕ mesons was introduced in the LHCb stripping framework, which is used by the inclusive ϕ cross-section measurement and further LHCb analyses. The inclusive ϕ analysis determined the reconstruction efficiency from Monte Carlo generated samples, whereas the efficiency related to the particle identification was determined on data. Several studies of the performance of the PID system were presented, where particular attention was devoted to the degree of statistical independence of the PID system's response for the two bachelor kaons. Since the inclusive ϕ cross-section measurement is one of the earliest analyses on LHCb data, intensive research on systematic effects was carried out related to both, reconstruction and particle identification. The analysis successfully went through the internal and external review process and was published in Physics Letters B [143] as the 9$^{\text{th}}$ publication on LHCb data.

The differential ϕ production cross-section was measured as a function of the ϕ transverse momentum p_T and rapidity y in the region $0.6 < p_T < 5.0\,\text{GeV}/c$ and $2.44 < y < 4.06$. The total ϕ production cross-section in this range is $\sigma(pp \to \phi X) = 1758 \pm 19(\text{stat})\,^{+43}_{-14}(\text{syst}) \pm 182(\text{syst})\,\mu\text{b}$, where the first systematic uncertainty depends on the p_T and y region and the second is related to the overall scale. Predictions based on the PYTHIA 6.4 generator underestimate the cross-section. Future event generator tunings will incorporate LHCb's minimum bias measurements like the inclusive ϕ cross-section determination and hereby allow for an even improved description of proton-proton collisions.

The analysis of ϕ production and the acquired better understanding of the LHCb particle identification system is of utmost importance for LHCb's studies of *CP* violation in B meson decays where ϕ mesons are present in the final state. One example for these is the $B_s^0 \to \phi\phi$ decay, where *CP* violation is predicted to vanish by the Standard Model, while physics beyond the Standard Model could introduce a non-vanishing *CP* violating phase. A pre-selection for this decay channel was implemented in LHCb's stripping framework as a premise for offline studies, on which also LHCb's recent triple product asymmetry measurement [7] bases on. The $B_s^0 \to \phi\phi$ signal was then extracted from early LHCb data and this analysis suggests a per-year expectation ($2\,\text{fb}^{-1}$) of 2130 ± 471 signal candidates. A statistical uncertainty of 0.23 ± 0.04 on the *CP* violating phase ϕ_s based on a data set corresponding to one year of data taking is derived from this signal yield and from Monte Carlo studies.

– blank page –

Acknowledgments

Ich danke Prof. Dr. Bernhard Spaan, der als Betreuer dieser Arbeit immer ansprechbar war, und Priv.-Doz. Dr. Reiner Klingenberg, der sich als Korreferent zur Verfügung gestellt hat.

Mein Dank gilt allen, die zum Gelingen der Inclusive-ϕ-Analyse beigetragen haben, wobei folgende Personen besonders hervorzuheben sind: Tobias Brambach hat im Verlaufe der Analyse mit als erster in das Thema „PID Korrelationen“ hinein geschaut und so manche der Probleme aufgezeigt, die in dieser Arbeit gelöst wurden. Florian Kruse und Julian Wishahi haben sehr hilfreiche Tupelwriter-Algorithmen in DaVinci implementiert. Michael Kaballo hat Tobiasens Ideen zur Analyse der Clone-Kandidaten umgesetzt sowie zur Umsetzung der Studien in Abschnitt 6.2.4 mit beigetragen. Auf Dr. Jesko Merkel, schließlich, geht nicht nur das Design von Abbildung 7.4 zurück, sondern auch Unterstützung im langwierigen Review-Prozess. Dr. Andrew Powell von der University of Oxford danke ich für die erfolgreiche Zusammenarbeit bei der Spezifikation der verschiedenen Inclusive-ϕ-Stripping-Lines.

Für hervorragende Zusammenarbeit bei der Inbetriebnahme und dem Betrieb des LHCb Beam Conditions Monitors danke ich Dr. Richard Jacobsson und Rainer Schwemmer vom CERN und der LHCb-Online-Gruppe. Gewisse nächtliche Telefonate werden mir noch lange in Erinnerung bleiben.

Dem Administratoren-Team des Computing Clusters PhiDo, insbesondere Dr. Carsten Raas, Danny van Dyk, Dr. Klaus Wacker und Matthias Domke, danke ich für die Unterstützung bei der von mir übernommenen Installation und Pflege der LHCb-Software. Besondere Anerkennung gebührt ihrem stetigen Bemühen, den Lieferanten dieses neuen Clusters geduldig zu erinnern, dass man die Rechner nicht nur zum Anschauen gekauft habe.

Ein großer Dank gebührt noch jenen, die diese Arbeit Probe gelesen haben. Tobias Brambach, Dr. Jesko Merkel, Stefan Schacht und Julian Wishahi haben durch ihre Kommentare sicherlich zu deren Perfektionierung beigetragen.

Schließlich danke ich meinen Eltern, die mir das Studium ermöglicht haben.

– blank page –

Appendix A

$B_s^0 \to \phi\phi$: Efficiencies on MC10

Plots of the efficiencies of the requirements on the discriminating variables used in the $B_s^0 \to \phi\phi$ channel are shown in this section for signal, $b\bar{b}$- and minimum bias- MC. In Figure A.1 to A.2 the only requirement on the kaons is PIDK > 5, whereas in Figure A.3 to A.5, all kaon related constraints from Table 3.2 are already applied.

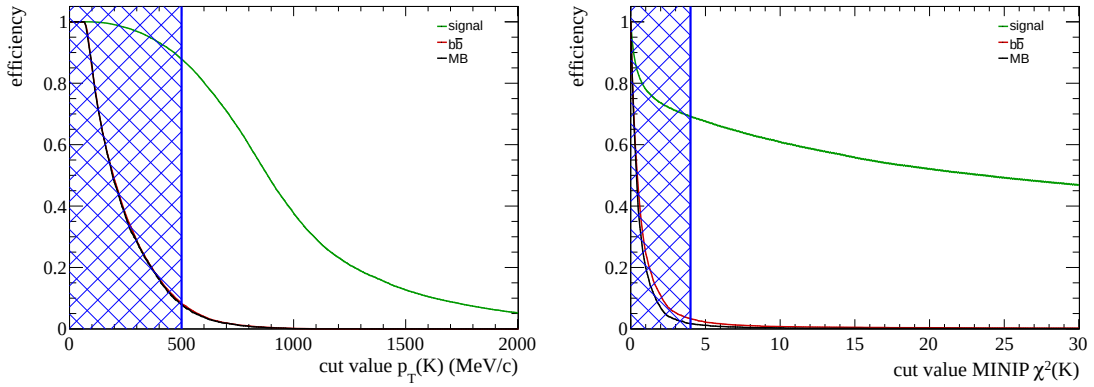

Figure A.1.: Selection efficiency of requirement on minimum kaon transverse momentum (left) and minimum kaon impact parameter significance (right) on MC10 for signal-, $b\bar{b}$- and minimum-bias- sample. The region excluded by the cuts in Table 3.2 is hatched. In both plots, the denominator is the number of all candidates that can be combined on that sample and where all kaons fulfil PIDK > -5.

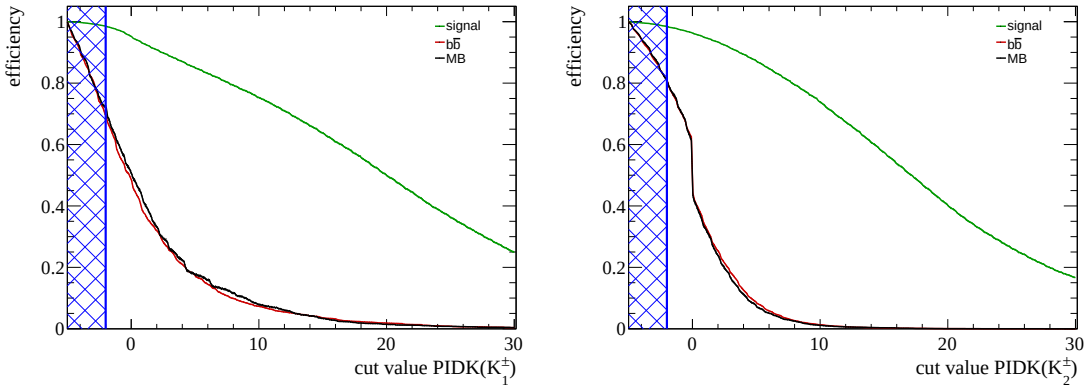

Figure A.2.: Selection efficiency of requirement on the PIDK of kaons originating from the ϕ with the lower (left) and the higher (right) transverse momentum (see caption of Figure A.1 for details).

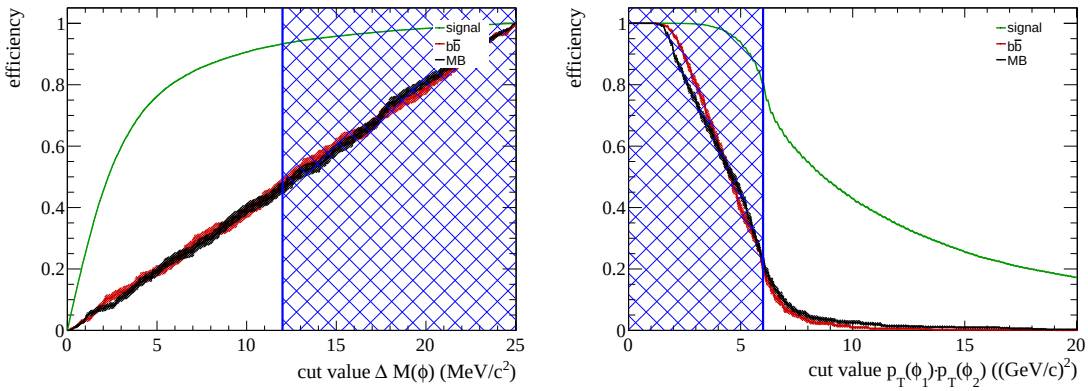

Figure A.3.: Selection efficiency of requirement on the maximal difference of the ϕ candidate mass from the nominal ϕ mass (left) and on the product of ϕ transverse momenta (right) on MC10 for signal-, $b\bar{b}$- and minimum-bias- sample. The region excluded by the cuts in Table 3.2 is hatched. In both plots, the cuts on kaon properties, shown in Figure A.1 to A.2 are already applied.

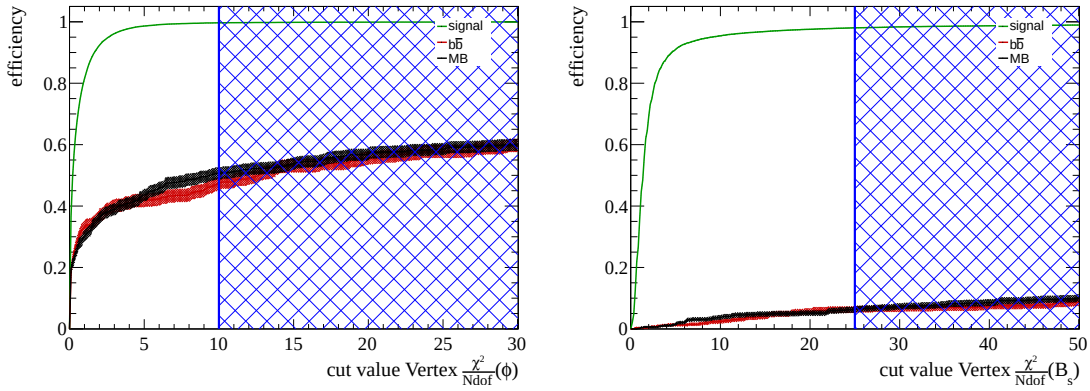

Figure A.4.: Selection efficiency of requirement on the vertex quality χ^2/Ndof of the ϕ (left) and the B_s^0 (right) candidates (see caption of Figure A.3 for details).

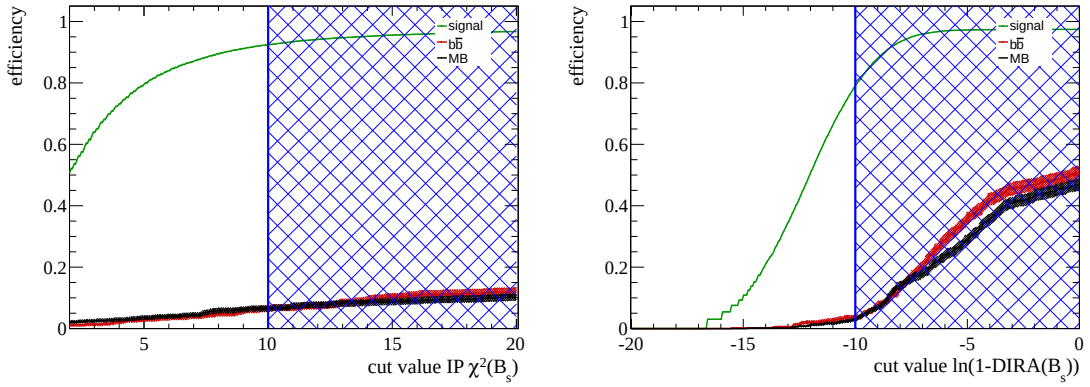

Figure A.5.: Selection efficiency of requirement on B_s^0 impact parameter significance (left) and natural logarithm of the difference between 1 and the B_s^0 direction angle (right) (see caption of Figure A.3 for details).

– blank page –

Appendix B

$B_s^0 \to \phi\phi$: Observables and parameters in Maximum-Likelihood fit

Table B.1.: Observables x_i in likelihood fit.

symbol	unit	quantity
m	MeV/c^2	B_s^0 candidate mass
t	ps	B_s^0 candidate lifetime
φ	rad	plane angle (see Figure 4.2)
$\cos(\theta_1)$	1	cosine of helicity angle (see Figure 4.2)
$\cos(\theta_2)$	1	cosine of helicity angle (see Figure 4.2)
ξ	1	tagging decision, see Equation 2.5
D	1	estimated tagging dilution

Table B.2.: Parameters λ in likelihood fit.

(a) CP and mixing parameters

symbol	unit	quantity
Γ	ps^{-1}	inverse B_s^0 meson lifetime
$\Delta\Gamma$	ps^{-1}	difference of inverse lifetimes of B_L and B_H
$\lvert A_0\rvert^2$	1	transversity amplitude
$\lvert A_\perp\rvert^2$	1	transversity amplitude
$\delta_\perp$	rad	phase of transversity amplitude
$\delta_\parallel$	rad	phase of transversity amplitude
Δm	ps^{-1}	mass difference between B_H and B_L
ϕ_s	rad	*CP* violating phase

(b) Mass parameters

symbol	unit	quantity
$m_{B_s^0}$	MeV/c^2	estimated B_s^0 meson mass
$\sigma_{m,1}$	MeV/c^2	B_s^0 mass width 1
$\sigma_{m,2}$	MeV/c^2	quotient of B_s^0 mass widths
$f_{\sigma_{m,1}}$	1	fraction in B_s^0 mass double Gaussian
$\alpha_{m,\mathrm{Pr}}$	$(\mathrm{MeV}/c^2)^{-1}$	prompt background, mass distribution slope
$\alpha_{m,\mathrm{LL}}$	$(\mathrm{MeV}/c^2)^{-1}$	long-lived background, mass distribution slope

(c) Lifetime and resolution parameters

symbol	unit	quantity
$\sigma_{\mathrm{sig},1}$	ps	signal, proper time resolution 1
$\sigma_{\mathrm{sig},2}$	ps	signal, proper time resolution 2
$f_{\sigma_{\mathrm{sig},1}}$	1	signal, fraction in double Gaussian describing the proper time resolution
σ_{Pr}	ps	prompt background width
τ_{LL}	ps	long-lived background lifetime
$\sigma_{\mathrm{LL},1}$	ps	long-lived background, proper time resolution 1
$\sigma_{\mathrm{LL},2}$	ps	long-lived background, proper time resolution 2
$f_{\sigma_{\mathrm{LL},1}}$	1	long-lived background, fraction in double Gaussian describing the proper time resolution

(d) Tagging parameters

symbol	unit	quantity
$\varepsilon_{\mathrm{tag}}$	1	signal tagging efficiency
$\varepsilon_{\mathrm{tag}}^{\mathrm{LL}}$	1	long-lived background tagging efficiency
$\varepsilon_{\mathrm{tag}}^{\mathrm{Pr}}$	1	prompt background tagging efficiency

APPENDIX C

Inclusive ϕ: Fit results

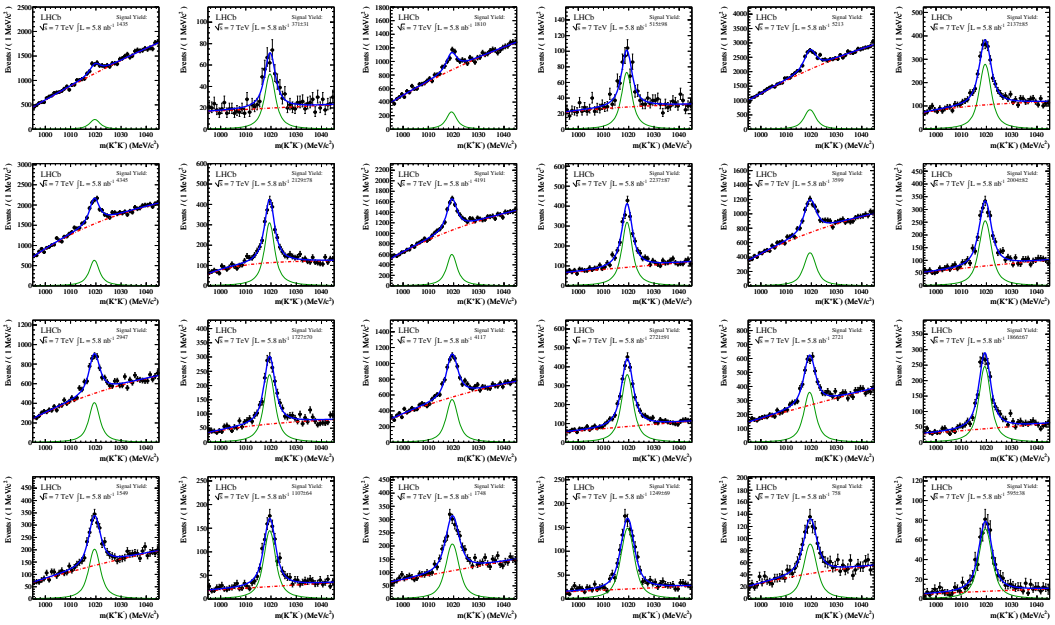

Figure C.1.: Data histograms and fitted function in the bins with y-index 4. From left to right, from top to bottom, the p_T bins (index 4...15) in ascending order. The plots are shown in pairs: (tag sample, probe sample).

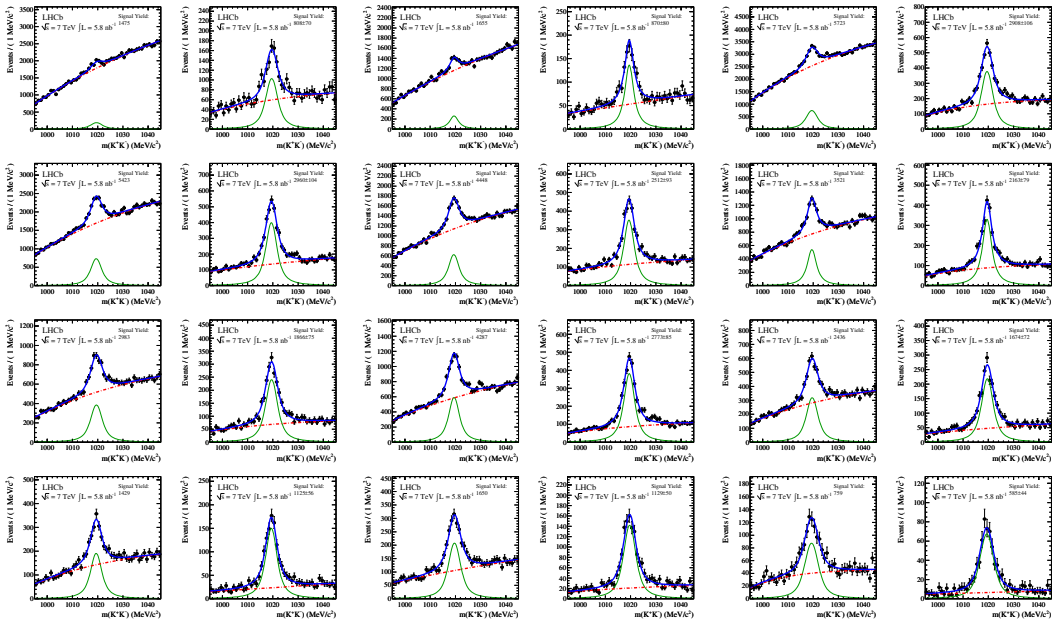

Figure C.2.: Data histograms and fitted function in the bins with y-index 5. From left to right, from top to bottom, the p_T bins (index 4...15) in ascending order. The plots are shown in pairs: (tag sample, probe sample).

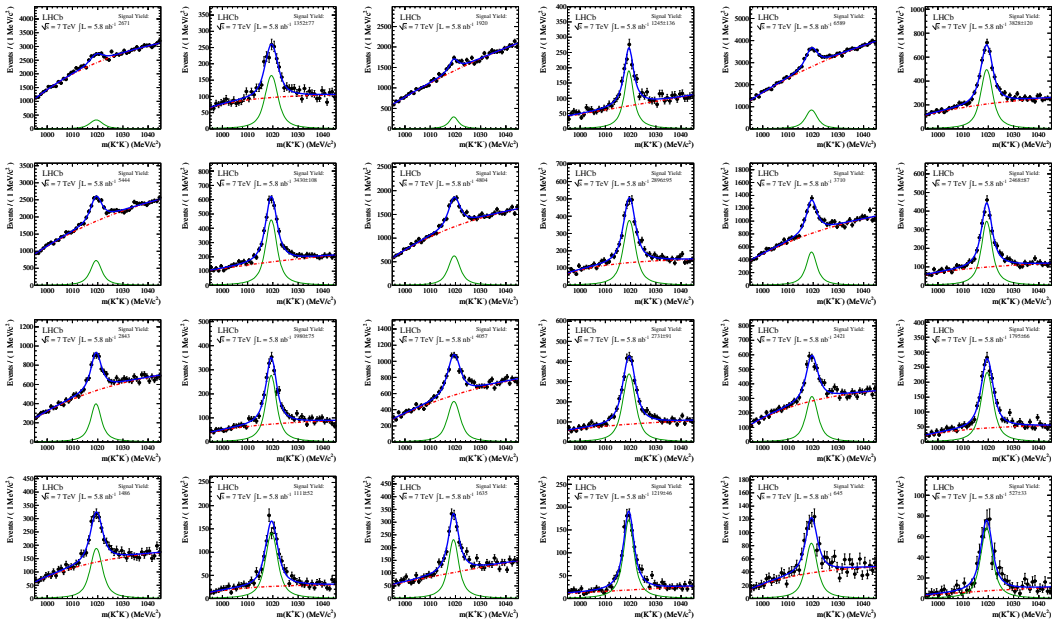

Figure C.3.: Data histograms and fitted function in the bins with y-index 6. From left to right, from top to bottom, the p_T bins (index 4...15) in ascending order. The plots are shown in pairs: (tag sample, probe sample).

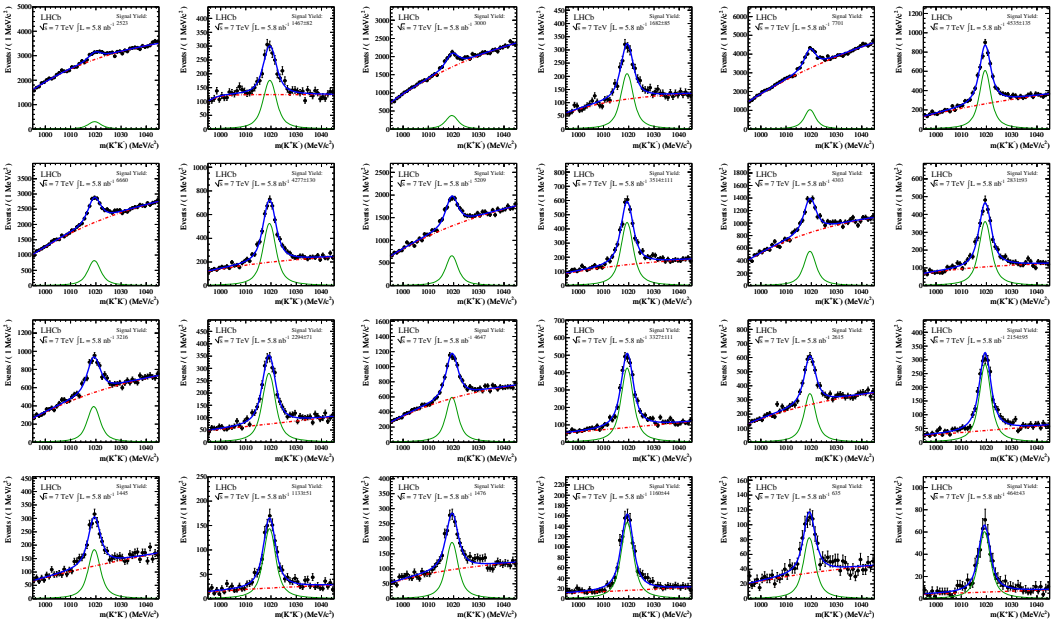

Figure C.4.: Data histograms and fitted function in the bins with y-index 7. From left to right, from top to bottom, the p_T bins (index 4...15) in ascending order. The plots are shown in pairs: (tag sample, probe sample).

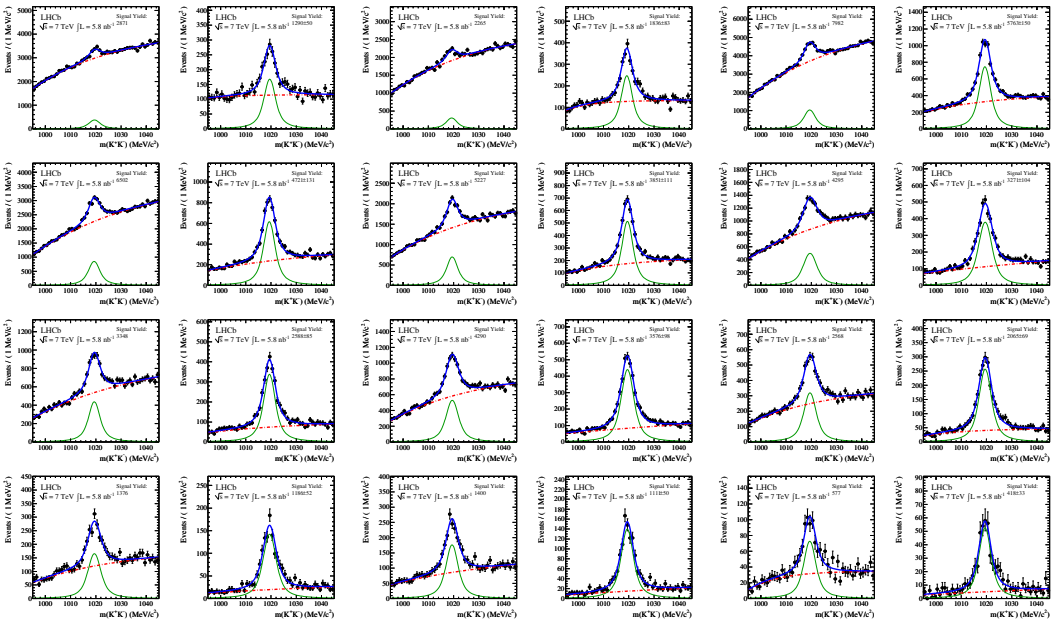

Figure C.5.: Data histograms and fitted function in the bins with y-index 8. From left to right, from top to bottom, the p_T bins (index 4...15) in ascending order. The plots are shown in pairs: (tag sample, probe sample).

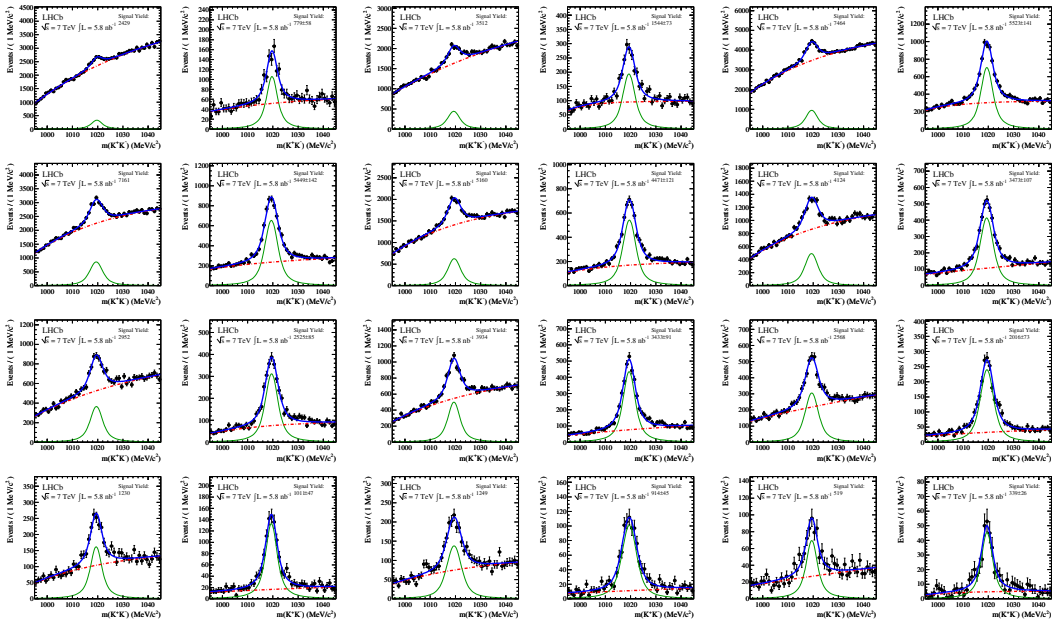

Figure C.6.: Data histograms and fitted function in the bins with y-index 9. From left to right, from top to bottom, the p_T bins (index 4...15) in ascending order. The plots are shown in pairs: (tag sample, probe sample).

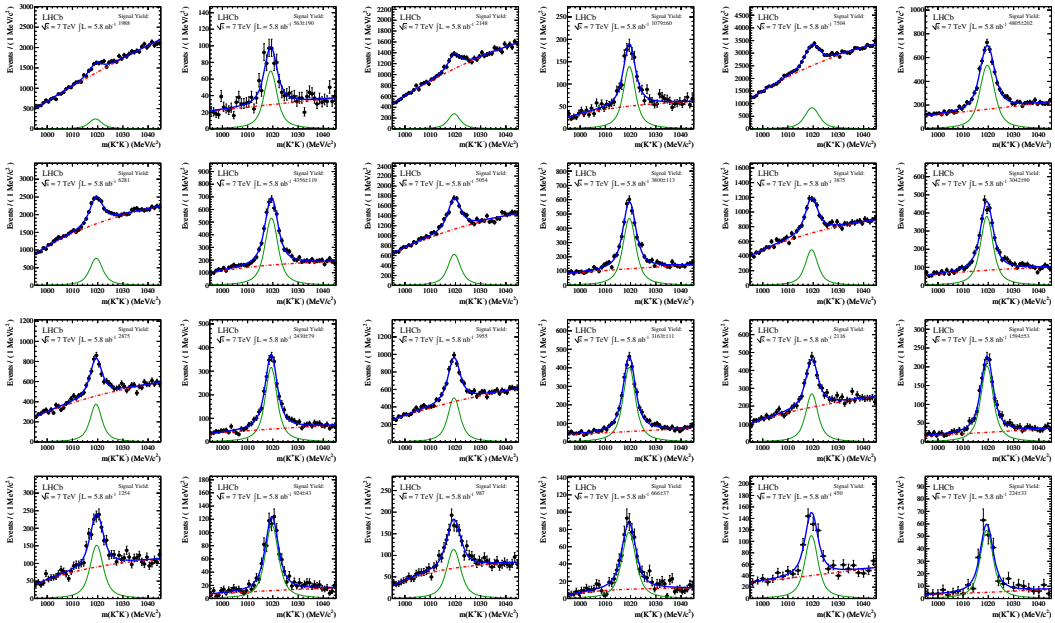

Figure C.7.: Data histograms and fitted function in the bins with y-index 10. From left to right, from top to bottom, the p_T bins (index 4...15) in ascending order. The plots are shown in pairs: (tag sample, probe sample).

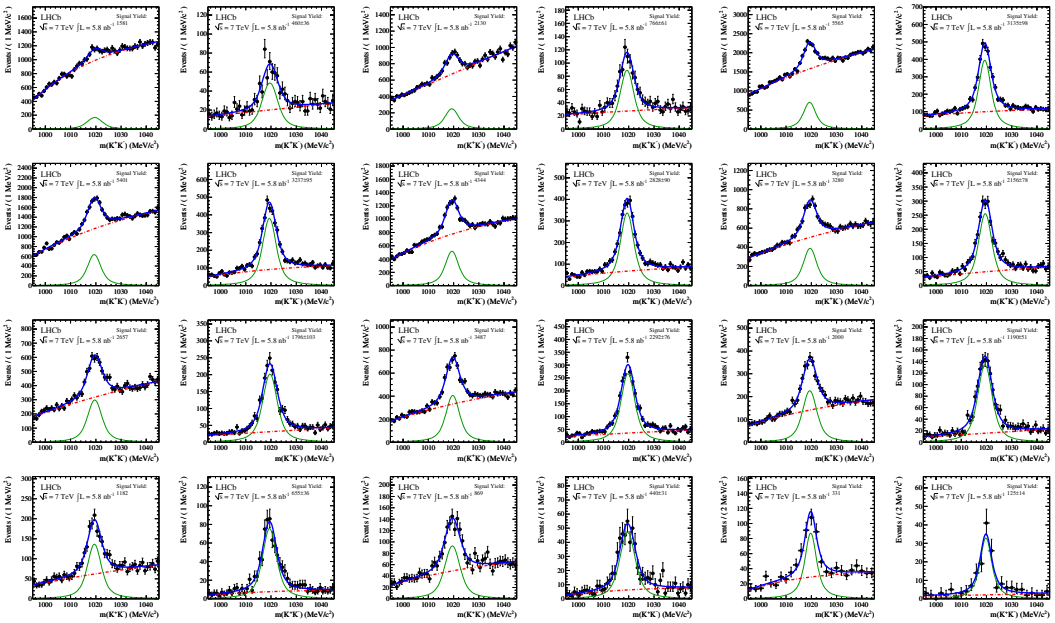

Figure C.8.: Data histograms and fitted function in the bins with y-index 11. From left to right, from top to bottom, the p_T bins (index 4...15) in ascending order. The plots are shown in pairs: (tag sample, probe sample).

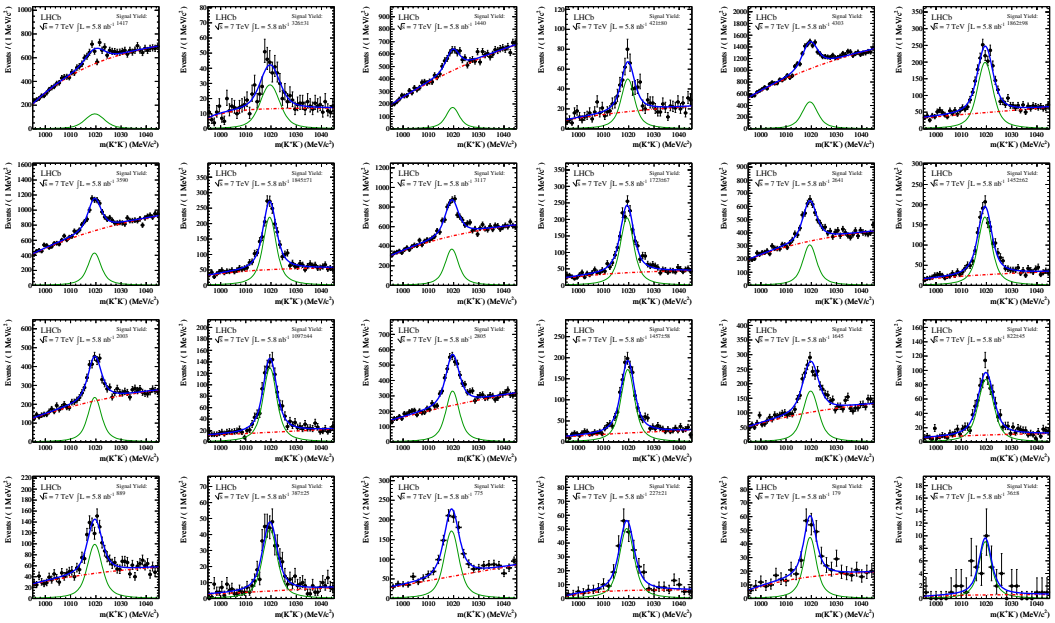

Figure C.9.: Data histograms and fitted function in the bins with y-index 12. From left to right, from top to bottom, the p_T bins (index 4...15) in ascending order. The plots are shown in pairs: (tag sample, probe sample).

– blank page –

APPENDIX D

Inclusive ϕ: Pull study results

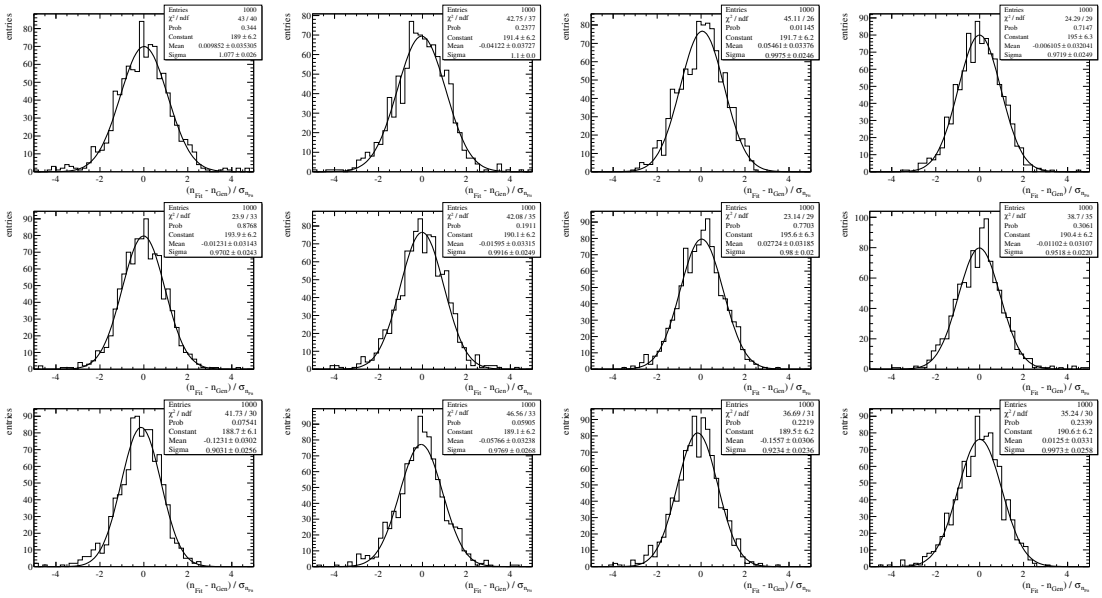

Figure D.1.: Fit pull for bins with y-index 4. From left to right, from top to bottom, the p_T bins (4...15) in ascending order.

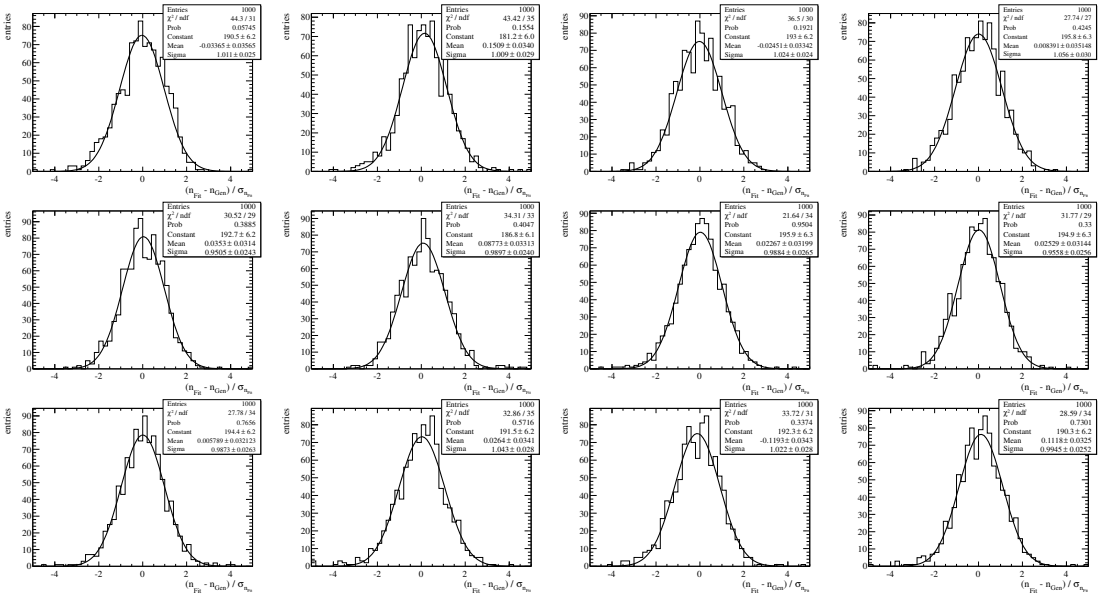

Figure D.2.: Fit pull for bins with y-index 5. From left to right, from top to bottom, the p_T bins (4...15) in ascending order.

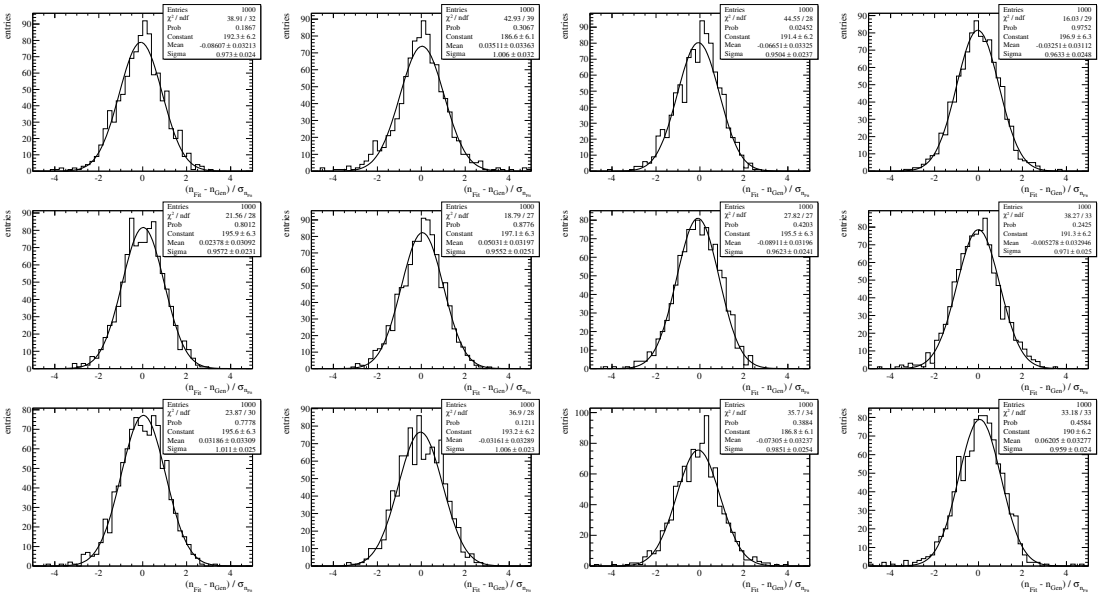

Figure D.3.: Fit pull for bins with y-index 6. From left to right, from top to bottom, the p_T bins (4...15) in ascending order.

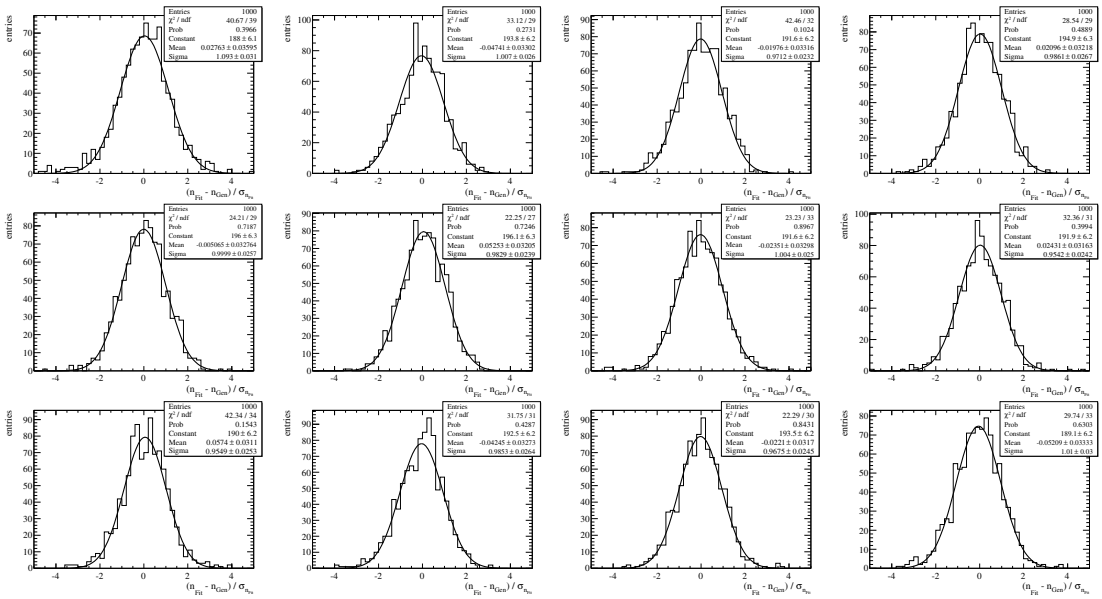

Figure D.4.: Fit pull for bins with y-index 7. From left to right, from top to bottom, the p_T bins (4...15) in ascending order.

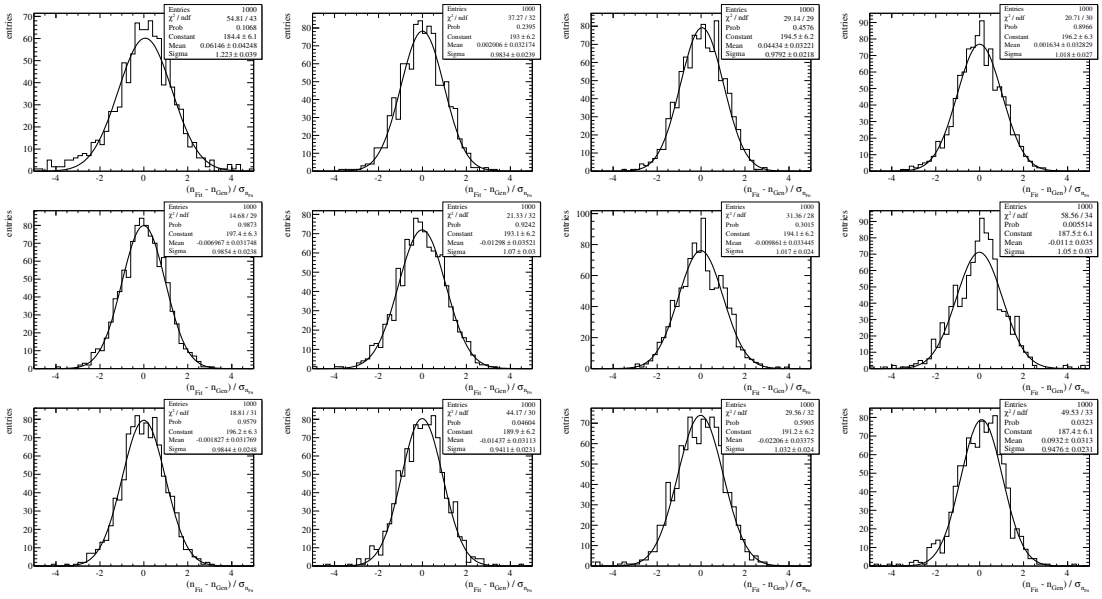

Figure D.5.: Fit pull for bins with y-index 8. From left to right, from top to bottom, the p_T bins (4...15) in ascending order.

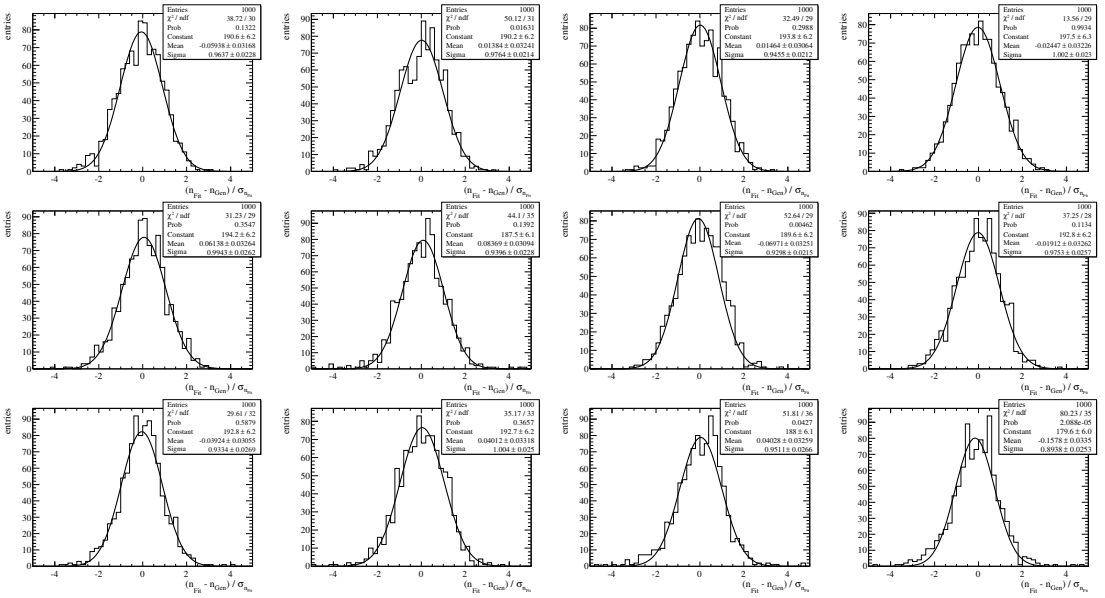

Figure D.6.: Fit pull for bins with y-index 9. From left to right, from top to bottom, the p_T bins (4...15) in ascending order.

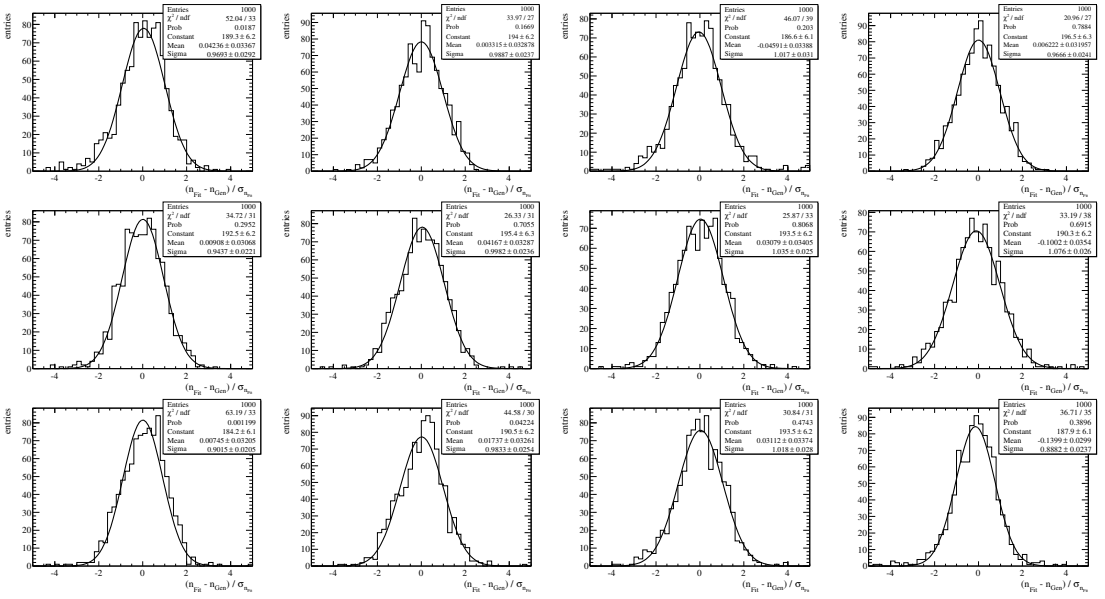

Figure D.7.: Fit pull for bins with y-index 10. From left to right, from top to bottom, the p_T bins (4...15) in ascending order.

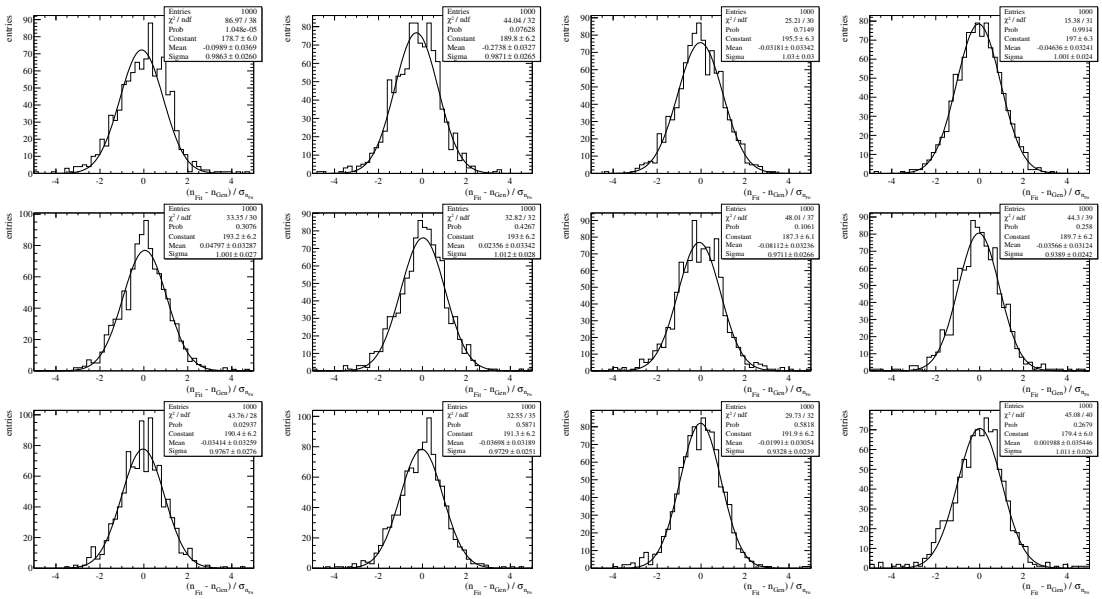

Figure D.8.: Fit pull for bins with y-index 11. From left to right, from top to bottom, the p_T bins (4...15) in ascending order.

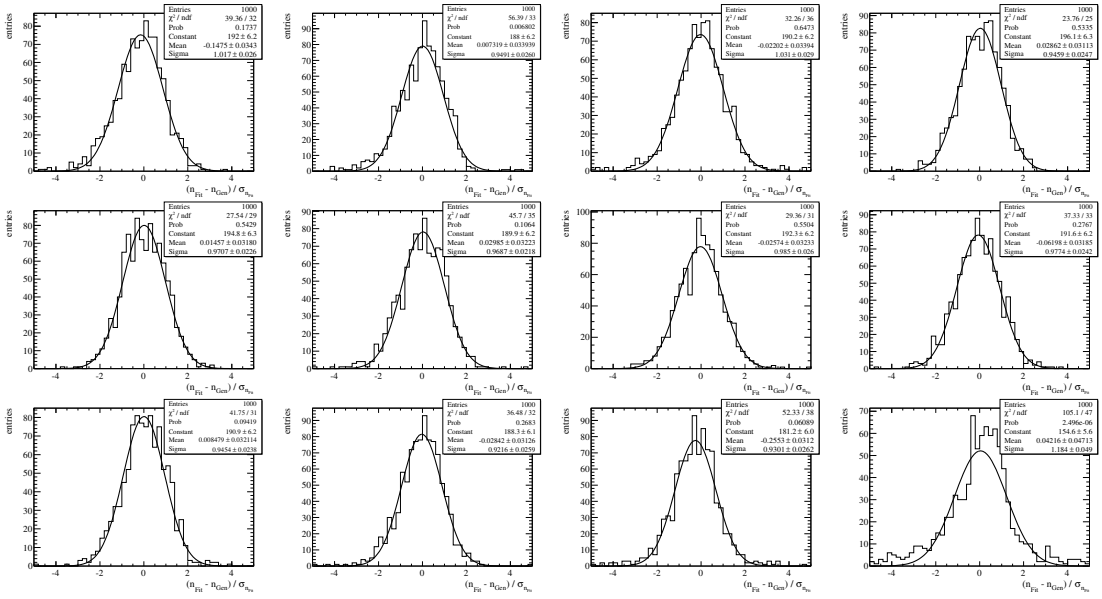

Figure D.9.: Fit pull for bins with y-index 12. From left to right, from top to bottom, the p_T bins (4...15) in ascending order.

– blank page –

APPENDIX E

Inclusive ϕ: Differential cross-sections

Table E.1.: Binned differential cross-section, in $\mu b/(MeV/c)$, as function of p_T (GeV/c) and y. The statistical and the bin-dependent systematic uncertainties are quoted. There is an additional bin-independent uncertainty of 10% related to the normalization (Table 6.1).

p_T / y	2.44-2.62	2.62-2.80	2.80-2.98
0.6-0.8	$1.001 \pm 0.140^{+0.076}_{-0.026}$	$0.853 \pm 0.114^{+0.081}_{-0.022}$	$1.069 \pm 0.108^{+0.093}_{-0.027}$
0.8-1.0	$0.959 \pm 0.112^{+0.129}_{-0.015}$	$0.797 \pm 0.084^{+0.074}_{-0.012}$	$0.819 \pm 0.079^{+0.053}_{-0.012}$
1.0-1.2	$0.758 \pm 0.043^{+0.089}_{-0.009}$	$0.776 \pm 0.038^{+0.063}_{-0.009}$	$0.795 \pm 0.026^{+0.042}_{-0.009}$
1.2-1.4	$0.648 \pm 0.033^{+0.067}_{-0.009}$	$0.627 \pm 0.028^{+0.049}_{-0.008}$	$0.604 \pm 0.026^{+0.024}_{-0.008}$
1.4-1.6	$0.469 \pm 0.023^{+0.037}_{-0.008}$	$0.511 \pm 0.022^{+0.033}_{-0.008}$	$0.521 \pm 0.022^{+0.023}_{-0.008}$
1.6-1.8	$0.422 \pm 0.020^{+0.039}_{-0.008}$	$0.381 \pm 0.017^{+0.021}_{-0.007}$	$0.409 \pm 0.018^{+0.015}_{-0.007}$
1.8-2.0	$0.334 \pm 0.016^{+0.027}_{-0.007}$	$0.323 \pm 0.015^{+0.014}_{-0.007}$	$0.276 \pm 0.012^{+0.009}_{-0.005}$
2.0-2.4	$0.209 \pm 0.008^{+0.010}_{-0.004}$	$0.192 \pm 0.007^{+0.006}_{-0.003}$	$0.201 \pm 0.007^{+0.003}_{-0.003}$
2.4-2.8	$0.127 \pm 0.005^{+0.003}_{-0.003}$	$0.112 \pm 0.005^{+0.002}_{-0.003}$	$0.111 \pm 0.004^{+0.002}_{-0.002}$
2.8-3.2	$0.078 \pm 0.004^{+0.002}_{-0.002}$	$0.069 \pm 0.003^{+0.002}_{-0.002}$	$0.063 \pm 0.003^{+0.002}_{-0.002}$
3.2-4.0	$0.040 \pm 0.002^{+0.001}_{-0.001}$	$0.038 \pm 0.002^{+0.001}_{-0.001}$	$0.034 \pm 0.001^{+0.001}_{-0.001}$
4.0-5.0	$0.014 \pm 0.001^{+0.001}_{-0.001}$	$0.014 \pm 0.001^{+0.001}_{-0.000}$	$0.011 \pm 0.001^{+0.000}_{-0.000}$

Table E.2.: continuing Table E.1

p_T/ y	2.98-3.16	3.16-3.34	3.34-3.52
0.6-0.8	$1.171 \pm 0.100^{+0.058}_{-0.029}$	$1.060 \pm 0.092^{+0.027}_{-0.043}$	$1.131 \pm 0.146^{+0.029}_{-0.176}$
0.8-1.0	$1.032 \pm 0.080^{+0.049}_{-0.015}$	$0.862 \pm 0.080^{+0.014}_{-0.013}$	$1.170 \pm 0.082^{+0.018}_{-0.058}$
1.0-1.2	$0.818 \pm 0.034^{+0.031}_{-0.009}$	$0.851 \pm 0.033^{+0.010}_{-0.010}$	$0.781 \pm 0.031^{+0.009}_{-0.009}$
1.2-1.4	$0.648 \pm 0.026^{+0.016}_{-0.008}$	$0.693 \pm 0.026^{+0.009}_{-0.008}$	$0.661 \pm 0.023^{+0.011}_{-0.008}$
1.4-1.6	$0.484 \pm 0.019^{+0.013}_{-0.006}$	$0.499 \pm 0.018^{+0.009}_{-0.007}$	$0.470 \pm 0.017^{+0.013}_{-0.006}$
1.6-1.8	$0.408 \pm 0.016^{+0.008}_{-0.007}$	$0.382 \pm 0.015^{+0.008}_{-0.006}$	$0.348 \pm 0.013^{+0.009}_{-0.005}$
1.8-2.0	$0.320 \pm 0.014^{+0.006}_{-0.007}$	$0.308 \pm 0.008^{+0.009}_{-0.006}$	$0.255 \pm 0.010^{+0.009}_{-0.004}$
2.0-2.4	$0.206 \pm 0.006^{+0.004}_{-0.004}$	$0.194 \pm 0.006^{+0.006}_{-0.003}$	$0.169 \pm 0.005^{+0.005}_{-0.003}$
2.4-2.8	$0.109 \pm 0.004^{+0.003}_{-0.002}$	$0.106 \pm 0.004^{+0.003}_{-0.002}$	$0.106 \pm 0.004^{+0.005}_{-0.002}$
2.8-3.2	$0.065 \pm 0.003^{+0.002}_{-0.002}$	$0.057 \pm 0.003^{+0.002}_{-0.001}$	$0.053 \pm 0.003^{+0.003}_{-0.001}$
3.2-4.0	$0.031 \pm 0.001^{+0.001}_{-0.001}$	$0.029 \pm 0.001^{+0.001}_{-0.001}$	$0.025 \pm 0.002^{+0.001}_{-0.001}$
4.0-5.0	$0.010 \pm 0.001^{+0.001}_{-0.000}$	$0.010 \pm 0.001^{+0.000}_{-0.000}$	$0.009 \pm 0.001^{+0.000}_{-0.000}$

Table E.3.: continuing Table E.2

p_T/ y	3.52-3.70	3.70-3.88	3.88-4.06
0.6-0.8	$1.341 \pm 0.158^{+0.034}_{-0.207}$	$1.164 \pm 0.157^{+0.030}_{-0.065}$	$1.341 \pm 0.193^{+0.120}_{-0.036}$
0.8-1.0	$0.816 \pm 0.075^{+0.013}_{-0.035}$	$1.065 \pm 0.075^{+0.018}_{-0.059}$	$0.975 \pm 0.115^{+0.018}_{-0.070}$
1.0-1.2	$0.785 \pm 0.032^{+0.010}_{-0.012}$	$0.690 \pm 0.031^{+0.010}_{-0.011}$	$0.760 \pm 0.039^{+0.013}_{-0.039}$
1.2-1.4	$0.609 \pm 0.023^{+0.012}_{-0.008}$	$0.561 \pm 0.022^{+0.010}_{-0.008}$	$0.531 \pm 0.027^{+0.012}_{-0.010}$
1.4-1.6	$0.484 \pm 0.018^{+0.016}_{-0.007}$	$0.433 \pm 0.017^{+0.011}_{-0.007}$	$0.409 \pm 0.021^{+0.016}_{-0.008}$
1.6-1.8	$0.336 \pm 0.013^{+0.008}_{-0.006}$	$0.315 \pm 0.014^{+0.011}_{-0.006}$	$0.279 \pm 0.014^{+0.011}_{-0.006}$
1.8-2.0	$0.231 \pm 0.010^{+0.006}_{-0.004}$	$0.228 \pm 0.011^{+0.009}_{-0.005}$	$0.213 \pm 0.011^{+0.007}_{-0.005}$
2.0-2.4	$0.164 \pm 0.005^{+0.007}_{-0.003}$	$0.140 \pm 0.005^{+0.006}_{-0.002}$	$0.131 \pm 0.006^{+0.003}_{-0.003}$
2.4-2.8	$0.082 \pm 0.002^{+0.004}_{-0.002}$	$0.078 \pm 0.004^{+0.003}_{-0.002}$	$0.070 \pm 0.004^{+0.004}_{-0.002}$
2.8-3.2	$0.059 \pm 0.003^{+0.004}_{-0.002}$	$0.049 \pm 0.003^{+0.002}_{-0.001}$	$0.039 \pm 0.003^{+0.006}_{-0.001}$
3.2-4.0	$0.022 \pm 0.001^{+0.001}_{-0.001}$	$0.019 \pm 0.001^{+0.002}_{-0.000}$	$0.022 \pm 0.002^{+0.003}_{-0.001}$
4.0-5.0	$0.008 \pm 0.001^{+0.001}_{-0.000}$	$0.007 \pm 0.001^{+0.001}_{-0.000}$	$0.007 \pm 0.002^{+0.000}_{-0.002}$

Bibliography

[1] A. D. Sakharov, *Violation of CP Invariance, C Asymmetry, and Baryon Asymmetry of the Universe*, *Pisma Zh. Eksp. Teor. Fiz.* 5 (1967) 32–35. JETP Lett. 5 (1967) 24.

[2] CDF Collaboration, D. Acosta et al., *Evidence for $B_s^0 \to \phi\phi$ Decay and Measurements of Branching Ratio and A_{CP} for $B^+ \to \phi K^+$*, *Phys. Rev. Lett.* 95 (Jul, 2005) 031801.

[3] CDF Collaboration, D. Acosta et al., *Updated Measurement of the $B_s^0 \to \phi\phi$ Branching Ratio Using 2.9 fb^{-1}*, CDF Public Note 10064, Feb, 2010, http://www-cdf.fnal.gov.

[4] CDF Collaboration, T. Aaltonen et al., *Measurement of Polarization and Search for CP-Violation in $B_s^0 \to \phi\phi$ Decays*, *Phys. Rev. Lett. (submitted)* (July, 2011) [arXiv:1107.4999].

[5] CDF Collaboration, D. Acosta et al., *First Search for T-violating Triple Products Asymmetries in $B_s^0 \to \phi\phi$ Decays*, CDF Public Note 10424, Apr, 2011, http://www-cdf.fnal.gov.

[6] G. Lüders, *Proof of the TCP theorem*, *Ann. Phys.* 2 (1957), no. 1 1–15.

[7] LHCb collaboration, R. Aaij et al., *Study of Triple Product Asymmetries in $B_s \to \phi\phi$ decays*, LHCb Conference Note LHCb-CONF-2011-052, CERN, Geneva, Aug, 2011.

[8] M. Lieng, *Studies of the Machine Induced Background, simulations for the design of the Beam Condition Monitor and implementation of the Inclusive ϕ Trigger at the LHCb experiment at CERN.* PhD thesis, TU Dortmund, 2011.

[9] T. Sjöstrand, S. Mrenna, and P. Skands, *PYTHIA 6.4 physics and manual*, *J. High Energy Phys.* 05 (May, 2006) 26, [hep-ph/0603175].

[10] LHCb collaboration, R. Aaij et al., *Prompt K_S production in pp collisions at $\sqrt{s} = 0.9$ TeV*, *Phys. Lett.* B693 (2010) 69–80, [arXiv:1008.3105].

[11] LHCb Collaboration, R. Aaij et al., *Measurement of J/ψ production in pp collisions at $\sqrt{s} = 7$ TeV*, *Eur. Phys. J. C* 71 (2011) 1645, [arXiv:1103.0423].

[12] LHCb Collaboration, R. Aaij et al., *Measurement of the $\bar{p}/p$ ratio in LHCb at $\sqrt{s}$ = 900 GeV and 7 TeV*, *LHCb-CONF-2010-009* (Aug, 2010).

[13] LHCb, R. Aaij et al., *Measurement of V^0 production ratios in pp collisions at $\sqrt{s} = 0.9$ and 7 TeV*, *JHEP* 08 (2011) 034, [arXiv:1107.0882].

[14] ACCMOR Collaboration, C. Daum et al., *Inclusive ϕ-meson production in 93 and 63 GeV hadron interactions*, *Nucl. Phys. B* 186 (1981), no. 2 205 – 218.

[15] E735 Collaboration, T. Alexopoulos et al., *ϕ meson production from $p\bar{p}$ collisions at $\sqrt{s} = 1.8$ TeV*, *Z. Phys. C* 67 (1995) 411–416.

[16] HERAb Collaboration, I. Abt et al., *K^{*0} and ϕ Meson production in Proton–Nucleus Interactions at $\sqrt{s} = 41.6$ GeV*, *Eur. Phys. J. C* 50 (2007) 315–328.

[17] ZEUS Collaboration, S. Chekanov et al., *Observation of the strange sea in the proton via inclusive ϕ-meson production in neutral current deep inelastic scattering at HERA*, *Phys. Lett. B* 553 (2003) 141–158, [hep-ex/0211025].

[18] ALICE Collaboration, K. Aamodt et al., *Strange particle production in proton-proton collisions at $\sqrt{s} = 0.9$ GeV with ALICE at the LHC*, *Eur. Phys. J. C* 71 (2011) 1594, [arXiv:1012.3257].

[19] PHENIX Collaboration, M. Naglis, *Anomalous ϕ Meson Suppression in Au+Au Collisions at $\sqrt{s_{NN}} = 200$ GeV Measured by the PHENIX Experiment at RHIC*, *Nucl. Phys. A* 830 (2009) 757c–760c, [arXiv:0907.4461].

[20] J. M. Cline, *Baryogenesis*, *ArXiv e-prints* (Sept., 2006) [hep-ph/0609145]. Lectures at Les Houches Summer School, 2006.

[21] M. Gavela et al., *Standard model CP violation and baryon asymmetry*, *Mod.Phys.Lett.* A 9 (1994) 795–810, [hep-ph/9312215].

[22] P. Schmüser, *Feynman-Graphen und Eichtheorien für Experimentalphysiker*. Springer, 1994.

[23] P. Langacker, *Structure of the standard model*, in *Precision Tests of the Standard Electroweak Model* (P. Langacker, ed.), p. 15. World Scientific Publ. Co., 1995. [hep-ph/0304186].

[24] W. Hollik, *Renormalization of the Standard Model*, in *Precision Tests of the Standard Electroweak Model* (P. Langacker, ed.), p. 37. World Scientific Publ. Co., 1995.

[25] A. J. Buras and M. K. Harlander, *A Top quark story: Quark mixing, CP violation and rare decays in the standard model*, in *Heavy Flavors* (A. Buras and M. Lindner, eds.), p. 58. World Scientific Publ. Co., 1992.

[26] S. Weinberg, *A Model of Leptons*, *Phys. Rev. Lett.* 19 (Nov, 1967) 1264–1266.

[27] H. Georgi and S. L. Glashow, *Unified Weak and Electromagnetic Interactions without Neutral Currents*, *Phys. Rev. Lett.* 28 (May, 1972) 1494–1497.

[28] D. J. Gross and F. Wilczek, *Asymptotically Free Gauge Theories. I*, *Phys. Rev. D* 8 (Nov., 1973) 3633–3652.

[29] H. David Politzer, *Asymptotic freedom: An approach to strong interactions*, *Phys. Rep.* 14 (Nov., 1974) 129–180.

[30] F. Englert and R. Brout, *Broken Symmetry and the Mass of Gauge Vector Mesons*, *Phys. Rev. Lett.* 13 (Aug, 1964) 321–323.

[31] G. S. Guralnik, C. R. Hagen, and T. W. B. Kibble, *Global Conservation Laws and Massless Particles*, *Phys. Rev. Lett.* 13 (Nov, 1964) 585–587.

[32] P. W. Higgs, *Broken Symmetries and the Masses of Gauge Bosons*, *Phys. Rev. Lett.* 13 (Oct, 1964) 508–509.

[33] I. I. Bigi and A. I. Sanda, *CP violation*, vol. 9 of *Camb. Monogr. Part. Phys. Nucl. Phys. Cosmol.* Cambridge University Press, 2000.

[34] G. Branco, L. Lavoura, and J. Silva, *CP Violation*, vol. 103 of *The International Series of Monographs on Physics*. Oxford University Press, 1999.

[35] C. S. Wu, E. Ambler, R. W. Hayward, D. D. Hoppes, and R. P. Hudson, *Experimental Test of Parity Conservation in Beta Decay*, *Phys. Rev.* 105 (Feb, 1957) 1413–1415.

[36] K. Kleinknecht, *Uncovering CP violation: Experimental clarification in the neutral K meson and B meson*, *Springer Tracts Mod. Phys.* 195 (2003) 1–142.

[37] J. H. Christenson, J. W. Cronin, V. L. Fitch, and R. Turlay, *Evidence for the 2π Decay of the K_2^0 Meson*, *Phys. Rev. Lett.* 13 (Jul, 1964) 138–140.

[38] J. Ellis, *Beyond the standard model with the LHC*, *Nature* 448 (07, 2007) 297–301.

[39] G. Salvini, *Introduction to the problems of the session AP2: Matter, dark matter and CP violation*, in *Proceedings of the Ninth Marcel Grossmann Meeting on General Relativity* (R. Jantzen, R. Ruffini, V. Gurzadyan, and U. di Roma, eds.), The Ninth Marcel Grossmann Meeting: On Recent Developments in Theoretical and Experimental General Relativity, Gravitation, and Relativistic Field Theories, World Scientific, 2002.

[40] S. P. Martin, *A Supersymmetry Primer*, *ArXiv e-prints* (1998) [hep-ph/9709356v6].

[41] N. Cabibbo, *Unitary Symmetry and Leptonic Decays*, *Phys. Rev. Lett.* 10 (Jun, 1963) 531–533.

[42] M. Kobayashi and T. Maskawa, *CP-Violation in the Renormalizable Theory of Weak Interaction*, *Progr. Theor. Phys.* 49 (1973), no. 2 652–657.

[43] A. J. Buras, *Flavour physics and CP violation*, *ArXiv e-prints* (2005) [hep-ph/0505175].

[44] Particle Data Group, K. Nakamura et al., *Review of Particle Physics*, *J. Phys. G* 37 (2010) 075021.

[45] L.-L. Chau and W.-Y. Keung, *Comments on the Parametrization of the Kobayashi-Maskawa Matrix*, *Phys. Rev. Lett.* 53 (Nov, 1984) 1802–1805.

[46] L. Wolfenstein, *Parametrization of the Kobayashi-Maskawa Matrix*, *Phys. Rev. Lett.* 51 (Nov, 1983) 1945–1947.

[47] C. Jarlskog, *Commutator of the Quark Mass Matrices in the Standard Electroweak Model and a Measure of Maximal CP Nonconservation*, *Phys. Rev. Lett.* 55 (Sep, 1985) 1039–1042.

[48] Heavy Flavor Averaging Group, D. Asner et al., *Results on Time-Dependent CP Violation, and Measurements Related to the Angles of the Unitarity Triangle: Winter 2011 (La Thuile & Moriond, Italy; Beauty, Netherlands; FPCP, Israel etc.)*, 2011, retrieved: 17.10.2011 from http://www.slac.stanford.edu/xorg/hfag/triangle/moriond2011/index.shtml.

[49] BABAR Collaboration, B. Aubert et al., *Measurement of Time-Dependent CP Asymmetry in $B^0 \to c\bar{c}K^{(*)0}$ Decays*, *Phys.Rev.* D 79 (2009) 072009, [arXiv:0902.1708].

[50] A. Poluektov on behalf of the Belle collaboration, *Recent EW results from Belle*, in *Moriond EW*, Mar, 2011.

[51] CDF Collaboration, T. Aaltonen et al., *First Flavor-Tagged Determination of Bounds on Mixing-Induced CP Violation in $B_s^0 \to J/\psi\phi$ Decays*, *Phys. Rev. Lett.* 100 (Apr, 2008) 161802, [arXiv:0712.2397].

[52] D0 Collaboration, V. M. Abazov et al., *Measurement of B_s^0 Mixing Parameters from the Flavor-Tagged Decay $B_s^0 \to J/\psi\phi$*, *Phys. Rev. Lett.* 101 (Dec, 2008) 241801, [arXiv:0802.2255].

[53] LHCb Collaboration, B. Adeva et al., *Roadmap for selected key measurements of LHCb*, *ArXiv e-prints* (2009), no. LHCb-PUB-2009-029 [arXiv:0912.4179].

[54] U. Nierste, *Three Lectures on Meson Mixing and CKM phenomenology*, *ArXiv e-prints* (Apr, 2009) 1–38, [arXiv:0904.1869].

[55] V. Weisskopf and E. Wigner, *Berechnung der natürlichen Linienbreite auf Grund der Diracschen Lichttheorie*, *Zeitschrift für Physik A Hadrons and Nuclei* 63 (1930) 54–73.

[56] Heavy Flavor Averaging Group, D. Asner et al., *Results for the PDG 2011 web update: B0 mixing: oscillations and mass difference*, 2011, retrieved: 17.10.2011 from http://www.slac.stanford.edu/xorg/hfag/osc/PDG_2011/#DMD.

[57] BABAR Collaboration, B. Aubert et al., *Measurement of the $\overline{B}^0$ lifetime and the $B^0\overline{B}^0$ oscillation frequency using partially reconstructed $\overline{B}^0 \to D^{*+}\ell^-\overline{\nu}_\ell$ decays*, *Phys. Rev. D* 73 (Jan, 2006) 012004, [hep-ex/0507054].

[58] Belle Collaboration, K. Abe et al., *Improved measurement of CP-violation parameters $\sin 2\phi_1$ and $|\lambda|$, B meson lifetimes, and B^0-$\overline{B}^0$ mixing parameter Δm_d*, *Phys. Rev. D* 71 (Apr, 2005) 072003, [hep-ex/0408111].

[59] CDF Collaboration, A. Abulencia et al., *Observation of $B_s^0 - \overline{B}_s^0$ Oscillations*, *Phys. Rev. Lett.* 97 (Dec, 2006) 242003, [hep-ex/0609040].

[60] BELLE Collaboration, Y. Nakahama et al., *Measurement of CP violating asymmetries in $B^0 \to K^+K^-K_S^0$ decays with a time-dependent Dalitz approach*, *Phys.Rev. D* 82 (2010) 073011, [arXiv:1007.3848].

[61] BABAR Collaboration, B. Aubert et al., *Measurement of CP-Violating Asymmetries in the $B^0 \to K^+K^-K_s^0$ Dalitz Plot*, arXiv:0808.0700.

[62] B. Andersson et al., *Parton Fragmentation and String Dynamics*, *Phys.Rept.* 97 (1983) 31–145.

[63] E. Norrbin and T. Sjöstrand, *Production and hadronization of heavy quarks*, *Euro. Phys. J.* C 17 (2000) 137–161.

[64] P. Z. Skands, *Tuning Monte Carlo generators: The Perugia tunes*, *Phys. Rev. D* 82 (Oct, 2010) 074018.

[65] M. Symalla, *Produktion von ϕ-Mesonen in inelastischen Proton-Kern-Wechselwirkungen*. Dissertation, Universität Dortmund, Mar, 2004.

[66] D. Perkins, *Introduction to high energy physics*. Cambridge University Press, 4 ed., 2000.

[67] CERN Communication Group, C. Lefèvre, *LHC: the guide*, Feb, 2009, http://cdsweb.cern.ch/record/1165534.

[68] L. Evans and P. Bryant, *LHC Machine*, *J. Instrum.* 3 (2008) S08001.

[69] ATLAS Collaboration, G. Aad et al., *The ATLAS Experiment at the CERN Large Hadron Collider*, *J. Instrum.* 3 (2008) 08003.

[70] CMS Collaboration, S. Chatrchyan et al., *The CMS experiment at the CERN LHC*, *J. Instrum.* 3 (2008) S08004.

[71] LHCb Collaboration, A. A. Alves Jr et al., *The LHCb Detector at the LHC*, *J. Instrum.* 3 (2008) S08005.

[72] ALICE Collaboration, K. Aamodt et al., *The ALICE experiment at the CERN LHC*, *J. Instrum.* 3 (2008) S08002.

[73] TOTEM Collaboration, G. Anelli et al., *The TOTEM Experiment at the CERN Large Hadron Collider*, *J. Instrum.* 3 (2008) S08007.

[74] LHCf Collaboration, O. Adriani et al., *The LHCf detector at the CERN Large Hadron Collider*, *J. Instrum.* 3 (2008) S08006.

[75] S. Catani et al., *QCD*, in *Proceedings of the Workshop on Standard Model Physics (and more) at the LHC* (M. L. Mangano and G. Altarelli, eds.), (Geneva), pp. 1–116, CERN, May, 2000. [hep-ph/0005025]. CERN-TH-2000-131.

[76] *The LHC sees its first circulating beam*, *CERN Courier* vol. 48 issue 8 (Oct, 2008). http://cerncourier.com/cws/archive/cern/48/8.

[77] M. Bajko et al., *Report of the Task Force on the Incident of 19th September 2008 at the LHC.*, LHC-PROJECT-Report-1168, CERN, Geneva, Mar, 2009.

[78] L. Rossi, *Superconductivity: its role, its success and its setbacks in the Large Hadron Collider of CERN*, *Supercond. Sci. Technol.* 23 (2010), no. 3 034001.

[79] C. Sutton, *The LHC is back: four remarkable weeks*, *CERN Courier* vol. 50 issue 1 (Jan/Feb, 2010). http://cerncourier.com/cws/archive/cern/50/1.

[80] S. Amato et al., *A Large Hadron Collider Beauty Experiment for Precision Measurements of CP Violation and Rare Decays*, Tech. Proposal CERN-LHCC-98-4, LHCC/P4, CERN, Geneva, Feb, 1998. Design adapted.

[81] S. Schleich, *FPGA based Data Acquisition and Beam Dump Decision System for the LHCb Beam Conditions Monitor*, Diploma Thesis, Exp. Phys. 5, Technische Universität Dortmund, Germany, 2008.

[82] P. Nason et al., *Bottom production*, *ArXiv e-prints* (Mar, 2000) [hep-ph/0003142].

[83] M. Pepe-Altarelli, *LHCb status and early physics prospects*, *Fortschritte der Physik* 58 (2010), no. 7-9 615–621.

[84] LHCb Collaboration, R. Antunes-Nobrega et al., *LHCb reoptimized detector design and performance*. Technical Design Report LHCb. CERN, 2003. CERN-LHCC-2003-030 LHCb-TDR-9.

[85] M. Alemia et al., *First operation of a hybrid photon detector prototype with electrostatic cross-focussing and integrated silicon pixel readout*, *Nucl. Instrum. Meth. A* 449 (2000), no. 1-2 48–59.

[86] M. Patel, *An Inclusive ϕ Stream for the LHCb High Level Trigger*, LHCb Note LHCb-2006-041, CERN, Geneva, Jul, 2006.

[87] S. White, R. Alemany-Fernandez, H. Burkhardt, and M. Lamont, *First Luminosity Scans in the LHC.*, in *Proceedings of 1st International Particle Accelerator Conference* (A. Noda et al., eds.), (Kyoto, Japan), pp. 486–487, Jun, 2010. http://cdsweb.cern.ch/record/1271694.

[88] V. Balagura, *Electroweak and QCD measurements at LHCb*, in *15th Lomonosov Conference on Elementary Particle Physics, Moscow, Russia*, Aug, 2011. http://cdsweb.cern.ch/record/1376421.

[89] S. van der Meer, *Calibration of the effective beam height in the ISR*, CERN-ISR-PO-68-31, CERN, Geneva, 1968.

[90] M. Ferro-Luzzi, *Proposal for an absolute luminosity determination in colliding beam experiments using vertex detection of beam–gas interactions*, *Nucl. Instrum. Methods Phys. Res., Sect. A* 553 (2005), no. 3 388 – 399.

[91] V. Balagura, *Notes on Van der Meer scan for absolute luminosity measurement*, *Nucl. Instrum. Methods Phys. Res., Sect. A* 654 (2011), no. 1 634 – 638, [arXiv:1103.1129].

[92] LHCb Collaboration, R. Aaij et al., *Absolute Luminosity Measurements at $\sqrt{s}$ = 7 TeV*, *J. Instrum. (submitted)* (Oct, 2011) [arXiv:1110.2866]. LHCb-PAPER-2011-015.

[93] I. Belyaev et al., *Handling of the generation of primary events in* GAUSS*, the LHCb simulation framework*, *Nuclear Science Symposium Conference Record (NSS/MIC)* (Nov, 2010) 1155.

[94] D. J. Lange, *The EvtGen particle decay simulation package*, *Nucl. Instrum. Meth. A* 462 (Feb, 2001) 152–155.

[95] S. Agostinelli et al., *G4–a simulation toolkit*, *Nucl. Instrum. Meth. A* 506 (2003), no. 3 250 – 303.

[96] G. A. Giurgiu, *B flavor tagging calibration and search for neutral B(s) meson oscillations in semileptonic decays with the CDF detector at Fermilab*. PhD thesis, Carnegie Mellon University, PA, USA, 2005. ISBN: 0542295881.

[97] H. G. Moser and A. Roussarie, *Mathematical methods for B^0_s $\bar{B}^0_s$ oscillation analyses*, *Nucl. Instrum. Meth. A* 384 (1997) 491–505.

[98] M. Calvi, G. Lanfranchi, O. Leroy, M. Musy, S. Poss, and S. Vecchi, *Calibration of flavour tagging with $B^+ \to J/\psi K^+$ and $B^0 \to J/\psi K^*$ control channels at LHCb*, LHCb Note LHCb-2009-020, CERN, Geneva, May, 2009.

[99] M. Calvi, O. Leroy, and M. Musy, *Flavour Tagging Algorithms and Performances in LHCb*, LHCb Note LHCb-2007-058, CERN, Geneva, May, 2007.

[100] A. Hoecker, P. Speckmayer, J. Stelzer, J. Therhaag, E. von Toerne, and H. Voss, *TMVA: Toolkit for Multivariate Data Analysis*, *PoS* ACAT (2007) 040, [physics/0703039].

[101] LHC Beam Operation Commitee, *Minutes of LBOC meeting held on 31st May 2011*, https://lhc-beam-operation-committee.web.cern.ch/lhc-beam-operation-committee.

[102] P. Koppenburg, *Nu, Mu and Pile-Up. The LHCb definitions of what we see and what we don't see*, 25.03.2011, retrieved: 12.04.2011 from https://twiki.cern.ch/twiki/bin/view/LHCb/NuMuPileUp.

[103] L. Collaboration, *LHCb Operations Plots Webpage*, 14.10.2011, design adapted, retrieved: 14.10.2011 from https://lbweb.cern.ch/groups/online/OperationsPlots/index.htm.

[104] LHCb collaboration, R. Aaij et al., *Measurement of* $\sigma(pp \to b\bar{b}X)$ *at* $\sqrt{(s)} = 7$ *TeV in the forward region*, *Phys. Lett. B* 694 (2010) 209–216, [arXiv:1009.2731].

[105] S. Barsuk and I. Belyaev, *The* $B_s^0 \to \phi\phi$ *reconstruction at LHCb*, LHCb Public Note LHCb-2003-094, CERN, Geneva, Oct, 2003.

[106] N. Styles, P. Clark, G. Cowan, F. Muheim, and Y. Xie, *Measuring the weak phase in the decay* $B_s^0 \to \phi\phi$ *at the LHCb experiment*, LHCb Public Note LHCb-PUB-2009-025, CERN, Geneva, Apr, 2010.

[107] G. Hartner, *VCTRAK: ZEUS Track & Vertex Reconstruction*, in *Videos and Transparencies of ZEUS Introductory Lectures* 15.07.2002, retrieved: 22.12.2009 from http://www-zeus.desy.de/lectures/vctrak_lecture.ps.

[108] S. Schleich, *Details of* $B_s^0 \to \phi\phi$ *stripping and MC09 studies*, in *CP measurements WG:* β_s *and mixing*, CERN, 17.09.2009. http://indico.cern.ch/getFile.py/access?contribId=5&resId=0&materialId=slides&confId=61824.

[109] S. Schleich, *Studies on* $B_s^0 \to \phi\phi$ *stripping*, in *CP measurements WG: beta-s and mixing*, CERN, 09.07.2009. https://indico.cern.ch/getFile.py/access?contribId=2&resId=0&materialId=slides&confId=61342.

[110] S. Schleich, $B_s^0 \to \phi\phi$ *stripping line*, in *Stripping Readiness Meeting*, CERN, 28.08.2009. https://indico.cern.ch/getFile.py/access?contribId=2&sessionId=0&resId=0&materialId=slides&confId=65374.

[111] S. Schleich, $B_s^0 \to \phi\phi$ *stripping on first data*, in *Stripping Workshop*, CERN, 17.12.2009. https://indico.cern.ch/getFile.py/access?contribId=19&resId=0&materialId=slides&confId=76164.

[112] S. Schleich, $B_s^0 \to \phi\phi$ *stripping update*, in *Trigger&Stripping meeting*, CERN, 25.01.2010. https://indico.cern.ch/getFile.py/access?subContId=3&contribId=1&resId=0&materialId=slides&confId=81335.

[113] S. Schleich, $B_s^0 \to \phi\phi$ *stripping line, rev. 125311*, 2011, http://svnweb.cern.ch/world/wsvn/lhcb/Stripping/trunk/Phys/StrippingSelections/python/StrippingSelections/StrippingBs2PhiPhi.py?rev=125311.

[114] J. He, *(on LHCb stripping mailing list)*, 11.06.2011, retrieved: 17.10.2011 from https://groups.cern.ch/group/lhcb-stripping/default.aspx.

[115] T. Blake and J. He, *Stripping 15 draft statistics*, 16.06.2011, retrieved: 17.10.2011 from https://twiki.cern.ch/twiki/bin/viewauth/LHCb/StrippingStatisticsStripping15draft.

[116] S. Amato, J. McCarron, F. Muheim, B. Souza de Paula, and Y. Xie, *LHCb's sensitivity to New CP-violating Phases in the Decay* $B_s \to \phi\phi$, LHCb Public Note LHCb-2007-047, CERN, Geneva, May, 2007.

[117] *MC09 Generation Statistics*, 31.03.2010, retrieved: 17.10.2011 from http://lhcb-release-area.web.cern.ch/LHCb-release-area/DOC/STATISTICS/MC09STAT/Generation_MC09-b5TeV-md100.html#13104011.

[118] *Automatic generation of Generator (and Simulation) Statistics Tables for 2010 production*, 07.01.2011, retrieved: 17.10.2011 from http://lhcb-release-area.web.cern.ch/LHCb-release-area/DOC/gauss/doc/UsersGuideStatMC10.php.

[119] P. Koppenburg et al., *Hlt2 efficiencies and rates*, 21.08.2009, retrieved: 12.04.2011 from https://twiki.cern.ch/twiki/bin/view/LHCb/Hlt2EffsRates.

[120] V. Gligorov (private communication), Jun, 2011.

[121] I. Dunietz, R. Fleischer, and U. Nierste, *In pursuit of new physics with B_s decays*, *Phys. Rev. D* 63 (2001) 114015, [hep-ph/0012219].

[122] I. Dunietz, H. Quinn, A. Snyder, W. Toki, and H. J. Lipkin, *How to extract CP-violating asymmetries from angular correlations*, *Phys. Rev. D* 43 (Apr, 1991) 2193–2208.

[123] J. D. Richman, *An Experimenter's Guide to the Helicity Formalism*, DOE research and development report CALT-68-1148, 1984.

[124] C.-W. Chiang and L. Wolfenstein, *Observables in the decays of B to two vector mesons*, *Phys. Rev. D* 61 (Mar, 2000) 074031.

[125] A. S. Dighe, I. Dunietz, and R. Fleischer, *Extracting CKM phases and $B_s - \bar{B}_s$ mixing parameters from angular distributions of nonleptonic B decays*, *Eur. Phys. J. C* 6 (1999) 647–662, [hep-ph/9804253].

[126] A. Ryd et al., *EvtGen: A Monte Carlo Generator for B-Physics*, Babar Analysis Document (BAD) 522, 2005.

[127] Heavy Flavor Averaging Group, D. Asner et al., *Averages of b-hadron, c-hadron, and tau-lepton Properties*, *ArXiv e-prints* (2010) [arXiv:1010.1589].

[128] BELLE Collaboration, K. F. Chen et al., *Measurement of polarization and triple-product correlations in $B \to \phi K^*$ decays*, *Phys. Rev. Lett.* 94 (2005) 221804, [hep-ex/0503013].

[129] BABAR Collaboration, B. Aubert et al., *Time-dependent and time-integrated angular analysis of $B \to \varphi K^0_S \pi^0$ and $\varphi K^{\pm}\pi^{\mp}$*, *Phys. Rev.* D78 (2008) 092008, [arXiv:0808.3586].

[130] CDF Collaboration, D. Acosta et al., *Measurement of the Polarization Amplitudes of the $B^0_s \to \phi\phi$ Decay*, CDF Public Note 10120, Apr, 2010, http://www-cdf.fnal.gov.

[131] F. James and M. Roos, *Minuit – a system for function minimization and analysis of the parameter errors and correlations*, *Comput. Phys. Commun.* 10 (1975), no. 6 343–367.

[132] W. Verkerke and D. Kirkby, *The RooFit toolkit for data modeling*, in *Proceedings of CHEP 03*, June, 2003. [physics/0306116].

[133] C. Langenbruch, U. Uwer, and S. Hansmann-Menzemer, *An unbinned likelihood fit for the measurement of ϕ_s in the decay $B^0_s \to J/\psi\phi$*, LHCb Public Note LHCb-2009-028, CERN, Geneva, Dec, 2009.

[134] G. Punzi, *Comments on Likelihood fits with variable resolution*, *ArXiv e-prints* (2004) [physics/0401045v1].

[135] LHCb Collaboration, R. Aaij et al., *Tagged time-dependent angular analysis of $B^0_s \to J/\psi\phi$ decays with the 2010 LHCb data*, LHCb Conference Note LHCb-CONF-2011-006, CERN, Geneva, May, 2011.

[136] R. Aaij et al., *Tagged time-dependent angular analysis of $B^0_s \to J/\psi\phi$ decays with the 2010 data*, LHCb Internal Note LHCb-ANA-2010-006 (draft v2), CERN, Geneva, May, 2010.

[137] R. Aaij et al., *Tagged time-dependent angular analysis of $B_s^0 \to J/\psi\phi$ decays with $\sim 337\,pb^{-1}$*, LHCb Internal Note LHCb-ANA-2011-036 (draft v4), CERN, Geneva, Oct, 2011.

[138] *Particle properties in MC09 and MC10*, retrieved: 17.10.2011 from `https://twiki.cern.ch/twiki/pub/LHCbPhysics/SettingsMc09/ParticleTable2009_NewBLifetimes.txt`.

[139] LHCb collaboration, R. Aaij et al., *Measurement of b-hadron masses with exclusive J/ψ decays in 2010 data*, LHCb Conference Note LHCb-CONF-2011-027, CERN, Geneva, May, 2011.

[140] T. Brambach, M. Kaballo, T. Karbach, F. Kruse, J. Merkel, S. Schleich, and J. Wishahi, *Measurement of the inclusive ϕ cross section in pp collisions at $\sqrt{s}$ = 7 TeV*, LHCb Analysis Note LHCb-ANA-2010-011, CERN, Geneva, Nov, 2010.

[141] T. Brambach, M. Kaballo, T. Karbach, F. Kruse, J. Merkel, S. Schleich, and J. Wishahi, *Measurement of the inclusive ϕ cross section in pp collisions at $\sqrt{s}$ = 7 TeV*, LHCb Analysis Note LHCb-ANA-2010-034, CERN, Geneva, May, 2011.

[142] LHCb Collaboration, R. Aaij et al., *Measurement of the inclusive ϕ cross-section in pp collisions at $\sqrt{s} = 7$ TeV with the LHCb experiment*, LHCb Conference Note LHCb-CONF-2010-014, Dec, 2010.

[143] LHCb Collaboration, R. Aaij et al., *Measurement of the inclusive ϕ cross-section in pp collisions at $\sqrt{s} =$ TeV*, *Phys. Lett. B* 703 (2011) 267–273, [`arXiv:1107.3935`].

[144] M. Gersabeck and P. Spradlin, *CM frame boost*, 2010, retrieved: 08.07.2010 from `https://twiki.cern.ch/twiki/bin/viewauth/LHCbPhysics/CharmCrossSection?redirectedfrom=LHCb.CharmCrossSection`.

[145] P. Hopchev, *LHCb Beam-Gas Imaging Results*, *CERN-Proceedings-2011-001* (Jul, 2011) [`arXiv:1107.1492`]. Presented at the LHC Lumi Days: LHC Workshop on LHC Luminosity Calibration, 13-14 January 2011, CERN, Geneva.

[146] LHCb Collaboration, R. Aaij et al., *Prompt K_s production in pp collisions at $\sqrt{s} = 0.9$ TeV*, *Phys. Lett. B* 693 (2010) 69–80, [`arXiv:1008.3105`].

[147] Particle Data Group, C. Amsler et al., *Review of particle physics*, *Phys. Lett.* B 667 (2008) 1–1340.

[148] *Brunel Releases*, retrieved: 17.10.2011 from `http://lhcb-release-area.web.cern.ch/LHCb-release-area/DOC/brunel/releases/`.

[149] T. Ruf (private communication), Jun, 2010.

[150] M. Kaballo, *Studies concerning the Acceptance of the LHCb Detector and the Measurement of the $pp \to \phi X$ Cross-Section at $\sqrt{s} = 7$ TeV with LHCb*, Diploma Thesis, Exp. Phys. 5, Technische Universität Dortmund, Germany, 2011.

[151] M. Kendall and A. Stuart, *Distribution theory*. No. vol. 1 in The advanced theory of statistics. Griffin, London, 3 ed., 1969.

[152] T. Brambach et al., *Measurement of the Inclusive ϕ Cross Section in pp Collisions at $\sqrt{s} = 7$ TeV*, in *41st Analysis and Software Week - Physics: Mature analysis review*, CERN, 15.09.2010. `https://indico.cern.ch/conferenceDisplay.py?confId=73580`.

[153] S. Miglioranzi and G. Corti, *Material Interaction Cross Section Studies*, LHCb Internal Note LHCb-INT-2011-002, CERN, Geneva, Jan, 2011.

[154] D. H. Wright et al., *Recent developments and validations in Geant4 hadronic physics*, *AIP Conf. Proc.* 867 (2006) 479–486.

[155] S. Hansmann-Menzemer et al., *Measurement of yield of K_s reconstructed with downstream tracks in 2009 data*, LHCb Analysis Note LHCb-ANA-2010-001, CERN, Geneva, Sep, 2010.

[156] P. Skands, *PYTHIA8: progress in soft and UE modeling*, in *Underlying-Event and Minimum-Bias Working Group Meeting*, LPCC, (LHC Physics Centre CERN), 08.02.2011.

[157] P. Skands priv. comm., Feb, 2011.

[158] A. Buckley, H. Hoeth, H. Lacker, H. Schulz, and J. E. von Seggern, *Systematic event generator tuning for the LHC*, *Eur. Phys. J.* C 65 (2010) 331–357, [arXiv:0907.2973].

[159] CMS Collaboration, V. Khachatryan et al., *Strange particle production in pp collisions at $\sqrt{s} = 900\,\text{GeV}$ and $7\,\text{TeV}$*, *J. High Energy Phys.* (2011) 1–40, [arXiv:1102.4282].